

**THE DEVELOPMENT OF A PARAFFIN WAX/NITROUS
OXIDE HYBRID ROCKET SLAB MOTOR**

by

Raisa Theba

Submitted in fulfilment of the academic requirements of

Master of Science

in Mechanical Engineering

School of Engineering

College of Agriculture, Engineering and Science

University of KwaZulu-Natal

Durban

South Africa

March 2019

Name of supervisors: Miss Kirsty Veale

Dr Clinton Bemont

PREFACE

The research contained in this dissertation was completed by the candidate while based in the Discipline of Mechanical Engineering, School of Agricultural, Earth and Environmental Sciences of the College of Agriculture, Engineering and Science, University of KwaZulu-Natal, Howard College, South Africa. The research was financially supported by The National Research Fund.

The contents of this work have not been submitted in any form to another university and, except where the work of others is acknowledged in the text, the results reported are due to investigations by the candidate.

Signed:

Date:

DECLARATION 1 - PLAGIARISM

I, Raisa Theba, declare that:

1. The research reported in this thesis, except where otherwise indicated, is my original research.
2. This thesis has not been submitted for any degree or examination at any other university.
3. This thesis does not contain other persons' data, pictures, graphs or other information, unless specifically acknowledged as being sourced from other persons.
4. This thesis does not contain other persons' writing, unless specifically acknowledged as being sourced from other researchers. Where other written sources have been quoted, then:
 - a. Their words have been re-written but the general information attributed to them has been referenced
 - b. Where their exact words have been used, then their writing has been placed in italics and inside quotation marks, and referenced.
5. This thesis does not contain text, graphics or tables copied and pasted from the Internet, unless specifically acknowledged, and the source being detailed in the thesis and in the References sections.

RTheba

Signed: Raisa Theba

Date: 11 March 2019

DECLARATION 2 - PUBLICATIONS

DETAILS OF CONTRIBUTION TO PUBLICATIONS that form part and/or include research presented in this thesis:

Publication 1:

Theba, R., Veale, K., & Bemont, C., (2015), An Investigation of Regression Rate in Paraffin-Based Hybrid Rocket Fuel Grains, Presentation and extended abstract, Stellenbosch, South Africa: International Aerospace Symposium of South Africa.

Publication 2:

Theba, R., Veale, K., & Bemont, C., (2016), Development of a Hybrid Rocket Slab Motor, 52nd AIAA/ASME/SAE/ASEE Joint Propulsion Conference, Salt Lake City, Utah, United States of America: American Institute of Aeronautics and Astronautics.

Publication 3:

Theba, R., Veale, K. L., & Bemont, C. P., (2017), Development of a Combustion Visualisation Hybrid Rocket Motor, SAIMEchE R&D Journal, Volume 33, Pages 97 – 104.

Associated Prior Publication 4:

Dlamini, M. A., Ramrathun, N., & Theba, R., (2014), Hybrid Slab Motor Visualisation Test Stand, BSc Dissertation, University of KwaZulu-Natal, Durban.

RTheba

Signed: Raisa Theba

Date: 11 March 2019

ACKNOWLEDGEMENTS

I would like to express my gratitude to my primary supervisor, Ms Kirsty Veale for her continued advice, support and encouragement throughout this project. I would further like to thank my second supervisor, Dr Clinton Bemont for his expertise and valuable insight.

I greatly appreciate the assistance and contribution from the workshop staff at the Mechanical Engineering Department, in particular Mr Sanil Mahabeer. I wish to thank my colleagues in the Aerospace Systems Research Group (ASReG) for their assistance with experiments and technical discussions, especially Udil Balmogim and Timothy Velthuysen. Special thanks to my colleague and friend, Chikhar S. Maharaj for his wealth of knowledge, insightfulness and support. My sincere gratitude to Dr Michael Brooks for his immense support and advice, and Mr Jean Pitot for his technical expertise. I would also like to thank them for assisting with the supervision of my testing.

A special thank you to Mr Yousuf Mahomed at Copalcor for kindly sponsoring the brass billet for this research.

My gratitude extends to the National Research Fund (NRF) for funding this research project, and to the Department of Science and Technology (DST) and the Council for Scientific and Industrial Research (CSIR) for their funding support.

Finally, my utmost appreciation to my family and friends, especially my parents and sister for always encouraging, motivating and supporting me. My dad has always provided excellent guidance throughout my academic career, without which this work would not have been possible.

ABSTRACT

Slab motors are used to determine and investigate the regression rate characteristics of hybrid rocket propellant combinations. This information is fundamental to the overall design and thus used to determine the payload, altitude and thrust parameters of a rocket.

The Phoenix Hybrid Sounding Rocket Programme in the University of KwaZulu-Natal's (UKZN) Mechanical Engineering Department uses paraffin wax and nitrous oxide in their series of hybrid sounding rockets. The regression rate behaviour of paraffin wax with nitrous oxide has not previously been investigated in slab motors.

This study focused on the regression rate behaviour and entrainment mechanism with regards to non-classical fuels including those with metal additives. This was used to gain a greater understanding of the increased regression rates associated with these fuels. The addition of metal additives, such as that of aluminium to fuel grains, was explored since the research suggested that it increases the regression rate of pure paraffin wax by 30%.

A hybrid rocket slab motor visualisation test stand was developed to observe and obtain regression rate data. The stand includes a feed system, injector and a combustion chamber. All the components were manufactured using brass and stainless steel materials for their nitrous oxide compatibility, strength, and thermal resistance. Quartz glass windows were incorporated into the combustion chamber design for visualisation purposes. Due to the presence of quartz glass the use of finite element analyses became critical and more complex in order to ensure that the glass could withstand the operating conditions of the slab motor. A side-glass spacer was implemented to minimise the effects of side burning and to observe the influence of regression rate. Tests were conducted at a 130 g/s oxidiser mass flow rate and an atmospheric chamber pressure. A data acquisition system using LabVIEW software was implemented to obtain tank readings for the duration of the burn and to ensure safe motor operation.

The regression rate of Sasolwax 0907 fuel was volumetrically determined and observed to be on average 3.74 mm/s. This shows a much higher regression rate than other paraffin wax compositions which have been found to regress at 1.5 mm/s. The characteristics of the entrainment process were validated for the investigated propellants, and the high regression rate mechanism of paraffin wax was observed in the liquid melt layer, droplet entrainment, and roll waves. Tests using aluminised wax fuel grains at atmospheric conditions proved to be unsuccessful with nitrous oxide as the oxidiser. A possible reason for this could be due to the aluminised fuel grains requiring increased heat transfer, therefore not producing sufficient vapourisation of the fuel. Moreover, decomposition of the oxidiser appeared to be inhibited by the combination of the oxidiser mass flow rate and the port area which prevented combustion.

TABLE OF CONTENTS

PREFACE	ii
DECLARATION 1 - PLAGIARISM.....	iii
DECLARATION 2 - PUBLICATIONS	iv
ACKNOWLEDGEMENTS	v
ABSTRACT.....	vi
TABLE OF CONTENTS.....	vii
LIST OF TABLES	xii
LIST OF FIGURES	xv
NOMENCLATURE.....	xix
CHAPTER 1: INTRODUCTION.....	1
CHAPTER 2: LITERATURE REVIEW	7
2.1 A brief history of hybrid rocketry	7
2.2 Overview of hybrid rocket propulsion	8
2.3 Hybrid rocket propellants.....	10
2.3.1 Nitrous Oxide	10
2.3.2 Sasolwax 0907	13
2.4 Regression rate theory	15
2.4.1 Classical regression rate theory.....	15
2.4.2 Non-classical regression rate theory	17
2.4.3 Regression rate enhancement techniques.....	20
2.4.3.1 Metal additives	20
2.4.3.2 Paraffin fuels	21
2.5 Regression rate studies	22
2.5.1 Pennsylvania State University (PSU).....	22
2.5.1.1 Slab Geometry Hybrid Motor (SGHM)	22
2.5.1.2 LGCP and XTC hybrid rocket motors	23

2.5.2 Tokai University.....	24
2.5.3 Stanford University	26
2.5.3.1 Pure paraffin.....	27
2.5.3.2 Blackened paraffin	27
2.5.3.3 SPIX-01.....	28
2.5.4 Beihang University.....	28
2.6 Literature discussion.....	31
CHAPTER 3: CONCEPTUAL DESIGN GENERATION	34
3.1 Glass material considerations.....	34
3.1.1 Polycarbonate.....	34
3.1.2 Borosilicate	35
3.1.3 Vycor.....	36
3.1.4 Quartz glass.....	37
3.2 Glass window concepts	38
3.2.1 Glass concept one – T-shape.....	38
3.2.2 Glass concept two - rectangular flat plate	39
3.2.3 Glass concept three – elongated oval concept.....	40
3.3 Combustion chamber material considerations.....	41
3.4 Combustion chamber motor concepts	42
3.4.1 Motor concept one.....	42
3.4.2 Motor concept two	45
3.4.3 Motor concept three	45
3.5 Gasket concepts.....	46
3.5.1 High-temperature silicone or gasket maker	46
3.5.2 Grease or oil	47
3.5.3 Viton.....	47
3.5.4 O-rings	47
3.5.5 Silicone sheet gaskets.....	48

3.6 Conceptual design discussion.....	48
CHAPTER 4: SLAB MOTOR DESIGN AND MANUFACTURE.....	51
4.1 Analytical Modelling.....	51
4.2 Aluminium Fuel Grain Mould.....	54
4.3 Fuel grain casting	55
4.4 Feed system layout	55
4.5 Manifold.....	57
4.6 Injectors	58
4.7 Combustion motor components.....	60
4.7.1 Geometry.....	61
4.7.2 Fuel grain fixing plate	64
4.7.3 Side panels	64
4.7.4 Top bulkhead.....	65
4.7.5 Injector and nozzle bulkheads.....	66
4.7.6 Maximum heat transfer	69
4.8 Quartz glass windows.....	70
4.9 Side-glass spacer	71
4.10 Silicone gaskets	71
4.10.1 Bolt calculations.....	72
4.10.2 Klinger Expert gasket design software.....	72
4.11 Finite element analyses	73
4.12 Igniters.....	78
4.13 Discussion	78
CHAPTER 5: CONTROL SYSTEM AND EXPERIMENTAL SETUP	80
5.1 The control panel.....	80
5.2 Experimental setup	83
CHAPTER 6: TESTING AND RESULTS	85
6.1 Testing methodology - sequence and parameters.....	85

6.1.1 Cold flow tests.....	85
6.1.2 Hot fire pure paraffin wax fuel grains	86
6.1.3 Hot fire 40% aluminised wax fuel grains.....	86
6.1.4 Additional tests.....	86
6.2 Cold flow testing	87
6.3 Hot fire tests with pure paraffin wax.....	87
6.3.1 Preliminary hot fire test 1 (SH002)	88
6.3.2 Hot fire tests 2 to 4 (SH003 to SH005)	90
6.3.3 Hot fire tests 5 to 12 (SH006 to SH013)	93
6.4 Hot fire tests with 40% aluminium additives	97
6.4.1 Hot fire test 13 to 16 (SH014 to SH017).....	97
6.5 Pure paraffin wax with 5 bar nozzle (SH018)	98
6.5.1 Hot fire test 17.....	98
CHAPTER 7: ANALYSIS AND DISCUSSION	100
7.1 Cold flow analysis	100
7.2 Preliminary hot fire test discussion	101
7.3 Successful hot fire tests discussion.....	101
7.3.1 Property analysis	103
7.3.2 Regression rate data	106
7.3.2.1 Oxidiser mass flow rates	106
7.3.2.2 Port area	109
7.3.2.3 Oxidiser mass flux.....	110
7.3.2.4 Regression rates	110
7.3.2.5 Ballistic coefficients.....	113
7.4 Unsuccessful hot fire tests	114
7.5 Entrainment Mechanism.....	116
CHAPTER 8: CONCLUSION	119
CHAPTER 9: FUTURE TESTING	122

9.1 Atmospheric tests for pure wax with e-matches.....	122
9.2 Atmospheric tests for 40% Al wax with e-matches	122
9.3 Pressurised tests.....	122
APPENDIX 2A	131
APPENDIX 4A	133
APPENDIX 4B	149
APPENDIX 4C	163
APPENDIX 4D	168
APPENDIX 4E	171
APPENDIX 4F.....	173
APPENDIX 4G	186
APPENDIX 4H.....	192
APPENDIX 5A	208
APPENDIX 5B	213
APPENDIX 7A	219
APPENDIX 7B	222

LIST OF TABLES

Table 2.1: Hybrid rocket advantages over liquid and solid rockets - comparison chart (SPG, 2012)	8
Table 2.2: Nitrous oxide properties (Dlamini, et al., 2014)	13
Table 2.3: Physical and chemical properties of Sasolwax 0907 (Genevieve, 2013)	14
Table 2.5: SU Test summary (Chandler et al., 2012)	27
Table 3.1: Mechanical properties of Polycarbonate (Boedeker, 2016)	35
Table 3.2: Mechanical properties of Borosilicate	36
Table 3.3: Mechanical properties of Vycor (Corning, 2015), (Grace Construction Products, 2012)	37
Table 3.4: Mechanical properties of Quartz Glass	38
Table 3.5: Properties of Stainless Steel 304 L	41
Table 3.6: Properties of Brass (Copper Development Association, 2017), (E-Z Lok, 2016)	42
Table 3.7: Viton gasket properties gaskets (Natal Gaskets, 2011)	47
Table 3.8: Silicone sheet gasket properties (Natal Gaskets, 2011)	48
Table 4.1: Assumptions for experimental calculations	51
Table 4.2: Pure paraffin wax parameters	53
Table 4.3: 40% aluminised paraffin wax parameters	54
Table 4.4: Discharge coefficients for respective orifice diameters	59
Table 4.5: Theoretical oxidiser mass flow rates	59
Table 4.6: Combustion chamber final dimensions (Theba, et al., 2017)	62
Table 4.7: Constants for nozzle calculations	67
Table 4.8: Nozzle diameter calculated for each chamber pressure	67
Table 4.9: Constants for Stainless Steel 304L (AK Steel Corporation, 2007)	69
Table 4.10: Constants for Brass C22000 (Copper Development Association, 2017)	69
Table 4.11: Constants for Quartz Glass (Heraeus Quarzglas, 2015)	70
Table 5.1: Pressure gauges and descriptions	81
Table 6.1: Combustion Results	88

Table 6.2: Initial, final and percentage mass change of fuel grain per test	91
Table 6.3: Initial, final and percentage length change of fuel grain per test	92
Table 6.4: Initial, final and percentage width change of fuel grain per test	92
Table 6.5: Initial, final and percentage thickness change of fuel grain per test	92
Table 7.1: Mass and volume comparison table	103
Table 7.2: Oxidiser mass flow rates determined from tank measurement graphs.....	108
Table 7.3: Total port areas for each successful test calculated from individual areas	110
Table 7.4: Oxidiser mass fluxes for each successful test based on oxidiser mass flow rates and port areas	110
Table 7.5: Volume differences for each test	111
Table 7.6: Time-averaged regression rates for each test with 5 seconds burn time	111
Table 7.7: Regression rates with 8.5 seconds burn time	112
Table 7.8: Typical values for the ballistic coefficients a and n , for hybrid motors (Genevieve, 2013)	113
Table 7.9: Ballistic Coefficient a calculated from measured parameters and a range of n determined from literature.....	114
Table 2A.9.1: Typical hybrid propellant combinations (Chiaverini & Kuo, 2007)	131
Table 2A.9.2: Nitrous oxide compatibility (Dlamini, et al., 2014)	132
Table 4A.9.1: Table of constants for pure paraffin wax	133
Table 4A.9.2: Table of constants for 40% aluminised paraffin wax.....	133
Table 4A.9.3: Table of constants for pure paraffin wax	136
Table 4A.9.4: Table of constants for 40% aluminised paraffin wax.....	136
Table 4A.9.5: Table of constants for pure paraffin wax	139
Table 4A.9.6: Table of constants for 40% aluminised paraffin wax.....	139
Table 4A.9.7: Table of constants for pure paraffin wax	142
Table 4A.9.8: Table of constants for 40% aluminised wax	142
Table 4B.9.1: Constants required for injector calculations	149
Table 4C.9.1: Constants for pressure loss calculations	163
Table 4D.9.1: Constants for pure paraffin wax	168

Table 4D.9.2: Constants for 40% aluminised paraffin wax	168
Table 4E.9.1: Constants for Stainless Steel 304L	171
Table 4E.9.2: Constants for Brass.....	171
Table 4E.9.3: Constants for Quartz Glass	171
Table 4F.9.1: Table of constants 1	173
Table 4F.9.2: Table of constants 2	176
Table 7A.9.1: Initial, final, change and average dimensions for the first successful hot fire test	219
Table 7A.9.2: Initial, final, change and average dimensions for the second successful hot fire test	219
Table 7A.9.3: Initial, final, change and average dimensions for the third successful hot fire test	220
Table 7A.9.4: Final mass calculations for the first successful hot fire test	220
Table 7A.9.5: Final mass calculations for the second successful hot fire test	220
Table 7A.9.6: Final mass calculations for the third successful hot fire test.....	220
Table 7A.9.7: Volumetric differences before and after the first successful hot fire test.....	221
Table 7A.9.8: Volumetric differences before and after the second successful hot fire test.....	221
Table 7A.9.9: Volumetric differences before and after the third successful hot fire test.....	221

LIST OF FIGURES

Figure 1.1: Motor configurations of solid, liquid and hybrid rockets (Chiaverini & Kuo, 2007).	1
Figure 2.1: Space Ship One (SPG, 2012).....	7
Figure 2.2: Hybrid Rocket Configuration (Chandler, 2012).....	9
Figure 2.3: Schematic of the Diffusion Process (SPG, 2012).....	16
Figure 2.4: Diffusion-limited combustion in a turbulent boundary layer (Chandler, 2012)	16
Figure 2.5: Sketch of the droplet entrainment mechanism (Chandler, 2012)	18
Figure 2.6: Schematic of SGHM with diagnostic devices (Chiaverini, et al., 2000)	22
Figure 2.7: Linear regression rates of paraffin-based solid fuel formulations in comparison with Stanford University curve fit (Evans et al., 2009).....	24
Figure 2.8: The schematic of the experimental set-up (Nakagwa et al., 2009).....	25
Figure 2.9: Schematic model of the regression mechanism of a paraffin-based solid fuel (Nakagwa et al., 2009).....	25
Figure 2.10: Stanford's HSM (Chandler et al., 2012)	26
Figure 2.11: Roll waves in blackened paraffin (Chandler et al., 2012)	28
Figure 2.12: Droplets in blackened paraffin (Chandler et al., 2012).....	28
Figure 2.13: SP1X combustion instability (Chandler et al., 2012)	28
Figure 2.14: Effect of Al addition on regression rate behaviour (Sun et al., 2014)	30
Figure 2.15: Axial variation of regression rate (Sun et al., 2014).....	30
Figure 3.1: Three-dimensional view of T-shaped glass	39
Figure 3.2: Section view showing placement of T-shaped glass	39
Figure 3.3: Three-dimensional view of rectangular glass	40
Figure 3.4: Section view showing placement of rectangular flat plate glass	40
Figure 3.5: Concept three - elongated oval shape	41
Figure 3.6: Combustion chamber concept one – section view.....	43
Figure 3.7: Combustion chamber concept one – side view.....	44
Figure 3.8: Welding joints for inner panels of combustion chamber.....	44
Figure 3.9: Combustion chamber section view final design (Theba, et al., 2017).....	46

Figure 3.10: Combustion chamber side view final design (Theba, et al., 2017).....	46
Figure 4.1: Pure paraffin wax fuel grain	53
Figure 4.2: 40% aluminised wax fuel grain	53
Figure 4.3: Aluminium fuel grain mould	55
Figure 4.4: Schematic of the feed system layout (Maharaj, et al., 2018).....	56
Figure 4.5: Manifold Engineering Drawings	57
Figure 4.6: Isometric drawings of manifold.....	57
Figure 4.7: Discharge coefficients (Biblarz & Sutton, 2001)	58
Figure 4.8: Injector engineering drawings	60
Figure 4.9: 3 D view of injectors	60
Figure 4.10: Machined brass combustion chamber base.....	62
Figure 4.11: Recess for glass	63
Figure 4.12: Isometric view of combustion chamber showing the recesses for the windows with chamfered edge	63
Figure 4.13: Chamber base - side view	64
Figure 4.14: Fuel grain fixing plate - isometric view.....	64
Figure 4.15: Side panels – isometric view	65
Figure 4.16: Top bulkhead – isometric view	65
Figure 4.17: Front bulkhead – isometric view	66
Figure 4.18: Injector - manifold assembly – side view	66
Figure 4.19: 2.5 bar nozzle bulkhead – front view.....	68
Figure 4.20: Manufactured combustion chamber assembly (Theba, et al., 2017)	68
Figure 4.21: Quartz glass (14 mm thick) – front view	70
Figure 4.22: Side-glass spacer a) clear b) shaded	71
Figure 4.23: Silicone gasket – front view	72
Figure 4.24: Silicone properties (Natal Gaskets, 2011)	73
Figure 4.25: Coefficients of thermal expansion	74
Figure 4.26: Outline of all parameters	74

Figure 4.27: Design points and resulting closure values.....	75
Figure 4.28. Pressure versus Closure curve (Theba, et al., 2017).....	75
Figure 4.29. Fixed support for gasket applied around the edges.....	76
Figure 4.30. Pressure applied to centre portion of glass exposed within the combustion chamber	76
Figure 4.31. Total deformation results	77
Figure 4.32. Equivalent stress results.....	77
Figure 4.33: Igniter assembly using an E-match.....	78
Figure 5.1: Feed system layout and components	80
Figure 5.2: Control panel graphical user interface	81
Figure 5.3: Control terminal right-hand side.....	82
Figure 5.4: Test stand setup	83
Figure 6.1: E- match igniter configuration 1	89
Figure 6.2: SH002 – Minimal burning at leading edge of paraffin wax fuel grain.....	89
Figure 6.3: SH002 – Cracked paraffin wax fuel grain	89
Figure 6.4: SH003 – Uneven burning of the fuel grain (more from the left than the right).....	90
Figure 6.5: SH003 – Paraffin wax fuel grain with dip and uneven burning	90
Figure 6.6: SH004 – Smooth paraffin wax fuel grain	91
Figure 6.7: SH005 – Burnt paraffin wax fuel grain	91
Figure 6.8: Setup of side-glass spacer, silicone gaskets and RTV	93
Figure 6.9: E-match igniter configuration 3 with larger match heads and in a different orientation	94
Figure 6.10: E-match igniter configuration 4 with different orientation of pyrotechnic head facing the fuel grain	94
Figure 6.11: SH012 – Pyrotechnic igniter with pure paraffin wax at atmospheric pressure.....	95
Figure 6.12: SH013 – Alternative pyrotechnic igniter position	95
Figure 6.13: SH007 – Evidence of combustion in unsuccessful firing - frame 1	96
Figure 6.14: SH007 – Evidence of combustion in unsuccessful firing - frame 2	96
Figure 6.15: SH007 – Evidence of combustion in unsuccessful firing - frame 3	96

Figure 6.16: 40% aluminised wax with side-glass spacer and e-match	97
Figure 6.17: E-match igniter configuration 2 - stacking of match heads on e-match	98
Figure 6.18: SH018 – Cracked glass.....	99
Figure 7.1: Smoothened tank measurement for cold flow test.....	100
Figure 7.2: Disfigured fuel grain.....	101
Figure 7.3: Combustion chamber section view indicating portion of fuel grain covered by chamber billet (Theba, et al., 2017)	102
Figure 7.4: Fuel grain mass changes before and after burn	103
Figure 7.5: Average length differences along the furthest ends of each fuel grain.....	104
Figure 7.6: Averaged width variation along widest sections of each fuel grain	105
Figure 7.7: Average thickness measurements at tallest points.....	106
Figure 7.8: Test 1 - Tank measurements	107
Figure 7.9: Test 1 - Smoothened tank measurements	107
Figure 7.10: Test 2 - Smoothened tank measurements	107
Figure 7.11: Test 3 - Smoothened tank measurements	108
Figure 7.12: Individual port areas used in oxidiser mass flux calculations	109
Figure 7.13: Liquid melt layer on the surface of the pure paraffin wax fuel grain (SH005)	117
Figure 7.14: Roll waves in pure paraffin wax fuel grain	117
Figure 7.15: Droplets being entrapped into the flame zone for pure paraffin.....	117
Figure 7.16: Zoomed in view of droplets.....	117

NOMENCLATURE

Roman

a	Regression rate coefficient
A	Area [m ²]
B	Blowing parameter
d	Diameter [m]
D	Diameter [m]
e	Roughness coefficient [m]
E	Young's Modulus [GPa]
f	Friction factor
F	Force [N]
g	Acceleration due to gravity [m ² /s]
G	Mass flux [kg/m ² s]
h	Heat
h_e	Effective heat
h_m	Effective heat
H	Head loss [m]
I	Current
k	Loss coefficient
l	Length [m]
L	Latent heat
m	Mass [kg]
\dot{m}	Mass flow rate [kg/s]
M	Mass burning rate [g/s]
N	Number of holes

P	Pressure [Pa]
Pr	Prandtl number
Q	Heat transfer [kW]
\dot{Q}	Heat flux [W/m ²]
r	Resistance per metre length [Ω /m]
\dot{r}	Regression rate [m/s]
R	Gas constant
Re	Reynolds number
S	Steel
t	Thickness [m]
T	Temperature [K]
v	Velocity [m/s]
V	Volume [m ³]
V	Voltage [V]
\dot{V}	Volumetric flow rate [m ³ /s]
w	Width [w]
x	Axial position in the combustion port
Y	Yield percentage

Greek

α	Dynamic pressure exponent
β	Blowing coefficient
γ	Specific heat ratio
ε	Strain
η	Kinetic viscosity
κ_g	Gas phase conductivity

λ	Thermal conductivity [W/mK]
μ	Dynamic viscosity [Ns/m ²]
ξ	Dynamic thickness exponent
ρ	Density [kg/m ³]
ρ_t	Melted fuel density
σ	Stress [MPa]
τ	Torque [Nm]
ν	Combustion gas viscosity
Ω	Resistance [Ω]

Subscripts

a	Ambient
ave	Average
a_{ent}	Entrainment parameter
A_t	Bolt stressed area [m ²]
b	Bolt
bd	Bore diameter [m]
bl	Bore length [m]
b_t	Burn time [s]
c	Convection
cc	Combustion chamber pressure [MPa]
cl	Clamping
C	Compression
C_d	Coefficient of discharge
C_h	Heat transfer coefficient
$\frac{C_H}{C_{H0}}$	Blocking factor

C_f	Skin friction coefficient
C_{f0}	Skin friction coefficient without blowing
C_l	Specific heat
C_p	Specific heat capacity [J/kgK]
C_{pl}	Specific heat of melted fuel at constant pressure
ent	Entrance
$exit$	Exit
f	Fuel
$flux$	Flux
F_r	Roughness parameter
g	Gas
ge	Groove
gs	Glass
gt	Gasket
i	Preload/initial tension
inj	Injector
k_{th}	Thermal conductivity
l	Loss
l, bar	Loss in bar
l, Pa	Loss in Pascals
m	Melting point
max	Maximum
o	Original
ol	Orifice length
ox	Oxidiser

<i>rad</i>	Radiation
<i>rec</i>	Recess
<i>s</i>	Seal
<i>set</i>	Compression set
<i>sh</i>	Shank
S_p	Proof strength [MPa]
<i>t</i>	Total
<i>tt</i>	Throat
T_1	Absolute temperature
u_∞	General melted fuel flow velocity
<i>v</i>	Vaporisation
<i>w</i>	Wire

Superscripts

<i>n</i>	Oxidiser mass flux coefficient
<i>m</i>	Ballistic coefficient

Abbreviations

<i>ABS</i>	Acrylonitrile-Butadiene-Styrene
<i>CEA</i>	Chemical Equilibrium with Applications
<i>EVA</i>	Ethylene-vinyl acetate
<i>GOX</i>	Gaseous oxygen
<i>GUI</i>	Graphical user interface
<i>HRM</i>	Hybrid rocket motor
<i>HSM</i>	Hybrid slab motor
<i>HTPB</i>	Hydroxyl-terminated Polybutadiene
<i>LGCP</i>	Long Grain Center Perforated
<i>LOX</i>	Liquid oxygen

<i>O/F</i>	Oxidiser to fuel ratio
<i>PSU</i>	Pennsylvania State University
<i>SF</i>	Safety factor
<i>STP</i>	Standard temperature and pressure
<i>SU</i>	Stanford University
<i>TU</i>	Tokai University
<i>XTC</i>	X-ray Translucent Casing

CHAPTER 1: INTRODUCTION

A rocket propulsion system in which the propellant components exist in different physical states prior to combustion is known as a hybrid rocket propulsion system. Solid rocket motors consist of the fuel and oxidiser pre-mixed into a single hard propellant grain. Liquid rocket engines comprise of the fuel and oxidiser, usually cryogenic and at low pressures, in the liquid phase (Chiaverini & Kuo, 2007). Hybrid rockets are a combination of solid and liquid motors adopting characteristics of both. Figure 1.1 (Chiaverini & Kuo, 2007) illustrates the configurations of the three rocket engines.

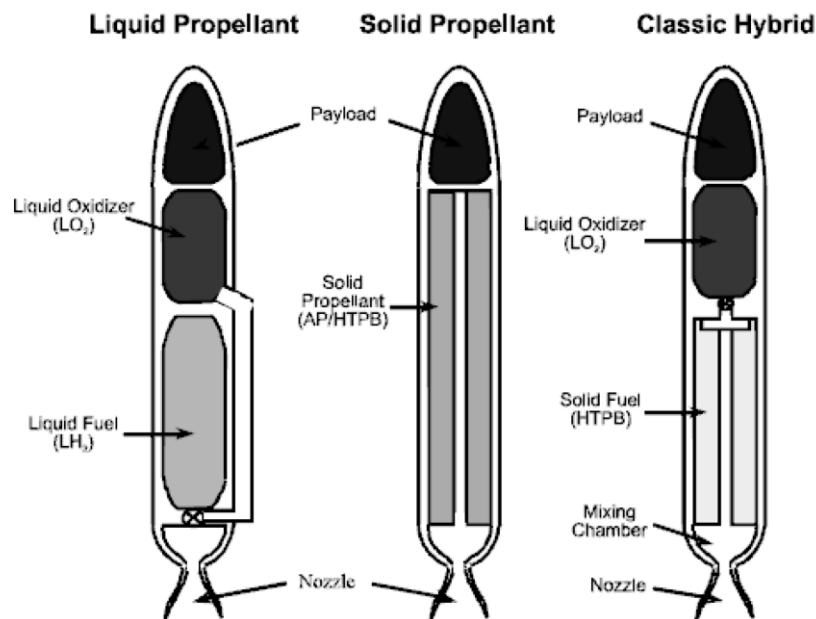


Figure 1.1: Motor configurations of solid, liquid and hybrid rockets (Chiaverini & Kuo, 2007)

There are several advantages to hybrid rockets that distinguish them from the traditional liquid or solid rocket propulsion systems. These include simplified throttling, safety and shutdown, propellant versatility, reliability and low cost. Disadvantages of hybrid rockets include low regression rates and combustion efficiencies, slow transients and oxidiser to fuel (O/F) shifts (Chiaverini & Kuo, 2007). This resulted in investigative studies into non-classical hybrid fuels such as paraffin wax.

Classical fuels such as HTPB rely on the diffusion flame theory for burning. They require complex multi-port fuel grain designs to deliver the required thrust due to low fuel regression rates. The adoption of paraffin wax, a non-classical fuel, replaces these fuel grains with simple, single port geometries (Chandler, et al., 2012). Paraffin wax has therefore increasingly been investigated because it relies on the droplet entrainment mechanism resulting in superior regression rate properties and combustion stability (Karabeyoglu, et al., 2002). Regression rate

refers to how fast the fuel burns in a direction perpendicular to the solid fuel surface (Theba, et al., 2016).

The solid fuel regression rate is one of the key parameters which influences the choice of propellant combination and the overall hybrid rocket motor design (Kumar & Ramakrishna, 2014), (Cai, et al., 2013). Understanding the regression rate of a hybrid rocket motor is therefore vital to the propulsion systems performance.

The rocket thrust (Equation 1.1) explains that the exhaust mass at high velocity generates thrust.

$$F = (\dot{m}_{ox} + \dot{m}_f)V_e + (P_e - P_o)A_e$$

(Equation 1.1)

The oxidiser mass flow in hybrid propulsion systems includes the mass from the fuel and from the oxidiser. Rocket thrust and the total mass flow rate of the propellants are proportional. An increase in the fuel's mass flow rate for a given oxidiser mass flow rate will enhance the propellant regression rate and therefore improve the resultant thrust of the motor (see (Equation 1.2)). Regression rate is therefore significant in hybrid propulsion design because relates directly to the total mass flow rate (Theba, et al., 2017).

$$\dot{m}_f = \rho A_e \dot{r}$$

(Equation 1.2)

The regression rate of a hybrid propulsion system influences factors such as thrust levels, O/F ratio shifts, specific impulse, additive concentrations and overall motor design. From a performance standpoint, hybrid rockets in general have a higher specific impulse than solid rockets, and a density impulse greater than liquid bi-propellant rockets (Patnala, et al., 2012), (Theba, et al., 2017). The specific impulse is defined as the total impulse produced for a given propellant weight or the efficiency of a rocket using a particular propellant (Hall, 2015). The impulse density uses the density of the propellants to measure the impulse obtained from a given volume of propellant (Young, 2014).

Paraffin wax has about a three times greater regression rate than classical hybrid fuels (Evans, et al., 2009). This is because paraffin-based fuels generate extensive droplet entrainment into the oxidiser stream. The degree to which the entrainment develops assists in its ability to combust upon reaction with the oxidiser (Karabeyoglu, et al., 2002).

Studies have shown that with the addition of metal additives, the performance capabilities of a hybrid rocket motor can potentially be improved by increasing the regression rate and density specific impulse of the fuel (Biblarz & Sutton, 2001). An increased density specific impulse would provide better performance of a rocket motor for a given volume of propellant (Young,

2014). Pennsylvania State University (PSU) experimentally determined that Silberline® aluminium particles, for example, induced an increase in the regression rate of pure paraffin wax by approximately 30% (Evans, et al., 2009). This is due to the aluminium particles enabling an increased heat transfer on the solid fuel surface, thus causing an increased regression rate (Evans, et al., 2009). Studies have also shown that an optimum formulation of 40% aluminium additives with 60% paraffin wax greatly improves the total impulse and hence regression rate of a hybrid rocket motor (McCormick, et al., 2005).

Although these fuels have revolutionised hybrid rocketry (Nakagawa, et al., 2009), the low density of paraffin wax fuels can reduce launch vehicle performance while it results in a relatively good thrust-to-weight ratio. This has been observed by the Discipline of Mechanical Engineering's Aerospace System's Research Group (ASReG), which developed the Phoenix Hybrid Sounding Rocket Programme (Genevieve, 2013).

The ultimate goal of the Phoenix Hybrid Sounding Rocket Programme is to develop a series of reusable, low-to-medium hybrid sounding rockets to fill the void that exists in South African launch capacity. The lack of a launch facility in the Southern hemisphere, and South Africa in particular, has hindered the advancement of local scientific communities and services such as the CSIR, the South African Weather Service and the Hermanus Magnetic Observatory. International procurement of these services is expensive and may be reduced or eliminated with a national launch capability (Genevieve, 2013).

The Phoenix Programme has built a hybrid sounding rocket using pure paraffin wax as fuel and nitrous oxide as oxidiser (Genevieve, 2013). Typically, increased regression rates would enable decreased fuel mass with increased performance characteristics (Karabeyoglu, 2008). By comparing the pure paraffin wax fuel grain regression rates with the aluminised fuel grains, an optimum formulation for increasing regression rates can be obtained without compromising the safety, simplicity and cost benefits that hybrid rockets provide (Karabeyoglu, 2008), (Theba, et al., 2017).

Sasol sponsors Sasolwax 0907 ($C_{50}H_{102}$) for the Phoenix programme. The behaviour of this wax composition has not previously been studied in a slab motor and is therefore unique. The long carbon chain length (50) of Sasolwax 0907 has shown to be a high-performance propellant (Karabeyoglu, et al., 2002). Further, its regression rate is untested with nitrous oxide at low oxidiser mass fluxes. Nitrous oxide is the oxidiser of choice in the Phoenix Programme because of its decomposition properties, availability, safety, and low cost. It is also easily stored and relatively safe to handle (Lohner, et al., 2006).

The proposed project aimed to develop a hybrid rocket slab motor visualisation test stand to experimentally determine and investigate the regression rate behaviour and combustion

mechanism of paraffin wax-based hybrid rocket fuel grains with nitrous oxide. The study focused on pure Sasolwax 0907 fuel grains including those with aluminium additives at atmospheric pressure. The combustion chamber, which housed a surface burning fuel grain included windows to visually observe the regression rate and combustion characteristics. The slab motor was designed to make use of an existing feed system and motor support, dedicated to a cylindrical lab-scale hybrid motor. The combustion chamber had to be easily modified to accommodate different oxidiser mass flow rates and combustion pressures.

The hybrid slab motor (HSM) aims to emulate a segment of the combustion reaction in a typical configuration of a hybrid rocket motor. Additional experiments on the same motor and their results will be used in a future study to determine the ballistic coefficients pertaining to the regression rate equation. These coefficients are vital for the performance characterisation and design of hybrid rockets utilising this particular propellant combination. This will in turn assist in the development of hybrid sounding rockets in the Phoenix Hybrid Sounding Rocket Programme.

A chapter overview of the thesis follows.

The literature survey in Chapter 2 discusses the progression of hybrid rockets to date and explains the structure of hybrid rockets in comparison to liquid and solid rockets. The properties of the propellant combination in this research were explored. The regression rate theory details the empirical derivation of the regression rate laws and the combustion mechanism which enhances the regression rate properties of non-classical fuels compared to classical fuels. Reference is made to slab motor testing conducted by Stanford University (SU) on a combination of paraffin wax and oxygen and illustrates their findings with regards to the entrainment mechanism. Studies at Tokai University (TU) investigate the effects of ethylene-vinyl acetate (EVA) on the viscosity and hence regression rate of a hybrid rocket motor. Pennsylvania State University (PSU) have conducted slab motor testing with HTPB and oxygen whereas their cylindrical lab-scale experiments include those with paraffin-based fuels. Beihang University's investigations focused on developing a numerical model and slab motor testing with HTPB-based fuel grains.

Chapter 3 entails the conceptual developments of the principle motor components. Safety aspects surrounding the tests were integral to the experimental process therefore different combustion chamber designs were proposed. Material options such as polycarbonate, borosilicate and vycor for the glass windows were explored. The required properties included excellent clarity, high-temperature resistance and strength. The costs and availability associated with the suggested materials posed a challenge in sourcing the glass windows. A sealing mechanism was essential to ensure that the combustion chamber performed at the required pressures. Viton, silicone and gasket maker were considered as seals for this purpose.

Iterative calculations were performed to obtain the fuel grain dimensions, oxidiser mass flow rates, oxidiser mass fluxes, and regression rates. The data acquired from NASA CEA and literature discussed in Section 2.5, provided the O/F ratios and ideal regression rates for the propellant combination implemented. The results from these calculations were used to determine the combustion chamber and injector designs. The slab motor design and manufacturing process are given in detail in Chapter 4.

The control and data acquisition were developed using LabVIEW software and is outlined in Chapter 5. This provided an interface to conduct safe testing, as well as to specify testing parameters such as burn time, ignition delay and purge time. The safety measures outlined in this chapter were also incorporated in the event of an emergency such as a system malfunction. A termination button was implemented to immediately stop the automatic sequence and empty out the nitrous oxide from the run tank. A distribution box was secured onto the test stand and included the wiring, Arduino boards and microcontrollers controlled with LabVIEW. The experimental setup is also discussed in this chapter.

Chapter 6 discusses the experimental methodology and procedures. A total of 6 tests were initially proposed and were dependent on time constraints and the success of the experiments. These experiments were used to confirm the repeatability and validity of the paraffin wax/nitrous oxide propellants at atmospheric pressure in a slab motor. Pure paraffin wax and 40% aluminised fuel grains were initially investigated at an oxidiser mass flow rate of 130 g/s and atmospheric conditions. Additional testing and the testing sequence parameters would be governed by the results of these experiments.

The results of the hot fire tests are also briefly discussed in Chapter 6. The ignition of nitrous oxide and paraffin wax was problematic under atmospheric conditions, in particular for aluminised fuel grains. Successful runs were only achieved with the presence of side burning of pure paraffin wax fuel. This resulted in the fuel grains being burnt along three different planes instead of burning being restricted to the top surface. The results from tests with different igniter configurations, 40% aluminised fuel grains and a pressurised test is also given in this chapter.

Chapter 7 discusses the results presented in Chapter 6. The graphs obtained from cold flow tests were used to verify the safety and operation of all components in the feed system. The injector oxidiser mass flow rate and error margin of the load cell were also determined from this test. The differences in the successful fuel grains were discussed and the respective oxidiser mass flow rates determined. Regression rates were thus calculated volumetrically. The entrainment mechanism was also observed via analysis of high speed and high-resolution video footage. Additional experiments would provide a better understanding of this behaviour and would

improve the accuracy of the results. Possible explanations for the failed experiments were also given.

Chapters 8 and 9 provide conclusions and an experimental methodology for future testing.

The classification of the regression rate behaviour of paraffin-based fuel grains will provide an opportunity to develop hybrid rockets with reduced mass fractions while at the same time achieving greater launch vehicle performance (Theba, et al., 2017).

CHAPTER 2: LITERATURE REVIEW

2.1 A brief history of hybrid rocketry

The company Starstruck was formed in 1981 and developed a liquid oxygen (LOX)/HTPB large sounding rocket motor called Dolphin. It was successfully launched in 1984 and produced a thrust of almost 160 kN. The flight, however, was terminated shortly after launch as the oxidiser valve froze after 3 seconds (Chiaverini & Kuo, 2007). Dolphin achieved its desired outcome despite the component failure.

In 1985, Starstruck was renamed AMROC. The company adopted a LOX/HTPB propellant combination and conducted 124 static scalable tests. The most successful was a 334 kN thrust motor which was incorporated into the single engine test (SET-1) Koopman Express sounding rocket (Chiaverini & Kuo, 2007). It was launched in 1989 and experienced similar problems with the oxidiser valve as Dolphin and therefore had inadequate thrust for lift-off (Chiaverini & Kuo, 2007).

After 1995 the Environmental Aerospace Corporation (eAc) created the Hyperion Sounding Rocket program. Nitrous oxide and HTPB were used as self-pressurised oxidiser and fuel respectively. A single port grain was used to increase the burning surface area and the result was a 205 second specific impulse. The first test of the sounding rocket attained an altitude of almost 8 km by replacing the oxidiser with ballast. The other two tests were able to achieve 36.5 km and 33.8 km with the full propellant load (Chiaverini & Kuo, 2007).

The Lockheed Martin Corporation flew a LOX/HTPB multiport fuel grain motor in December 2002 which successfully produced an initial thrust of 267 kN, reaching an altitude of 71 km. Scaled Composites and SpaceDev fired a nitrous oxide/HTPB suborbital vehicle called Space Ship One in 2003 which attained a thrust of 890 kN (Chiaverini & Kuo, 2007).



Figure 2.1: Space Ship One (SPG, 2012)

2.2 Overview of hybrid rocket propulsion

This section details the motor function of hybrid rockets, describing the difference between solid and liquid rockets as well as the configuration of a hybrid. It also discusses the propellant combination and properties used in this research, regression rate theory, and previously developed slab motors.

Hybrid rockets acquire some of the advantages and disadvantages of solid and liquid rocket engines and provide further unique benefits. In a liquid rocket motor, both the liquid oxidiser and liquid fuel are fed from two injection streams and mixed in a pre-combustion chamber before entering the combustion chamber itself. Solid rockets on the other hand consist of fuel and oxidiser, that are molecularly bonded, or intimately mixed as a single bulk solid (Chandler, 2012). Hybrid rockets generally consist of a liquid oxidiser fed from an oxidiser tank which flows over a solid fuel grain that is housed in the combustion chamber. Hybrids reduce the complexities of liquid rockets and the lack of controlled ignition in solid rockets. They also have increased design flexibility due to their independence of chamber pressure (Chandler, et al., 2012). Their inherent safety has been one of the key factors in major research conducted in this field. Table 2.1 (SPG, 2012) lists the advantages of hybrid rockets over solid and liquid rockets.

Table 2.1: Hybrid rocket advantages over liquid and solid rockets - comparison chart (SPG, 2012)

	Solid Rockets	Liquid Rockets
Simplicity	Chemically simpler	Mechanically simpler
	Tolerant of processing errors	Tolerant of fabrication errors
Safety	Reduced chemical explosion hazard	Reduced fire hazard
		Less prone to hard starts
Operability	Throttling, start/stop/restart capability	Operation requires only a single liquid
Performance	Higher specific impulse	Higher fuel density
		Easy inclusion of high energy additives
Environmental	No perchlorates required	Solid fuel presents reduced contamination hazard
	Non-toxic exhaust products	
Cost	Reduced development costs	
	Reduced recurring costs	

As mentioned in Chapter 1, the disadvantages of hybrid rocket engines include low regression rates, reduced combustion efficiencies, slow transients and O/F ratio shifts (Chiaverini & Kuo, 2007). Conventional hybrid propellants burn slowly in comparison to solid rocket motors. They often require complex multiport fuel grains to improve performance which creates design complexities (Karabeyoglu, et al., 2002). Incomplete mixing is also a drawback in hybrid motors compared to solid and liquid rocket engines. This is due to the large boundary diffusion flame which reduces the impulse efficiencies (Chiaverini & Kuo, 2007). The O/F shift also reduces the

performance of a hybrid motor because of the increase in port diameter throughout the burn. Delayed ignition and throttling result in slow transients which additionally affect the performance of a hybrid rocket motor (Humble, et al., 1995).

A typical hybrid rocket configuration is depicted in Figure 2.2 (Chandler, 2012). The oxidiser tank of a hybrid rocket motor feeds the oxidiser into the injector via pressurisation. A valve which is opened at the end of the injector enables the oxidiser to travel into the combustion chamber where the solid fuel grain, often cylindrical in shape with a concentric port through its length, is situated. An igniter provides the heat required to initiate the combustion. Within the combustion chamber, the combustion gas expands rapidly and passes through a convergent-divergent nozzle. The momentum created by the hot gasses creates a force on the motor and propels the rocket.

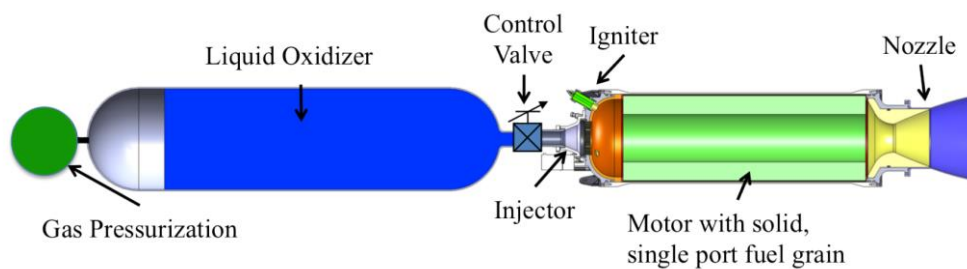


Figure 2.2: Hybrid Rocket Configuration (Chandler, 2012)

The combustion chamber in a hybrid rocket propulsion system provides the location for both solid fuel grain storage and propellant combustion. The chamber design is therefore dependent on the fuel grain configuration. The length and port diameter or port height (for slab motors) are chosen based on the respective fuel grain dimensions.

A longer combustion chamber offers the opportunity for more stable combustion as there is more room for even mixing of propellants (Biblarz & Sutton, 2001). A longer port length however, has also shown to sometimes decrease the regression rate of some propellants due to the axial dependence which is reliant on the motor configuration (Biblarz & Sutton, 2001). Pre and post combustion chamber lengths are selected based on the motor requirements and propellants.

Pre-combustion chambers are often used in large hybrid rocket motors or when multiport fuel grains are employed. Pre-combustion chambers provide even mixing and greater uniformity of the oxidiser stream before they pass through the multiport fuel grain (Biblarz & Sutton, 2001). For single port fuel grains, the pre-combustion chamber would ensure sufficient room for dispersion of the oxidiser before mixing with the fuel grain. In the case of nitrous oxide, this would ensure improved decomposition.

Post-combustion chambers are not often used because they cause severe erosion of the chamber material due to the combustion products. More lining is required to prevent burn-through thus

increasing the mass of the system (Biblarz & Sutton, 2001). These disadvantages outweigh the benefit of complete burning that the post-combustion chamber offers but is dependent on the choice of propellants.

As mentioned in Chapter 1, single port non-classical fuels are increasingly being used in hybrids as they have high volumetric efficiency and result in fewer design complexities in the system. They however require long length/diameter ratios compared to multiport fuel grains to increase combustion efficiency (Biblarz & Sutton, 2001).

Injection of the oxidiser into the combustion chamber can take place in one of two ways, either with direct injection or injection into a pre-combustion chamber (Biblarz & Sutton, 2001). Multiport fuel grains require injection into a pre-combustion chamber to enable even mixing prior to combustion. Single port fuel grains however, generally adopt the direct injection method into the fuel grain port. This reduces the need for homogenised oxidiser streams (Biblarz & Sutton, 2001) thereby decreasing the design complexities.

There are multiple ways to ignite a hybrid rocket system. Larger motors often acquire a solid rocket motor pyrograin or a small solid rocket motor embedded in the chamber near the outlet of the injector (Biblarz & Sutton, 2001). Pyrotechnic igniters are most often used because they are reliable. Electrical ignition is also sometimes employed (Biblarz & Sutton, 2001). These ignition methods will be considered for the hybrid rocket slab motor.

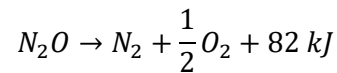
2.3 Hybrid rocket propellants

Hybrid rocket propellants have the benefits of both solid and liquid propulsion systems combined because of the two-phase requirements, which therefore provides a large inventory of propellant combinations (Biblarz & Sutton, 2001). Table 2A.9.1 in Appendix 2A gives typical hybrid rocket propellant combinations and their O/F ratios. Propellants are usually selected based on a number of characteristics such as cost, performance, density of storage conditions, toxicity, corrosivity, stability, as well as chemical and material properties. Other factors such as ability to ignite upon contact, or hypergolicity, and combustion products are also considered (Biblarz & Sutton, 2001). This section focuses on the two propellants used in the Phoenix Hybrid Sounding Rocket Programme, namely nitrous oxide and Sasolwax 0907.

2.3.1 Nitrous Oxide

Nitrous oxide is an odourless and colourless introduced to rocket science as an oxidiser by Robert Goddard in 1914 (Biblarz & Sutton, 2001). Its cost, safety, availability and handling advantages have made it very popular as an oxidiser in many rocket programmes such as the Hypertec by eAc in Space Ship One, and in the NASA/Stanford Peregrine effort (Dyer, et al., 2007).

In spite of its low-density impulse and moderate specific impulse, nitrous oxide is a preferred oxidiser for hybrid rocketry because of its operational simplicity, its non-toxicity and stability under room temperature conditions, and its high density and low pressures during storage (Biblarz & Sutton, 2001). It is relatively safe and easier to handle compared to oxidisers such as LOX. It is also known for its exothermic decomposition reaction which produces large amounts of energy. This energy is beneficial in terms of motor performance and stability but makes it susceptible to chemical explosion hazards. The reaction is shown in (Equation 2.1) (Biblarz & Sutton, 2001). Nitrous oxide can easily be broken down into its constituents to produce nitrogen and oxygen, which is beneficial during rocket flights (Buitrago, 2014).



(Equation 2.1)

Nitrous oxide is a self-pressurising gas at atmospheric conditions and therefore eliminates the need for pumps or external pressurisation systems. Heating of the ullage is necessary to achieve required mass flow rates because the boil-off pressure varies with temperature. Hard starts, back shocks, and a loss of pressure can cause adiabatic compression. This occurs across the injector during idle, filling, and cold flow tests. This can result in deflagration, or detonation of the nitrous oxide and hence catastrophic consequences. The reduced pressure differential across the injector initiates boiling of the nitrous oxide. The oxidiser injection may then become less stable and harder to predict or control. The boiling liquid consists of gas pockets which produce a compressible system and leads to a ‘pulsing’ effect. The compressibility of nitrous oxide and boiling can be minimised by the following methods (Buitrago, 2014):

1. Filling the ullage with an inert gas such as nitrogen, helium, or argon. This increases the pressure of the tank but depending on the gas used, may have adverse effects on the system’s performance.
2. Feeding the pressurising gas into the emptying vessel from an external tank to maintain the pressure.
3. Implementing a high flow pressure regulator to the system to keep the pressure constant and provide a more smooth and predictable performance.
4. Implementing positive displacement by using a piston or bladder, which separates the liquid, and gas.
5. Pre-pressurising the nitrous oxide system to eliminate boiling the liquid across the injector.

Certain situations and materials can cause nitrous oxide to be extremely sensitive to shock. These include nitrous oxide reaching its supercritical state in which it becomes a supercritical fluid at

36°C and therefore compressible (Buitrago, 2014). The interaction with hydrocarbons and iron oxide also presents shock-sensitive circumstances. Precautions therefore have to be taken when designing a hybrid rocket system that uses nitrous oxide as the oxidiser to prevent contact with incompatible materials that may result in explosions.

The following safety recommendations have been suggested when dealing with nitrous oxide propulsion systems (Space Propulsion Group, Inc., 2012):

- The area surrounding the testing should be marked and blocked off, and personnel should be a safe distance away.
- Supercharging is favourable as nitrous oxide blow down systems can be potentially hazardous if burnt in the vapour phase.
- A vertical arrangement of the oxidiser tanks is recommended to ensure that the vapour from the ullage is always separated from the combustion chamber by a liquid layer.
- The igniter should be switched on before the nitrous oxide flow is enabled to prevent build-up in the combustion chamber.
- Small concentrations of nitrous oxide are sensitive in nature and therefore careful cleaning procedures should be implemented.
- Components such as valves, O-rings, gaskets and other materials used in the system should all be nitrous oxide compatible.
- Fuel contamination, especially in liquid form, can result in catastrophic failure.

The propulsion system should be designed to minimise the possibility of a decomposition event occurring. Table 2.2 shows the properties of nitrous oxide and Table 2A.9.2 in Appendix 2A shows the nitrous oxide compatibility chart.

Table 2.2: Nitrous oxide properties (Dlamini, et al., 2014)

Molecular Weight	Molecular weight:	44.013 g/mol
Solid Phase	Melting point:	-90.82 °C
	Latent heat of fusion (1.013 bar at melting point):	148.57 kJ/kg
Liquid Phase	Liquid density (1.013 bar at boiling point):	1230.458 kg/m ³
	Boiling point (1.013 bar):	-88.47 °C
	Latent heat of vaporisation (1.013 bar at boiling point):	374.286 kJ/kg
	Vapour pressure (at 20°C):	50.525 bar
Critical Point	Critical temperature:	36.37 °C
	Critical pressure:	72.45 bar
	Critical density:	452.011 kg/m ³
Gaseous Phase	Gas density (1.013 bar at boiling point):	2.982 kg/m ³
	Gas density (1.013 bar at 15°C):	1.8724 kg/m ³
	Compressibility factor (1.013 bar at 15°C):	0.99391
	Specific gravity:	1.53
	Specific volume (1.013 bar at 25°C):	0.553 m ³ /kg
	Heat capacity at constant pressure (1.013 bar at 25°C):	0.0389 kJ/(kgK)
	Heat capacity at constant volume (1.013 bar at 25°C):	0.304 kJ/(kgK)
	The ratio of specific heats (1.013 bar at 25°C):	1.2804
	Viscosity (1.013 bar at 0°C):	13.631 µPas
	Thermal conductivity (1.013 bar at 0°C):	16.464 mW/mK

2.3.2 Sasolwax 0907

Paraffin wax is an odourless, non-irritating, non-sensitising, whitish microcrystalline solid. It is often used in cosmetic products such as creams, lipsticks and lip care to adjust the hardness or softness of the product. It is also sometimes used as a gum base, in food coatings, and as confectionary dividing agent.

The technical term for the paraffin wax used in UKZN's Phoenix Programme is Sasolwax 0907 or pentacontane. It is an alkane. Its chemical formula is C₅₀H₁₀₂ (Genevieve, 2013) and is a solid at room temperature. Its congealing point is between 83 °C and 94 °C (Sasol Performance Chemicals, 2015).

Physical and chemical properties are given in Table 2.3 (Genevieve, 2013).

Table 2.3: Physical and chemical properties of Sasolwax 0907 (Genevieve, 2013)

		C₃₁H₆₄	C₅₀H₁₀₂
Molecular Weight	g/mol	436.8	703.4
Enthalpy of Formation	J/mol	-697200	-1438200
Melting Temperature	K	339.6	381
Boiling Temperature	K	727.4	544
Vaporisation Temperature	K	-	558
Density - Solid Phase	kg/m ³	930	900
Density - Liquid Phase	kg/m ³	654.4	720
Heat of Fusion	J/kg	167200	221000
Heat of Vaporisation	J/kg	163500	-
Dynamic Viscosity - Liquid Phase	Pa.s	0.00065	0.0047
Thermal Conductivity - Liquid Phase	W/m K	0.12	0.246
Specific Heat - Solid Phase	J/kg K	2030	2000
Specific Heat - Liquid Phase	J/kg K	2920	3000
Surface Tension - Liquid Phase	N/m	0.0071	-

Paraffin wax has many advantages: it is non-toxic, non-hazardous, non-explosive, and recyclable. It is also an inert substance that makes it easy to handle and therefore saves manufacturing and transportation costs because it can be produced on site. Sasolwax 0907 does not require polymerisation or curing agents and has an infinite shelf life (Sasol Performance Chemicals, 2015). The combustion products usually consist of carbon dioxide and water.

Paraffin wax's high regression rate properties are particularly appealing for hybrid rocket motors because of the entrainment mechanism it exhibits (as discussed in Section 2.2). It is hydrophobic and therefore additives can be used to alter the material properties resulting in throttleable control of the propulsion system and enhanced regression rates. This fuel's performance is comparable to kerosene in liquid rocket engines as it has a slightly higher specific impulse and is 17% denser (Cantwell, et al., 2010).

A paraffin wax fuel grain is often cast using a centrifugal process. The liquid wax is poured into a mould and a centrifugal force is applied during solidification which assists in providing a crack-free and void-free fuel grain. The wax has a cooling shrinkage of 15-25% (DeSain, et al., 2009), and this contributes to the formation of the central port which is moulded from a round bar, positioned concentrically in the mould.

Sasolwax 0907 has remarkable benefits over other classical fuels but is not without limitations. It is a brittle substance and potentially prone to cracking under motor vibration. Structural and mechanical problems are also associated with paraffin-based fuels since the integrity of the fuel grain is reduced with burning (McCulley, 2012). The wax tends to soften and slough; these assists in the ejection of the melted fuel before combustion during axial launch loads (McCulley, 2012).

2.4 Regression rate theory

Hybrid rocket motors have many advantages over solid rocket motors and liquid rocket engines, namely; safety, low cost and environmental friendliness. As mentioned in Chapter 1, the performance is hindered by a critical parameter called the regression rate. The regression rate is the rate at which the fuel grain recedes over its length and is measured in units of velocity (Theba, et al., 2017).

Regression rate studies are crucial to the physical dimensions of the hybrid system as it affects the performance capabilities, thrust levels and hence overall design (Theba, et al., 2017). The use of high regression rate non-classical fuels such as paraffin wax, with regression rate enhancement techniques, show great potential in a wide variety of applications such as launch vehicle performance, solar system exploration, and space tourism (Theba, et al., 2017).

This section focuses on classical and non-classical regression rate theories.

2.4.1 Classical regression rate theory

Conventional hybrid rockets use classical fuels which burn via a combustion process that results in sublimation, pyrolysis and vaporisation of the fuel. This process is known as the turbulent diffusion flame theory and is associated with low regression rates as the fuels burn too slowly. This hampers the performance capabilities of the motor. A schematic of the diffusion process is given in (SPG, 2012). Multiport fuel grains or a larger burning surface area of the fuel, are generally used to increase the regression rate. The work conducted by Marxman, Gilbert, Muzzy and Wooldridge in the 1960's established that the classical regression rate model is highly dependent on diffusion-limited combustion (Marxman, et al., 1963).

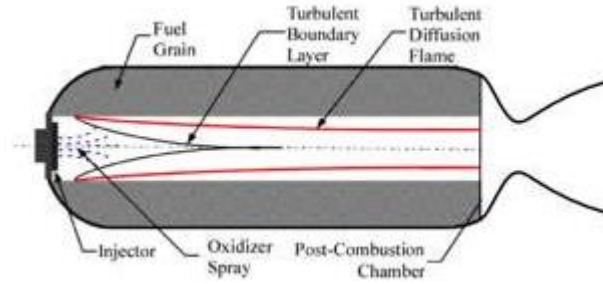


Figure 2.3: Schematic of the Diffusion Process (SPG, 2012)

The combustion behaviour exhibited by hybrid motors differs greatly from solid and liquid rocket engines. The mixing of both liquids before the chamber and a molecularly bonded solid fuel grain provide a relatively stable O/F ratio in liquid and solid motors respectively (Biblarz & Sutton, 2001). In comparison, the cylindrically shaped fuel grain in a hybrid has an axial dependency due to fuel build-up along the length of the fuel grain (Biblarz & Sutton, 2001). As the fuel burns, the increasing port diameter results in an O/F shift (Chiaverini & Kuo, 2007).

Diffusion-limited combustion is modelled as a turbulent diffusion flame whereby the reactions occur in an infinitely thin flame zone within the boundary layer. Combustion is dominated by the heat transfer from the flame to the fuel surface (Chandler, 2012), (Theba, et al., 2017). Figure 2.4 (Chandler, 2012) depicts the combustion process and includes several other key factors. The boundary layer comprises of two zones, dominated below by the fuel and above by the oxidiser. A combustible concentration, slightly less than the stoichiometric amount, initiates the reaction. Marxman determined that the flame height resides between 10% to 20% of the boundary layer thickness (Chandler, 2012). In reference to the model, the flame zone is assumed to be infinitely thin as the reaction rate is assumed to be infinitely fast, governed by thermal diffusion rendering chemical kinetics negligible (the Damköhler number is much larger than 1). The addition of mass causes destabilisation and results in the typical Reynold's transition being reduced to 10^4 (Chandler, 2012).

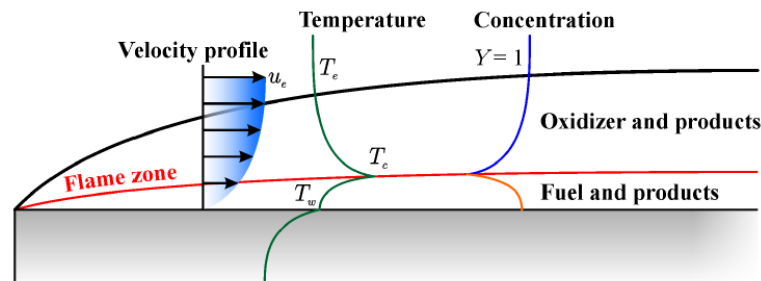


Figure 2.4: Diffusion-limited combustion in a turbulent boundary layer (Chandler, 2012)

An empirically based power law for the regression rate, developed by Marxman, relates the local instantaneous fuel-burning rate to the local instantaneous mass flux. His theory assumes that the

fuel grain is a flat plate in which steady-state processes occur, and the boundary layer is turbulent over the entire length of the fuel grain. Marxman's theory incorporates several of the factors that affect regression rate and their relation. Conduction and convection dominate the heat transfer process and radiation is only included in the case of metal additives. He also considers the blocking effect, which is the result of mass leaving the solid fuel surface and becoming absorbed by the boundary layer and inhibiting heat transfer from the flame. It should be noted that Marxman's theory is not accurate for cylindrically shaped motors and was developed from several other theories. His theory is however based on a slab configuration and is therefore directly applicable to this study. Marxman's work is summarised in Karabeyoglu & Zilliac, (2006) (Karabeyoglu & Zilliac, 2006).

The spatially and temporally averaged regression rate equation is (Karabeyoglu & Zilliac, 2006):

$$\dot{r} = aG_{ox}^n x^m$$

(Equation 2.2)

2.4.2 Non-classical regression rate theory

In the 1990s, research conducted by Stanford University into cryogenic fuels for the use of hybrid rockets led to an interesting discovery of high regression rate paraffin-based fuels. These fuels do not solely rely on evaporation like classical polymeric fuels and are therefore able to achieve higher regression rates (Boronowsky, 2011), (Theba, et al., 2017). Convection and radiation cause heat to transfer into the fuel grain and a thin liquid layer forms on the surface. The turbulent oxidiser stream causes an instability and shears the surface of the liquid layer resulting in roll waves. Droplets are entrained into the boundary layer due to the low viscosity of the molten fuel. Once the droplets reach the diffusion flame combustion occurs (Boronowsky, 2011), (Theba, et al., 2017). Figure 2.5 depicts the process. The droplet entrainment mechanism is thought to significantly rely on the low surface tension and low viscosity of the molten fuel being used. It should be noted that not all fuels that form a melt layer will react in this way (Boronowsky, 2011), (Theba, et al., 2017). Fuels such as ABS (Acrylonitrile-Butadiene-Styrene) have a 7 times higher viscosity than paraffin and even though it forms a melt layer, it is too viscous to allow droplet entrainment (Boronowsky, 2011).

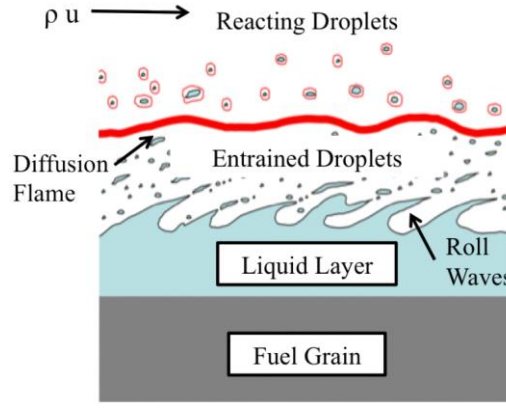


Figure 2.5: Sketch of the droplet entrainment mechanism (Chandler, 2012)

The droplet entrainment mechanism alters the regression rate theory. Karabeyoglu therefore developed a new theory based on the classical regression rate theory and incorporates the mass transfer due to entrainment. Three modifications are taken into consideration (Chandler, 2012):

1. The effective heat of gasification is reduced.
2. Heat transfer is enhanced as the roll waves increase the surface area and the effective roughness of the fuel grain.
3. The blocking factor is altered due to the two-phase flow within the boundary layer. This changes the convective heat flux.

These factors all contribute to the high regression rates achieved by paraffin-based fuels. Karabeyoglu's work is summarised below by (Boronowsky, 2011), (Chandler, 2012). The total regression rate of a hybrid fuel (\dot{r}_t) is the sum of the regression rates for vaporisation (\dot{r}_v) and entrainment (\dot{r}_{ent}).

$$\dot{r}_t = \dot{r}_v + \dot{r}_{ent}$$

(Equation 2.3)

The combination of entrainment and evaporative mass transfer at the liquid-gas interface is given as an energy balance:

$$\dot{r}_v + \left[R_{he} + R_{hv} \left(\frac{\dot{r}_v}{\dot{r}_l} \right) \right] \dot{r}_{ent} = F_{rad} \frac{C v_g^{0.2}}{\rho_f} \left(1 + \frac{\dot{Q}_r}{\dot{Q}_c} \right) B \frac{C_H}{C_{H0}} G^{0.8} x^{-0.2}$$

(Equation 2.4)

Where,

$$R_{he} = \frac{h_m}{h_e + L_v}$$

(Equation 2.5)

And,

$$R_{hv} = \frac{C_l \Delta T_1}{h_e + L_v}$$

(Equation 2.6)

where $\frac{C_H}{C_{H0}}$ is the blocking factor, v_g is the gas velocity, ρ_f is the fuel density, \dot{Q}_{rad} is the heat flux from radiation, and \dot{Q}_c is the heat flux from convection. B is the blowing parameter, G is the instantaneous oxidiser mass flow, x is the axial distance down the port, h_m and h_e are the effective heats, L_v is the latent heat of vaporisation, C_l is the specific heat, T_1 is the absolute temperature, and F_r is the roughness parameter.

The roughness factor accounts for the increased heat transfer due to wrinkling and is empirically defined (Theba, et al., 2017):

$$F_r = 1 + \frac{14.1 \rho_g^{0.4}}{G^{0.8} \left(\frac{T_g}{T_v} \right)^{0.2}}$$

(Equation 2.7)

The gas density ρ_g , the average gas phase temperature T_g and the vaporisation temperature T_v are used to determine the roughness factor.

Manipulation of the above equations results in a simplified model of the entrainment regression rate equation (Theba, et al., 2017):

$$\dot{r}_{ent} = a_{ent} \frac{G^{2\alpha}}{\dot{r}^\xi}$$

(Equation 2.8)

where a_{ent} is the entrainment parameter, α is the dynamic pressure exponent, and ξ is the dynamic thickness exponent.

(Equation 2.3) to (Equation 2.8) form a non-linear set of algebraic equations that result in a total regression rate equation, much like in the classical case but using a spatially averaged regression rate equation instead. Liquefying hybrids have little axial variation therefore m is set to 0. The regression rate \dot{r} reduces to,

$$\dot{r} = a G_{ox}^n$$

(Equation 2.9)

where, G_{ox} is the oxidiser mass flux, a is the regression rate coefficient, and n is the oxidiser mass flux exponent. The coefficients are dependent on the propellant combination.

2.4.3 Regression rate enhancement techniques

Extensive research has been conducted on improving the regression rate, which is governed by the operating conditions, composition, and thermophysical properties of the solid fuel grain. Combustion processes, heat transfer and fluid dynamics incorporate several complex interactions that occur simultaneously within the combustion chamber and the fuel grain. Factors that contribute to the physical phenomena include (Chiaverini & Kuo, 2007):

- solid fuel pyrolysis
- metal vaporisation
- oxidiser atomisation and vaporisation
- mixing and combustion
- gas phase species mass diffusion
- turbulent flow with mass addition
- conduction
- convection
- radiation
- time-varying flow channel configuration

These phenomena all need to be considered in the selection of the regression rate enhancement technique. High energy oxidisers and binders may be included in the solid fuel grain to increase its mass burning rate (Chiaverini & Kuo, 2007). Nevertheless, these enhancement techniques have environmental concerns as the combustion products compromise the safety provided by hybrid rockets and alter the inertness of the solid fuel grain. Alternatively, metal additives accelerate the pyrolysis process without the adverse effects of binders and oxidisers (Chiaverini & Kuo, 2007). They also improve the O/F ratio.

2.4.3.1 Metal additives

Metal additives inherit the safety features which distinguish hybrid rocket propulsion systems from solid and liquid rocket engines while at the same time enhancing its regression rate and hence performance. The addition of metal particles increases the specific impulse, the density specific impulse, and dampens the pressure oscillations (Chiaverini & Kuo, 2007). The higher the mass fraction of the particles, the greater the specific impulse achieved. This in turn reduces the required O/F ratio, decreasing the mass fraction of oxidiser required. The result is simplified rocket hardware with a smaller oxidiser tank (Cantwell, et al., 2010). Additives are usually in powdered form and are therefore also easy to include in the casting process of the fuel grain. They generally provide a denser grain thus shortening its length (Chiaverini & Kuo, 2007).

The choice of metal additive is governed by the material characteristics such as the metal's density, heat of oxidation and reactivity (Pastrone, 2012). Beryllium, for example, has the highest heat of oxidation but its by-products are extremely toxic and is therefore not a viable option. Boron also has an extremely high oxidation heat but due to difficult ignition and incomplete combustion, it is also not feasible (Chiaverini & Kuo, 2007). Lithium on the other hand, is highly reactive but has a low heat of oxidation (Pastrone, 2012). Magnesium is also an increasingly popular choice but is expensive (Chiaverini & Kuo, 2007). Aluminium has been the most researched metal additive because of its thermal properties, ease of processing and ignition, high density, and low cost. Its combustion products are also relatively inert which is not commonly obtained from metal additives (Chiaverini & Kuo, 2007). It is therefore the best candidate for implementing particle additives into hybrid rocket propulsion systems and was thus selected to be investigated in this study.

The employment of metal particles reduces the strength of the fuel grain and often causes two-phase flow in the nozzle and losses due to incomplete combustion (Pastrone, 2012). Particle attributes such as shape, dimension and coating also play a vital role in the additive selection process (Pastrone, 2012). Micron-sized particles have increased regression rates between 10% to 20%, although nano-sized particles exhibit up to a 60% enhancement in the fuel mass burning rates of metal additives (Karabeyoglu, et al., 2003). Nano-sized particles have shown promise in mitigating the above-mentioned drawbacks of metal additives as they have a high surface to volume ratio, reduced ignition and burning time, and provide complete combustion (Pastrone, 2012). They however increase the complexity of the fuel grain fabrication, are pre-oxidised unless they are very carefully processed and stored and are expensive. For the purposes of this study, and due to budget limitations, the focus will be placed on aluminium particles within the 100 μm to 200 μm range (Maharaj, et al., 2018). In addition, focus will be on an optimal concentration of 40% aluminium which has shown to regression rate properties of paraffin wax (Cantwell, et al., 2010).

2.4.3.2 Paraffin fuels

A simple single port fuel grain is sufficient for liquefying fuels such as paraffin wax and simplifies the design of the rocket motor while improving the overall efficiency of the fuel up to 97% (Chandler, et al., 2012). Studies conducted have shown that paraffin-based fuels have a 3 to 4-fold increase in regression rate compared to classical fuels (Chandler, et al., 2012). This is due to the hydro-dynamically unstable liquid layer which forms on the surface of the melt layer of the fuel grain resulting in droplet entrainment (Theba, et al., 2017).

The hydrophobic nature of paraffin wax enables the additives to alter its properties. An additive such as ethylene-vinyl acetate (EVA) may be used to alter the viscosity of paraffin and therefore

tailor it for a variety of applications (Nakagawa, et al., 2009). Additives may also be used to increase its low mechanical strength although this adversely affects viscosity and surface tension (Evans, et al., 2009).

The regression rate of a hybrid rocket is affected by several aspects of the system. The regression rate theory developed initially by Marxman is dependent on the oxidiser mass flux and the propellant combination. Factors such as O/F ratios, fuel grain dimensions, combustion chamber pressures, injection techniques and particle additives all affect the regression rate of a hybrid rocket engine (Karabeyoglu & Zilliac, 2006). Additional factors that increase regression rate include the use of cryogenic fuels, increasing surface roughness and swirl injection. It should also be noted that the regression rate is influenced by scaling effects; it has to be scaled appropriately for the system in question (Karabeyoglu, et al., 2003), (Dlamini, et al., 2014).

2.5 Regression rate studies

Four universities have primarily conducted research on HSM's and are described in the sections that follow. The aim of each project as well as the results are summarised. PSU have also conducted lab-scale experiments with aluminised paraffin wax. Their findings are summarised in Section 2.5.1.

2.5.1 Pennsylvania State University (PSU)

Although the study at PSU focused mainly on HTPB and its additives, for the purposes of this study, this section summarises their slab motor testing on HTPB and GOX and focuses on the regression rate data for pure paraffin wax and aluminium additives in the lab-scale motor.

2.5.1.1 Slab Geometry Hybrid Motor (SGHM)

PSU has been conducting research on regression rate studies. PSU initially developed a high-pressure hybrid slab motor (SGHM) with X-ray diagnostics to determine local and real-time regression rates of HTPB with gaseous oxygen (GOX). The motor had two opposing fuel grain slabs and a schematic is given in Figure 2.6 (Chiaverini, et al., 2000).

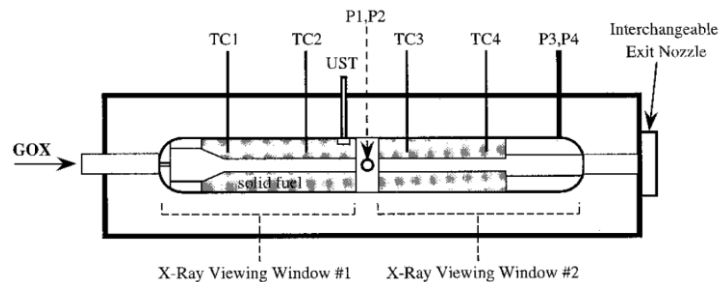


Figure 2.6: Schematic of SGHM with diagnostic devices (Chiaverini, et al., 2000)

A real time X-ray radiography system was used to obtain instantaneous solid fuel regression rate data. Thermocouples were placed along different axial locations of the fuel grain to obtain temperature readings. The results showed that the regression rates had a strong axial dependence at the front end of the fuel grain (Chiaverini, et al., 2000). Thermal radiation influenced the regression rates at low oxidiser mass fluxes, while the HTPB mass flux was increased with the addition of aluminium powder (Chiaverini, et al., 2000).

2.5.1.2 LGCP and XTC hybrid rocket motors

Students continued the investigations of HTPB with paraffin binders in a centre-perforated hybrid motor. This included the addition of aluminium powders which have shown to increase the regression rate of paraffin wax by 3-4 times that of HTPB. When considering the fuel density, the mass burning rate portrayed a 7-fold increase (Evans, et al., 2009).

In PSU's study, two different lab-scale hybrid motors were used to investigate paraffin-based fuels, namely; the Long Grain Center-Perforated (LGCP) hybrid motor and the X-ray Translucent Casing (XTC) hybrid rocket motor (Evans, et al., 2009). The XTC has the ability to measure instantaneous regression rates and is similar to the slab motor but is axisymmetric. GOX was the chosen oxidiser and the tests were run for oxidiser mass fluxes within the range of 60 kg/m²s to 300 kg/m²s. A nominal chamber pressure range of 2.17 MPa to 4.24 MPa was selected as there was no apparent pressure effect on the regression rate data over the oxidiser mass flux range investigated. The grains were cast in paper phenolic tubes with an outer diameter, inner diameter, and length of 11.4 cm, 6.4 cm and 45.7 cm respectively. The duration of the tests ranged between 5 and 7 seconds (Evans, et al., 2009).

The LGCP was used to initially test paraffin wax containing 3% carbon black by weight to determine a baseline. Aluminised paraffin comprising of 13% Silberline® aluminium by weight was analysed within the XTC motor (Evans, et al., 2009). The data obtained from the two test sets were compared with paraffin wax solid fuel data investigated by Karabeyoglu et al (2004) (Karabeyoglu, et al., 2004) and are shown in Figure 2.7. The graph shows similar results for data obtained by Karabeyoglu and PSU.

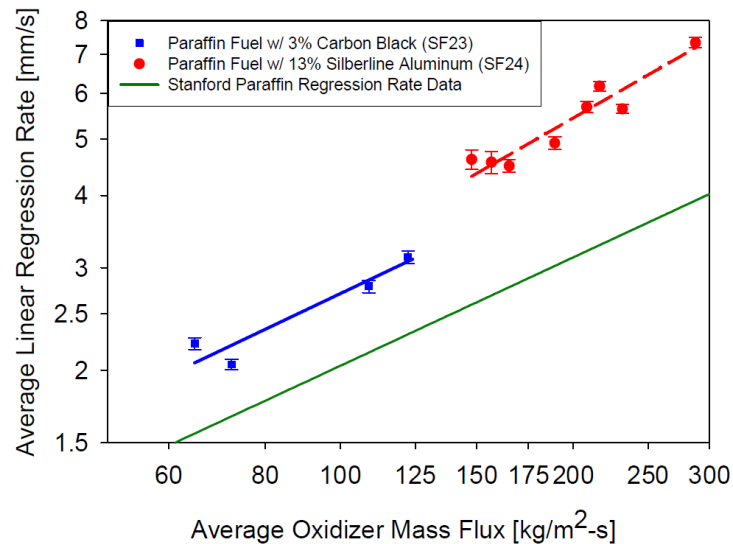


Figure 2.7: Linear regression rates of paraffin-based solid fuel formulations in comparison with Stanford University curve fit (Evans, et al., 2009)

The regression rates were slightly higher for PSU which could be due to manufacturing techniques or the difference in the formulation of the solid fuel grains. Extrapolation of the oxidiser mass fluxes yield an increase in regression rate for paraffin wax with 13% Silberline® nano-sized aluminium flakes in comparison to pure paraffin wax. This increase was found to be approximately 30% times that of pure HTPB. The difference between the aluminised results and Stanford's regression rate curve shows a 60% increase (Evans, et al., 2009). This is due to the Kelvin-Helmholtz type of surface instability wave which develops on the solid fuel surface (Evans, et al., 2009). The aluminium particles are captured within the molten paraffin wax and the droplets are sheared from the fuel surface as a result of the oxidiser flow. Regression rate data provide similar results for HTPB where there is an increase in the regression rate of aluminised HTPB. However, when compared with aluminised paraffin, the aluminised HTPB regression rates were lower because the aluminium particles collected on the surface of the HTPB fuel and were only stripped away by aerodynamic forces, which entrained them in the flow (Evans, et al., 2009).

2.5.2 Tokai University

Students at Tokai University (TU) investigated the relationship between regression rates and viscosities and how they could control these properties by adding ethylene vinyl-acetate (EVA) copolymer. A hybrid rocket slab motor was also developed to observe the burning surface of a paraffin wax (Fisher-Tropsch FT-105) fuel (Nakagawa, et al., 2009).

The experimental set-up used at TU is depicted in Figure 2.8. The oxygen tank was regulated to provide a pressure of 2 MPa at the exit. An orifice was used to control the oxidiser mass flow rate and a pressure sensor was installed and used to calculate it. The chamber was designed to operate at atmospheric pressure as there was no obstruction at its exit. Nitrogen was the purge gas of

choice and quartz glass was used for the visualisation window. The fuel grain was sandwiched between the windows and was 100 mm x 10 mm x 10 mm in dimension. A chamfer on the leading edge of the fuel grain was created upstream of the grain to assist in ignition by the nichrome wire. A high-speed camera and data acquisition system were both used to capture the results and observe the reaction (Nakagawa, et al., 2009).

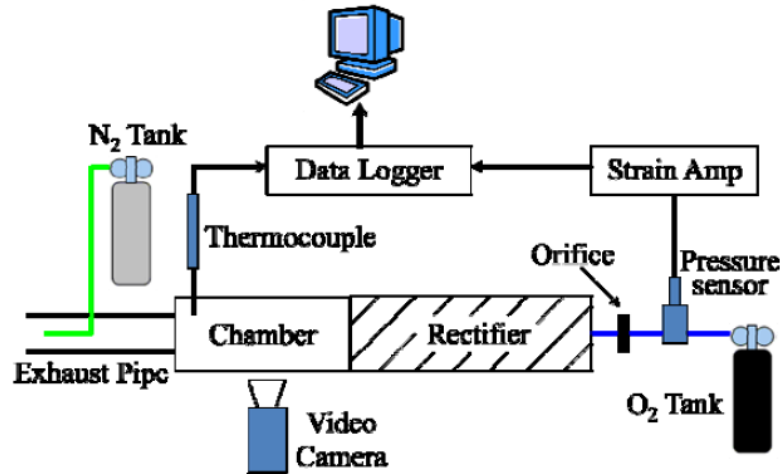


Figure 2.8: The schematic of TU's experimental layout (Nakagawa, et al., 2009)

TU investigated the molten layer on the solid fuel surface with a high-speed camera. The observations confirmed the theory behind the regression rate mechanism. Some of the molten fuel was entrained within the gas phase and the rest flowed out along the surface of the solid fuel grain due to mechanical processes. The latter case did not require additional heat flux from the combustion gas to leave the solid phase (Nakagawa, et al., 2009).

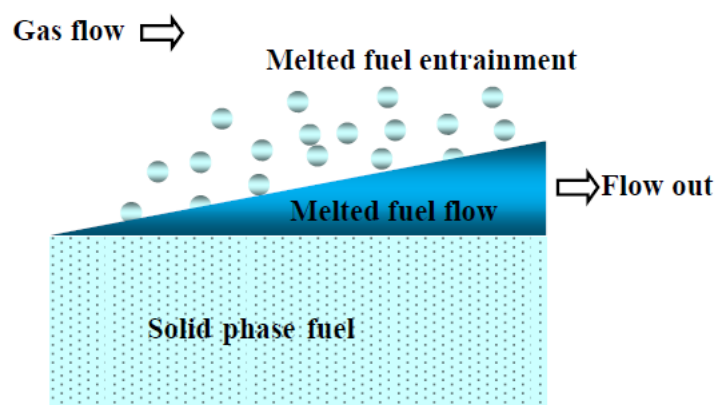


Figure 2.9: Schematic model of the regression mechanism of a paraffin-based solid fuel (Nakagawa, et al., 2009)

2.5.3 Stanford University

Stanford University (SU) developed a HSM to observe the combustion process that governs the regression rate mechanism of hybrid fuels. Paraffin-based and other hybrid fuels such as high-density polyethylene (HDPE) and HTPB were examined and compared. The focus in this section is only on the paraffin-based fuels tested. All experiments were conducted with GOX as the oxidiser. The use of hybrid fuels also enables design flexibility of a propulsion system as the regression rate is almost independent of the chamber pressure (Chandler, et al., 2012).

Stanford's apparatus consisted of a flow conditioning system, a feed system, and a combustion chamber depicted in Figure 2.10. A metering valve was used to control the oxidiser flow and nitrogen was used as purge gas (Chandler, et al., 2012).

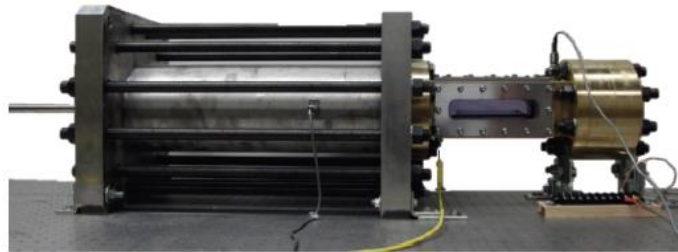


Figure 2.10: Stanford's HSM (Chandler, et al., 2012)

The fuel grain was epoxied to a cantilevered support in the chamber and is 2.5 x 1 x 12.7 cm in dimension. The port area was sufficiently large to prevent side burning of the glass and walls. The leading edge of the grain was chamfered to assist with combustion. A 26-gauge nichrome wire was used for ignition purposes and stuck to the chamfered edge of the fuel grain using epoxy. High-speed cameras were used to capture the video footage of the reaction within the chamber (Chandler, et al., 2012).

Five tests were run to observe the droplet mechanism of the different hybrid fuels. Two additional tests were included for explanation purposes. The summary of each test is given in (Chandler, et al., 2012) with the test summary in Table 2.4 (Chandler, et al., 2012).

.

Table 2.4: SU Test summary (Chandler, et al., 2012)

		Paraffin-based fuels			Classical fuels	
		Paraffin	Blackened paraffin	SP1X	HDPE	Blackened HTPB
Test date		23 May 2012	23 May 2012	22 May 2012	23 May 2012	23 May 2012
Average Oxidizer Mass Flux (g/cm ² s)		3.19	2.61	3.31	2.88	2.94
Programmed burn time (s)		2.5	2.5	2.5	3	3
Approx. actual burn time (s)		3.5	3.5	3.4	4.7	4.1
Burned mass (g)		6.7	6.0	5.9	1.7	2.8
Average O/F		32	29	36	152	82
Side view camera settings	Frame rate (frames per s)	1200	1200	1200	1200	1200
	Fstop	4.6	4.6	4.6	4.6	4.6
	Shutter speed (s)	1/32,000	1/32,000	1/32,000	1/32,000	1/32,000
Top view camera settings	Frame rate (frames per s)	1200	1200	240 *	1200	1200
	Fstop	4.4	3.5	4.9	3.5	3.5
	Shutter speed (s)	1/32,000	1/32,000	1/32,000	1/32,000	1/32,000

2.5.3.1 Pure paraffin

The pure paraffin used in the experiments is called FR5560 (C₃₂H₆₆) and was purchased from the Candlewic Company. The flame appeared to be thicker at the beginning of the burn and then evened out as the run progressed. This contributed to a stable combustion. Droplets were also visible above the flame. The molten layer of the wax appeared to be pushed towards the end of the fuel grain and onto the fuel support. The images of these tests can be found in the reference (Chandler, et al., 2012).

2.5.3.2 Blackened paraffin

A black dye was used to limit the radiation that penetrates through the fuel grain. there was an observation of a flame vortex rolling towards the end of the fuel grain. When the burn began there was a red glowing zone which faded and became the natural white and blue colour of flame. Droplets were again noticeable throughout the run, but the liquid layer could not be detected (Chandler, et al., 2012).

Another test was run with blackened paraffin with the cameras set to zoom in on the flame. In this experiment the liquid layer as well as the instabilities surrounding it were visible. Bursts of droplets were observed above the flame zone and are considered responsible for paraffin having a higher regression rate than classical fuels as there is significant entrainment due to the roll waves (Chandler, et al., 2012).



Figure 2.11: Roll waves in blackened paraffin (Chandler, et al., 2012)



Figure 2.12: Droplets in blackened paraffin (Chandler, et al., 2012)

2.5.3.3 SPIX-01

This test consisted of paraffin wax with additives to alter the regression rate properties and strength of the fuel. The run revealed that the flame propagated much slower across the altered fuel grain when compared to the pure paraffin case. The flame illuminated the boundary layer, which appeared to fluctuate thus causing combustion instabilities. Very few droplets were visible. The wax flowed over onto the sides and back of the fuel grain.

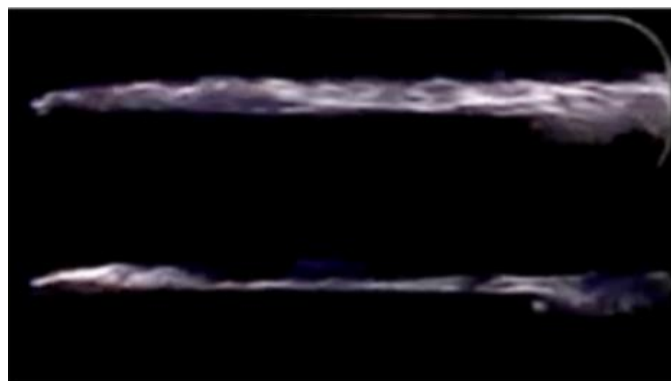


Figure 2.13: SPIX combustion instability (Chandler, et al., 2012)

2.5.4 Beihang University

A numerical model was developed and used to investigate the effects of adding aluminium particles to a HTPB hybrid rocket motor (HRM). The model included the Navier-Stokes governing equations, a discrete phase model, a turbulence model, a gas-solid coupling model, a combustion model, and a CFD code. The discrete phase model was used to simulate the injection of an aluminium particle into the flow field. The CFD code was used to solve the energy equations of gas and solid at the grain surface, momentum, the coupling mass, and the initial parameters of the aluminium droplet. The results mentioned in this section from the experimental data and

numerical model were consistent for determining the regression rate and were therefore deemed accurate for future investigations (Sun et al., 2014).

The regression rate from the numerical model was evaluated against the experimental data obtained from a HSM. All the conditions were the same between the experimental environment and the simulation. The results can be seen in the paper by Sun et al., (2014) (Sun et al., 2014). The maximum regression rate error noted was 17.67 % at the front of the fuel grain. The average regression rate from the numerical simulation was found to be 2.64 % higher than the experimental values. The fuel grain surface temperature distribution was also found to be within the range established by Chiaverini et al. depending on the operating conditions and longitudinal axis location. The inconsistencies in the results are believed to be principally caused by not considering the radiant heat flux, idealisation of the pyrolysis model and simplification of the reaction model. The numerical model developed is therefore considered to have a reliable accuracy margin for simulating the fluid dynamics, combustion process, and heat flux inside the chamber (Sun et al., 2014).

The characteristic velocity obtained from the simulation for 20% aluminium was higher compared to the simulated result in pure HTPB for all oxidiser mass fluxes. This was due to the increase in energy released with the aluminium combustion. On the other hand, the vacuum specific impulse obtained from the simulation for 20% aluminium only remained higher than the pure HTPB case up to an oxidiser mass flux of 100 kg/m²s. This was explained by the low energy release of aluminium at low oxidiser mass flux levels, which resulted in inefficient combustion of the fuel. The combustion efficiencies obtained for pure HTPB had a larger range than that of 20% aluminium. Metallised fuel grains are less sensitive to an O/F shift. An intersection between the efficiency of the characteristic velocity and the efficiency of the specific impulse were explained by the low efficiency of aluminium at low oxidiser mass fluxes. An increase in the oxidiser mass flux resulted in the aluminium producing more energy and therefore being more efficient (Sun et al., 2014).

Studies show that with the addition of aluminium, the regression rate and mass burning rate of a hybrid fuel can be enhanced. Figure 2.14 shows that with an increase in the aluminium weight fraction, the average regression rate \dot{r}_{ave} and mass burning rates \dot{M} are increased. A 40% weight fraction produced a 75% increase in the regression rate and a 135% increase in the mass burning rate. This was due to the higher density provided by aluminised HTPB. The investigations demonstrated significant improvement in performance capabilities of a hybrid rocket propulsion system with the use of metallised fuel grains. The employment of a high mass burning rate with a low regression rate can sustain the motor performance and at the same time extend its burn time.

This is significant for hybrid motors as they generally require large fuel surface areas to produce high thrust (Sun et al., 2014).

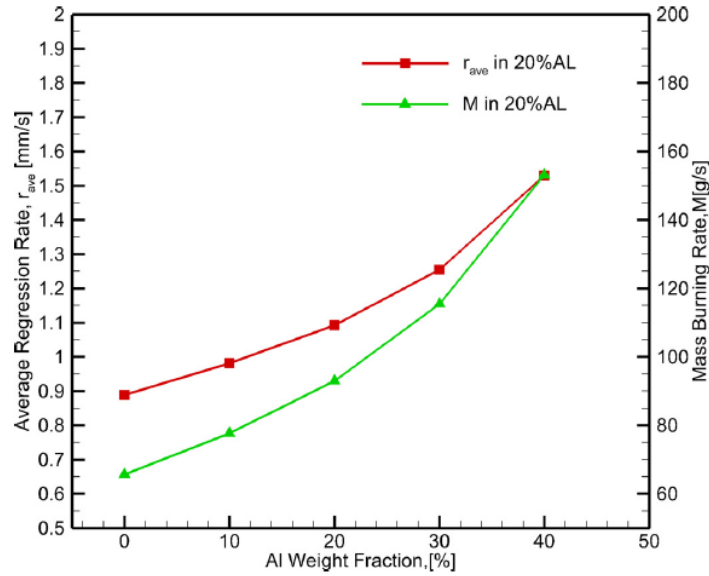


Figure 2.14: Effect of Al addition on regression rate behaviour (Sun et al., 2014)

Figure 2.15 portrays an increase in the regression rate at the fore end of the fuel grain, and a decrease along the axial distance of the fuel grain to a minimum value, at which point it increased once more. The high convective heat transfer at the beginning of the run can explain this when the boundary layer was still thin and there was an associated high temperature gradient. The regression rate thus decreased as the boundary layer grew. Along the axis of the fuel grain, the total mass flux increased because of the addition of fuel. This, in turn, caused an increase in the heat flux and therefore the regression rate (Sun et al., 2014).

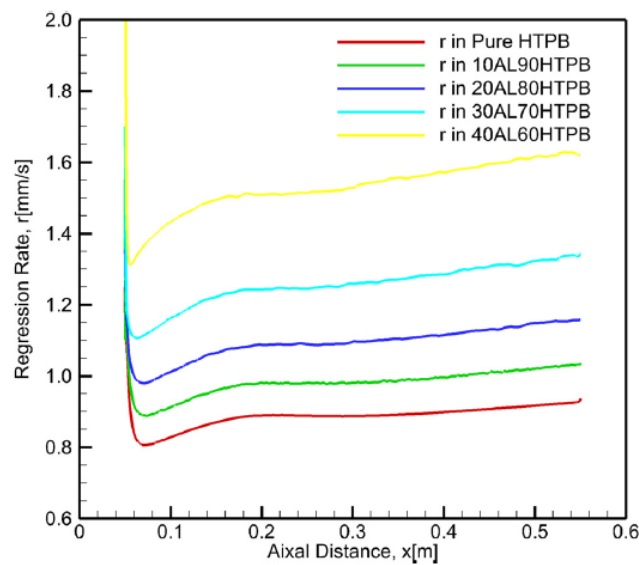


Figure 2.15: Axial variation of regression rate (Sun et al., 2014)

2.6 Literature discussion

The regression rate behaviour of Sasolwax 0907 with nitrous oxide has not been investigated in a hybrid rocket slab motor. Hybrid rockets are simpler, safer and cost effective compared to solid and liquid rockets (Chiaverini & Kuo, 2007). This is mainly due to the fuel and oxidiser being in different phases. The oxidiser travels through the feed system and injector into the combustion chamber, where the solid fuel grain is located, and combustion occurs upon ignition (Chandler, 2012). The combustion chamber design is therefore dependent on the configuration of the solid fuel grain. A longer combustion chamber would provide a medium for even mixing and greater uniformity of the propellants. Pre and post combustion chamber requirements will be considered based on the fuel grain configuration and injection oxidiser mass flow rates. The port diameter, or port height in the case of the HSM is a significant parameter which governs the regression rate behaviour of the hybrid fuel (Biblarz & Sutton, 2001).

Nitrous oxide has many advantages over oxidisers such as liquid oxygen. It is readily available, cheap, non-toxic, safe to handle, and stable at room temperature conditions. Its exothermic reaction and slow kinetics of decomposition are beneficial for hybrid rocket motor performance and stability (Biblarz & Sutton, 2001). Nitrous oxide is however, susceptible to explosion hazards therefore safety considerations need to be implemented. Material compatibility is an important factor in the design of a hybrid rocket motor with nitrous oxide as the oxidiser and Table 2A.9.2 was used in the selection process for the motor materials. Adiabatic compression may cause hard starts, back shock or a loss of pressure and should be minimised by supercharging of the nitrous oxide tank or implementing a high flow pressure regulator into the system (Buitrago, 2014).

Sasolwax 0907 or pentacontane has many advantages as a hybrid rocket fuel. It is an inert substance with high regression rates primarily due to the low viscosity and low surface tension associated with these fuels. Increased regression rates may be achieved with the addition of metal additives (Karabeyoglu, et al., 2002). Paraffin wax's simplicity in manufacturing of single port fuel grains results in improved efficiency of the system (Chandler, et al., 2012). The limitations of paraffin wax as a hybrid solid fuel include brittleness, prone to cracking, reduced integrity during burning and shrinkage during manufacturing (McCulley, 2012). These factors were considered in the manufacturing and testing conducted with paraffin wax fuel grains.

Marxman's theory and thus Karabeyoglu's work was derived from slab motor testing and is therefore directly applicable to this study. The classical regression rate theory developed by Marxman states that polymeric fuels rely solely on vapourisation of the molten fuel into the oxidiser stream (Marxman, et al., 1963). These fuels therefore have low regression rate characteristics (Marxman, et al., 1963). Non-classical regression rate theory summarised in Section 2.4.2 from Karabeyoglu's work at SU, is based on the high regression rates observed from

paraffin-based hybrid fuels due to the low viscosity and low surface tension properties (Karabeyoglu & Zilliac, 2006). Studies have shown that metal additives further improve the performance of these fuels (Dyer, et al., 2007).

The investigations conducted by PSU demonstrated that the addition of metal additives such as aluminium increased the regression rates of HTPB and paraffin solid fuels. Nano-sized aluminium particles increase the regression rate of classical fuels by approximately 2 times that of pure HTPB (Evans, et al., 2009). Paraffin-based fuels regress by about 3 times that of HTPB and 7 times with the addition of aluminium particles (Evans, et al., 2009). All of the above experiments were carried out within a range of oxidiser mass fluxes between 100 kg/m²s and 300 kg/m²s.

The data obtained by PSU also showed that the combustion efficiencies and regression rate were greatly dependent on the type of aluminium particles used (Evans, et al., 2009). This included the size and manufacturing process. Viton-coated Alex® aluminium particles, for example, showed the most promise in increasing regression rate and combustion efficiencies. These flakes are thought to assist in the rapid ignition and deliver complete combustion (Evans, et al., 2009).

It should be noted that the difference in regression rate data obtained by PSU from the LGCP versus the XTC motors is partially due to scaling effects, manufacturing techniques and fuel formulations.

Work on TU's HSM was successful in determining the relationship between the regression rate and viscosity, and thus the heat flux of paraffin-based fuels. They were also able to visualise the regression rate mechanism in which a portion of the molten fuel is entrained in the gas flow while the rest escapes out of the chamber (Nakagawa, et al., 2009). Due to this mechanism, paraffin-based fuels have superior regression rate properties compared to classical fuels such as HTPB. The experiments conducted also provided insight into how the regression rate of paraffin can be adjusted with the addition of EVA without jeopardising the launch vehicle's performance (Nakagawa, et al., 2009).

The results of SU tests were aligned with the droplet entrainment mechanism theory which explains the high and low regression rates of hybrid fuels such as paraffin and HTPB respectively (Chandler, et al., 2012).

It was found that with an increase in the weight fraction of aluminium, there is an increase in the regression rate of the HTPB fuel grain in Beihang University's research (Sun et al., 2014). At each oxidiser mass flux, the regression rate was found to be about 0.2 mm/s larger than the pure HTPB case. This was due to the increased heat flux to the fuel grain surface caused by the addition of aluminium particles (Sun et al., 2014). The regression rate power law was considered. The oxidiser mass flux exponent n determined for pure HTPB is 0.4467 and is 0.3706 for 20%

aluminium with 80% HTPB (Sun et al., 2014). These values are lower than the theoretical value obtained from the turbulent heat transfer theory and may be due to scaling effects of the motor and injector, as well as the use of a simplified model in this study (Sun et al., 2014).

A typical hybrid rocket motor configuration was applied to the slab motor designed in this study. The slab shaped fuel grain effectively represents a segment of a cylindrically shaped fuel grain in a typical hybrid rocket motor. It was designed similarly to the motors described in Sections 2.5.2 and 0 by TU and SU. The HSM for the Phoenix Programme did not consist of a flow rectifier as the motor is meant to mimic the conditions of a typical hybrid rocket motor in order to simulate a real-world use. The literature presented in this chapter verify that paraffin wax has increased regression properties compared to classical fuels. Regression rate was determined to be about 1.5 mm/s for pure paraffin wax from NASA CEA for FR5560. The addition of aluminium powder is shown to improve the regression characteristics of the fuel and will be investigated. Blackened paraffin was shown to provide clarity when observing combustion attributes, and although it will not be implemented in this study. The associated images will be useful in identifying the relevant features in the present work.

CHAPTER 3: CONCEPTUAL DESIGN GENERATION

The focus of this study was to determine the regression rate and combustion characteristics of paraffin wax fuel with nitrous oxide as the oxidiser in a slab motor. The most important components of the design were the combustion chamber and its constituent components, namely; the glass windows, injectors, and nozzles.

The combustion chamber housed the solid fuel grain tightly on either side that ensured safe motor operation and expulsion of exhaust gases. The chamber had to also be easily adaptable to different oxidiser mass flow rates and combustion pressures up to a maximum of 10 bar. The burn time for the experiments were assumed to be 5 seconds.

Two windows were to be incorporated into the combustion chamber; initially, one on the side and another at the top to visualise the combustion mechanism. Special consideration was given to ensure that the glass did not experience extraneous stress or thermal shock in the extreme operating environment.

Proper sealing methods had to further be implemented into the system.

All materials used had to be compatible with nitrous oxide. Various concepts were therefore explored to determine the most suitable chamber and window design, including materials.

3.1 Glass material considerations

The slab motor combustion chamber features windows on the sides and at the top to visualise the combustion process. The material used had to satisfy specific requirements such as being both completely transparent and able to withstand high temperatures. Several materials were considered for the windows.

3.1.1 Polycarbonate

Polycarbonate was one of the materials considered. Polycarbonate is a thermoplastic transparent material which consists of two phenyl groups and two methyl groups (Buitrago, 2014). These molecular chains contribute to the stiffness of polycarbonate and hence its mechanical properties (Polymer Technology & Services, 2016). It is commonly used in construction and rooftop glazing due to its excellent physical properties, namely hardness and strength (Plastipedia, 2016). Polycarbonate was a material considered because it is amorphous (Plastipedia, 2016) and environmentally friendly (Buitrago, 2014). This engineering plastic has the mechanical properties shown in Table 3.1 (Boedeker, 2016).

SU used it in the combustion analyses of their slab motor at atmospheric pressures. One of their researchers observed that at low pressures (below 5 bar) it performs well, but once the chamber

is pressurised to higher values (above 10 bar), the polycarbonate deforms. Polycarbonate is very cheap and locally accessible but for the reason mentioned above, and the fact that the maximum temperature is 120 °C, polycarbonate was not a viable option for this chamber.

Table 3.1: Mechanical properties of Polycarbonate (Boedeker, 2016)

Density	1.2 g/cm ³
Tensile strength	70-80 N/mm ²
Thermal coefficient of expansion	7.02 x 10 ⁻⁷ m/m° C
Maximum temperature	120 °C
Maximum continuous use temperature	125 °C
Maximum intermittent use temperature	140 °C
Melting point	149 °C
Thermal conductivity	0.1873 W/m K
Young's Modulus	2.2 GPa
Poisson's Ratio	0.3

3.1.2 Borosilicate

Borosilicate was another material option for the visualisation windows. It is clear, colourless and transparent, and commonly known under its branded names Pyrex or Duran (Goodfellow Ceramic & Glass, 2009). Borosilicate glass is often used for laboratory glassware such as beakers and vials (Corning, 2014). It is also used in optics, optoelectronics, photonics and analytical equipment (Glassblowing Industries, 2014), and is commonly used in cookware (Duran Group, 2014).

Borosilicate glass has a superior chemical resistance compared to other types of glass; it is highly resistant to neutral or acidic solutions, concentrated acids, and mixtures. It is also resistant to chlorine, bromine, iodine, and organic substances. However, when subjected to hydrofluoric acid, phosphoric acid and strong alkali, it may cause corrosion of the glass above temperatures of 100 °C (Duran Group, 2014).

Production of this type of glass requires high temperatures compared with regular glass and it therefore has high heat resistance. Its low thermal expansion coefficient contributes to its ability to withstand material stresses better than regular glass and as a result does not crack or break easily. It is also the reason why borosilicate glass performs particularly well under high

temperatures (Goodfellow Ceramic & Glass, 2009). For these reasons, it was a suitable option for the combustion chamber glass windows. The mechanical properties of borosilicate are displayed in Table 3.2 (MakeItFrom, 2014), (Corning, 2014), (Duran Group, 2014), (Goodfellow Ceramic & Glass, 2009).

Table 3.2: Mechanical properties of Borosilicate

(Goodfellow Ceramic & Glass, 2009), (MakeItFrom, 2014), (Corning, 2014), (Duran Group, 2014),

Density	2.23 g/cm ³
Tensile strength	280 MPa
Thermal coefficient of expansion	32.5 x10 ⁻⁷ cm/cm °C
Maximum temperature	500 °C
Softening point	825 °C
Melting point	860 °C
Thermal conductivity	1.14 W/m K
Young's Modulus	68-81 GPa
Poisson's ratio	0.21
Thermal expansion	3.3-5.1 x10 ⁻⁶ m/m K
Specific heat capacity	830 J/Kg K

Although borosilicate is relatively inexpensive and is readily available in South Africa, none of the companies could manufacture the glass to the specifications required for its intended purpose in this project.

3.1.3 Vycor

Vycor is produced by the leaching of borosilicate and has similar properties and performance to quartz glass and it is a more economical option. The rolled sheets are ground and polished for excellent optical and visual impact (Grayglass, 2013).

Vycor's glass composition results in excellent physical and mechanical properties such as a low coefficient of expansion and withstanding thermal shock. It also has exceptional performance in harsh environments such as acids and steam. Vycor, much like quartz glass, can endure extremely high temperatures compared to other glasses (Prazisions glas&optik, 2014). Its properties can be found in Table 3.3 (Corning, 2015).

Table 3.3: Mechanical properties of Vycor (Corning, 2015), (Grace Construction Products, 2012)

Density	2.18 g/cm ³
Tensile Strength	ASTM D412, Die C Min. 985 KPa
Thermal coefficient of expansion	7.5×10^{-7} cm/cm °C
Maximum operating temperature	900 °C
Softening point	1530 °C
Annealing point	1020 °C
Thermal conductivity	1.38 W/m K
Young's Modulus	6.75×10^3 kg/mm ²
Poisson's ratio	0.19

Vycor would be a suitable material for the windows of the HSM but is not locally available and would be prohibitively expensive to import.

3.1.4 Quartz glass

Quartz glass has unique properties which make it ideal for a wide range of applications. Its properties include but are not limited to; good chemical resistance, high resistance to corrosion, low to zero thermal expansion, incredible hardness, excellent thermal shock resistance, and excellent optical transmission (Goodfellow Ceramic and Glass Division, 2014), (Accuratus, 2013), (Technical Glass Products, 2010). Its mechanical properties are listed below in Table 3.4 (Goodfellow Ceramic and Glass Division, 2014), (Accuratus, 2013), (Technical Glass Products, 2010).

The glass windows would be purchased with the required design specifications because the Mechanical Engineering Department at UKZN does not have the necessary capability. The ability to manufacture the required shape would have to be considered in the design.

Table 3.4: Mechanical properties of Quartz Glass

(Goodfellow Ceramic and Glass Division, 2014), (Accuratus, 2013), (Technical Glass Products, 2010)

Density	2.2 g/cm ³
Tensile strength	48 MPa
Thermal coefficient of expansion	0.55 x10 ⁻⁶ /°C
Maximum temperature	950-1300 °C
Softening point	1683 °C
Annealing point	1215 °C
Thermal conductivity	1.4 W/m K
Young's Modulus	72 GPa
Poisson's ratio	0.17
Specific heat capacity	740 J/Kg K

3.2 Glass window concepts

Sections 3.2.1 to 3.2.3 describe the conceptual designs considered for the shape of the glass windows.

3.2.1 Glass concept one – T-shape

The first concept was based on the design described in Publication 4 (Dlamini, et al., 2014).

The initial shape of the glass was T-shaped so that it could be easily slotted into the inner panels of the combustion chamber described in Section 3.4.1. A three-dimensional view is shown in Figure 3.1. The way in which it would be fitted is shown in Figure 3.2. This particular concept would prevent side burning as the glass would be situated such that it would be in contact with the fuel grain. This was essential for the study as it would limit the regression rate of the fuel grain to the top surface. Accurate regression rate data would therefore be obtainable.

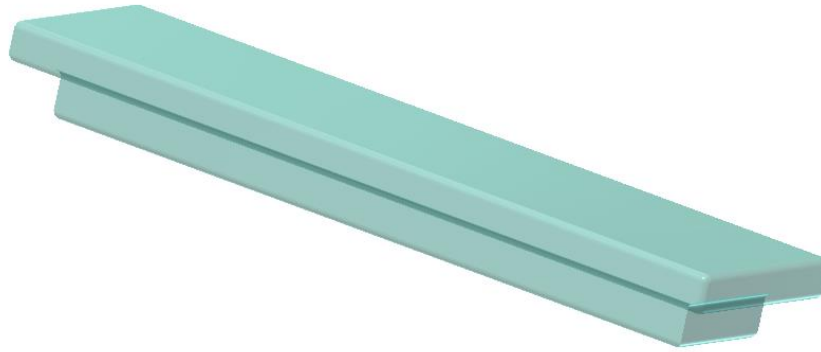


Figure 3.1: Three-dimensional view of T-shaped glass

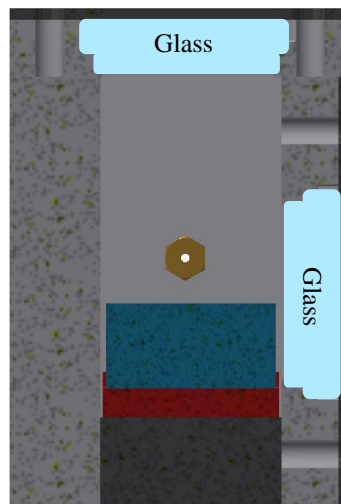


Figure 3.2: Section view showing placement of T-shaped glass

This shape, however, has many corners which increased areas of localised stress. It is also bulky (14 mm thick) which leaves the glass vulnerable to cracks from external chamber pressure. For this reason, it was not a viable option.

3.2.2 Glass concept two - rectangular flat plate

The second conceptual design envisaged the glass as a rectangular flat plate which would reduce the areas of maximum stress intensity in the T-section. This concept looked much like the one in Figure 3.1 and Figure 3.2. The glass however, would be held in the combustion chamber by two panels as illustrated in Figure 3.4, the design of which is described in detail in Section 3.4.2. It would be surrounded by a gasket (possibly rubber) to prevent direct contact with the metal and to reduce stress on the glass. This would also enable expansion and contraction, including movement of the glass. This set-up is depicted in Figure 3.4.

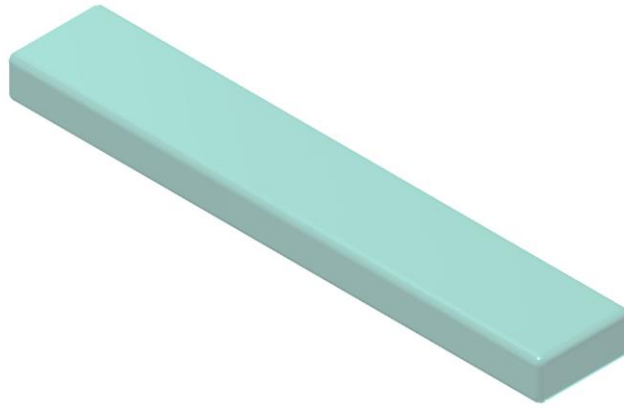


Figure 3.3: Three-dimensional view of rectangular glass

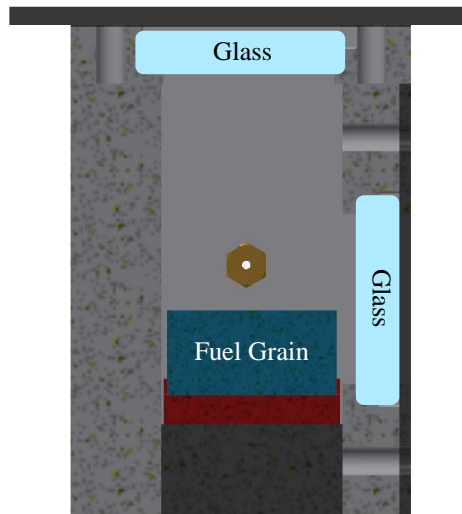


Figure 3.4: Section view showing placement of rectangular flat plate glass

This concept reduced many of the areas of localised stress from the T-shape, and manufacturing of this shape would be fairly simple. An alternative design was proposed that would further reduce the areas of localised stress regions and is described in Section 3.2.3.

3.2.3 Glass concept three – elongated oval concept

After some consideration, the glass shape was modified to include semi-circular ends and is shown in Figure 3.5. All of the edges were to be filleted to further reduce areas of localised stress. This shape would be more challenging especially when considering the tolerances that may be required. The chamber would then be modified to include this particular shape.



Figure 3.5: Concept three - elongated oval shape

3.3 Combustion chamber material considerations

Table 2A.9.2 in Appendix 2A lists materials that are compatible with nitrous oxide, which is an important consideration as discussed in Section 2.2. For the requirements of this motor, stainless steel and brass were the most suitable options, although brass is corrosive in the presence of moisture.

Stainless steel was the material initially chosen due to its mechanical properties such as strength, conductivity and temperature resistance. The selection process of stainless steel is described in detail in Publication 4 (Dlamini, et al., 2014). The mechanical properties of stainless steel are listed in Table 3.5.

Table 3.5: Properties of Stainless Steel 304 L

(Macsteel, 2014), (Harvey, 1982), (Peckner & Bernstein, 1977),

(Boyer & Gall, 1985), (ASM International Handbook Committee, 1990)

Mechanical Properties of Stainless Steel 304 L	
Property	Value
Tensile Strength, Ultimate	600 MPa
Tensile Strength, Yield	310 MPa
Melting Point	1400 °C
Density	8000 kg/m ³
Hardness (Brinell)	170
Thermal Conductivity	1620 W/m K
Coefficient of Thermal Expansion	17.3 x 10 ⁻⁶ /K
Specific Heat Capacity	500 J/kg K

Brass was also an option for the combustion chamber. Although its strength, melting point and thermal conductivity are lower than stainless steel, its reduced hardness value made it an ideal material for machinability. Table 3.6 gives the material properties of brass.

Table 3.6: Properties of Brass (Copper Development Association, 2017), (E-Z Lok, 2016)

Mechanical Properties of Brass	
Property	Value
Tensile Strength, Ultimate	469 MPa
Tensile Strength, Yield	310 MPa
Melting Point	1316.48 K
Density	8802.21 kg/m ³
Hardness (Brinell)	60
Thermal Conductivity	188.52 W/m K
Coefficient of Thermal Expansion	18.36 x 10 ⁻⁶ /K
Specific Heat Capacity	376.81 J/kg K

The following section focuses on the combustion chamber shape, size and its construction. The final decision for material will be discussed at the end of this chapter.

3.4 Combustion chamber motor concepts

The combustion chamber for the hybrid rocket slab motor provided storage for the solid fuel propellant as well as location for the combustion reaction. The inner dimensions were therefore designed based upon the solid fuel grain dimensions with consideration of oxidiser mass flow rate and oxidiser mass flux. The combustion chamber was to also enable visualisation of combustion of the propellants and regression rate of the solid fuel grain. Allowances for glass windows were also made in the design process.

An iterative process was followed to determine parameters such as fuel grain dimensions, oxidiser mass flow rate, burn time, and oxidiser mass flux. This is described in detail in Chapter 4 and were used to determine the final combustion chamber and glass window dimensions.

Sections 3.4.1 to 3.4.3 discusses the combustion chamber configurations that were considered.

3.4.1 Motor concept one

The first conceptual design was developed based on the original combustion chamber fabricated as part of Publication 4 (Dlamini, et al., 2014). The design consisted of thick inner panels that were bolted together to hold them in place and form the rectangular box shape of the combustion chamber. These panels would include a rectangular-shaped recess to house the glass windows, with the thickness dependent on the windows. The outer panels would be bolted onto the inner panels to secure the glass windows and would only consist of a rectangular cut-out for viewing.

Gaskets would then be used to ensure sealing between the base, the side panels and glass, and all bulkheads.

The inner dimensions of the combustion chamber would be calculated using the fuel grain dimensions. The width would allow a 1 mm or 2 mm tolerance to enable smooth insertion of the fuel grain fixing plate and fuel grain itself (Figure 3.6). The snug fit of the fuel grain within the combustion chamber would minimise side burning and ensure more accurate regression rate data. The inner port height would be determined with consideration of the glass windows, oxidiser mass flow rate and oxidiser mass flux. An initial port length of 200 mm was proposed, depending on the length of the fuel grain and is shown in Figure 3.7. The thickness of the inner panels would be dependent on the thickness of glass used (between 6 mm and 14 mm), which would be established from finite element analyses (FEA) if the proposed design was selected. The thickness of the outer panels and bulkheads would be clarified by calculations and were initially assumed to be between 10 mm and 16 mm thick. These would have to be able to withstand bending and warping but not so much so that manufacturing would be difficult (due to the material properties of stainless steel) and the combustion chamber would be so heavy that it would not be easily transported.

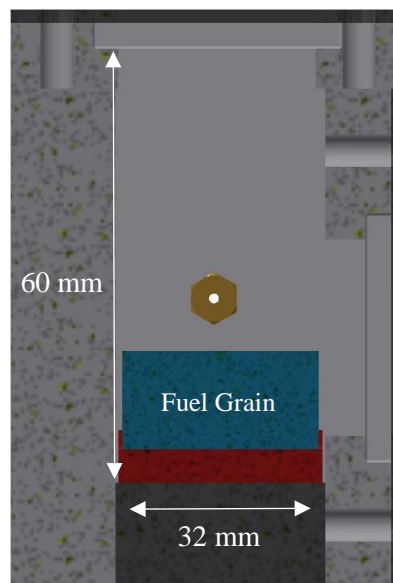


Figure 3.6: Combustion chamber concept one – section view

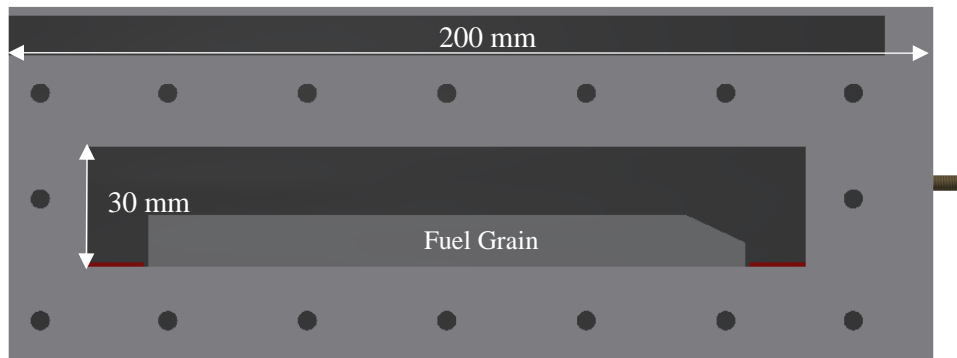


Figure 3.7: Combustion chamber concept one – side view

Although the manufacture and assembly of this design would be straightforward, factors such as sealing and structural integrity were of concern. An alternative solution included welding of the inner panels which would provide a more durable design.

Welding joints would have been inserted as depicted in yellow in Figure 3.8.

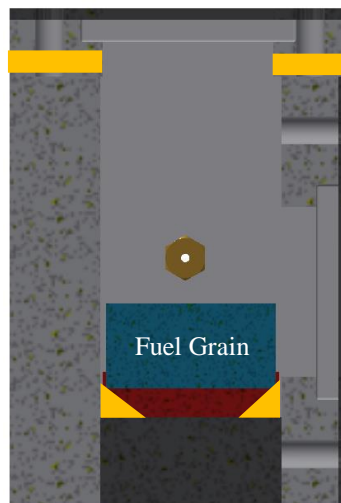


Figure 3.8: Welding joints for inner panels of combustion chamber

Welding in this manner appeared to be satisfactory but considering the small widths of the combustion chamber, between 10 mm to 30 mm, complexities arose as the welding rod may not have been able to efficiently reach some of the inner portions of the combustion chamber. Welding on the outside of the combustion chamber was deemed to be a better option as it would also avoid combustion instabilities (Gill & Nurick, 1976) as a result of welding.

All panels and bulkheads mentioned in the designs would be laser or waterjet cut depending on their thickness. They would then be CNC machined to the required design specifications.

3.4.2 Motor concept two

The second concept was similar to the first, however it included machined recesses in both the inner and outer panels that would house the glass. In this case both panels would be the same thickness and would reduce the possibility of warping of the thin outer panels.

The length of the combustion chamber was also reconsidered, as the initial proposed length was presumed to be too short. This would therefore not provide sufficient space for decomposition of the nitrous oxide and hence recirculation and mixing with the paraffin wax fuel grain, and safe discharging of the exhaust gases. The extent of the injector head distance into the pre-combustion chamber had to also be taken into consideration.

A length of two times that of the fuel grain would be used in the port length of the combustion chamber. This would ensure sufficient pre and post combustion distances as the fuel grain would be positioned in the centre of the combustion chamber.

The panels and bulkheads mentioned in concept two would be manufactured as described in Section 3.2.1.

3.4.3 Motor concept three

The third motor concept included the use of a brass billet to manufacture the inner C portion of the combustion chamber. This is represented by the gold colour as indicated in Figure 3.9. Stainless steel would provide difficulty and increased costs as the machining would be challenging due to the dimensions of the combustion motor. Brass was more suitable in this case but more expensive.

This concept would ensure proper sealing of the port area and structural integrity of the motor. It would also provide a secure fit of the glass windows within the billet. The outer panels would then only include a visualisation port in the shape of the glass. An additional window was also added to provide symmetry of the system to achieve accurate regression rate measurements.

The side panels in this design would be relatively long and warping due to rapid heating of the combustion chamber was of particular concern. Calculations would thus provide a suitable thickness while ensuring proper assembly of each component. The position of the glass was also a matter of concern because the side panels were to incorporate grooves to house the glass. Section 4.7 discusses the methodology and design parameters, including the suitable thickness for each panel.

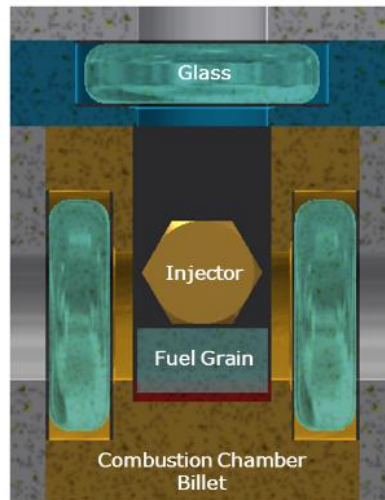


Figure 3.9: Combustion chamber section view final design (Theba, et al., 2017)

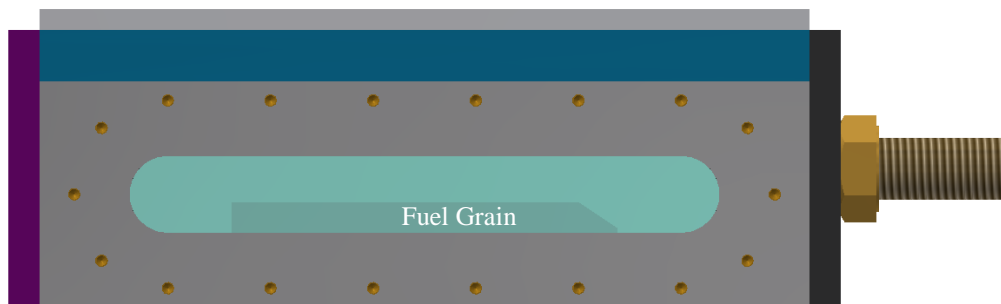


Figure 3.10: Combustion chamber side view final design (Theba, et al., 2017)

3.5 Gasket concepts

Gaskets were to be used as a separating medium between the glass and the steel. This would prevent the glass from being in contact with the steel and therefore ensuring an even stress distribution to prevent areas of localised stress due to manufacturing flaws. It would also enable some movement and flexibility of the glass to account for the thermal expansion or contraction. Most importantly, the gasket would ensure that the combustion chamber is sealed.

3.5.1 High-temperature silicone or gasket maker

Initially high-temperature silicone or gasket maker was to be used to line the grooves of the steel in which the glass would be positioned. This would create a buffer between the two materials and give the glass room for movement. Although this concept was appealing, there were concerns about the layer of silicone being uneven and therefore producing unnecessary stresses on the glass which could otherwise be avoided. This process requires at least 24 hours for the gasket to cure and would not be ideal once testing was under way as more than one test per day would have to be conducted.

3.5.2 Grease or oil

An alternative method to ensure sealing of the combustion chamber between the side panels and bulkheads was to use grease or oil between them. The steel would be coated before the panels were to be bolted together. This technique would eliminate the curing time required by the gasket maker, allowing for more than one test to be conducted per day. This method however, did not provide an adequate solution for the sealing of the metal panels.

3.5.3 Viton

Another concept for the gasket would be to use Viton. Viton's characteristics make it a suitable material for the experimental conditions; it has a relatively low tensile strength and is quite flexible. Its maximum operating temperature is only 250 °C, which is a limiting factor. Table 3.7 shows the properties of Viton gaskets (Natal Gaskets, 2011).

Table 3.7: Viton gasket properties gaskets (Natal Gaskets, 2011)

Properties of Viton Gaskets	
Tensile strength	5 MPa
Compression set	62%
Hardness (A)	75 ± 5
Elongation at break	200%
Specific gravity	1.95
Tear Strength	30 kg/cm
Recommended maximum temperature	250 °C
Recommended maximum pressure	1000 kPa

3.5.4 O-rings

Viton or silicone O-rings were also considered. These would be placed in the recesses where the glass sits. Although this concept could have provided the required sealing, it would not provide a suitable buffer for the glass against the steel.

3.5.5 Silicone sheet gaskets

A suitable gasket was identified to be silicone which has a slightly higher tensile strength and elongation at the break point than Viton, although its maximum operating temperature is slightly lower.

Table 3.8 shows the properties of silicone gaskets (Natal Gaskets, 2011).

Table 3.8: Silicone sheet gasket properties (Natal Gaskets, 2011)

Properties of Silicone Sheet Gaskets	
Tensile strength	8 MPa
Compression set	40%
Hardness (A)	60 \pm 5
Elongation at break	350%
Specific gravity	1.16
Tear strength	20 kg/cm
Recommended maximum temperature	180 °C
Recommended maximum pressure	1000 kPa

The purpose of the gaskets used in the combustion chamber between the metal and glass needed to be of a material that would allow movement of the glass, expansion and contraction of the steel, but also ensure sealing. Silicone sheet gasket material was the most viable option and was used for the purposes outlined in this section.

3.6 Conceptual design discussion

The combustion chamber design was critical to its performance and the safe working environment for the glass.

The material selection for the glass presented in this chapter were all viable options, in particular borosilicate and vycor. Polycarbonate may have sustained the atmospheric testing but would not have endured the pressurised experiments. Borosilicate and vycor were practical solutions although the costs and availability associated with them did not make the choice feasible. Quartz glass was established to be the best alternative because of its mechanical properties. It was slightly more expensive than Vycor but was readily available and is discussed further in Section 4.8.

The thickness and shape of the glass was of particular concern due to the expected high temperatures and pressures within the operating environment of the combustion chamber. The elongated oval shape of the glass windows was selected due to the least areas of localised stress compared to the other concepts discussed. The thickness of glass would be verified by FEA. The short burn time of 5 seconds was also considered as this would decrease the exposure time of the glass consequently alleviating the forces exerted.

Stainless steel has been successfully employed in rocket motors with many different propellant combinations (Gill & Nurick, 1976), it has a high tensile strength and melting point, and good thermal coefficient of expansion. However, its hardness factor would create challenges in manufacturing of the C-shaped base of the combustion chamber described in Section 3.4.3. Brass has similar properties to stainless steel however not as superior with respect to the tensile strength and melting point. Nevertheless, the hardness value of brass made it a suitable material for machining of the combustion chamber billet. Both stainless steel and brass are ductile at low temperatures (Gill & Nurick, 1976), which is a requirement of a cryogenic oxidiser such as nitrous oxide. These materials are therefore compatible thus preventing degradation of the oxidiser flow and material characteristics of the combustion chamber.

The first few motor conceptual models presented in this section did not fulfil all combustion chamber requirements as they posed challenges in structural integrity of the chamber itself, the glass, combustion instabilities and sealing.

The combustion chamber had to provide storage of the solid fuel propellant and safe motor operation. The third concept mentioned was identified to be the most suitable design as it eliminated the need for welding while still providing proper sealing and structural integrity of the motor.

Factors such as the lengths and thicknesses of all panels had to be considered to minimise warping while allowing for sufficient recirculation and mixing of the propellants.

One window on each side, with one at the top offered symmetry to the system. This would allow for better and more accurate regression rate observations during testing.

Recesses would be machined into the sides of the combustion chamber billet for the glass to be positioned. The side panels would then be bolted onto the billet. Tolerances had to be considered to allow for sufficient movement and flexibility of the glass. Calculations would determine the specified tolerances with expansion and contraction calculations under operating conditions. Gaskets would also be implemented to prevent the glass from coming into contact with the metal, and for sealing. Silicone sheet gaskets were identified to be the most suitable solution.

The final design of the combustion chamber and its constituent components is discussed in detail in Chapter 4.

CHAPTER 4: SLAB MOTOR DESIGN AND MANUFACTURE

The development of the HSM visualisation test stand entailed the design, manufacture and assembly of several different components. These include the feed system, the injectors as well as the motor itself. The material considerations were imperative to ensure safe and reliable operation of the system when using nitrous oxide. The system specifications included the capability of adapting to different oxidiser mass flow rates and chamber pressures. Windows had to also be incorporated to visualise the combustion and observe the regression rate characteristics. The work in this chapter is closely linked to the associated journal paper, Publication 3 (Theba, et al., 2017) with extracted paragraphs as indicated.

4.1 Analytical Modelling

There is a lack of regression rate data for Sasolwax 0907 used as a hybrid fuel with nitrous oxide in a slab motor. Data from the literature for O/F ratio and regression rates were used as initial assumptions and these are given in Table 4.1. The optimal O/F ratio for pure paraffin wax and 40% aluminised fuel grains was found to be 8 and 3.5 respectively, with the use of nitrous oxide (Genevieve, 2013). The regression rates for these fuel grain compositions were calculated using NASA CEA (Chemical Equilibrium with Applications) to determine the ideal operating parameters of the hybrid rocket slab motor.

Table 4.1: Assumptions for experimental calculations

Variable	Value
O/F ratio (pure paraffin)	8
O/F ratio (40% Al paraffin)	3.5
Regression rate (pure paraffin)	1.5 mm/s
Regression rate (40% Al paraffin)	2 mm/s

The assumptions mentioned above were used to calculate the oxidiser mass flow rates with assumed values of fuel grain dimensions and a burn time of 5 seconds. The assumptions were based on the fuel grain dimensions used by TU (Nakagawa, et al., 2009) and SU (Chandler, et al., 2012). Equations 4.1 to 4.5 (Biblarz & Sutton, 2001) were applied in the experimental calculations, and were modelled and manipulated using an iterative process, details of which can be found in Appendix 2A.

The volume of fuel, V_f was first calculated using the assumed fuel grain dimensions namely, the length, L_f , the width, w_f , and the thickness, t_f .

$$V_f = L_f \times w_f \times t_f$$

(Equation 4.1)

The fuel mass, m_f is defined by the multiplication of the fuel's density, ρ_f by V_f :

$$m_f = \rho_f \times V_f$$

(Equation 4.2)

The averaged fuel mass flow rate, \dot{m}_f was calculated from the ratio of m_f and the assumed burn time, b_t of 5 seconds:

$$\dot{m}_f = \frac{m_f}{b_t}$$

(Equation 4.3)

The oxidiser mass flow rate was then calculated by multiplying the O/F ratios given in Table 4.1 with \dot{m}_f for each fuel grain:

$$\dot{m}_{ox} = O/F \times \dot{m}_f$$

(Equation 4.4)

The total mass flow rate, \dot{m}_t is the sum of \dot{m}_f and \dot{m}_{ox} :

$$\dot{m}_t = \dot{m}_f \times (1 + O/F)$$

(Equation 4.5)

The fuel surface area, A_f was then determined by multiplying L_f and w_f :

$$A_f = w_f \times L_f$$

(Equation 4.6)

The regression rate, \dot{r} could then be obtained by dividing \dot{m}_f by the multiplication of ρ_f and A_f :

$$\dot{r} = \frac{\dot{m}_f}{\rho_f \times A_f}$$

(Equation 4.7)

The regression rates determined from these calculations were used in the comparison with experimental results. It is the simplified formula mentioned in Section 2.4 for non-classical hybrid fuels.

The injector diameter (detailed in Section 4.6) and oxidiser mass flow rate calculations were compared and were significant in defining the fuel grain dimensions. Equations 4.4, 4.7 and 4.8 were used to obtain an injector diameter that would be easily manufactured with a correlating sufficient oxidiser mass flow rate. A fuel grain size of 150 mm long, 30 mm wide and 15 mm thick was assumed to be sufficient, based on previous slab motor testing discussed in Section 2.5, for the purposes of testing in order to provide an adequate burn time and to obtain regression rate results. It is slightly bigger than the ones used by TU and SU but would enable a longer burn time in order to visualise the combustion mechanism and obtain adequate regression results. A pure paraffin wax fuel grain is shown in Figure 4.1 and a 40% aluminised grain in Figure 4.2. The chamfers on the leading edge (circled in red on the right-hand side) of each fuel grain assisted in the ignition of the fuel grain.

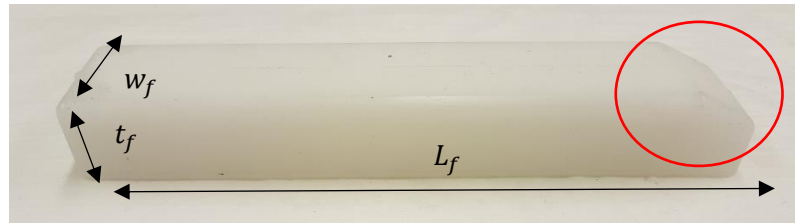


Figure 4.1: Pure paraffin wax fuel grain



Figure 4.2: 40% aluminised wax fuel grain

The final fuel grain dimensions, oxidiser mass flow rate and injector diameter specifications are shown in Table 4.2 and Table 4.3.

Table 4.2: Pure paraffin wax parameters

Pure Paraffin Wax	
Length (mm)	150
Width (mm)	30
Thickness (mm)	15
Ox Mass Flow Rate (kg/s)	0.13
Injector Diameter (mm)	1.5

Table 4.3: 40% aluminised paraffin wax parameters

Aluminised Paraffin Wax	
Length (mm)	144
Width (mm)	30
Thickness (mm)	15
Ox Mass Flow Rate (kg/s)	0.1
Injector Diameter (mm)	1.3

The aluminised fuel grain's length is shorter than that of pure paraffin wax due to the higher oxidation heat of the aluminium additive resulting in a denser grain (Chiaverini & Kuo, 2007). The metallised particles have the effect of increasing the regression rate and decreasing the O/F ratio, thereby reducing the required fuel mass to produce the same performance or thrust (Karabeyoglu, et al., 2003). The optimal oxidiser mass flow rate for the aluminised fuel grains was calculated to be lower than that of the pure paraffin wax so that the same performance could be achieved.

For the purposes of testing and verification of the results, the aluminised fuel grains were manufactured with the same length as that of the pure paraffin fuel grains for consistency between tests. A higher oxidiser mass flow rate is expected for the 150 mm length of the aluminised fuel grain due to the increased heat transfer of the aluminium particles (McCormick, et al., 2005).

4.2 Aluminium Fuel Grain Mould

The fuel grain mould was designed from aluminium as it was cheap, easily manufactured and could be used for many fuel grain castings. It was also resistant to the maximum operating temperature of 150 °C. The mould was designed as two halves which were bolted together longitudinally to form a mould for the fuel grain. The inner dimensions were the same as that of the fuel grain – 150 mm x 30 mm x 15 mm. The mould also had a protruding section to create the chamfered leading edge on the fuel grain. This is indicated in Figure 4.3. Manufacturing of the mould was completed on a CNC machine.



Figure 4.3: Aluminium fuel grain mould

4.3 Fuel grain casting

A high-temperature furnace was used to cast the fuel grains. The mass of paraffin wax required for the stipulated fuel grain dimensions was weighed out and melted at 120 °C. It was then poured into the preheated mould. The molten wax was left to cool in the oven with the mould which prevented voids or cracks within the fuel grain and reduced the shrinkage rate.

The same method was followed to cast the fuel grains with aluminium additives. However, the mixture of molten wax and powder had to be stirred until it reached its congealing point (84 °C), to prevent settling of the particles. Once this temperature was reached, the mixture was poured into the mould and left to cool as described above.

4.4 Feed system layout

The feed system's design was compatible with the HSM and the cylindrical lab-scale motor. It is described in detail in Maharaj et al., (2018) (Maharaj, et al., 2018). Since the feed system needed to accommodate both motors, it had to be easily configurable which was achieved with the use of a flexible hose and adaptors. The design was safe and had minimum bends and fittings to reduce the pressure loss across the feed system. All the tubing was made of stainless steel for compatibility with nitrous oxide. Figure 4.4 (Maharaj, et al., 2018) illustrates the feed system layout.

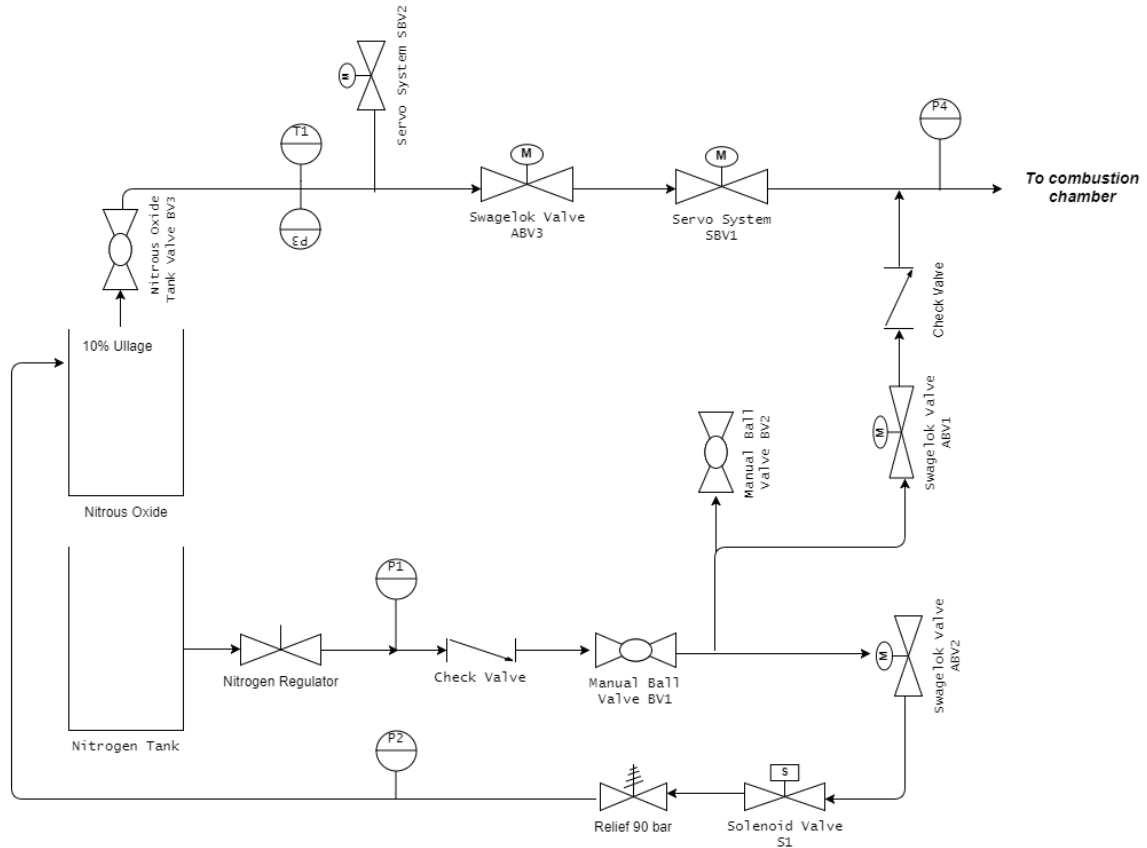


Figure 4.4: Schematic of the feed system layout (Maharaj, et al., 2018)

Three automated ball valves were installed for supercharging with nitrogen, purging the system with nitrogen, and enabling oxidiser flow. The purge line ensured safe operation and was used in case of an emergency by displacing any remaining oxidiser in the system, thereby extinguishing any flames. Supercharging the oxidiser desensitised the nitrous oxide to prevent cavitation and to provide a high-pressure differential during start-up. The servo motor ball valve 1 (SBV1) is an additional valve on the main injection line for safety. In the event of an emergency SBV2 dumps or discharges all of the nitrous oxide from the tank. A manual ball valve enables the flow of nitrogen into the nitrous oxide tank to supercharge. This valve is opened manually before the testing procedure begins.

The nitrogen and nitrous oxide inlets were connected to the respective tanks with PTFE flexible hoses. The nitrous oxide outlet incorporates a relief valve that is certified to 75 bar. In the event that this valve experienced a pressure above this value, it would release the nitrous oxide into the atmosphere. This is an additional safety precaution.

An array of pressure transducers (discussed in Section 5.1) and thermocouples described in (Maharaj, et al., 2018) are integrated in the system at various points for the respective measurements. In the case of the HSM, these recordings were not utilised for the initial tests for the purposes of system validation. They will however, be used in future testing to obtain the

relevant pressure and temperature measurements within the combustion environment. These components are interfaced to a LabVIEW control and data acquisition system discussed in Chapter 5.

The main injection or feed line consists of ½ inch stainless steel tubing. The larger diameter reduced the pressure drop across the line thus increasing the oxidiser mass flow rate, which was crucial for the cylindrical lab-scale motor in particular. This was not essential for the purge, dump, and supercharging lines, which comprised ¼ inch stainless steel tubing.

4.5 Manifold

The manifold for the HSM was designed much like the injectors and is shown in Figure 4.5 and Figure 4.6. An M24 brass bolt was used to enable the threaded end of the injector to comfortably screw into the front end of the manifold. The manifold acted as an adaptor between the injector and the feed system. The O-ring grooves were used for sealing between the manifold and injector bulkhead. The injector was screwed into the front end of the M24 bolt depicted in the middle view of Figure 4.6. The flow direction was from the end of the threaded part of the bolt labelled as ¼ inch NPT in Figure 4.6. This thread specification was for the flexible hose adaptor.

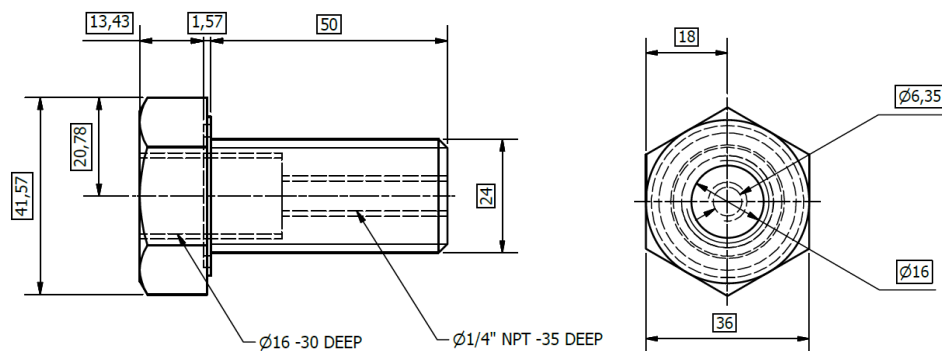


Figure 4.5: Manifold Engineering Drawings

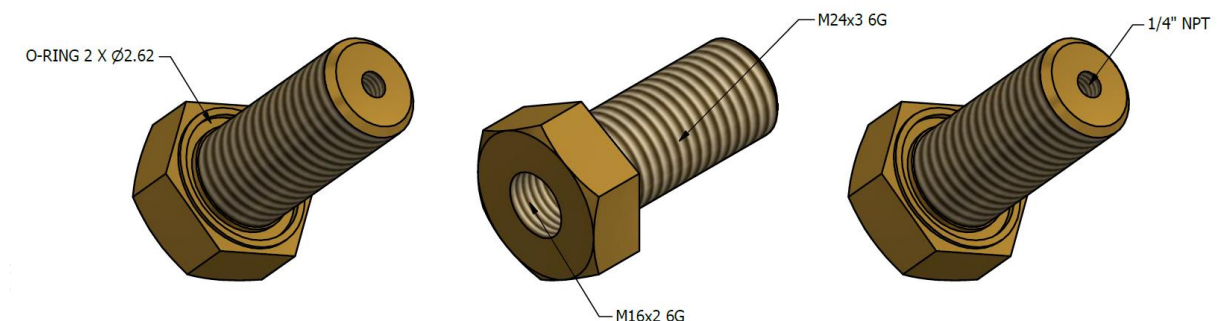


Figure 4.6: Isometric drawings of manifold

4.6 Injectors

Rocket motor injectors are used to ensure decomposition of the nitrous oxide to achieve efficient combustion. They also affect a system's combustion stability and therefore have to be designed in consideration of the flow geometry, element pattern, and assembly. The literature surrounding the design are given in Publication 4 (Dlamini, et al., 2014), and the extensive iterative calculations are given in Appendix 4B. The process outlined in Section 4.1 was followed to determine appropriate oxidiser mass flow rates, orifice sizes and pressure drop using (Equation 4.8)

. The results of these calculations were that oxidiser mass flow rates between 57 g/s and 130 g/s were required, depending on the chamber pressure.

$$\dot{m}_{ox} = C_d \times N_{inj} \times A_{inj} \times \sqrt{2\rho_{ox}\Delta P}$$

(Equation 4.8)

The coefficient of discharge, C_d was determined from Figure 4.7 (Biblarz & Sutton, 2001) through interpolation for each injector diameter, and is presented in Table 4.4. The number of injector orifices N_{inj} was chosen to be one for ease of manufacturing, the oxidiser density ρ_{ox} of 930 kg/m³ (Sasol, 2010), and the pressure drop ΔP across the injector was a minimum of 8.5 bar (calculated from 15% of the nitrous oxide at STP). Table 4.5 provides the oxidiser mass flow rates expected at various combustion chamber pressures, for each of the selected injector diameters.

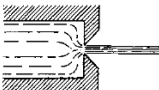
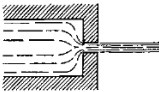
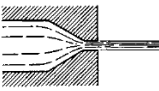
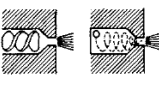
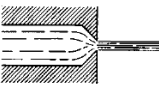
Orifice Type	Diagram	Diameter (mm)	Discharge Coefficient
Sharp-edged orifice		Above 2.5 Below 2.5	0.61 0.65 approx.
Short-tube with rounded entrance $L/D > 3.0$		1.00 1.57 1.00 (with $L/D \sim 1.0$)	0.88 0.90 0.70
Short tube with conical entrance		0.50 1.00 1.57 2.54 3.18	0.7 0.82 0.76 0.84–0.80 0.84–0.78
Short tube with spiral effect		1.0–6.4	0.2–0.55
Sharp-edged cone		1.00 1.57	0.70–0.69 0.72

Figure 4.7: Discharge coefficients (Biblarz & Sutton, 2001)

Table 4.4: Discharge coefficients for respective orifice diameters

Short tube with conical entrance	
Orifice diameter (mm)	Coefficient of discharge
0,5	0,7
1	0,82
1,3	0,788
1,5	0,767
1,57	0,76
2,54	0,84

Table 4.5: Theoretical oxidiser mass flow rates

Theoretical oxidiser mass flow rates at specified chamber pressures			
Injector diameter (mm)	1	1.3	1.5
Discharge coefficient	0.82	0.788	0.767
Oxidiser mass flow rate @ atm (g/s)	62	101	130
Oxidiser mass flow rate @ 5 bar (g/s)	59	97	125
Oxidiser mass flow rate @ 10 bar (g/s)	57	92	120

The injector for the HSM was manufactured from an M16 brass bolt. The use of a bolt eliminated the need for welding of steel and brass components and reduced the risk of instabilities in the motor. The effect of instabilities is discussed in detail in Publication 4 (Dlamini, et al., 2014). The mechanical properties of the brass used is given in Table 3.6 (Copper Development Association, 2017), (E-Z Lok, 2016) made it an ideal choice for the intended purpose, especially because of its compatibility with nitrous oxide and the manufacturability of the orifice size. Brass has a reduced hardness value (Brinell 60) compared to stainless steel (Brinell 170) which improves its machinability.

The injector consists of a single orifice and is shown in Figure 4.8. Three injectors were designed with orifice diameters of 1 mm, 1.3 mm and 1.5 mm to accommodate the different oxidiser mass flow rates required to obtain sufficient regression rate measurements. The threaded end of the bolt was tapered twice on the inside to allow for a transition of the flow from the larger diameter of the feed system to the small diameter of the orifice and is shown in Figure 4.8. Figure 4.9 shows the three-dimensional view of the injectors. The calculations for the pressure loss across the entire injector are given in Appendix 4C. The minimum total pressure loss across the injector was determined to be 9 bar.

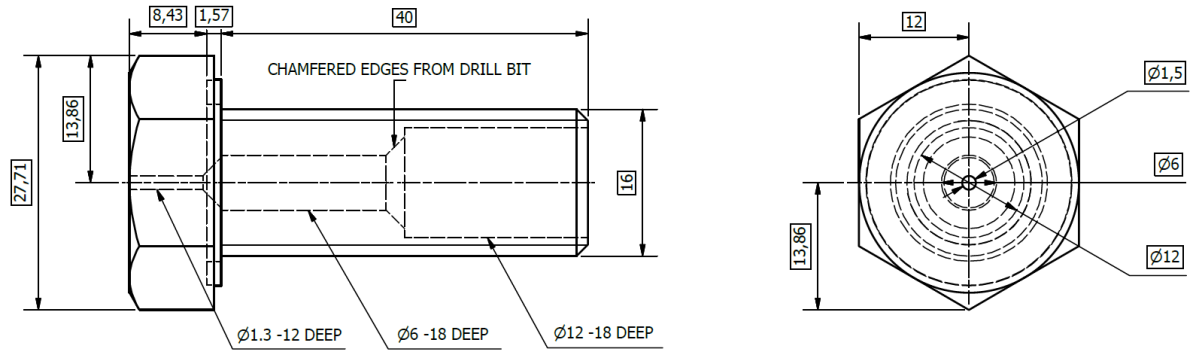


Figure 4.8: Injector engineering drawings

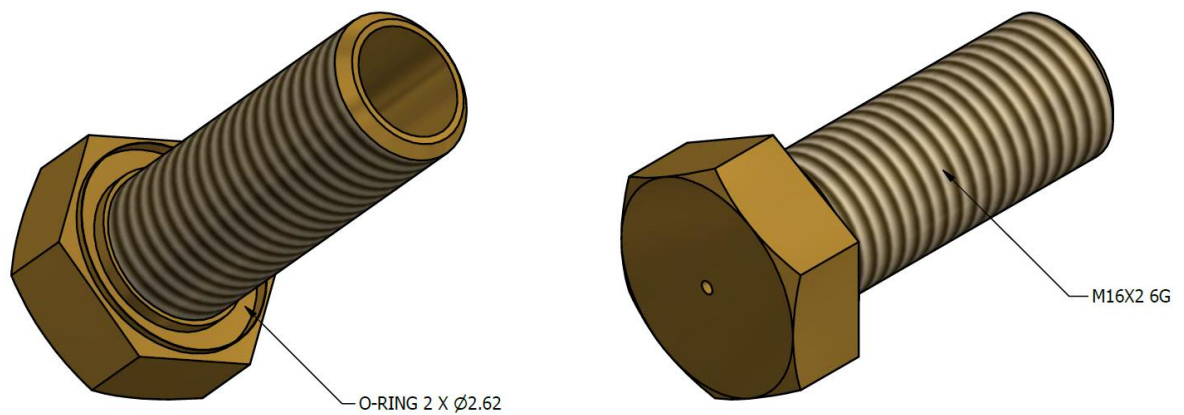


Figure 4.9: 3 D view of injectors

4.7 Combustion motor components

The hybrid rocket slab motor combustion chamber required windows for safe visualisation of the combustion process between the paraffin wax and nitrous oxide. It was therefore designed to be compatible with both materials and to withstand the operating temperatures and pressures. NASA CEA suggests that the combustion reaction between nitrous oxide and paraffin wax yields temperatures above 3000 K. It should be noted that this temperature refers to that within the combustion boundary layer and not in the entire combustion chamber. Also, due to the short burn time of 5 seconds, heat transfer is expected to be small and therefore no insulation was required on the inside of the combustion chamber (Dlamini, et al., 2014). However, the undetermined maximum operating temperature of the combustion chamber during firings was accounted for with materials that provided for great heat dissipation, high thermal conductivity and a low thermal expansion coefficient.

The combustion chamber is used to enclose the fuel grain and provide a contained space for combustion, and is designed according to the fuel grain dimensions. The design incorporated two windows, one on either side to obtain symmetry and hence simpler calculations for the purposes

of system verification. The top window discussed in Chapter 3 will be incorporated at a later stage. This particular motor is to be used in experiments at atmospheric pressure, 5 and 10 bar. All the design work was carried out on the chamber components at 20 bar in order to provide a safety factor of 2.

4.7.1 Geometry

The geometry of the HSM combustion chamber is rectangular. The length was assumed to be twice that of the fuel grain (300 mm). This was to ensure sufficient turbulence to increase decomposition of the nitrous oxide sooner, before it reaches the fuel grain, thereby promoting the reaction between the fuel and oxidiser, and also to allow for safe expulsion of the exhaust gases. Increasing the combustion chamber length aids in mixing of the reactants and allows for more stable combustion (Biblarz & Sutton, 2001). The inner height of the chamber had to allow for sufficient room so that the combustion reaction could be clearly visualised. This inner height also affects the regression rate of the propellants and is called the port height, or port area. The port height was determined to be 47 mm using the following equations (Dlamini, et al., 2014):

$$\dot{r} = aG_{ox}^n$$

(Equation 4.9)

Where, $a = 0.155 \times 10^{-3}$ and $n = 0.5$ (McCormick, et al., 2005).

The port area, A_p was then calculated from G_{ox} and \dot{m}_{ox} :

$$A_p = \frac{G_{ox}}{\dot{m}_{ox}}$$

(Equation 4.10)

The port width, w was based on the fuel grain width and used to calculate the port height, l :

$$A_p = l \times w$$

(Equation 4.11)

The inner width of the combustion chamber was 32 mm, slightly larger than that of the fuel grain width. This was to allow for a tolerance and for the fuel grain plate to move without restraint. The closer the glass was situated to the fuel grain, the less risk there was of side burning which would affect the regression rate results. Table 4.6 (Theba, et al., 2017) shows the final combustion chamber size.

Table 4.6: Combustion chamber final dimensions (Theba, et al., 2017)

Combustion Chamber Dimensions	
Parameter	Distance (mm)
Inner width	32
Inner height	47
Inner length	300
Total width	88
Total height	116
Total length	324

Brass was the material of choice for the combustion chamber base for the reasons discussed in Section 4.6. It can withstand very high temperatures and has a low coefficient of thermal expansion.

The chamber was machined from a brass billet since the motor is of rectangular shape. This was to ensure complete sealing of the inner portion of the chamber without requiring welding which could cause combustion instabilities (Dlamini, et al., 2014).

A local company, Copalcor® sponsored the brass billet for this project. This significantly reduced the time and machining costs for manufacturing the base of the combustion chamber if stainless steel were used.

The brass billet walls were machined to 20 mm on either side and were trimmed down to 15.5 mm around the viewing ports, as shown in Figure 4.10, Figure 4.11 and Figure 4.12, so that the silicone gaskets and glass could be placed within the recess. This incorporated a 1 mm tolerance around the edges of the glass, which allowed for some movement as well as expansion and contraction of the brass during firings.



Figure 4.10: Machined brass combustion chamber base

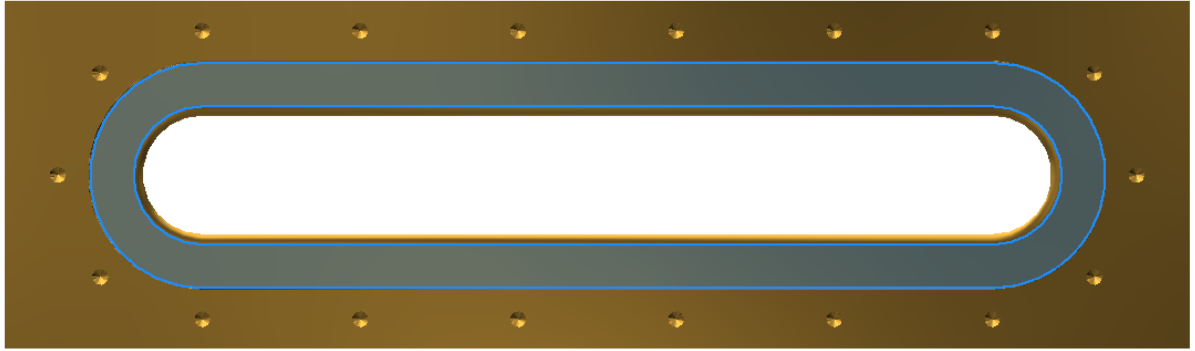


Figure 4.11: Recess for glass

These recesses included a small chamfered edge (Figure 4.12) to alleviate the pressure around the glass and to eliminate sharp corners that would increase the maximum stress intensity.

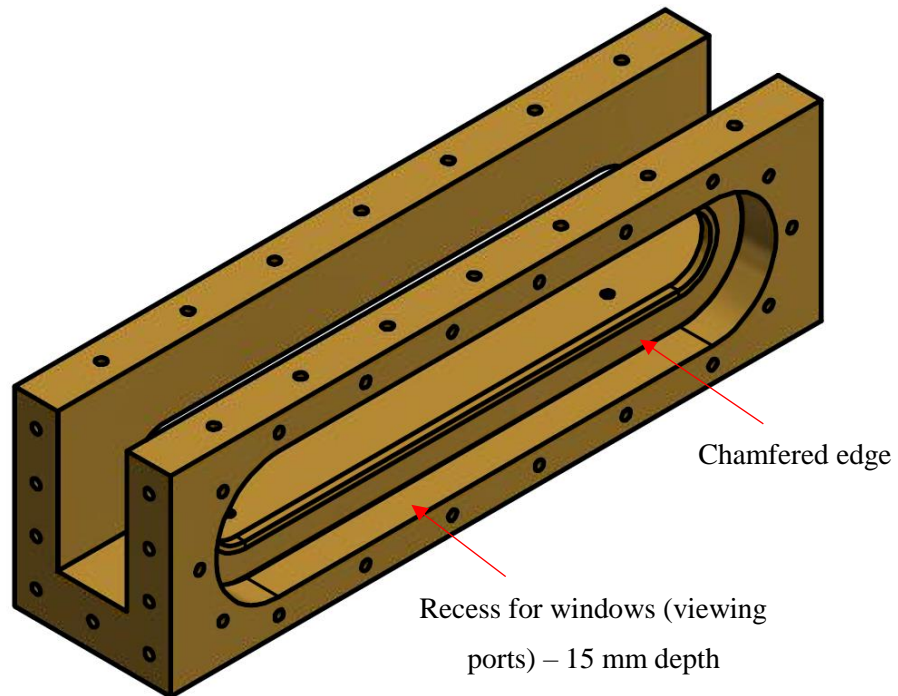


Figure 4.12: Isometric view of combustion chamber showing the recesses for the windows with chamfered edge

The base of the chamber was machined to a thickness of 24 mm.

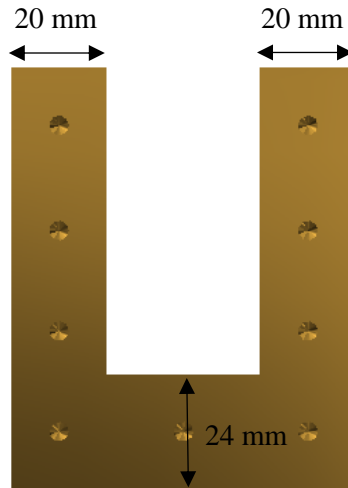


Figure 4.13: Chamber base - side view

4.7.2 Fuel grain fixing plate

A fuel grain fixing plate was designed so that the fuel grain could be secured to the plate and removed from the combustion chamber, given a width of 30 mm. The plate was laser cut from a 6 mm flat stainless steel plate as shown in Figure 4.14. 3 mm cap screws were used to secure the fuel grain fixing plate to the combustion chamber base. The fuel grain was fixed to this plate with epoxy glue.

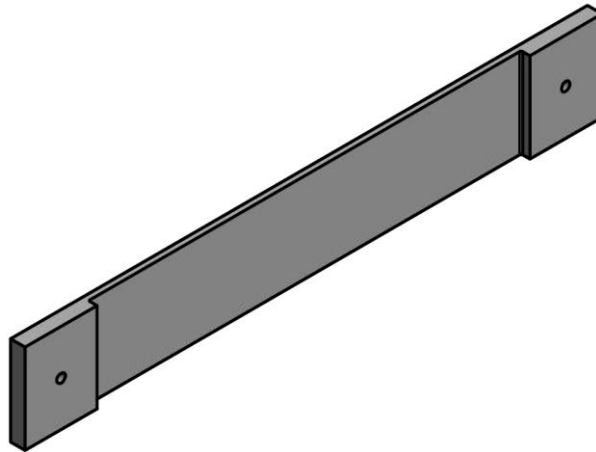


Figure 4.14: Fuel grain fixing plate - isometric view

4.7.3 Side panels

The side panel shown in Figure 4.15 was cut from 8 mm stainless steel 304. It is 80 mm in height and 300 mm in length. To minimise deformation caused by the length of the panel, the above-mentioned thickness of the side panels was chosen. The panels were designed to be fitted against the glass plates (Theba, et al., 2017).

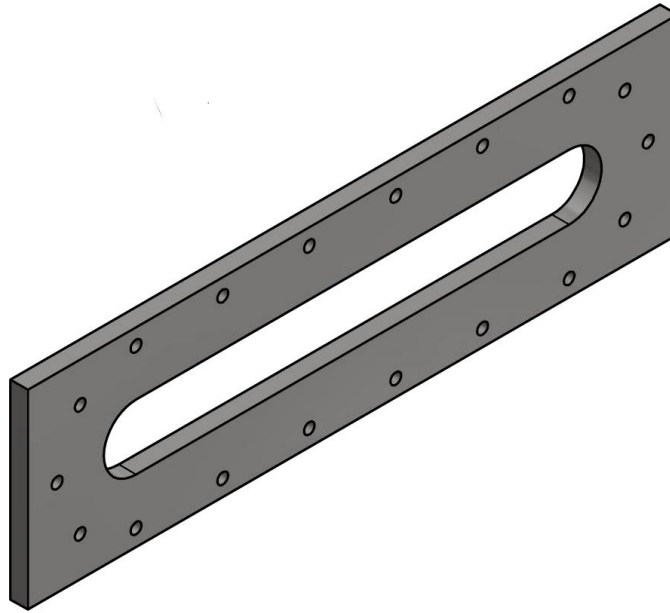


Figure 4.15: Side panels – isometric view

The side panels were bolted to the brass base once the glass and gaskets were in place.

4.7.4 Top bulkhead

The top bulkhead was designed to be 20 mm thick, to allow for modifications should an additional glass window be later incorporated into the bulkhead. This would provide for the combustion to be visualised from a different view. The dimensions were the same as the side panels as shown in Figure 4.16 (Theba, et al., 2017).

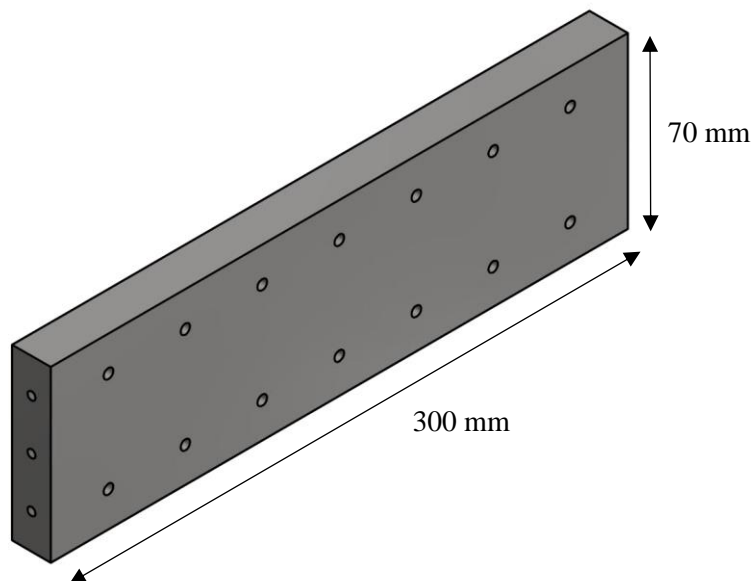


Figure 4.16: Top bulkhead – isometric view

4.7.5 Injector and nozzle bulkheads

The front and back bulkheads were 12 mm thick to ensure that they would not fail under operating conditions. Both bulkheads were 88 mm wide and 108 mm high. The front bulkhead was connected to the feed system, and the injector was screwed into it as indicated in Figure 4.17.

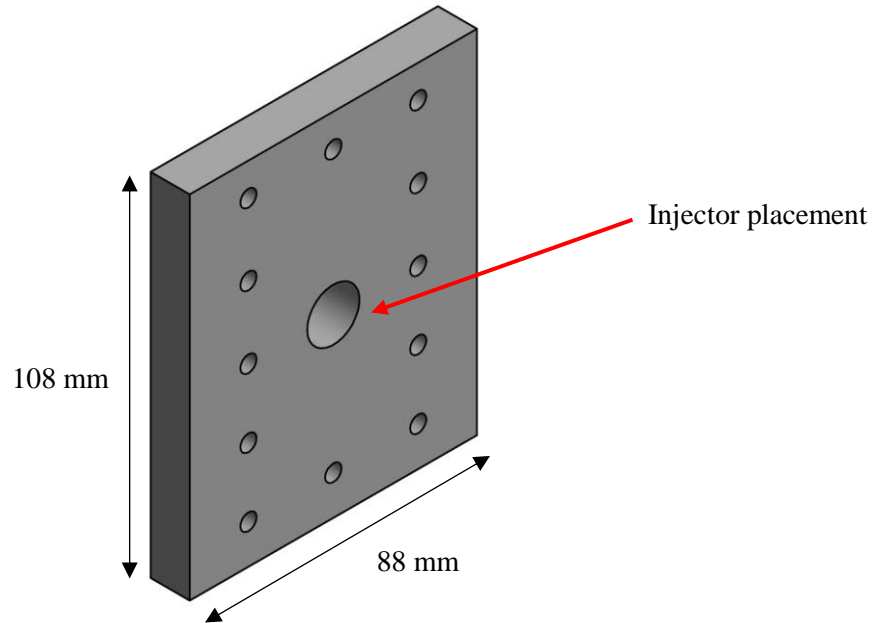


Figure 4.17: Front bulkhead – isometric view

The assembly of the injector, manifold, and front bulkhead is depicted in Figure 4.18. The injector was fastened into the front bulkhead from the left, and the manifold from the right. Viton O-rings were used for sealing.

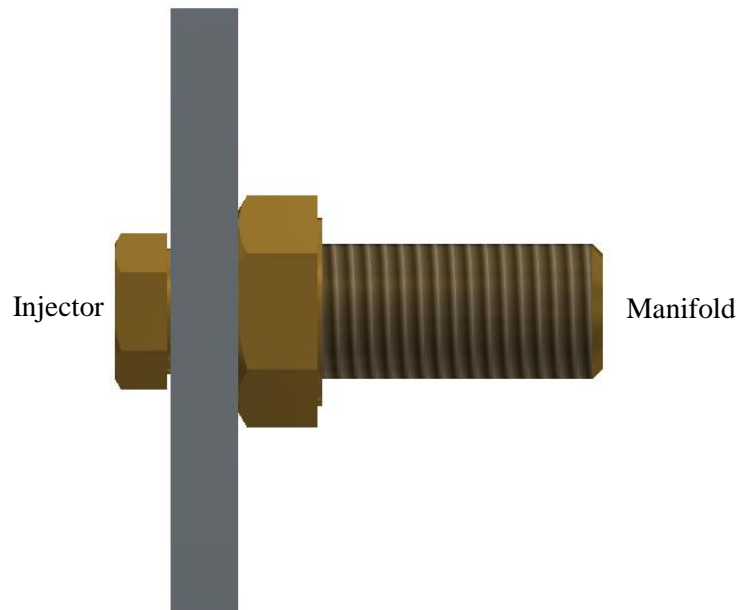


Figure 4.18: Injector - manifold assembly – side view

For the testing that was conducted at atmospheric pressure, the combustion chamber was left open at the exit. To obtain pressurised tests of 5 and 10 bar, bulkheads incorporating nozzles were designed. The HSM did not include thrust measurements, thus the nozzle bulkheads were designed with straight holes to ensure choked flow at the correct pressures without the complexity of a nozzle. (Equation 4.12)

(Fox, et al., 2010) was used and the calculations are given in Appendix 4D.

$$\dot{m}_t = \frac{A_t P_t}{\sqrt{T_t}} \times \sqrt{\frac{\gamma}{R}} \times \left(\frac{\gamma + 1}{2}\right)^{-\frac{\gamma+1}{2(\gamma-1)}}$$

(Equation 4.12)

The throat area A_t was determined from (Equation 4.12) to obtain the throat diameter d_t . T_t is the total temperature predicted by NASA CEA, γ is the specific heat ratio, and R the specific gas constant.

Table 4.7 shows the values of the constants used.

Table 4.7: Constants for nozzle calculations

Variable	Value
O/F ratio	8
Mass flow rate of oxidiser	0.05 kg/s
Total temperature	3000 K
Specific heat ratio, γ	1.25
Gas constant	332

Table 4.8 gives the nozzle diameter required for each of the pressurised tests.

Table 4.8: Nozzle diameter calculated for each chamber pressure

Pressure (bar)	Nozzle Diameter (mm)
2.5	15.8
5	10.8
10	7.5

The nozzle bulkheads were designed with the same dimensions with only the throat diameter specific for each pressurised test. Figure 4.19 depicts the 2.5 bar nozzle.

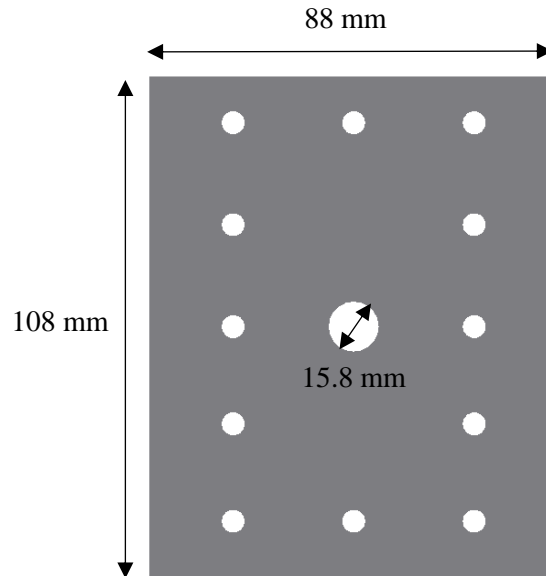


Figure 4.19: 2.5 bar nozzle bulkhead – front view

All panels and bulkheads were bolted onto the brass combustion chamber base using M5 stainless steel bolts. Stainless steel was chosen for the panels and bulkheads due to its resistance to corrosion at elevated temperatures, its durability, high tensile strength and good thermal conductivity, and is discussed in detail in Publication 4 (Dlamini, et al., 2014). The materials as well as the dimensions of the parts which make up the combustion chamber were all designed to withstand the operating conditions of the experiments. Figure 4.20 below illustrates the assembly of the combustion chamber (Theba, et al., 2017). The engineering drawings including the bill of parts is given in Appendix 4H.

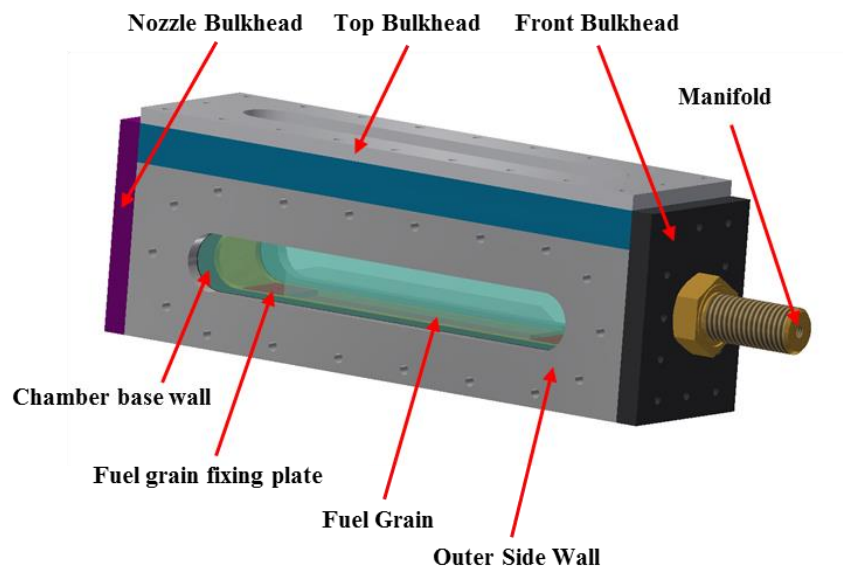


Figure 4.20: Manufactured combustion chamber assembly (Theba, et al., 2017)

4.7.6 Maximum heat transfer

Heat transfer calculations were performed using (Equation 4.13)

(Smith, 2013) on the combustion chamber and quartz glass to validate that the design could withstand the temperatures involved. These calculations were used as to provide an estimate in this regard and the details are given in Appendix 4E.

$$Q_{max} = m \times C_p \times \Delta T$$

(Equation 4.13)

The maximum heat transferred, Q_{max} was determined for each material from the mass m , the specific heat capacity C_p , and the change in temperature ΔT . Table 4.9 provides the constants for stainless steel (AK Steel Corporation, 2007), Table 4.10 for brass (Copper Development Association, 2017), and Table 4.11 for quartz glass (Heraeus Quarzglas, 2015).

Table 4.9: Constants for Stainless Steel 304L (AK Steel Corporation, 2007)

Stainless Steel 304L	
Variable	Value
Specific heat capacity	500 J/kg K
Melting point	1723.15 K
Ambient temperature	300 K
Thermal conductivity	21.4 W/m K

Table 4.10: Constants for Brass C22000 (Copper Development Association, 2017)

Brass C22000	
Variable	Value
Specific heat capacity	376.81 J/kg K
Melting point	1316.48 K
Ambient temperature	300 K
Thermal conductivity	188.52 W/m K

Table 4.11: Constants for Quartz Glass (Heraeus Quarzglas, 2015)

Quartz Glass	
Variable	Value
Specific heat capacity	670 J/kg K
Melting point	1956 K
Ambient temperature	300 K
Thermal conductivity	2.68 W/m K

4.8 Quartz glass windows

The glass was designed to be an elongated oval flat plate in order to reduce areas of localised stress on the sides and corners and can be seen in Figure 4.21.



Figure 4.21: Quartz glass (14 mm thick) – front view

As discussed in Publication 3 (Theba, et al., 2017), the glass was designed to be 14 mm thick. This was observed to be a suitable thickness to prevent cracking and warping under the pressurised environment of the combustion chamber. The glass also had filleted edges of 5 mm all around to further reduce the areas of localised stress. The length of the glass was longer than the fuel grain length to allow for clarity with a length of 254 mm. FEA's were conducted on the glass for thicknesses between 6 mm and 14 mm to determine which would be most suitable to satisfy the design requirements (Theba, et al., 2017).

In case of a system malfunction, the glass would be the first to break therefore creating a failure mode for emergencies.

The properties of quartz glass made it the best option for the visual aspects of this project. It has a high melting point and high tensile strength compared to other transparent mediums. Its clarity also assisted in obtaining features of the combustion mechanism from the video footage of the tests.

4.9 Side-glass spacer

The need to avoid sharp corners and t-shaped windows led to the quartz glass being a flat plate. A gap however, still existed between the fuel grain and the quartz glass. Reducing this gap would minimise or eliminate side burning of the fuel and restrict burning to the fuel grain's top surface only. An alternative transparent material needed to be used for this purpose. A side-glass spacer was purchased for this reason and was not required to take any load (where the quartz window did have to). Its melting point is considerably lower than quartz glass (approximately 250 °C (Hitech Safety Glass, 2008)) but because of its low cost, each piece was sacrificed for each test. The size of the gap was too small to cut toughened glass or to have the semi-circular ends (as in the case of the quartz glass). Flat, straight, rectangular pieces were used instead. However, two types of glass were used, one clear and the other shaded and were secured to either side of the inside of the chamber. The shaded glass would assist in gaining increased clarity by filtering the bright light from the flame. Each piece was 200 mm long, 30 mm in height and 6 mm thick as shown in Figure 4.22.

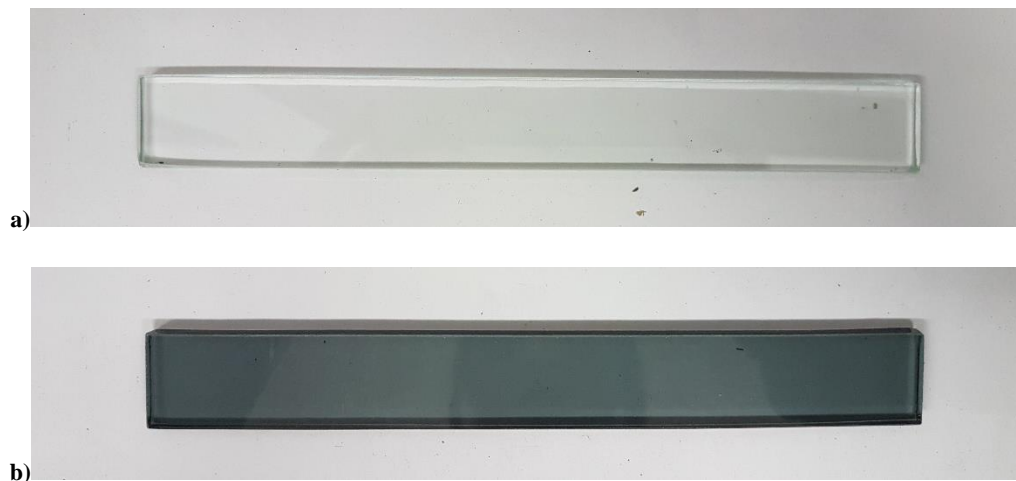


Figure 4.22: Side-glass spacer a) clear b) shaded

4.10 Silicone gaskets

Gaskets were required to ensure sealing of the combustion chamber, to provide a cushion for the glass against the brass, and to aid in the flexibility or movement of the glass. Silicone sheet gaskets with a thickness of 1.5 mm were used. These gaskets could also easily be cut to the required shape for the grooves around the glass.



Figure 4.23: Silicone gasket – front view

4.10.1 Bolt calculations

Bolt calculations were essential in determining whether the grade, material and size of the bolt would be sufficient to seal the gasket without stripping the bolt's threads. The calculations for the front bulkhead, nozzle end bulkheads, top bulkhead and side panels are given in Appendix 4F. The reverse method of these calculations was also applied to ensure that the total stress applied on the gasket from torque tightening would not exceed the maximum sealing stress of the gasket. The results (Appendix 4F) indicated that the design was adequate.

Supplementary calculations are included that demonstrate the change in thickness expected from the gasket at maximum pressure (20 bar), and the change in thickness of the gasket at various compression sets. These results assisted in establishing the thickness of the recesses (15.5 mm) on the combustion chamber that accommodated the glass.

4.10.2 Klinger Expert gasket design software

The gaskets required for the glass windows were essential for the side, top, front and back panels that were to be bolted onto the chamber base. Research was therefore conducted on different gasket materials and calculations used to determine a suitable one. The factors that had to be considered were not only the material but also the grade and size of bolts used to ensure that the gaskets achieved their sealing stress. Klinger Expert software was found to be useful in this regard. Variables such as the bolt grade, tightening torque, sealing medium and temperature were input into the programme as per the design specifications, and the software produced a graphical analysis of the gasket stress based on the gasket material used. This process was conducted for all the additional panels that were bolted onto the base of the combustion chamber. This software package unfortunately does not contain silicone gaskets in its database. Alternative gaskets were therefore considered and the Klinger Expert calculations performed on these. It should be noted that the calculations in question were used merely for estimation purposes. Gasket calculations are further discussed in Appendix 4F.

4.11 Finite element analyses

This section originates from Publication 2 published by The American Institute of Aeronautics and Astronautics as a part of this Master's degree work (Theba, et al., 2016).

Finite Element Analyses were performed on ANSYS simulation software to determine the structural integrity of the combustion chamber and the ability of the glass to withstand the applied pressures. It should be noted that all FEA's were performed at a combustion chamber pressure of 20 bar to include a safety factor of 2 on all the tests. The models were run with a quarter or half geometry to reduce computational expenses and time.

Before the side panels with the glass windows could be modelled on ANSYS, the gasket had to be simulated independently to formulate a pressure versus closure curve. This curve approximates the change in thickness of the gasket with increasing pressures and resulted in a gasket meshed with a single layer of elements through the thickness, thereby not drastically increasing the solving time while giving an accurate approximation of reality. The curve is a function of material properties from uniaxial compression tests ensuring that the gasket behaviour is accurate. This is done so that the gasket can be meshed as a thin body and uses the pressure versus closure curve to approximate its behaviour as opposed to simulating the gasket in its entirety with its full material properties. In the latter case, the mesh size gradient will be too large when compared to the rest of the model, thereby increasing computational time. In a full-sized model, the gasket material definition only requires the input of the pressure versus closure curve and will determine the gasket behaviour from this instead of calculating the deformation using gasket material properties such as Young's Modulus and Poisson's Ratio.

To obtain the above-mentioned curve, the gasket material data is entered into the Engineering Data table, meshed and simulated under increasing pressures so that the difference in vertical displacement between the top and bottom faces can be determined. Figure 4.24 and Figure 4.25 shows the material properties that were entered into the ANSYS Engineering Data section.

Property	Value	Unit
Density	2330	Kg/m ³
Reference Temperature	22	C
Young's Modulus	50	Mpa
Poisson's Ratio	0.49	
Bulk Modulus	8.33E+08	Pa
Shear Modulus	1.68E+07	Pa

Figure 4.24: Silicone properties (Natal Gaskets, 2011)

Temperature (Deg C)	Coefficient of Thermal Expansion (Deg C ⁻¹)
20	2.46E-06
250	3.61E-06
500	4.15E-06
1000	4.44E-06
1500	4.44E-06

Figure 4.25: Coefficients of thermal expansion

A fixed support constraint was applied underneath the gasket with a 20 bar pressure on the top. The closure value was the maximum vertical deformation. The gasket also had to be meshed with at least three higher order elements in thickness to ensure accuracy. A sweep method was applied for the mesh with 3 divisions in the thickness. The mesh was coarse but sufficient for this model. The model was run at 10 design points from 1 bar to 20 bar and the maximum vertical deformation or closure values, recorded for each point. This was done by incorporating a parameter set shown in Figure 4.26, into the system so that the design points could run simultaneously and the results obtained from a table, thereby reducing computational times. The input and output parameters were selected from the drop-down menus, such as the pressure magnitude and directional deformation maximum to obtain the required results.

ID	Parameter Name	Value	Unit
Input Parameters			
Static Structural (B1)			
P2	Pressure Magnitude	0	Mpa
Output Parameters			
Static Structural (B1)			
P1	Directional Deformation Maximum	0.0001582	mm
Charts			
Parameter Chart 0			

Figure 4.26: Outline of all parameters

Name	Pressure Magnitude	Directional Deformation Maximum
Units	Mpa	mm
DP 0 (Current)	0	0.0001582
DP 1	0.1	0.0017192
DP 2	0.25	0.0042979
DP 3	0.5	0.0085959
DP 4	0.75	0.012894
DP 5	0.1	0.0017192
DP 6	1.25	0.02149
DP 7	1.5	0.025788
DP 8	1.75	0.030086
DP 9	2	0.034384

Figure 4.27: Design points and resulting closure values

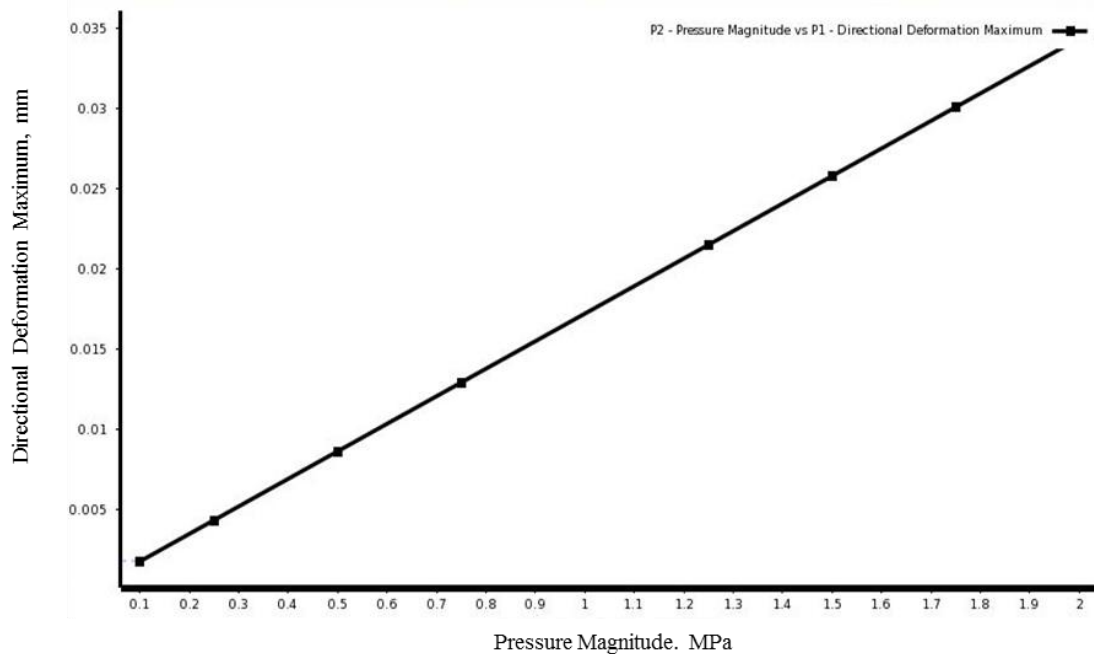


Figure 4.28. Pressure versus Closure curve (Theba, et al., 2017)

These values were then input on the full-scale model of the combustion chamber and the gaskets modelled as gasket bodies.

Independent simulations were also conducted on the quartz glass to determine whether the thickness of 14 mm would be sufficient to withstand the pressures and temperatures within the combustion environment. Similar to the gaskets, a fixed support was placed on one side of the glass around the edges as shown in Figure 4.29 (in purple).

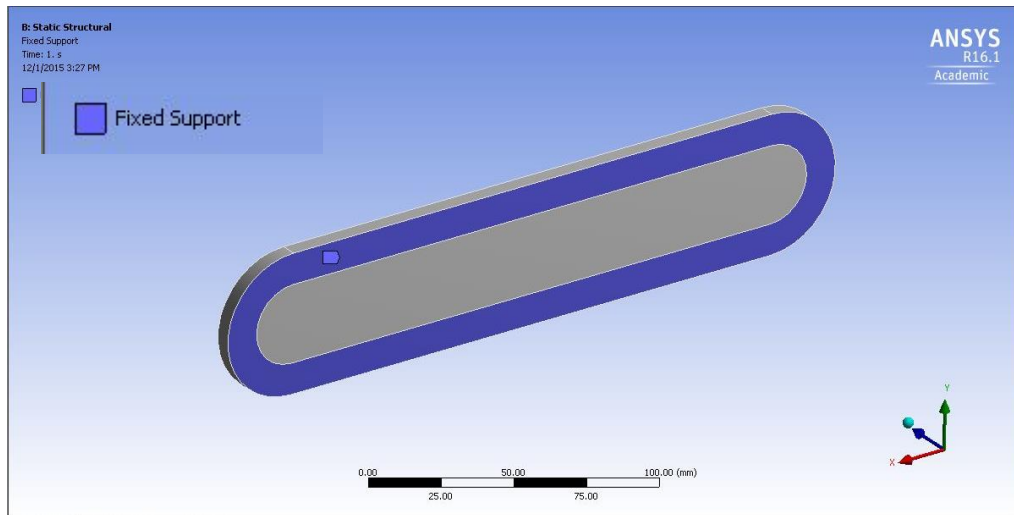


Figure 4.29. Fixed support for gasket applied around the edges

A pressure of 20 bar was placed on the other side of the glass in the central area that would be exposed to the inside of the combustion chamber as shown in Figure 4.30 (in red).

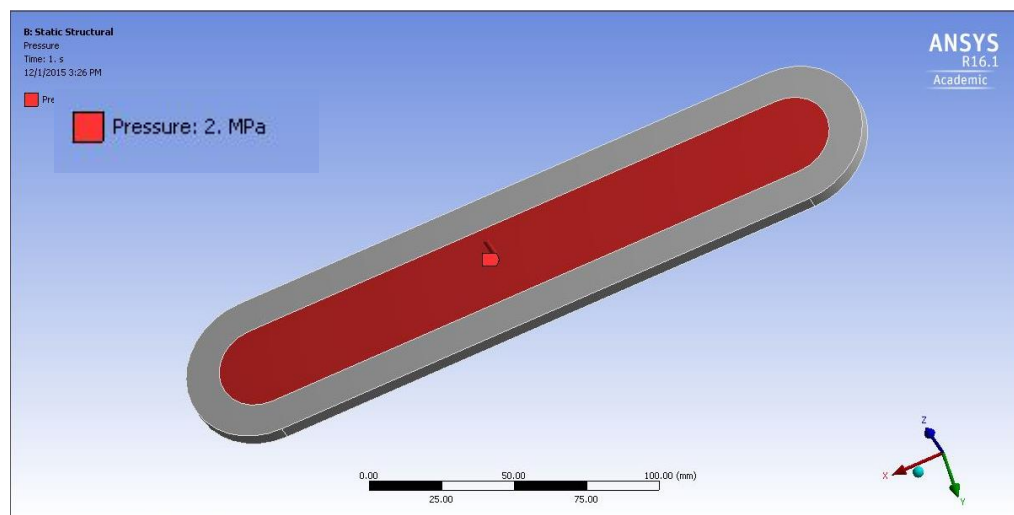


Figure 4.30. Pressure applied to centre portion of glass exposed within the combustion chamber

The maximum total deformation experienced by the glass was less than 1 mm in the centre as presented in Figure 4.31.

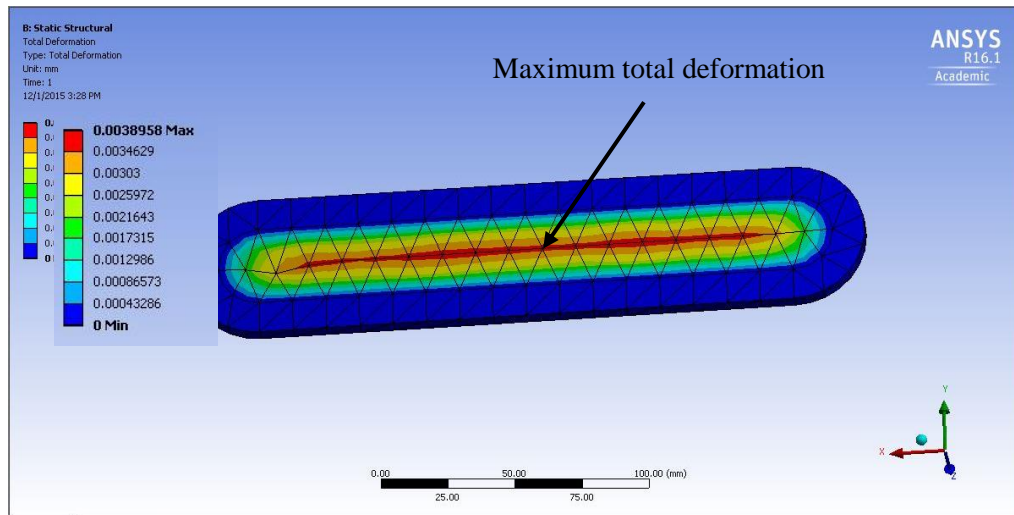


Figure 4.31. Total deformation results

The maximum stress experienced by the glass was around the edges at the points where the glass and brass meet was determined to be 20 MPa. The design tensile strength of quartz glass is 48 MPa at its maximum operating temperature of 1300 °C (Heraeus Quarzglas, 2015).

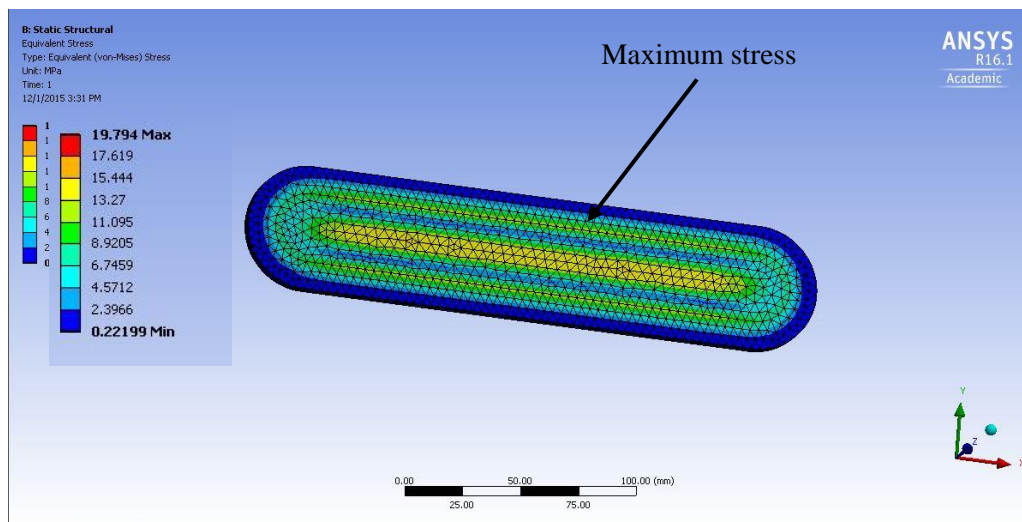


Figure 4.32. Equivalent stress results

The design of the glass was therefore adequate for the system operating conditions.

The flexibility of the silicone gaskets and the tolerances around the glass provided space for the glass to move freely without being in contact with the brass or steel. FEA verified that the assembly of the glass within the chamber would be subject to stresses below its tensile strength. The small burn time would also assist in the glass not being exposed to temperatures above its maximum operating temperature at any significant depth (Theba, et al., 2016).

4.12 Igniters

The igniter for the slab motor used Striker match heads, a type of firelighter, to create an electric match (e-match). A copper wire was wrapped around it tightly, and the wire secured to the match with hot glue and then connected to a lead which was fastened to a 12 V battery. When the igniter was turned on using a switch on the control panel (discussed in Chapter 5), the copper heated up and ignited the match, which in turn vaporised the wax. The igniter assembly is shown in Figure 4.33.



Figure 4.33: Igniter assembly using an E-match

4.13 Discussion

The hybrid rocket slab motor was designed based on an iterative process and parameters for fuel grain dimensions and oxidiser mass flow rates that were determined from previous slab motors and NASA CEA. The design was done so as to enable visualisation of regression rate and validation of the HSM at atmospheric conditions. Parameters were therefore selected. The combustion chamber was designed to accommodate chamber pressures of up to 10 bar and oxidiser mass flow rates up to 150 g/s. A safety factor of 2 was incorporated into the system.

The fuel grain mould was designed to produce multiple fuel grains of pure paraffin wax and aluminised fuel grains with different additive concentrations. The mould included a chamfer at the leading edge of the fuel grain to assist with ignition. The mass of paraffin wax was weighed and melted before being left to cool gradually inside the furnace in the mould. The aluminium mixtures were mixed until its congealing point to prevent settling of the particles, before gradual cooling.

The feed system's design was interchangeable for both the HSM and cylindrical lab-scale motor. It was simple with shorter tubing and fewer bends so as to reduce pressure losses. Safety was increased by incorporating redundant valves, a dump line and relief valve. The main oxidiser injection line consisted of 1/4" tubing with both an automated ball valve and servo motor valve, the latter of which was used for redundancy. The feed system also included pressure transducers to record the pressures at various points in the system.

A manifold was designed to connect the injectors to the feed system. Three injectors of 1 mm, 1.3 mm and 1.5 mm were manufactured to allow for different oxidiser mass flow rates. The injectors and manifold were made from brass bolts because of the material's machinability and the small orifice sizes required. The injectors were screwed into one end of the front bulkhead and the manifold onto the other.

A brass billet was used for the manufacture of the combustion chamber base because of its machinability and to reduce the complexity of welding several plates together to form the motor. It was designed based on the fuel grain dimensions and to allow for sufficient decomposition of the oxidiser and expulsion of exhaust gases. The sides were machined so that the glass windows and silicone gaskets could be fitted. A fuel grain fixing plate was fastened to the combustion chamber base and housed the fuel grain. The side panels and all bulkheads were manufactured from stainless steel and bolted onto the base. Heat transfer calculations were performed to estimate the thermal durability of the combustion chamber during testing.

Quartz glass was used for the windows to observe the combustion process. The windows were 254 mm long with rounded ends filleted edges to minimise the areas of maximum localised stress intensity. The glass was fixed to the combustion chamber in between the chamber base and side panels. Silicone gaskets were used as a separating medium to enable flexibility and movement of the brass and glass respectively. A side-glass spacer was also used to minimise side burning.

Nozzle bulkheads were manufactured from 12 mm thick stainless steel plates. Combustion chamber pressures of 2.5 bar, 5 bar and 10 bar were to be tested to determine whether regression rates are dependent on combustion chamber pressures. These were not used in the current study but will be used to perform further investigations at higher pressures in future research.

Finite element analyses were conducted to ensure that the 14 mm thick quartz glass windows would be able to withstand the operating conditions. The analysis included the modelling of the silicone gaskets and showed that the design was sufficient.

E-matches were used for ignition of the HSM. Copper wire was coiled around the e-match to form the bridge wire which was connected to a 12 V battery. The igniter was placed at the leading edge of the fuel grain for maximum heat transfer.

Once all of the relevant components that formed the hybrid rocket slab motor were designed and manufactured to specification, the assembled motor required a trial with the control system and the data acquisition system to confirm standard operating procedures. Thereafter, cold flow experiments were conducted.

CHAPTER 5: CONTROL SYSTEM AND EXPERIMENTAL SETUP

The control and data acquisition system are described in Maharaj, et al., (2018) (Maharaj, et al., 2018) and was developed for both the cylindrical lab-scale and slab motors because the same feed system was used. One cDAQ chassis by National Instruments, two Arduino boards, and other auxiliary hardware were secured into a distribution box that was fixed onto the test stand. They were controlled using LabVIEW software and all measurements were taken at 2 kHz. The control system's LabVIEW graphical user interface uses the layout of the feed system to control the respective components. This is shown in Figure 5.1 with the detailed schematic in Figure 4.4.

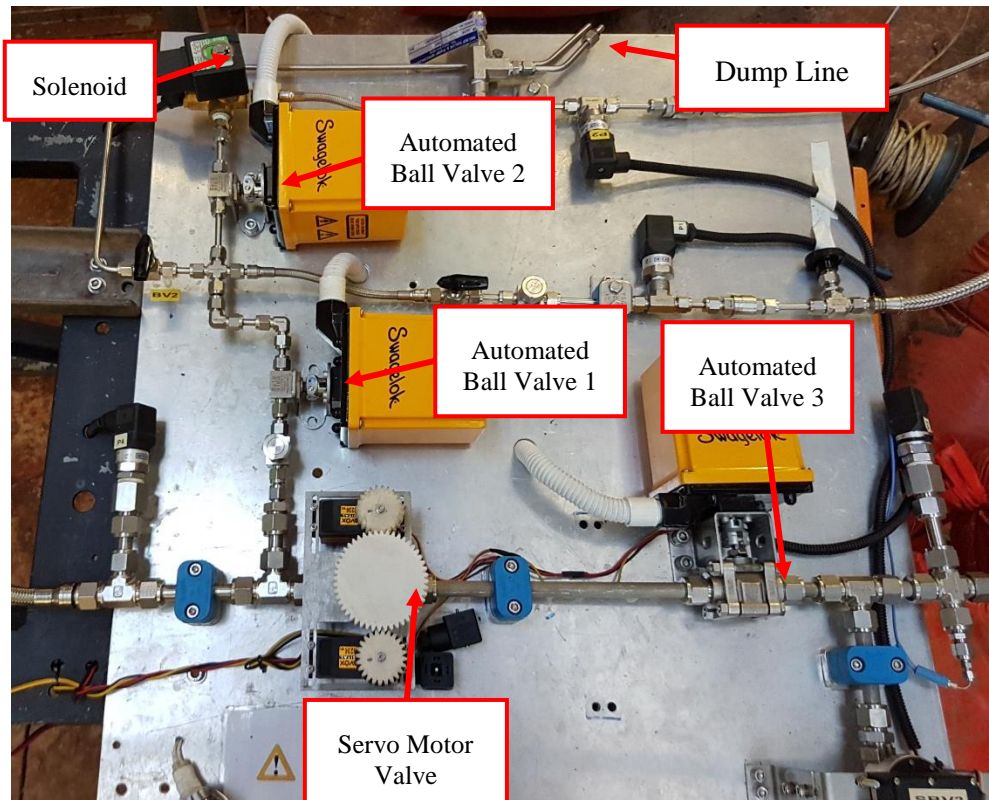


Figure 5.1: Feed system layout and components

5.1 The control panel

The graphical user interface (GUI) depicted in Figure 5.2, was developed to control the feed system separately, with an auto-sequence function employed for testing. The functional controls of the GUI are discussed in this section.

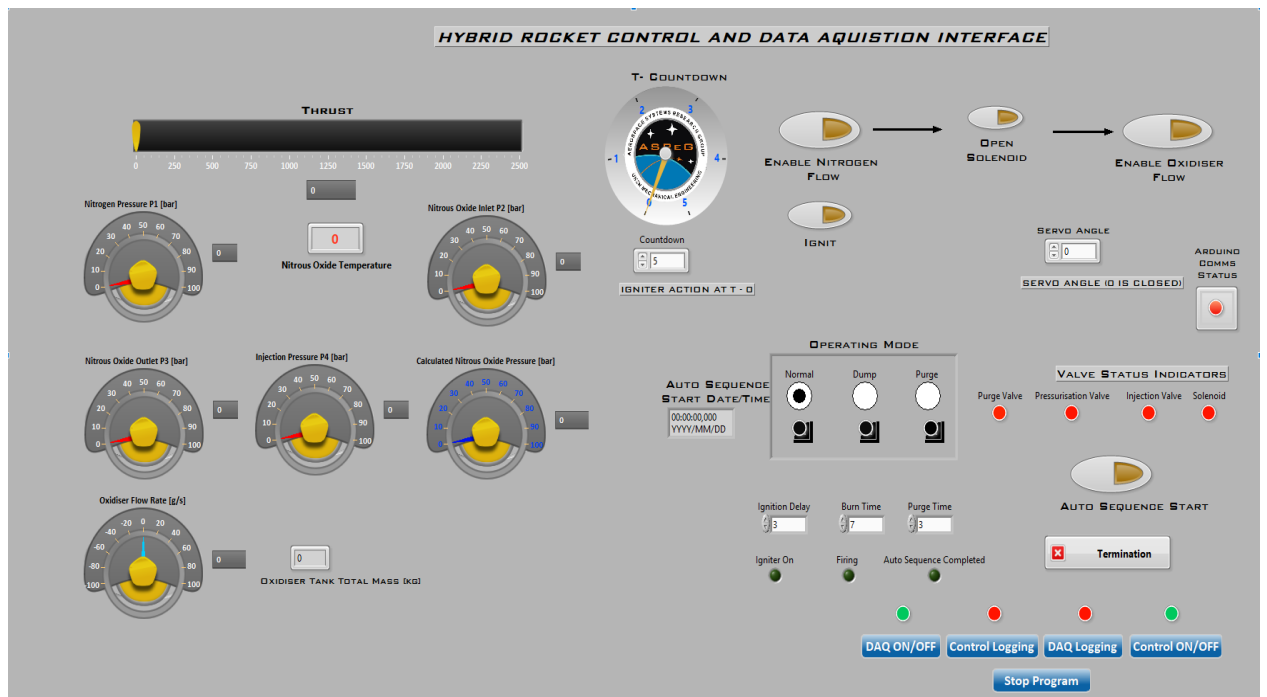


Figure 5.2: Control panel graphical user interface

The left-hand side of the control panel consisted of gauges to display the nitrogen and nitrous oxide pressures at various points between the feed system and combustion chamber. Table 5.1 shows the description of each pressure measurement.

Table 5.1: Pressure gauges and descriptions

Pressure Gauge (bar)	Description
Nitrogen Pressure P1	Regulator output pressure
Nitrous Oxide Inlet P2	Supercharge pressure
Nitrous Oxide Outlet P3	Into feed line
Injection Pressure P4	Inlet into chamber
Calculated Nitrous Oxide Pressure	Calculated from a vapour pressure curve

The nitrous oxide temperature display depicted the real-time temperature for the oxidiser as it enters the injection line. This temperature was constantly monitored to ensure that it did not exceed 40 °C, which is the supercritical fluid temperature for nitrous oxide (Mangold, 1983). The display in the LabVIEW GUI showed the mass of the oxidiser tank. A continuous time algorithm determined the change in tank mass over the burn time which represented the oxidiser flow rate measurement on the gauge in the bottom left-hand corner.

Figure 5.3 represents the right-hand side of the control panel, the control terminal. The countdown for the auto-sequence is displayed in the clock in the top left-hand corner. The buttons outlined

in red are used to manually control each of the respective valves and the igniter. The servo angle display represents the degree of opening of the oxidiser injection ball valve to control the flow. An angle between 0 and 90 degrees can be manually selected and is controlled by the servo motor. This feature was incorporated as an additional safety aspect to the system and to throttle down the injection pressure if required. The operating mode selector provides a simple indication of which mode the system is in at any time.

The three inputs at the bottom of the screen (outlined in blue) allow the user to enter the required parameters for the auto sequence. The ignition delay represents the time given for the igniter to vaporise the wax before the inlet of the oxidiser flow. It was essential for the igniter to be switched on before the nitrous oxide flow to prevent a build-up of the oxidiser in the chamber that would result in a hard-start. The burn time is as suggested and is the time between the opening and closing of the oxidiser inlet valves. The purge time is the time given for the nitrogen flow to flush the system of remnants of the oxidiser for safety measures. The auto sequence switch follows the programmed functions automatically during hot fire testing. The termination button in the bottom right-hand corner allows the user to manually stop the auto sequence control.

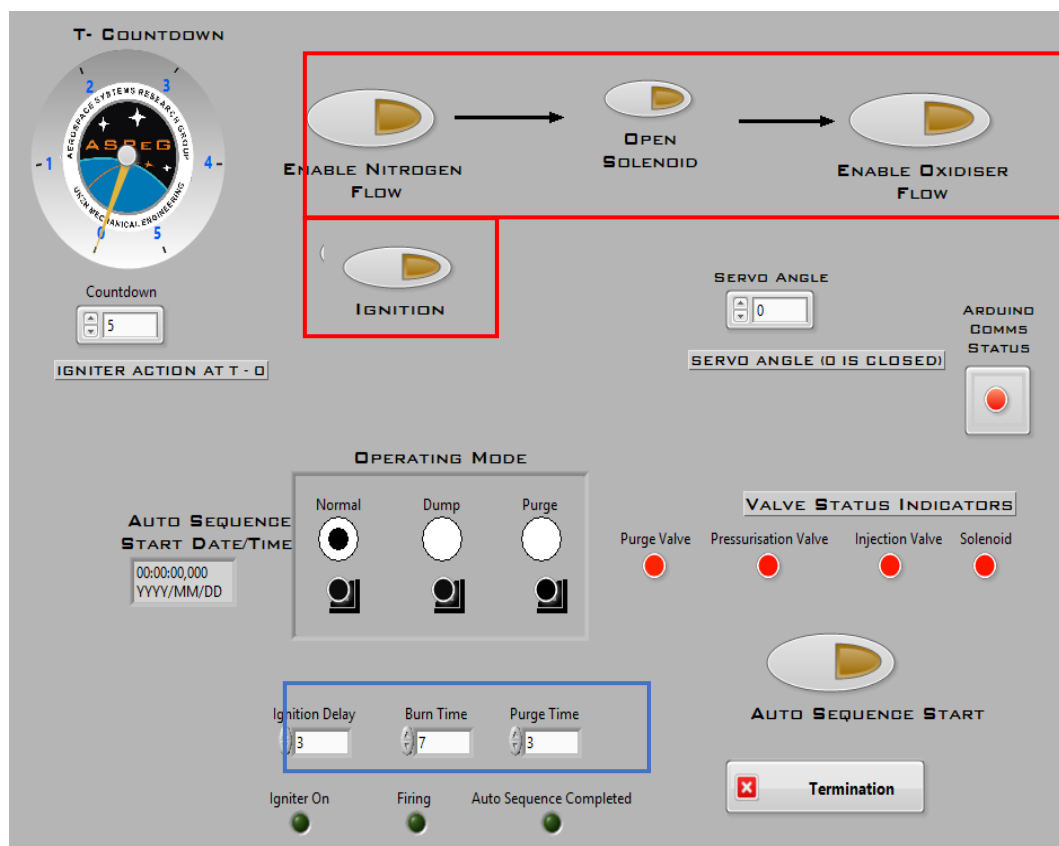


Figure 5.3: Control terminal right-hand side

The graphical layout (block diagram) of the HSM and the cylindrical lab-scale motor is given in Appendix 5A, and details of the control system are discussed in Maharaj, et al., (2018) (Maharaj, et al., 2018).

Two functions on the user interface, namely, the pre and post combustion chamber pressures were not used because the HSM did not accommodate for these readings during these experiments. Future testing, however, may incorporate them.

The test data was analysed using DIAdem software. All the relevant graphs such as the tank measurements chart were presented and used for oxidiser mass flow rate calculations. The tank mass gauge also provided a simple method to determine whether re-filling of the oxidiser run tank was necessary.

5.2 Experimental setup

Experiments were conducted in a secluded area outside the Mechanical Engineering building. This area was cordoned off during testing to prevent people passing by. The control terminal was located approximately 50 m away from the test area and inside the building for safety. The test stand was fixed to the ground inside the test area shown in Figure 5.4.



Figure 5.4: Test stand setup

Due to the test stand being designed to be interchangeable for the different motors, the HSM was bolted onto moveable platforms (red) on the stand to allow for movement in the direction to the load cell's axis only. The combustion chamber injector was connected to the feed system by means of a PTFE flexible hose.

The flexible hose was connected to the main injection line on the feed system. The feed system configuration and components are described in Section 4.4.

The nitrogen and nitrous oxide tanks were positioned on the far side of the combustion chamber and were also connected to the feed system with flexible hoses.

The nitrous oxide run tank was suspended in a mild steel frame hung from a load cell which measures the tank mass. The frame was surrounded by 40 kg sandbags for safety. A 12 V battery was used for the igniter connection.

Go Pro Hero 3+ cameras were placed on the rods on either side of the chamber next to the windows. The cameras were set to record at a high-resolution of 1080 p at 60 fps in order to obtain clear footage of the burn.

Test reports were completed for each test to ensure that all the required safety protocols were adhered to and all preparation procedures followed. An example of the report is given in Appendix 5B.

CHAPTER 6: TESTING AND RESULTS

This chapter first describes the preliminary testing that was used to modify parameters such as the ignition source, igniter position, chamber pressure and addition of side-glass spacer to reduce side burning for the proceeding main hot fire tests. The main hot fire test methodology is outlined in Section 6.1 below. They were then used to validate the HSM design, determine regression rate results, and behaviour of Sasolwax 0907 with nitrous oxide discussed in Chapter 7.

6.1 Testing methodology - sequence and parameters

The potentially large number of tests called for a testing methodology with a priority list to be drawn up. Sections 6.1.1 to 6.1.3 indicate the types of tests and the order in which they were carried out. Three tests were conducted for each type of test under the same conditions to ensure repeatability and accuracy of the results.

1. Three pure paraffin wax fuel grains with the 1.5 mm single orifice injector at atmospheric pressure.
2. Three 40% aluminised wax tests at atmospheric pressure with the 1.5 mm single orifice injector.

6.1.1 Cold flow tests

Cold flow testing was necessary to ensure safe operation of all hardware and software components of the system. These tests were initially conducted with nitrogen for safety, without an ignition source or fuel grain, and with the 1.5 mm injector.

The cold flow testing was first used to validate the control system and feed system functions. The manual switches on the LabVIEW GUI were used to assess the operating behaviour for each component on the feed line. This was carried out by opening and closing of the relevant valves from the control system. If any of the components did not respond as expected, it was inspected and modified as necessary until the response was as required.

Once all of the hardware components were tested manually, the auto-sequence function was tested. The same process was followed as per the manual cold flow testing. If the system did not respond as required, the hardware and programming aspects were inspected and modified as necessary. Hot fire testing could not be conducted until the LabVIEW software was properly integrated with the hardware components on the feed system and the valves responded as per the inputs on the control panel. Thereafter, nitrous oxide was used for cold flow testing.

With the auto-sequence function responding as required, the system was run with nitrous oxide to accurately determine the error margin of the load cell (Maharaj, et al., 2018) and the oxidiser mass flow rate of the injector. The results were determined from data obtained by the LabVIEW

software, such as the rate of change of the oxidiser run tank mass. After which, hot fire tests were conducted.

6.1.2 Hot fire pure paraffin wax fuel grains

The investigations of pure paraffin wax at atmospheric pressure and the 1.5 mm injector were used to set a baseline for future experiments. These tests consisted of a gap between the quartz glass and fuel grain. An e-match was used with two match heads on either side, with the pyrotechnic portion facing and in contact with the fuel grain, for increased ignition energy. The first tests were used to determine the optimal ignition delay required for combustion.

Once the optimal ignition delay was determined, pure paraffin wax fuel grain hot fire tests were conducted. If the tests were successful with the original igniter configuration, three tests were conducted for regression rate measurements of pure paraffin wax fuel grains. In the event that these tests were unsuccessful, different igniter configurations, including more match heads and a pyrotechnic igniter were to be explored.

Due to the gap between the quartz glass and fuel grain, side burning was expected. This created complexities in visualising the regression rate in a single plane. The gap was to be reduced by installing a side-glass spacer. Hot fire tests were then conducted with this setup. As before, if combustion was unsuccessful, additional match heads in various positions with an e-match were used, failing which a pyrotechnic igniter was employed.

If the tests with the side-glass spacer proved to be unsuccessful, one of the bulkheads incorporating a nozzle were to be used to determine if a pressurised environment would assist in achieving combustion.

6.1.3 Hot fire 40% aluminised wax fuel grains

Once three successful pure paraffin wax tests were achieved, 40% aluminised wax fuel grain testing was to be conducted, as per the methodology discussed in Section 6.1.2. This would provide an understanding of the effect of aluminium additives in Sasolwax 0907 with nitrous oxide.

6.1.4 Additional tests

Before additional tests are conducted, the combustion chamber will be modified to incorporate pressure transducers and thermocouples in order to obtain pressure and temperature measurements in different positions of the combustion chamber during testing.

Future testing was to include the types of tests discussed in Sections 6.1.1 to 6.1.3 but with injector orifice sizes of 1 mm and 1.3 mm. These tests were to be used to obtain additional regression rate measurements of pure paraffin wax and 40% aluminised paraffin wax tests, therefore providing

sufficient data to calculate the ballistic coefficients of the simplified regression rate (Equation 4.9).

The above-mentioned experiments were to be followed by pressurised testing at 2.5 bar, 5 bar and 10 bar with each injector. Three tests will be conducted for each type of test and used to verify whether regression rate is independent of chamber pressure.

The largest orifice injector size of 1.5 mm, with a theoretical oxidiser mass flow rate of 130 g/s was used for the tests presented below. This injector was chosen to determine a baseline for all other testing as discussed in this chapter. Results and observations of the tests will be presented in this chapter, followed by analyses and discussions in Chapter 7.

6.2 Cold flow testing

The cold flow tests were used to determine the nitrous oxide mass flow rate using the 1.5 mm injector and the accuracy of the load cell device. These will be discussed in Section 7.1.

The system proved to be fully functional. The next section presents the hot fire tests conducted, including their conditions, parameters and results.

6.3 Hot fire tests with pure paraffin wax

Preliminary hot fire tests were carried out to verify the ignition source, and to determine igniter time delay, oxidiser mass flow rate, and implementation of the combustion chamber side-glass spacer. Final testing was used to validate the HSM design, take regression rate measurements of paraffin wax burning with nitrous oxide, and observe their regression rate characteristics. As discussed in Section 6.1, pure paraffin wax fuel grains were investigated with the 1.5 mm injector and oxidiser mass flow rate of 130 g/s at atmospheric pressure. The nitrous oxide run tank was supercharged to between 60 bar and 65 bar for each test. Each fuel grain's mass, volume and dimensions were recorded before each hot fire test.

Table 6.1 presents the tests that exhibited combustion, the duration of each and a general remark. The table does not include the results for the tests in which combustion did not occur. Results of the specific tests will be given in Sections 6.3, 6.4 and 6.5 that follow with analyses and discussions in Chapter 7.

Table 6.1: Combustion Results

Test #	Fuel Grain	Ignition Source	Ignition Delay	Comb Time	Comments
SH002	Pure Wax	e-match	2 s	0 ms	Preliminary hot fire tests - igniter extinguished before ox inlet
SH003	Pure Wax	e-match	1 s	9000 ms	Successful
SH004	Pure Wax	e-match	1 s	8000 ms	Successful
SH005	Pure Wax	e-match	1 s	9000 ms	Successful
SH007	Pure Wax	e-match	2 s	433 ms	Combustion not sustained
SH012	Pure Wax	Pyrotechnic	2 s	517 ms	Igniter failure
SH013	Pure Wax	Pyrotechnic	3 s	100 ms	Igniter failure
SH016	40% Al	e-match	2 s	417 ms	Igniter failure
SH018	Pure Wax	e-match	2 s	6000 ms	Ignition with 5 bar nozzle, chamber insufficiently sealed

6.3.1 Preliminary hot fire test 1 (SH002)

The first few hot fire tests consisted of pure paraffin wax fuel grains with an e-match, made from copper wire that was coiled around a match head to form a resistance igniter, and connected to a 12 V battery. It was placed with the pyrotechnic match head in contact with and directly in front of the leading edge of the fuel grain and stuck down with a thin double-sided tape. Two individual match head halves were positioned on either side of the e-match to increase ignition energy. The lead wires travelled over the top surface of the fuel grain. This configuration is shown in Figure 6.1 with a pure paraffin wax fuel grain.



Figure 6.1: E-match igniter configuration 1

The ignition time delay in SH002 was estimated to be 2 seconds to establish the ideal entry of the oxidiser flow. This time was determined to be too long since the ignition flame went out before the oxidiser inlet was opened. Minimal burning can be seen at the leading edge of the fuel grain in Figure 6.2.



Figure 6.2: SH002 – Minimal burning at leading edge of paraffin wax fuel grain

The fuel grain also experienced cracking as shown in Figure 6.3 and a possible reason will be discussed in Section 7.2.



Figure 6.3: SH002 – Cracked paraffin wax fuel grain

6.3.2 Hot fire tests 2 to 4 (SH003 to SH005)

The second hot fire test (SH003) used the same fuel grain as in SH002. The same igniter configuration was used but with the ignition delay reduced from 2 seconds to 1 second. This was to ensure that the igniter did not burn out before the entry of the oxidiser into the combustion chamber. All of the other parameters were kept constant. The test was successful.

There appeared to be little unburned wax around the remainder of the fuel grain in the combustion chamber. There was soot formation on the injector, on the glass and on other inner surfaces of the combustion chamber. The fuel grain also burnt unevenly; more from the left side than the right as depicted in Figure 6.4. The lead wires were burnt which suggests that they remained in the chamber for the initial part of the burn.

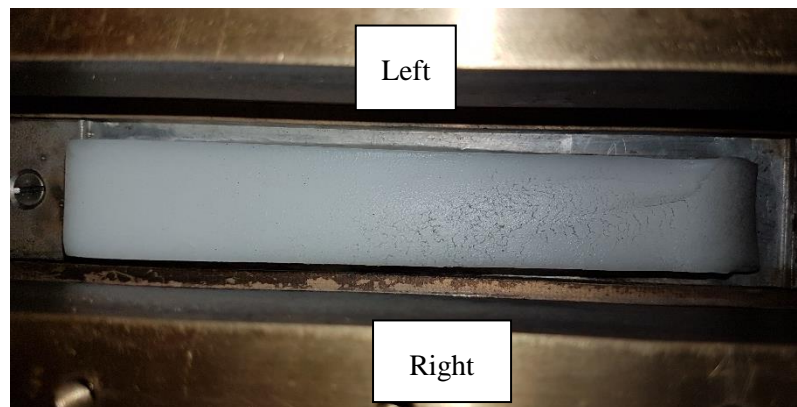


Figure 6.4: SH003 – Uneven burning of the fuel grain (more from the left than the right)

A deformation was noted on the front left side of the fuel grain, including more fuel being burnt at the front end of the fuel grain compared to the back as shown in Figure 6.5. Reasons for this observation are discussed in Section 7.2.



Figure 6.5: SH003 – Paraffin wax fuel grain with dip and uneven burning

Two more hot fire tests were conducted with the same conditions and parameters as this test and the results are documented below.

The third hot fire test (SH004) was also successful and the results were very similar to SH003. There was a slight depression in the same position as Figure 6.5. Irregular burning and soot formation were also observed. In this case the fuel grain flew out of the combustion chamber when the oxidiser inlet retracted and the purge flow started. Upon observation of the video footage it was determined that this did not have an impact on the results of the test. The only visible difference between this fuel grain and the other two was that the surface was smoother in comparison, as can be seen in Figure 6.6. A possible explanation is discussed in Section 7.3.



Figure 6.6: SH004 – Smooth paraffin wax fuel grain

The results for the fourth hot fire test (SH005) were very similar to SH003 and SH004 in terms of burn profiles and is shown in Figure 6.7.



Figure 6.7: SH005 – Burnt paraffin wax fuel grain

The following tables show the mass and dimension changes for each successful hot fire test. Table 6.2 shows the initial, final and percentage mass change of each fuel grain in the successful hot fire tests.

Table 6.2: Initial, final and percentage mass change of fuel grain per test

	Mass (g)		
	SH003	SH004	SH005
Initial	68.9	78.2	71.5
Final	40.7	39.9	32.9
Difference	28.2	38.3	38.6
% Mass burnt	40.929	48.977	53.986

Table 6.3 shows the initial, final and percentage length change of the fuel grains per test.

Table 6.3: Initial, final and percentage length change of fuel grain per test

	Length (mm)		
	SH003	SH004	SH005
Initial	148.5	149.64	148
Final	139.75	139.89	138.39
Difference	8.75	9.75	9.61
% Change	5.89	6.52	6.49

Table 6.4 shows the initial, final and percentage width change for each of the fuel grains from the successful hot fire tests.

Table 6.4: Initial, final and percentage width change of fuel grain per test

	Width (mm)		
	SH003	SH004	SH005
Initial	29	29.7	29
Final	22.81	23.3	21.34
Difference	6.19	6.4	7.66
% Change	21.34	21.55	26.41

Table 6.5 shows the initial, final and percentage thickness change of each fuel grain.

Table 6.5: Initial, final and percentage thickness change of fuel grain per test

	Thickness (mm)		
	SH003	SH004	SH005
Initial	17	20	19
Final	14.79	14.84	13.94
Difference	2.21	5.16	5.06
% Change	13.00	25.80	26.63

The third fuel grain (SH005) lost the greatest mass as can be seen from the tabulated mass differences for this test. It can also be seen that burning occurred most from the sides of each fuel grain (Table 6.4), followed closely by the thickness. These results are graphically presented, analysed and discussed in detail in Section 7.2.

6.3.3 Hot fire tests 5 to 12 (SH006 to SH013)

Hot fire tests one to five included a gap between the fuel grain and the quartz glass. For accurate regression rate measurements, a side-glass spacer was added on either side of the combustion chamber. This restricted burning of the fuel grain to the top surface only by preventing significant oxidiser flow at the sides.

As before, silicone gaskets were used as a seal and spacer between the glass and the brass. RTV was used to seal the remaining gaps around the side-glass spacer as it was not possible to obtain these with semi-circular ends. Figure 6.8 shows the setting of the side-glass spacer and RTV. The three-dimensional drawing (Figure 3.9) is shown in Section 3.4. The silicone gaskets are located between the quartz glass and brass, which is not visible in the figure.

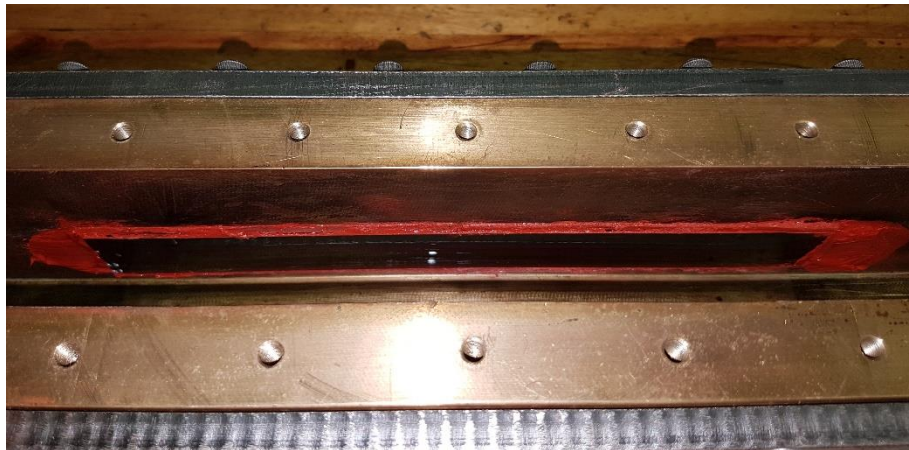


Figure 6.8: Setup of side-glass spacer, silicone gaskets and RTV

The igniter configuration for the fifth hot fire test (SH006) was the same as in previous tests, using an e-match and a 1 second ignition delay. One window was also covered on the outside with a tinted film to assist with filtering of light from intense radiation, in order to reduce the camera exposure in the hope of obtaining clearer images and footage. This test experienced an ignition failure and was therefore unsuccessful.

The ignition delay was increased to 2 seconds for the next hot fire test (SH007) with all other variables kept constant. In this case, combustion occurred but was not sustained.

Different igniter configurations of the e-match with match heads were employed for hot fire tests 8 to 11 (SH008, SH009, SH010 and SH011), such as the ones shown in Figure 6.9 and Figure 6.10. In Figure 6.9, larger match heads were used and were placed so that they were facing the opposite direction of the oxidiser flow. A third, smaller e-match was placed in front of the large match heads and facing the direction of the pyrotechnic heads. Figure 6.10 shows multiple match heads, one of which is an e-match, in a vertical orientation with the pyrotechnic portions in contact with the fuel grain. Two match heads were also included in the front of the row of match heads

for increased ignition energy. These configurations were employed to determine whether the orientation of and number of match heads would assist in greater vaporisation of the paraffin wax with greater ignition energy and hence successful combustion. The results were similar to SH007 mentioned above.



Figure 6.9: E-match igniter configuration 3 with larger match heads and in a different orientation

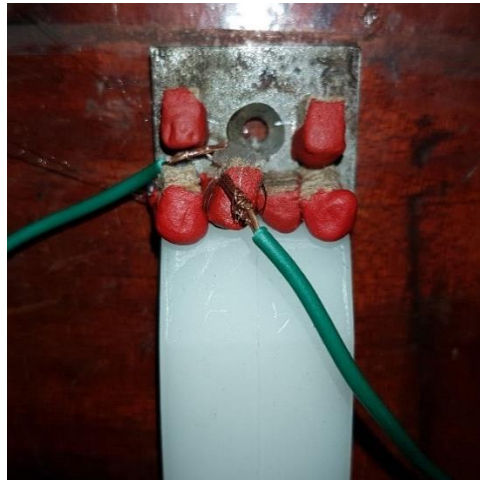


Figure 6.10: E-match igniter configuration 4 with different orientation of pyrotechnic head facing the fuel grain

As a result of the failed attempts, the next two hot fire tests (SH012 and SH013) were attempted with a pyrotechnic mixture in order to provide a higher ignition energy than the e-match and obtain a more reliable method of ignition (Biblarz & Sutton, 2001). The initial position was directly in front of the fuel grain shown in Figure 6.11, much like in the case of the e-match. The igniter position represented in this figure would provide direct heat and thus burning of the fuel grain.

Testing was conducted with an ignition delay of 2 and 3 seconds respectively. The pyrotechnic igniter has a higher burn time which allowed for a longer ignition delay resulting in more vaporisation of the wax before ignition. However, both of these experiments were unsuccessful.



Figure 6.11: SH012 – Pyrotechnic igniter with pure paraffin wax at atmospheric pressure

A different position of the pyrotechnic igniter (Figure 6.12) was implemented to determine if that would have an effect on ignition. The position in this case was chosen so that it would not be in line of sight with the oxidiser, preventing the igniter from being pushed out of the combustion chamber early and therefore allowing for more vaporisation of the fuel.



Figure 6.12: SH013 – Alternative pyrotechnic igniter position

Analysis of the video footage showed that both experiments underwent a brief period of combustion, which was however, not sustained.

The results of all the unsuccessful tests were similar in that the igniter worked as predicted, but the combustion duration was not sustained. Analysis of the test footage clearly revealed combustion for varying fractions of a second. The series of images (Figure 6.13, Figure 6.14 and Figure 6.15) below are from one of these tests (SH007) and depicts the footage frame by frame. Table 6.1 in Section 6.3 above lists the combustion times for these firings.



Figure 6.13: SH007 – Evidence of combustion in unsuccessful firing - frame 1



Figure 6.14: SH007 – Evidence of combustion in unsuccessful firing - frame 2



Figure 6.15: SH007 – Evidence of combustion in unsuccessful firing - frame 3

The only perceivable difference between the successful and unsuccessful tests was the implementation of the side-glass spacer to limit the burning fuel surface to the top. This will be discussed further in Section 7.3.

6.4 Hot fire tests with 40% aluminium additives

The challenge in achieving successful hot fire tests for pure paraffin wax at atmospheric pressure suggested that this was possibly due to a low heat of oxidation or insufficient thermal energy to vaporise the paraffin wax. For this reason, hot fire tests for 40% aluminised wax fuel grains were investigated with similar igniter configurations shown in Figure 6.1, Figure 6.9, Figure 6.10 and Figure 6.11. The same 1.5 mm injector was used for these experiments.

6.4.1 Hot fire test 13 to 16 (SH014 to SH017)

Four different hot fire tests (SH014 to SH017) with 40% aluminised paraffin wax were attempted with the different igniter configurations discussed in Section 6.3. In these tests the igniter was extinguished upon entry of the oxidiser flow with one test experiencing a brief period of combustion. Figure 6.16 shows the test setup and the elimination of the side gaps with a 40% aluminised wax fuel grain.



Figure 6.16: 40% aluminised wax with side-glass spacer and e-match

More match heads were installed to assist with greater ignition energy. Figure 6.17 shows a top view of the stacking of the match heads around the e-match. An additional match head was placed on top of the e-match (shown in Figure 6.1) with two halves on either side. Ignition delay times of 2 seconds and 3 seconds were also tried but these tests were not successful.

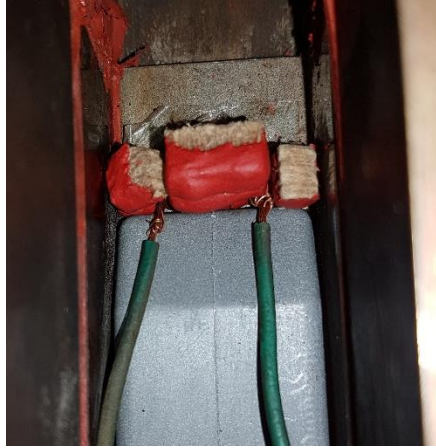


Figure 6.17: E-match igniter configuration 2 - stacking of match heads on e-match

Possible explanations for the ignition failures will be discussed in Section 7.3.

Hot fire testing of aluminised wax fuel grains was abandoned due to unsuccessful testing conducted at atmospheric pressure and time constraints. Future testing might include a 40% aluminised wax fuel grain at atmospheric pressure, with the 1.5 mm injector and without the side-glass spacer.

6.5 Pure paraffin wax with 5 bar nozzle (SH018)

To determine whether the side-glass spacer was a problem primarily for atmospheric testing due to pressure dependence, the 5 bar nozzle bulkhead was fitted onto the system for an additional hot fire test. RTV and silicone gaskets were used to seal all the bulkheads, not just the side panels as before.

6.5.1 Hot fire test 17

The pressurised test was successful with the window glass and a pure paraffin wax fuel grain. This was despite the system not being sealed properly with leaking taking place around the bulkheads although silicone gaskets and RTV were in place. Sparks were seen around the combustion chamber during the test and the video footage verified this.

The side-glass spacer shattered, although this was expected because the edges were sealed with RTV thus causing a pressure gradient, or due to thermal shock. In addition, the quartz glass cracked within the first 2 seconds of combustion. Figure 6.18 shows the cracks on one window. It was not feasible to order replacement quartz glass due to costs and the lead time for delivery. A decision was therefore taken to conduct high pressure testing only once sufficient regression rate results have been obtained for all three of the injectors at atmospheric pressure. The pressurised tests will verify whether regression rate is independent of chamber pressure.



Figure 6.18: SH018 – Cracked glass

Black soot was observed all around the inside of the combustion chamber, on all exposed surfaces. The silicone gaskets were also burnt.

This test will be discussed in Section 7.3.

CHAPTER 7: ANALYSIS AND DISCUSSION

The unique nature surrounding this project and the lack of research for hybrid rocket slab motors using paraffin wax with nitrous oxide calls for an in-depth analysis of both the successful and unsuccessful firings.

7.1 Cold flow analysis

As mentioned in Section 6.2 the cold flow testing was conducted to ensure the reliable and safe working operation of the hardware and software components of the system.

Figure 7.1 shows the smoothened tank measurement graph derived from DIAdem, eliminating the effects of noise. The x-axis represents the time of the burn in seconds, and the y-axis the change in mass of the nitrous oxide run tank. The nitrous oxide run tank was supercharged to between 60 and 65 bar, before the automated sequence for testing began.

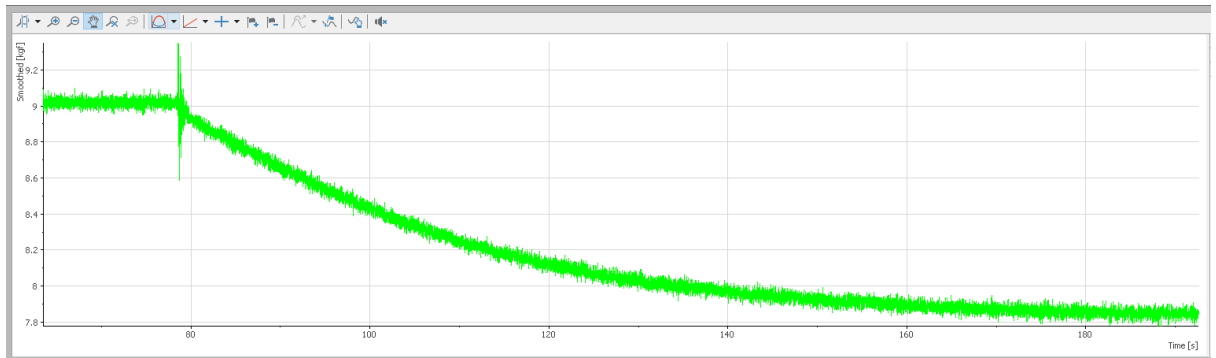


Figure 7.1: Smoothened tank measurement for cold flow test

The graph appears to be hyperbolic in shape which suggests that the injector did not produce a linear flow characteristic. Evaporative cooling may be the reason for this. The oxidiser run tank experienced an enthalpy change during firings which caused it to cool down. This would in turn affect the oxidiser mass flow rate upstream and may have led to back pressure or the flow being choked.

Calculations from the graph produced an average oxidiser mass flow rate of 42 g/s. This was much lower than the theoretical oxidiser mass flow rate of 130 g/s. Reasons for this could be due to the flow being choked and the discharge coefficient of the injector orifice not being accurate.

The error margin due to the load cell was determined to be ± 10 g/s (Maharaj, et al., 2018).

7.2 Preliminary hot fire test discussion

The first unsuccessful hot fire test (SH002) was due to an ignition timing error as mentioned in Section 6.3.1. The igniter was extinguished before the oxidiser flow entered the combustion chamber.

Thermal shock may have been the reason for cracks in the fuel grain resulting from the very low temperature of the nitrous oxide.

7.3 Successful hot fire tests discussion

The results of the three successful tests (SH003 to SH005) in Section 6.3.2 will now be discussed. It should be noted that each test represents one sample and that statistical variations are expected.

The fuel grain from SH003 burnt more from the left-hand side than from the right. The uneven burning of the fuel grain could have been due to one of the lead wires being trapped in between the glass and the fuel grain, and not being pushed out of the combustion chamber when combustion began. This was concluded from the observation of the charred lead wires which was only visible for this test.

There were cracks in the fuel grain as a result of its reuse from SH002, but none were visible in the fuel grain after the test. If these were light surface cracks, they may have regressed with burning of the fuel grain. Alternatively, if they were open void cracks then the heat from combustion may have resulted in the fuel grain repairing itself.

There was a small deformation towards the front left side of all three fuel grains as depicted in Figure 7.2. This may have been due to the presence of the liquid layer when the system throttled down and hence nitrous oxide impingement on the fuel grain. If the injector orifice was not perfectly centred on the bolt head due to manufacturing tolerances, this would have led to the flow being directed at an angle within the combustion chamber and not accurately through the central port.



Figure 7.2: Disfigured fuel grain

All three fuel grains burnt more at the front which is represented by the thinner and shorter portions on the right-hand side shown in Figure 7.2. The thin boundary layer formation in the front of the fuel grain may have resulted in increased burning at the leading edge. This is due to a large temperature gradient and increased heat transfer (Sun et al., 2014). Liquid wax may have also been pushed back along the sides due to the oxidiser flow. A small build-up of unburnt wax was observed towards the aft end of the fuel grain.

The fuel grains also exhibited burning in a slightly concave manner on either side. This could be due to a combination of the molten fuel from the centre portion of the fuel grain dripping downwards due to gravitational forces, and because of the lower portion of the fuel grain being covered by the combustion chamber base up to 2 mm of the thickness of the fuel grain. The latter would have contributed to minimal burning in this region as opposed to the top portion of the fuel grain. The configuration mentioned is illustrated in Figure 7.3 (Theba, et al., 2017).

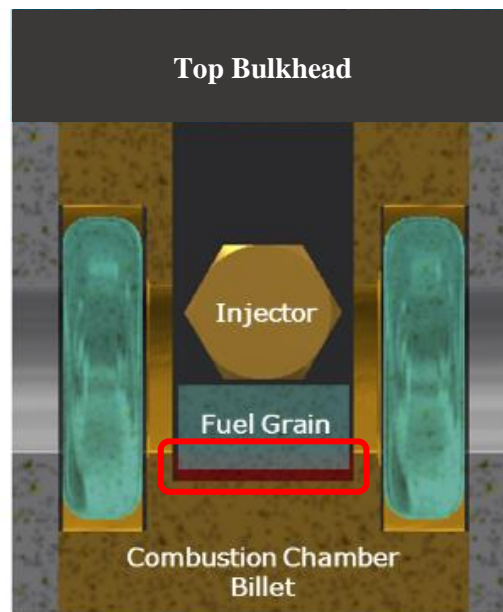


Figure 7.3: Combustion chamber section view indicating portion of fuel grain covered by chamber billet (Theba, et al., 2017)

The smoother fuel grain surface mentioned in Section 6.3.2 for SH004 may be the consequence of it having burnt out slowly. The purge process forced the molten liquid layer to solidify and is observed by the formation of wave patterns due to the soot on the fuel grain's surface for SH003 and SH005. This was not the case for the fuel grain in SH004. There was no visible soot residue on the SH004 fuel grain which may have contributed to the smoothness of the fuel grain because it was thrown out of the combustion chamber and cooled down at a slower rate.

The successful hot fire tests yielded similar results to each other, these are analysed in the sections that follow.

7.3.1 Property analysis

The three successful hot fire experiments showed repeatability of the atmospheric testing of nitrous oxide with pure paraffin wax. All three fuel grains burnt similarly in terms of burn profile, mass, volume, and dimensions. The mass and volume of each test were measured using a small scale and measuring cylinder respectively.

Table 7.1 shows the results obtained.

Table 7.1: Mass and volume comparison table

Mass (g)	Test 1	Test 2	Test 3
Initial	68,9	78,2	71,5
Final	40,7	39,9	32,9
Difference	28,2	38,3	38,6
Volume (cm ³)	Test 1	Test 2	Test 3
Initial	69	78	72
Final	44	43	35
Difference	25	35	37

Figure 7.4 shows a graph of the mass changes over the burn time of all three fuel grains. Details of the mass calculations are given in Section 6.3 and Appendix 7A. The three successful tests SH003, SH004 and SH005 are referred to as Test 1, Test 2 and Test 3 respectively in the following sections.

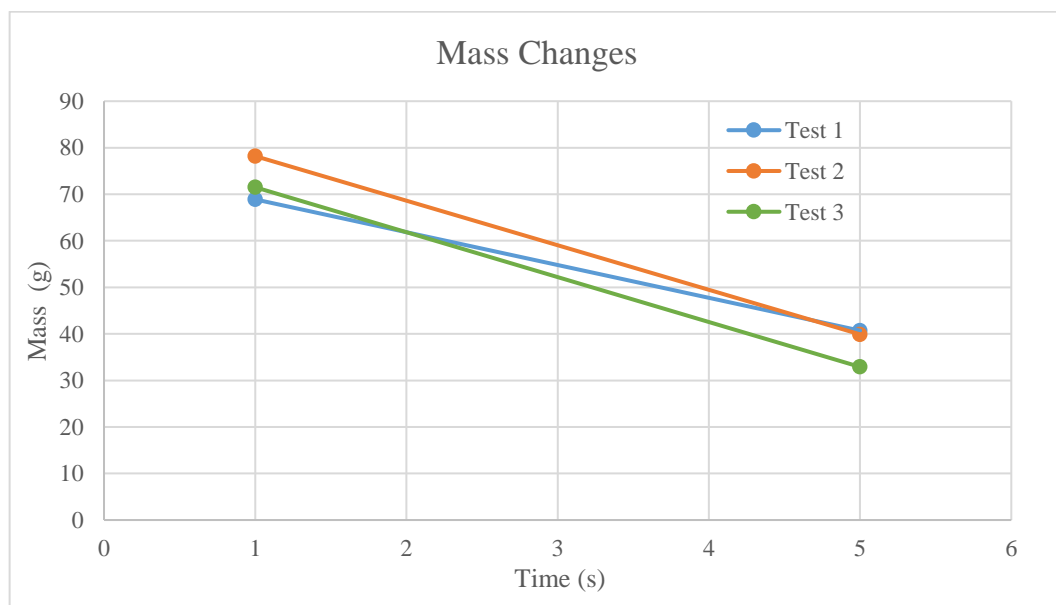


Figure 7.4: Fuel grain mass changes before and after burn

The mass changes for the last two successful tests show a similar gradient which suggests that they burnt a similar amount of wax over the given time. Test 2 and Test 3 burnt 38.3 g and 38.6 g of wax respectively. Test 3 burnt the largest proportion of wax, 54%. Test 1, however, has a less steep gradient compared to the other two tests. In this case, only 28.2 g (41%) of wax was burnt, approximately 10 g less. This fuel grain was at least 2 mm shorter than the other two fuel grains at the start of the burns due to the fuel grain casting process. The increased oxidiser mass flow rate and reduced burning could have been due to factors such as the differences in supercharging of the oxidiser run tank pressures, the cracked fuel grain, the difference in fuel grain thickness, and the side burning restrictions due to the igniter lead wires that were trapped. The conditions for all three tests were kept constant with only the fuel grain dimensions varying between 1 mm and 3 mm. The height and width variations caused a change in the port area, hence oxidiser mass flux and thus the regression rate.

Similar trends are seen for each dimension difference in all three tests. The length, width and thickness of each fuel grain were measured using a Vernier calliper. The length measurements were taken by placing the Vernier calliper both vertically and horizontally to the length of the fuel grain for comparison. In the instances where the results differed, an average length was calculated using two sample points on the fuel grain. The length differences are shown graphically in Figure 7.5.

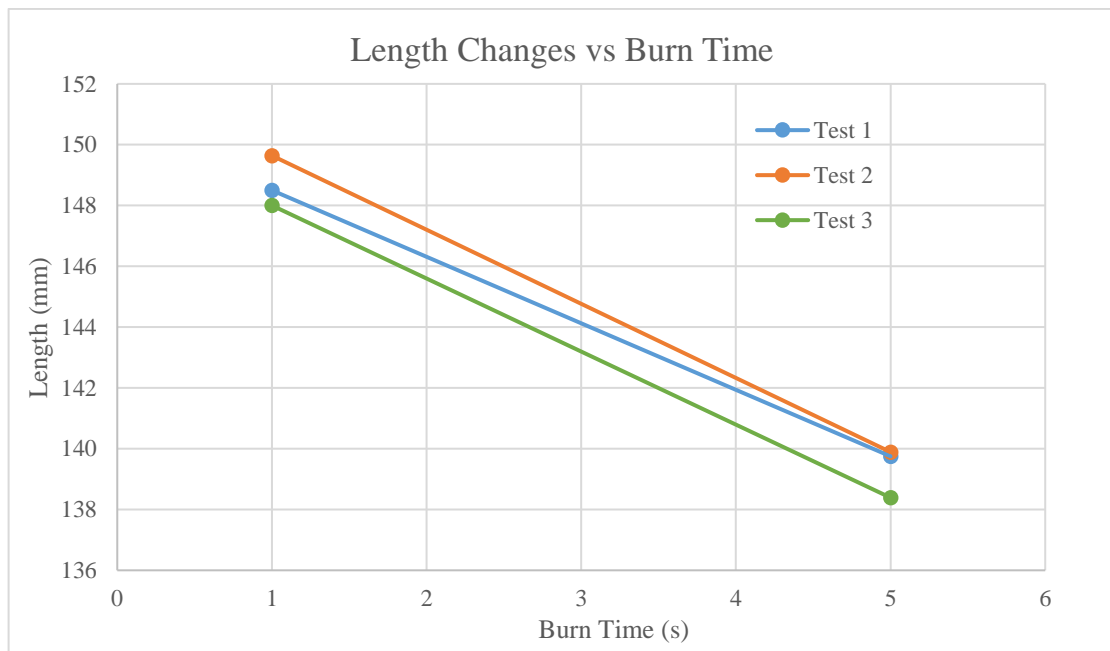


Figure 7.5: Average length differences along the furthest ends of each fuel grain

As given in Table 6.3, Test 2 showed the largest length change of 6.52%. The fuel grain in this case was more than 1 mm longer than both the other tests before the experiments. Calculations showed that an increase in fuel grain length would result in an increased oxidiser mass flow rate

and therefore regression rate. The theoretical findings are verified by the experimental analysis in this instance.

The width of each fuel grain was measured in the front and back at different thicknesses before being averaged. These measurements were taken at the widest portion of the fuel grain. Figure 7.6 shows the average width changes.

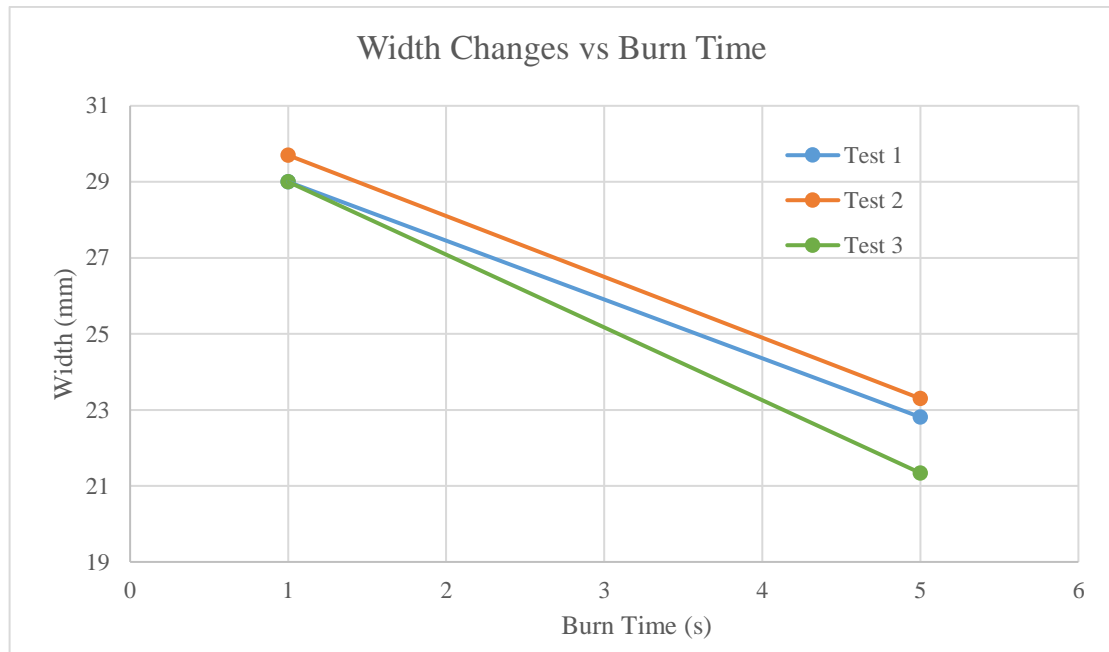


Figure 7.6: Averaged width variation along widest sections of each fuel grain

The results from Table 6.4 and Figure 7.6 show that all three fuel grains burnt the most amount of mass, an average of 23.1% from the sides. Side burning therefore had a significant effect on the regression rates of these tests.

The reduced burning from the side in Test 1 (clear from its lower gradient) may have been due again to the igniter lead wires being caught between the fuel grain and combustion chamber, for the initial part of the burning thereby inhibiting regression from the sides in this test.

Similar to the width variations, thickness calculations were carried out using the same method. The average change in thickness was found to be 21.81% with the lowest value of 13% for Test 1. The difference in thickness for Test 1 shows a shallow gradient compared to the other two tests as shown in Figure 7.7, which further suggests that the fuel grain thickness would have affected the oxidiser mass flux. The calculated oxidiser mass flux for Test 1 was at least 3 kg/m²s (see Section 7.2.2) more than the other two tests.

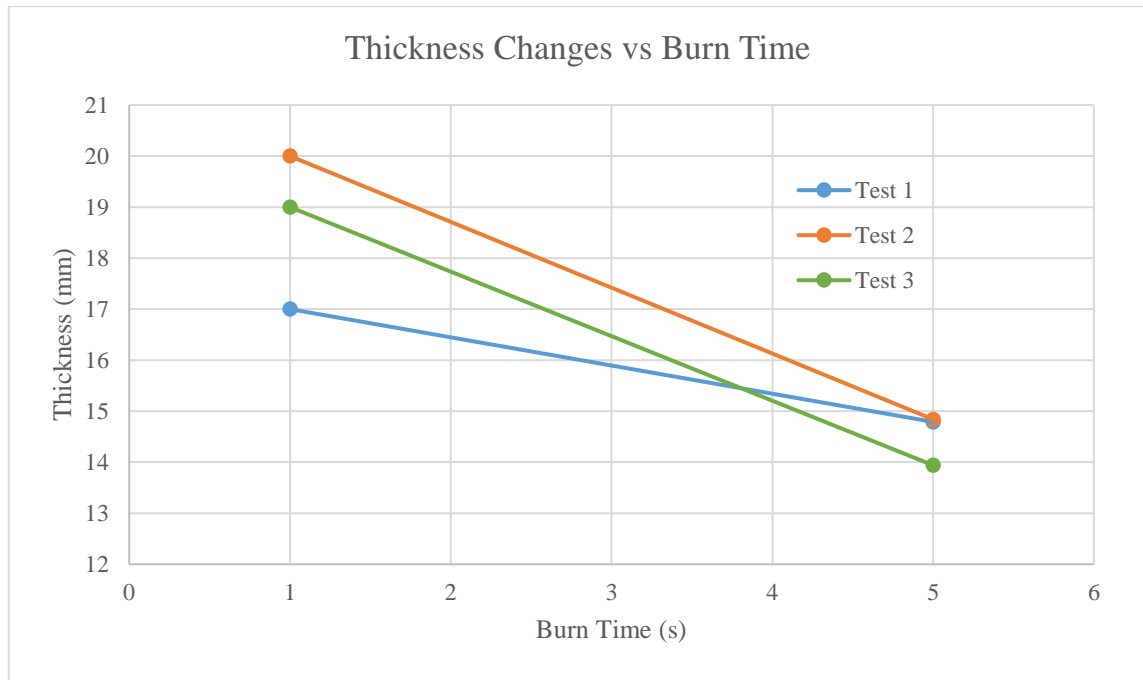


Figure 7.7: Average thickness measurements at tallest points

The results for Test 2 and Test 3 are consistent. In the case of Test 1 the inconsistencies are likely due to the smaller fuel grain at start-up, higher supercharging pressure of the nitrous oxide, and the increased oxidiser mass flow rate and oxidiser mass flux.

The experiments show that the fuel grain geometry plays a vital role in the performance of a hybrid rocket motor. The fuel grain in Test 1 had the smallest thickness and burnt the least amount of wax. This value was also the outlier when comparing all of the percentage changes for each dimension in all three tests. Despite the width having a significant impact on the regression rates of these tests, the results for Test 1 suggest that the thickness is a critical parameter for increased regression rates.

7.3.2 Regression rate data

This section discusses the variables that were required to obtain regression rate data.

7.3.2.1 Oxidiser mass flow rates

To calculate the regression rate for each test National Instruments DIAdem software was used to obtain the graphs of the change in tank measurement over time. The tank measurement represents the mass of oxidiser used for the duration of the burn. The initial tank measurement graphs included a lot of noise as shown in Figure 7.8. A filter was applied to each to reduce the noise and therefore obtain smoother graphs, as shown in Figure 7.9. DIAdem uses the Savitzky-Golay Filter for its smooth function (National Instruments, 2010). Figure 7.9, Figure 7.10 and Figure 7.11 show the smoothened tank measurement results for Test 1, Test 2 and Test 3 respectively.

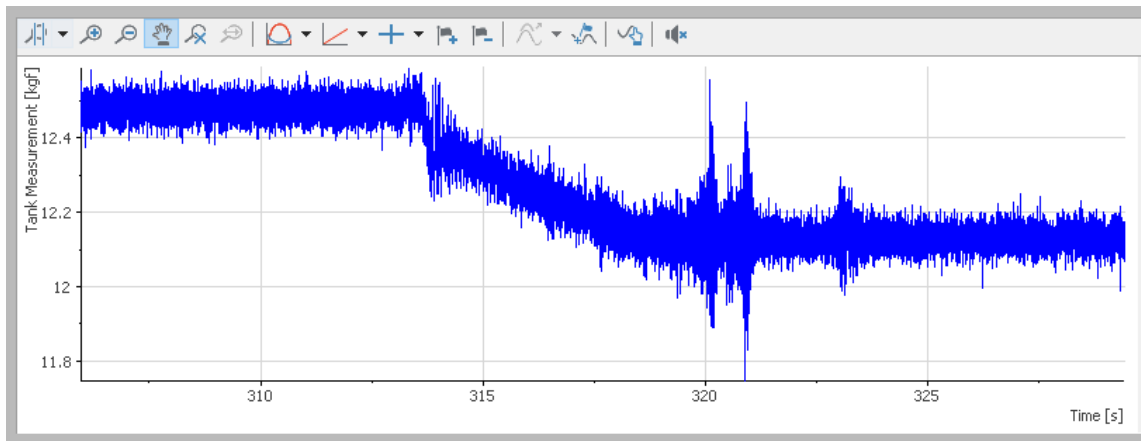


Figure 7.8: Test 1 - Tank measurements

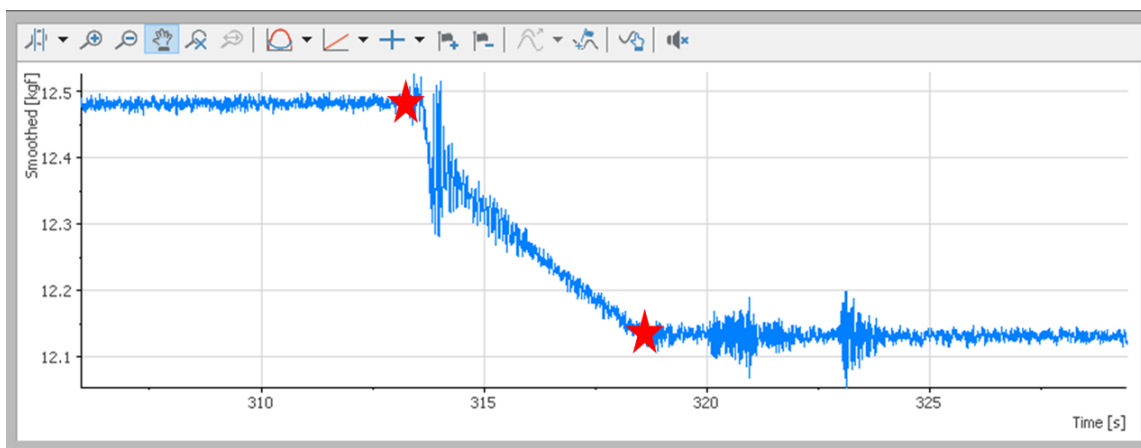


Figure 7.9: Test 1 - Smoothened tank measurements

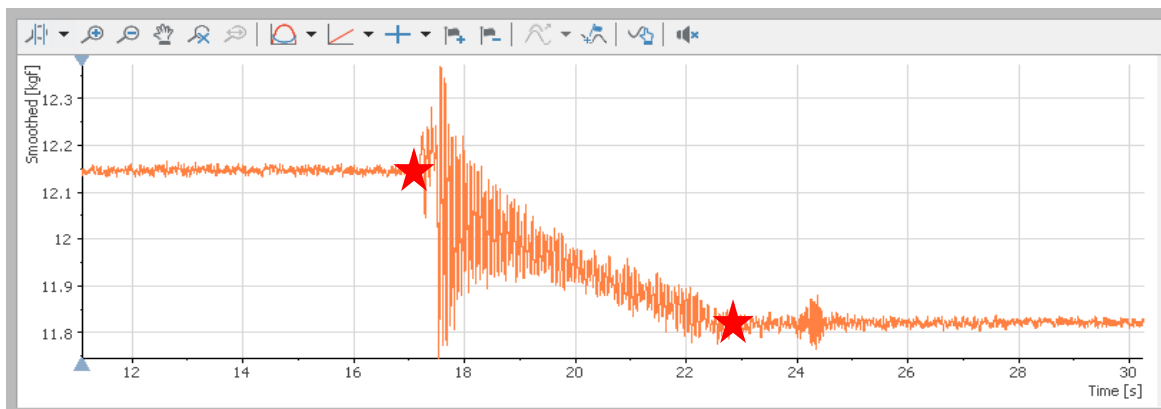


Figure 7.10: Test 2 - Smoothened tank measurements

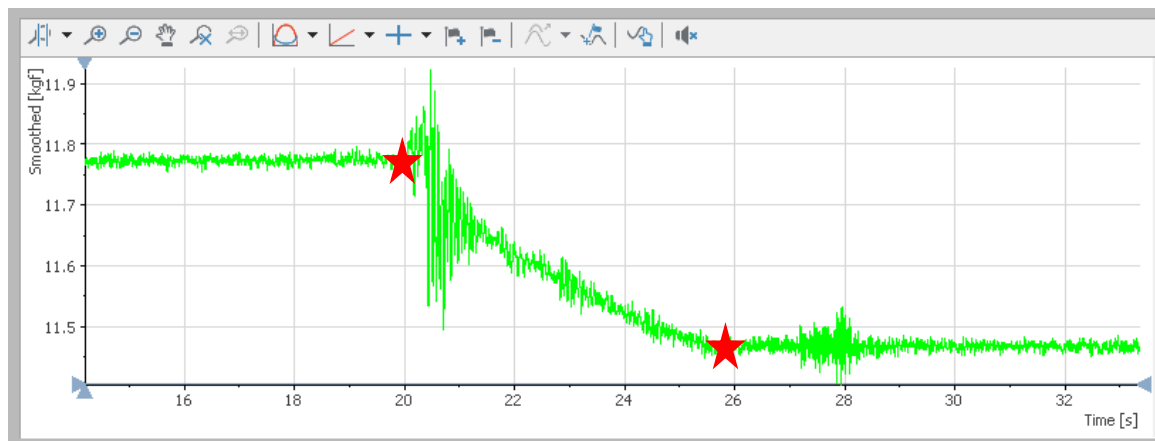


Figure 7.11: Test 3 - Smoothened tank measurements

The first spikes depicted in all three graphs were due to the initial shock of the nitrous oxide entering the system. The irregularities shortly after the burn represent the powering or throttling down of the system. The atmospheric tests created combustion instabilities and were observed by ‘popping’ sounds.

More oxidiser was consumed for Test 1 and this is verified by the change in mass of the run tank. The results are consistent with what was observed in Section 7.3.1. Possible variations in supercharging pressures by 2 to 5 bar would have affected the oxidiser mass flow rate for Test 1. The smaller fuel grain would have also led to a change in the oxidiser mass flow rate for this test as it would have altered the port area.

The smoothened tank measurement graphs were used to calculate the oxidiser mass flow rate. The values of x and y were determined from the graph at points on the corners of each slope as indicated by stars in Figure 7.9, Figure 7.10 and Figure 7.11. The ratio of the difference of x values over y values was calculated. Sample calculations are given in Appendix 7B. Table 7.2 shows the calculated oxidiser mass flow rates for each test. The time lapse for each test was 5 seconds, which was the input to the GUI.

Table 7.2: Oxidiser mass flow rates determined from tank measurement graphs

	Test 1	Test 2	Test 3
Oxidiser Mass Flow Rate (g/s)	62.61	56.84	55.97

An average oxidiser mass flow rate of 58.47 g/s was calculated. This is significantly lower than the theoretical oxidiser mass flow rate of 130 g/s. The errors associated with these calculations are systemic because they are caused by load cell calibration or inaccuracies. In addition, the theoretical results do not consider factors such as residual oxidiser in the feed system or valves, evaporative cooling, or the varying oxidiser mass flow rate throughout the burn. The discharge

coefficients used in the theoretical calculations may have also had an effect on the results. The oxidiser mass flow rate is increased with a reduction in the discharge coefficient for the short tube with conical entrance injector orifice. If the injector reacted according to a different orifice type, this would alter the discharge coefficient and hence oxidiser mass flow rate.

The O/F ratio for this set of results yields a value of 8.34 and was calculated using (Equation 4.3) and (Equation 4.4). This is in line with the theoretical value of 8 obtained from NASA CEA. The O/F ratio in a given hybrid motor however, continuously changes with the burn and is not accounted for.

7.3.2.2 Port area

The port areas had to be calculated for each test individually because of the slight variations in fuel grain dimensions. This was necessary for accurate calculations of oxidiser mass flux and the regression rate. The total port areas were calculated by summing up the individual areas depicted in Figure 7.12.

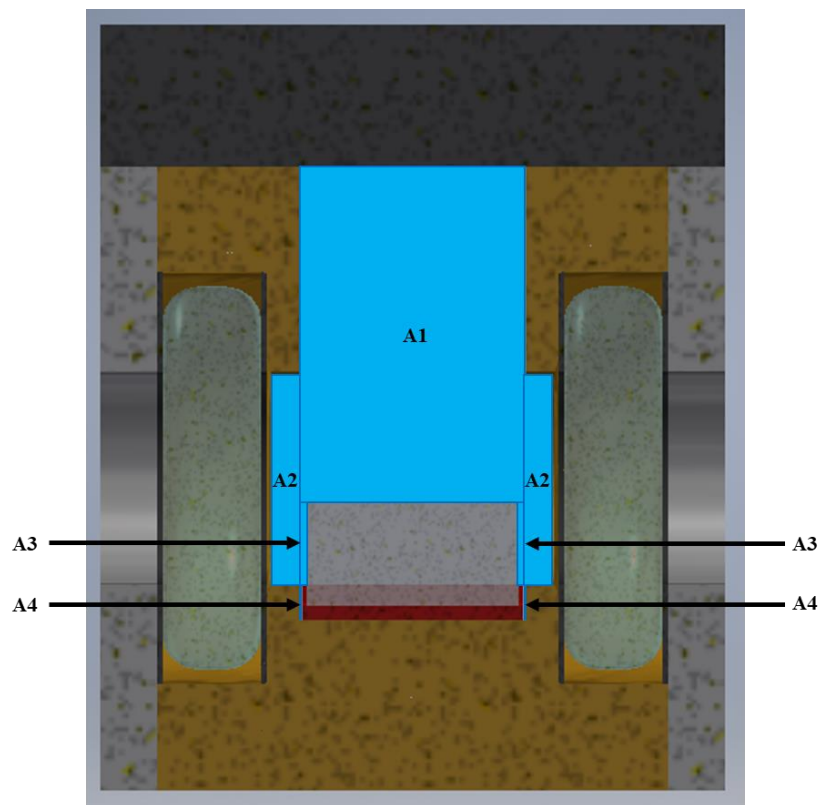


Figure 7.12: Individual port areas used in oxidiser mass flux calculations

Table 7.3 shows the total port areas calculated.

Table 7.3: Total port areas for each successful test calculated from individual areas

	Test 1	Test 2	Test 3
Port Area (mm²)	1597	1496	1539

An average port area was determined to be 1544 mm². This value was used to determine a sample range of ballistic coefficients in Section 7.2.5.

7.3.2.3 Oxidiser mass flux

Once the oxidiser mass flow rates and port areas were determined, the oxidiser mass flux was calculated using (Equation 4.10) for each test and is shown in Table 7.4.

Table 7.4: Oxidiser mass fluxes for each successful test based on oxidiser mass flow rates and port areas

	Test 1	Test 2	Test 3
Oxidiser Mass Flux (kg/m²s)	39,21	37,99	36,37

An increased oxidiser mass flow rate for Test 1 resulted in a higher oxidiser mass flux. The average oxidiser mass flux was 37.86 kg/m²s.

7.3.2.4 Regression rates

Once the oxidiser mass fluxes were determined, the regression rate for each test was calculated as follows:

1. The volumetric change for each fuel grain was determined using a measuring cylinder. These results are given in
2. Table 7.5.
3. The burn time input into the GUI of the data acquisition system was 5 seconds for all tests. A time-averaged regression rate was thus determined.
4. Regression rate is a linear variable; the volume differences were therefore cube rooted to obtain a linear regression rate.

Table 7.5 below provides the volume differences for each fuel grain obtained by using the measuring cylinder.

Table 7.5: Volume differences for each test

Volume (cm³)	Test 1	Test 2	Test 3
Initial	69	78	72
Final	44	43	35
Difference	25	35	37

As mentioned in point 2, the burn time was taken to be 5 seconds. Using (Equation 7.1), the linear regression rate was determined.

$$\dot{r} = \frac{\sqrt[3]{V}}{5}$$

(Equation 7.1)

Table 7.6 shows the results for the linear regression rates.

Table 7.6: Time-averaged regression rates for each test with 5 seconds burn time

	Volume (cm³)	Volume (mm³)	Cube root volume (mm)	Linear Regression Rate (mm/s)
Test 1	28,2	25000	29.240	5.848
Test 2	38,3	35000	32.710	6.542
Test 3	38,6	37000	33.322	6.664

Critical examination of the video footage for all three tests revealed discrepancies in the time lapse from the start to the end of each run. The burn times obtained from the recordings were between 8 and 9 seconds as shown in Table 6.1. The oxidiser flow caused the servo valve to freeze thus causing a slow reaction time from the control system inputs which could have been the reason for the discrepancy in burn times. The oxidiser tank measurement graphs depict a more accurate burn time by showing the time between when the oxidiser inlet flow valve was opened and closed. Combustion commenced when sufficient oxidiser was in the system and only terminated once all of the oxidiser in the combustion chamber was consumed. The burn times obtained from the graphs show a closer correlation to the video footage. An approximate burn time average of 8.5 seconds was therefore taken for new regression rate calculations. The results are shown in Table 7.7.

Table 7.7: Regression rates with 8.5 seconds burn time

	Volume (cm³)	Volume (mm³)	Cube root volume (mm)	Linear Regression Rate (mm/s)
Test 1	28.2	25000	29.240	3.440
Test 2	38.3	35000	32.710	3.848
Test 3	38.6	37000	33.322	3.920

The linear regression rates obtained from the different burn times differ by almost 3 mm/s. A time averaged regression rate for Sasolwax 0907 with nitrous oxide was calculated to be 3.74 mm/s with an oxidiser mass flux of 37.86 kg/m².

Theoretical calculations for the HSM tests show that an increase in oxidiser mass flow rate would result in a higher oxidiser mass flux and thus an improved regression rate. The experimental values however, show the contrary. This may be attributed to the difference in port areas for each test. An increased oxidiser mass flow rate and larger port area resulted in a higher oxidiser mass flux for Test 1 and the lowest regression rate. Test 3 produced the largest regression rate. This suggests that the smaller port area coupled with the intermediate oxidiser mass flow rate allowed for greater decomposition of the nitrous oxide. This may be further explained by greater turbulence due to higher pressures within a small area which would improve the decomposition of nitrous oxide. This concept is not properly understood due to the small sample of results and statistical variation. Future testing will assist in a deeper understanding of this ambiguity. Variables such as Reynold's number and throttling down of the flow for larger port areas should be considered.

The regression rates discussed above cannot be directly compared to any existing research. Factors such as the oxidiser mass flux, oxidiser, fuel composition, carbon chain length or type of motor used would have an impact on the regression rate. Grosse, (2009) has determined average regression rates between 9.7 mm/s to 14.6 mm/s with oxidiser mass flow rates between 50 g/s to 150 g/s, and an oxidiser mass flux range of 10 g/cm²s to 50 g/cm²s for Sasolwax 0907. These results however, cannot be directly linked to this research due to the scaling effects governed by the use of a cylindrical lab-scale motor.

7.3.2.5 Ballistic coefficients

The three successful firings were all carried out at an average calculated oxidiser mass flow rate of 58.5 g/s and atmospheric pressure. The small variations in oxidiser mass flux were due to the differences in fuel grain dimensions as a consequence of the fuel grain casting process. These sets of results were therefore insufficient to determine the ballistic coefficients a and n . Alternatively, the literature data for pure paraffin wax and nitrous oxide motors were consulted to obtain one of the ballistic coefficients and thereby calculate the other. Further testing of the HSM at different oxidiser mass flow rates and chamber pressures will validate these results.

Table 7.8 indicates the different ballistic coefficient values for different hybrid propellant combinations (Genevieve, 2013).

Table 7.8: Typical values for the ballistic coefficients a and n , for hybrid motors (Genevieve, 2013)

Fuel	Oxidiser	a	n	Reference
HTPB	GOX	0.025×10^{-3}	0.65	Karabeyoglu et al. (2002)
HTPB	GOX	0.0304×10^{-3}	0.681	Sutton and Biblarz (2001)
HTPB	GOX	0.087×10^{-3}	0.53	George et al. (2001)
HTPB	GOX	0.077×10^{-3}	0.53	George et al. (2001)
HTPB	N ₂ O	0.094×10^{-3}	0.325	Lohner et al. (2006)
Paraffin wax	GOX	0.091×10^{-3}	0.69	Karabeyoglu et al. (2002)
Paraffin wax	LOX	0.117×10^{-3}	0.62	Karabeyoglu et al. (2003)
Paraffin wax	H ₂ O ₂	0.0344×10^{-3}	0.959	Brown and Lydon (2005)
Paraffin wax	N ₂ O	0.132×10^{-3}	0.555	Grosse (2009)
Paraffin wax	N ₂ O	0.155×10^{-3}	0.5	McCormick et al. (2005)
HDPE	N ₂ O	0.0462×10^{-3}	0.352	Lohner et al. (2006)
PMMA	N ₂ O	0.0466×10^{-3}	0.377	Lohner et al. (2006)

The values observed for paraffin wax with nitrous oxide are quite similar, in particular for the n value. Although both references used nitrous oxide, the carbon chain length of the paraffin wax differed between the two with Sasolwax 0907 (C₅₀H₁₀₂) and FR5560 (C₃₂H₆₆) respectively. Despite this, the n value remained similar which suggests that n would have only changed slightly for different C-H lengths. This was also observed for different oxidiser mass flux ranges (Grosse, 2009), (McCormick, et al., 2005). A range of n was therefore used to illustrate the change in a that would be achieved with the average regression rate (3.74 mm/s) and oxidiser mass flux (37.86 kg/m²s) obtained from this slab motor testing. The results are given in Table 7.9.

Table 7.9: Ballistic Coefficient a calculated from measured parameters and a range of n determined from literature

n	$a \times 10^{-3}$
0,4	0,874177
0,425	0,7982609
0,45	0,7289376
0,475	0,6656345
0,5	0,6078288
0,525	0,5550432
0,55	0,5068416
0,575	0,462826
0,6	0,4226328

An increase in the n value shows a clear decrease in the ballistic coefficient a . This is due to n being dependent on and valid only within a specific oxidiser mass flux range, and a on the regression rate (Grosse, 2009). The results are what would be expected from a constant regression rate. For an average of the n values from

Table 7.9, a would be 0.55×10^{-5} for the averaged regression rate of 3.74 mm/s. This is significantly greater (5 times) than the a values obtained from the references. This is the result of the reduced oxidiser mass flux (by a factor of 10) for the HSM in this research compared to those established in Grosse, (2009). The results are also based on a cylindrical lab-scale motor and scaling effects would have to be considered. It should be noted that these results are not conclusive and need to be validated by further testing.

7.4 Unsuccessful hot fire tests

Possible reasons for the unsuccessful firings are listed below and then discussed in detail:

1. Low combustion chamber pressure
2. Insufficient vaporisation of the wax
3. Ignition timings
4. High oxidiser mass flow rate
5. The Blocking Effect
6. The Kelvin-Helmholtz Surface Instability Theory

The only difference identified between the successful tests and certain failed attempts was the incorporation of the side-glass spacer to eliminate or minimise side burning. The unsuccessful firings exhibited a brief period of combustion and Table 6.1 shows the combustion times

measured from video recordings for each of these tests. This suggests that the reduced port area, by an average of 20%, resulted in an increased combustion chamber pressure and inhibited combustion. The oxidiser was possibly not able to completely decompose due to lack of oxygen. The resultant lower convective heat transfer within the chamber subsequently decreased the turbulence of the oxidiser and hence encapsulation of the molten wax in the oxidiser stream (Sun et al., 2014). Only a portion of the vaporised wax would have combusted and was not able to sustain the entire combustion process.

Ignition delay times were also a contributing factor to the failed combustion firings. Video footage showed that the igniter extinguished before or because of the oxidiser inlet. These times were critical to ensure that vaporisation of the wax was sufficient for combustion to take place. An oxidiser mass flow rate that was too high could have also been a cause of the doused igniter.

Another possible reason may be due to a phenomenon known as the blocking effect. Heat transfer from the flame is hindered due to mass from the fuel surface being entrapped within the boundary layer (Karabeyoglu & Zilliac, 2006). This is a complication of hybrid rocket motors and may have also contributed to incomplete combustion. In this case, the vaporised fuel would significantly reduce the heat transferred from the flame. This may be aggravated by the relatively small port area of this particular motor in conjunction with the testing being conducted at atmospheric pressure. The pressurised test proved that the smaller port area with a high oxidiser mass flux was therefore limited to nitrous oxide and paraffin wax experiments at atmospheric pressure. The increased chamber pressure assisted the decomposition process of nitrous oxide. Research on slab motors suggests that this was not an issue when oxygen was used (Chandler, et al., 2012), (Nakagawa, et al., 2009).

For aluminised fuel grains, the research suggests that the size of the aluminium particle greatly influences combustion (Pastrone, 2012). As discussed in Section 2.5, larger particles have a low surface to volume ratio. Section 2.4.3 mentioned that the size of particle used in this research was between 100 μm to 200 μm . The Kelvin-Helmholtz surface instability theory applied in this case (Evans, et al., 2009). At low oxidiser mass fluxes such as those observed in this research (between 35 kg/m^2 and 40 kg/m^2), aluminium has a low energy of release which inhibits ignition (Sun et al., 2014). This is consistent with the findings in the experiments conducted. In addition, the increased conductivity and thermal mass of the aluminium particles may have been a contributing factor.

In the case of the pressurised test with pure paraffin wax, the combustion chamber was not sealed properly with RTV being used as a sealant, so accurate regression rate measurements could not be obtained. A small piece of the fuel grain was left behind which suggests almost complete burning. This is verified by the soot deposit all over the entire inner surfaces of the combustion chamber. However, incomplete combustion was observed as revealed by the soot deposit which

suggests a deficiency in oxygen, the products which would have otherwise been water and carbon dioxide.

As discussed in Section 6.5, the silicone gaskets burnt which likely also led to leaking during the test. Tanged graphite gaskets were purchased for future testing to ensure adequate seals between the brass and stainless steel panels and bulkheads.

Despite not being able to acquire regression rate measurements, the duration of combustion (6 seconds) of the pressurised hot fire test suggests that the increased combustion chamber pressure resulted in a higher convective heat transfer and flux, aiding in the combustion process.

The nature and position of the crack on both windows suggested that it was either due to thermal shock between the heat of the igniter and the low temperature of the nitrous oxide upon entry, or stress due to the combustion pressure, or both. A pressure transducer will be fitted onto the combustion chamber in order to accurately determine the combustion chamber pressure upon entry of the oxidiser and ignition.

Additional tests will validate the HSM design for pressurised testing and verify the independence of regression rate on combustion pressures.

7.5 Entrainment Mechanism

The entrainment mechanism theory describes the process by which non-classical fuels combust and the reason for increased regression rates compared to classical fuels. Low viscosity and surface tension of paraffin fuels result in the increased regression rate behaviour of these fuels. Research in slab motors have verified this theory with oxygen as the oxidiser (Chandler, et al., 2012). This study aimed to validate the concept with nitrous oxide. The images presented below were taken from the video footage of the window covered with a black tint for clarity. This also assisted in being able to distinguish between the fuel grain and the flame. The oxidiser flow is from right to left, with the chamfered edge of the fuel grain at the front (Figure 4.1 and Figure 4.2).

At the start of each burn, an orange glow appeared and then faded into a bluish colour, which represents the flame zone above the fuel's surface. Figure 7.13 depicts the liquid melt layer on the surface of the fuel grain. The limitations of the camera and increased radiation penetration into the fuel grain decreases the visual distinction between the flame and liquid layer. The liquid layer is very thin and is seen as an orange sheet on the fuel grain surface. The flame is the bluish zone above this.



Figure 7.13: Liquid melt layer on the surface of the pure paraffin wax fuel grain (SH005)

Once the surface of the fuel grain is melted, the wax vapourises. With the assistance of roll waves as shown in Figure 7.14, droplets become entrained in the flow due to convective heat. Roll waves are caused by the shearing of the surface of the liquid layer due to the turbulent flow of the oxidiser stream (Chandler, et al., 2012).



Figure 7.14: Roll waves in pure paraffin wax fuel grain

Due to the low viscosity of the fuel, droplets are encapsulated in the boundary layer. Figure 7.15 and Figure 7.16 illustrate the bursts of droplets above the flame.

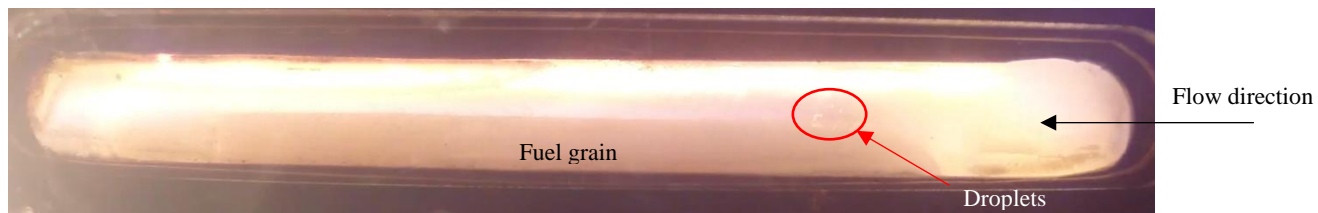


Figure 7.15: Droplets being entrained into the flame zone for pure paraffin

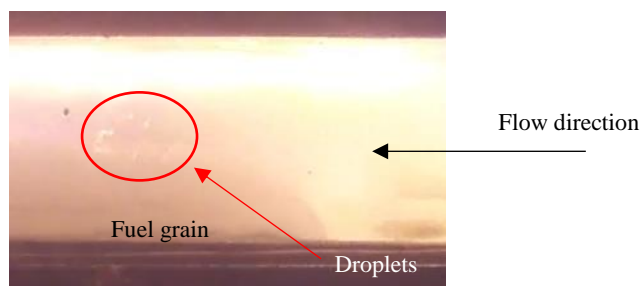


Figure 7.16: Zoomed in view of droplets

The results presented in Section 7.2.6 are consistent with the entrainment mechanism that explains the high regression rate characteristics of paraffin-based fuel grains. The findings therefore validate this theory for Sasolwax 0907 paraffin wax combinations for hybrid fuels. A better camera, ultrasonic or X-ray equipment, and tests conducted with blackened paraffin would provide improved imagery by limiting radiation penetration into the fuel grain.

This study has successfully validated the use of nitrous oxide and Sasolwax 0907 as a hybrid fuel at atmospheric pressure in a slab motor. The results of the three tests were similar in terms of burning profile, mass and dimension changes, considering statistical variations. Additional testing will be conducted to establish reliable ballistic coefficients a and n for Sasolwax 0907 with nitrous oxide. The results will be used to assist in the advancement of the Phoenix Hybrid Rocket Sounding Programme by obtaining more accurate data with regards to regression rate of the propellant combination and performance characteristics.

CHAPTER 8: CONCLUSION

The project achieved its objective in designing, manufacturing and testing a hybrid rocket slab motor to visualise and determine the regression rate behaviour of paraffin-based fuel grains. This project was unique in nature in that paraffin-based fuel grains with nitrous oxide oxidiser have not previously been investigated in a slab motor.

The control system, feed system, injector and combustion chamber with windows enabled the visualisation of the combustion process and the observation of the regression rate of solid paraffin wax with nitrous oxide oxidiser. The results showed that the nitrous oxide compatible materials sufficiently withstood the combustion environment during testing however, the quartz glass windows did not survive the pressurised experiment. The seals that were used in the pressurised test were discerned to be inadequate therefore tanged graphite gaskets were purchased for future testing. These will provide a more reliable seal as observed for the cylindrical lab-scale motor.

Cold flow tests showed nominal and safe operation of the system before hot fire testing was conducted. Three pure paraffin wax tests were accomplished at atmospheric pressure with a theoretical oxidiser mass flow rate of 130 g/s and the use of e-matches for ignition. The average mass combusted was found to be 35 g, with an oxidiser mass flow rate of 58.5 g/s, oxidiser mass flux of 37.86 kg/m²s, and regression rate of 3.74 mm/s. The discrepancies in the mass of fuel burnt and oxidiser mass flow rates are considerable due to factors such as slight variations in supercharging pressures, port areas, and the coefficient of discharge for the injector. The small variances between the fuel grain dimensions altered the port area and hence oxidiser mass flux. This showed that the port geometry was critical in the results of the regression rates obtained. The supercharge pressures were also not consistent because the operation is manually controlled and the ambient conditions affected the oxidiser mass flow rate from the tank. The coefficients of discharge and nitrous oxide decomposition properties more likely contributed to the variations in results. These factors may have influenced the difference in the regression rates observed. Side burning also had a major influence in the regression rate, as indicated by this research.

Side burning was reduced by installing side-glass spacers in order to obtain regression rate in a singular plane, to accurately mimic a full-scale hybrid rocket motor. The consequences were a series of unsuccessful pure paraffin wax firings. Different igniter configurations with e-matches and pyrotechnic igniters were employed to increase the ignition energy, all of which failed. This suggests that the ignition method had no significant impact in achieving combustion. Four 40% aluminised wax fuel grains were also investigated with the same results. Some of the experiments observed a brief combustion period that was not sustained. A possible explanation was that the combination of a high oxidiser mass flow rate with a smaller port area hindered the decomposition of nitrous oxide and mixing with the vaporised wax. It is likely that high turbulence, and possibly

associated localised pressure variations caused nitrous oxide decomposition when there was no side-glass spacer. Other reasons included the low combustion chamber pressure, ignition timings, the blocking effect and the Kelvin-Helmholtz surface instability theory.

The 5 bar nozzle was installed to conduct testing to determine the effects of a pressurised system on the behaviour of paraffin-based fuel grains with nitrous oxide. This test demonstrated that the increased chamber pressure with the smaller port area resulted in sufficient decomposition of nitrous oxide for combustion to occur. Whereas the smaller port area at atmospheric pressure contributed to the failure of the previous tests. This suggests that an undetermined optimal port area with a sufficiently pressurised environment is essential to obtaining regression rate results from Sasolwax 0907 with nitrous oxide.

The regression rate results obtained from the HSM testing were insufficient to obtain the ballistic coefficients a and n . Literature data provided the basis for calculating one of the ballistic coefficients for the time-averaged regression rate of 3.74 mm/s determined in this study. The similar n values from research suggests that carbon chain length does not significantly affect this parameter. A range of n was therefore taken to obtain a values for an oxidiser mass flow rate of 58.5 g/s and oxidiser mass flux of 37.86 kg/m²s. An average regression rate coefficient a was thereby calculated to be 0.55×10^{-5} . Due to differences in factors such as oxidiser mass flow rates, oxidiser mass fluxes, chamber pressures and scaling effects, results obtained in this study cannot be directly compared to existing research.

Experiments for visualising the combustion process between paraffin wax and oxygen exists, and investigative research into the reaction with nitrous oxide in a slab motor had not been explored prior to this study. The entrainment mechanism responsible for the high regression rates of pure paraffin wax was observed in this study for Sasolwax 0907 with nitrous oxide. The characteristics of droplets, roll waves, and the liquid layer were all observed in the burn. This combustion process increases the regression rate of non-classical fuels due to the low viscosity and surface tension of the liquid layer and further validates the increased regression rate obtained from the specific propellant combination. A camera with a higher shutter speed and optics would provide improved video footage and clarity regarding these characteristics. It is beneficial in understanding the nature of nitrous oxide decomposition and ignition characteristics in future hybrid rocket motors with this propellant combination.

The hybrid rocket slab motor designed and developed in this project has successfully been used to conduct experimental testing on paraffin wax-based fuel grains with nitrous oxide. Three successful hot firings were achieved with similar results. Aluminised wax fuel grains could not be successfully investigated at atmospheric pressures. The high oxidiser mass flux may have resulted in insufficient mixing and low convective heat transfer at atmospheric pressure for nitrous

oxide with aluminised wax fuel grains. The size of the aluminium particle may have also contributed to the reduced convective heat transfer. Additional testing should be conducted at increased port areas and pressures to determine the regression rate of aluminised fuel grains in a slab motor. A more energetic igniter, such as pyrotechnics with decreased mass fractions of aluminium additives might also be tested.

Additional experiments need to be carried out to verify the results obtained in this study as well as to further investigate the ballistic coefficients, regression rates and combustion chamber pressures of Sasolwax 0907 with nitrous oxide in a slab motor.

Future research objectives and a testing methodology are described in Chapter 9 to determine the ballistic coefficients a and n for nitrous oxide and Sasolwax 0907. These are vital for accurate regression rate measurements for the particular propellant combination and hence for future rocket design.

The data obtained from this research provides valuable insight into the performance characteristics and regression rates of the particular grade of paraffin wax (Sasolwax 0907) with nitrous oxide and will assist in the development of low altitude rockets produced in the UKZN Phoenix Hybrid Rocket Sounding Programme. Rockets with smaller payloads and high thrusts can therefore be developed.

CHAPTER 9: FUTURE TESTING

An updated experimental methodology was defined for future testing so that the ballistic coefficients can be determined. Testing for different oxidiser mass fluxes is required to identify these parameters.

A testing methodology for future experiments is listed below:

9.1 Atmospheric tests for pure wax with e-matches

1. Injectors with smaller orifice sizes to reduce the oxidiser mass flow rates in line a reduced port area (1 mm and 1.3 mm).
2. The oxidiser inlet flow can be controlled by introducing the intermediate valve position before permitting the full oxidiser flow, with the side-glass spacers.

9.2 Atmospheric tests for 40% Al wax with e-matches

1. The 1.5 mm injector can be used for tests without the side-glass spacers.
2. If one or both of the experiments mentioned in 9.1 are successful, the testing parameters can be applied to hot fire testing with 40% aluminised paraffin wax tests.

If the 40% aluminised tests are still unsuccessful, experiments with lower mass fractions can be attempted under the above-mentioned conditions.

9.3 Pressurised tests

1. A ¼" hole will be drilled and NPT tapped into the front injector bulkhead to accommodate a pressure sensor at the fore-end of the slab motor combustion chamber.
2. The same will be done for the nozzle plate bulkhead to determine pressure readings at the back.
3. A stainless steel plate will be used to enclose the one side of the chamber window to preserve the quartz glass.
4. The manifold will be welded to the injector bulkhead to prevent leaking and eliminate the requirement of O-rings.
5. The oxidiser mass flow rate will be determined by the atmospheric testing conducted.
6. Initial pressurised tests will be run with a 2.5 bar nozzle before attempting the tests on 5 bar and 10 bar nozzles.
7. These tests will initially be attempted using e-matches before pyrotechnics are implemented, if required.

The initial tests did not include pressure transducers or thermocouples because the objective was to first ensure repeatability of slab motor testing for the specified propellant combination. After

which, modifications will be done to the combustion chamber to incorporate the measurement devices.

REFERENCES

- Accuratus, 2013. *Fused Silica, SiO₂ Glass Properties*. [Online]
Available at: <http://accuratus.com/fused.html>
[Accessed 14 January 2016].
- Advanced Glass and Ceramics, 2014. *Frits-Filters-Gas Adsorption-HPLC-Lasers Optics-Reference Electrodes-Sensors/Detectors*. [Online]
Available at: <http://www.porousglass.com/>
[Accessed 16 January 2016].
- AK Steel Corporation, 2007. *304/304L Stainless Steel*. [Online]
Available at:
http://www.aksteel.com/pdf/markets_products/stainless/austenitic/304_304l_data_sheet.pdf
[Accessed 10 February 2016].
- ASM International Handbook Committee, 1990. *Metals Handbook*. 10 ed. Ohio: ASM International.
- Biblarz, O. & Sutton, G. P., 2001. *Rocket Propulsion Elements*. 7 ed. New York: John Wiley & Sons.
- Boedeker, 2016. *Polycarbonate Specifications*. [Online]
Available at: http://www.boedeker.com/polyc_p.htm
[Accessed 20 March 2016].
- Booyens, D., Smyth, J., Moodley, S. & Pitot, J., 2010. *Hybrid Rocket Motor Design*, Durban: University of KwaZulu-Natal.
- Boronowsky, K. M., 2011. *Non-homogeneous Hybrid Rocket Fuel for Enhanced Regression Rates Utilizing Partial Entrainment*, San Jose: San Jose State University.
- Boyer, H. E. & Gall, T. L., 1985. *Metals Handbook*. 2 ed. Ohio: American Society for Metals.
- Buitrago, C., 2014. *courses.sense.buffalo*. [Online]
Available at: http://wwwcourses.sens.buffalo.edu/ce435/PC_CB.pdf
[Accessed 20 March 2014].
- Cai, G. et al., 2013. Scale Effect of Fuel Regression Rate in Hybrid Rocket Motor. *Aerospace Science and Technology*, 24(1), pp. 141-146.
- Cantwell, B., Karabeyoglu, A. & Altman, D., 2010. Recent Advances in Hybrid Propulsion. *International Journal of Energetic Materials and Chemical Propulsion*, 9(4), pp. 305-326.

- Chandler, A. A., 2012. *An Investigation of Liquefying Hybrid Rocket Fuels with Application to Solar System Exploration*, San Francisco: Stanford University.
- Chandler, A., Jens, E., Cantwell, B. J. & Hubbard, G. S., 2012. Visualisation of the Liquid Layer Combustion of Paraffin Fuel for Hybrid Rocket Applications. *48th AIAA/ASME/SAE/ASEE Joint Propulsion Conference & Exhibit*, August, pp. 1-11.
- Chiaverini, M. J. & Kuo, K. K., 2007. *Fundamentals of Hybrid Rocket Combustion and Propulsion*. 1 ed. Virginia: American Institute of Aeronautics and Astronautics.
- Chiaverini, M. J. et al., 2000. Regression Rate Behavior of Hybrid Rocket Solid Fuels. *Journal of Propulsion and Power*, 16(1), p. 125.
- Copper Development Association, 2017. C22000. [Online]
Available at: <https://alloys.copper.org/alloy/C22000>
[Accessed 2 February 2017].
- Corning, 2014. *Properties of Pyrex, Pyrexplus and Low Actinic Pyrex Code 7740 Glasses*. [Online]
Available at: <http://www.quartz.com/pxprop.pdf>
[Accessed 16 January 2016].
- Corning, 2015. *Base Vycor 7913*. [Online]
Available at: http://coresix.com/files/4213/8375/8794/Vycor_7913.pdf
[Accessed 10 January 2016].
- DeSain, J. D. et al., 2009. *Tensile Tests of Paraffin Wax for Hybrid Rocket Fuel Grains*. Denver, 45th AIAA/ASME/SAE/ASEE Joint Propulsion Conference & Exhibit.
- Dlamini, M. A., Ramrathun, N. & Theba, R., 2014. *Hybrid Slab Motor Visualisation Test Stand*, Durban: University of KwaZulu-Natal.
- Duran Group, 2014. *It Comes Down to these Properties*. [Online]
Available at: <http://www.duran-group.com/en/about-duran/duran-properties.html>
[Accessed 18 February 2016].
- Dyer, J. et al., 2007. *Design and Development of a 100 km Nitrous Oxide/Paraffin Wax Hybrid Rocket Vehicle*. Cincinnati, 43rd AIAA/ASME/SAE/ASEE Joint Propulsion Conference & Exhibit.
- Evans, B. et al., 2009. *Hybrid Rocket Investigations at Penn State University*. Denver, 45th AIAA/ASME/SAE/ASEE Joint Propulsion Conference & Exhibit, p. 15.

E-Z Lok, 2016. *Brass Mechanical Properties*. [Online]

Available at: <https://www.ezlok.com/technical-info/mechanical-properties/brass>

[Accessed 2 February 2017].

Fox, R. W., Pritchard, P. J. & McDonald, A. T., 2010. *Introduction to Fluid Mechanics*.

Seventh ed. Hoboken: John Wiley & Sons (Asia) Pte Ltd.

Genevieve, B., 2013. Development of a Hybrid Sounding Rocket Motor. *Development of a Hybrid Sounding Rocket Motor*.

Gill, G. S. & Nurick, W. H., 1976. *Liquid Rocket Engine Injectors*, Cleveland, Ohio, United States of America: NASA Lewis Research Center.

Glassblowing Industries, 2014. *Borosilicate/Borofloat Discs and Plates*. [Online]

Available at: <http://glassblowing.co.za/borosilicate-borofloat-discs-and-plates/>

[Accessed 10 January 2016].

Goodfellow Ceramic & Glass, 2009. *Borosilicate Glass - Properties of Borosilicate Glass (Pyrex/Duran) by Goodfellow Ceramic & Glass Division*. [Online]

Available at: <http://www.azom.com/article.aspx?ArticleID=4765>

[Accessed 16 January 2016].

Goodfellow Ceramic and Glass Division, 2014. *Fused Silica/Quartz Glass - Properties and Applications of Fused Silica/Quartz Glass by Goodfellow Ceramic & Glass Division*. [Online]

Available at: <http://www.azom.com/article.aspx?ArticleID=4766>

[Accessed 16 January 2016].

Grace Construction Products, 2012. *Self-Adhering Sheet Flashing*. [Online]

Available at: https://gcpat-tools.com/construction/en-ca/Documents/076526_Self-Adhering_Sheet_Flashing_Vycor_Plus_Flashing_GSWB-003A.docx

[Accessed 21 March 2018].

Grayglass, 2013. *Vycor*. [Online]

Available at: <http://www.grayglass.net/glass.cfm/Industrial-Products/Vycor/catid/4/conid/89>

[Accessed 18 June 2016].

Grosse, M., 2009. *Effect of a Diaphragm on Performance and Fuel Regression of a Laboratory Scale Hybrid Rocket Motor Using Nitrous Oxide and Paraffin*. Denver, 45th

AIAA/ASME/SAE/ASEE Joint Propulsion Conference & Exhibit .

Hall, N., 2015. *Specific Impulse*. [Online]

Available at: <https://www.grc.nasa.gov/www/k-12/airplane/specimp.html>

[Accessed 2 June 2016].

- Harvey, P. D., 1982. *Engineering Properties of Steels*. 1 ed. Ohio: American Society for Metals.
- Heraeus Quarzglas, 2015. *Making of fused quartz and fused silica*. [Online]
Available at:
https://www.heraeus.com/en/hqs/fused_silica_quartz_knowledge_base/production_process/makingoffusedsilica.aspx
[Accessed 8 February 2016].
- Hitech Safety Glass, 2008. *Hitech Safety Glass*. [Online]
Available at:
hitechsafetyglass.co.za/index.php?option=com_content&view=article&id=15&Itemid=10
[Accessed 14 July 2017].
- Humble, R. W., Henry, G. N. & Larson, W. J., 1995. *Space Propulsion Analysis and Design*, United States of America: McGraw-Hill.
- Juvinall, R. C. & Marshek, K. M., 2006. *Fundamentals of Machine Component Design*. 4 ed. Hoboken: John Wiley & Sons (Asia) Pte Ltd.
- Karabeyoglu, A., 2008. *Hybrid Rocket Propulsion for Future Space Launch*. [Online]
Available at: <https://aa.stanford.edu/events/50thAnniversary/media/Karabeyoglu.pdf>
[Accessed 20 June 2014].
- Karabeyoglu, A. M. & Zilliac, G., 2006. *Hybrid Fuel Regression Rate Data and Modelling*. Sacramento, 42nd AIAA/ASME/SAE/ASEE Joint Propulsion Conference & Exhibit.
- Karabeyoglu, A. M. et al., 2003. *Scale-up Tests of High Regression Rate Liquefying Hybrid Rocket Fuels*. Reno, American Institute of Aeronautics and Astronautics.
- Karabeyoglu, M. A., Altman, D. & Cantwell, B. J., 2002. Combustion of Liquefying Hybrid Propellants: Part 1, General Theory. *Journal of Propulsion and Power*, 18(3), p. 610.
- Karabeyoglu, M. A. et al., 2004. Scale-Up Tests of High Regression Rate Paraffin-Based Hybrid Rocket Fuels. *Journal of Propulsion and Power*, 20(6), pp. 1037-1045.
- Kumar, R. & Ramakrishna, P. A., 2014. Measurement of Regression Rate in Hybrid Rocket Using Combustion Chamber Pressure. *Acta Astronautica*, 103(1), pp. 226-234.
- Lohner, K. et al., 2006. *Fuel Regression Rate Characterization Using a Laboratory Scale Nitrous Oxide Hybrid Propulsion System*. Sacramento, 42nd AIAA/ASME/SAE/ASEE Joint Propulsion Conference & Exhibit.

Macsteel, 2014. *Stainless steel*. [Online]

Available at: <http://www.macsteel.co.za/products/stainless-steel>

[Accessed 25 March 2014].

Maharaj, C. S., Pitot, J. F., Veale, K. L. & Bemont, C. P., 2018. *Performance Characterisation of Metal Additives in Paraffin Wax Hybrid Rocket Fuel Grains*, Durban: University of KwaZulu-Natal.

MakeItFrom, 2014. *Borosilicate Glass*. [Online]

Available at: <http://www.makeitfrom.com/material-properties/Borosilicate-Glass/>

[Accessed 14 January 2016].

Mangold, H. K., 1983. Liquefied gases and supercritical fluids in oilseed extraction. *Journal of the American Oil Chemists' Society*, 60(2), pp. 226-228.

Marxman, G. A., Wooldridge, C. E. & Muzzy, R. J., 1963. *Fundamentals of Hybrid Boundary Layer Combustion*. Palm Beach, American Institute of Aeronautics and Astronautics.

McCormick, A. et al., 2005. *Design, Optimization, and Launch of a 3" Diameter N₂O/Aluminized Paraffin Rocket*. Tucson, 41st AIAA/ASME/SAE/ASEE Joint Propulsion Conference & Exhibit.

McCulley, J. M., 2012. *Design and Testing of Digitally Manufactured Paraffin*, Logan: Utah State University.

Nakagawa, I., Hikone, S. & Suzuki, T., 2009. *A Study on the Regression Rate of Paraffin-Based Hybrid Rocket Fuels*. Denver, 45th AIAA/ASME/SAE/ASEE Joint Propulsion Conference & Exhibit.

Natal Gaskets, 2011. *Rubber Materials*. [Online]

Available at: <http://www.natalgaskets.com/rubber.php#Page2>

[Accessed 20 August 2016].

Natal Gaskets, 2011. *Rubber Materials*. [Online]

Available at: <http://www.natalgaskets.com/rubber.php#Page3>

[Accessed 20 August 2016].

National Instruments, 2010. *Smoothing Functions*. [Online]

Available at: http://zone.ni.com/reference/en-XX/help/370859H-01/genmaths/genmaths/calc_smoothfunctions/

[Accessed 26 June 2017].

- Pastrone, D., 2012. Approaches to Low Fuel Regression Rate in Hybrid Rocket Engines. *International Journal of Aerospace Engineering*, 2012(10), pp. 1-12.
- Patnala, S., Chattaraj, T. & Joshi, P. C., 2012. Combustion Studies on Paraffin Wax in Gaseous Oxygen and Nitrous Oxide. *ARPJ Journal of Engineering and Applied Sciences*, 7(7), pp. 806-812.
- Peckner, D. & Bernstein, I. M., 1977. *Handbook of Stainless Steels*. 1 ed. New York: McGraw Hill Book Company.
- Plastipedia, 2016. *Polycarbonate PC*. [Online]
Available at: <http://www.bpf.co.uk/Plastipedia/Polymers/Polycarbonate.aspx>
[Accessed 20 March 2014].
- Polymer Technology & Services, 2016. *A Guide to Polycarbonate in General*. [Online]
Available at: http://www.ptslc.com/intro/polycarb_intro.aspx
[Accessed 16 January 2016].
- Prazisions glas&optik, 2014. *Vycor 7913 High temperature glass with 96% SiO₂ content*. [Online]
Available at: <https://www.pgo-online.com/intl/katalog/vycor.html>
[Accessed 4 August 2017].
- Sasol Performance Chemicals, 2015. *Personal Care - Waxes and Petroleum Jellies*. [Online]
Available at: http://www.sasol.com/sites/sasol/files/content/files/Personal_Care_Products.PDF
[Accessed 8 July 2016].
- Sasol, 2010. *Safety Data Sheet - Sasolwax 0907*, Hamburg: Sasol.
- Smith, G., 2013. *Heat and Mass Transfer Notes*. Durban: University of KwaZulu-Natal.
- Space Propulsion Group, Inc., 2012. *Nitrous Oxide Safety*. [Online]
Available at: <http://www.spg-corp.com/nitrous-oxide-safety.html>
[Accessed 24 July 2015].
- SPG, 2012. *Hybrid Rocket Propulsion Overview*. [Online]
Available at: <http://www.spg-corp.com/space-propulsion-group-resources.html>
[Accessed 17 March 2016].
- Sun et al., X., 2014. Regression Rate and Combustion Performance Investigation of Aluminum Metallized HTPB/98HP Hybrid Rocket Motor with Numerical Simulation. *Aerospace Science and Technology*, 42(1), pp. 287-296.

Technical Glass Products, 2010. *Properties of Fused Quartz*. [Online]
Available at: http://www.technicalglass.com/technical_properties.html
[Accessed 16 January 2016].

Theba, R., Veale, K. & Bemont, C., 2016. *Development of a Hybrid Rocket Slab Motor*. Salt Lake City, 52nd AIAA/SAE/ASEE Joint Propulsion Conference.

Theba, R., Veale, K. & Bemont, C., 2017. Development of a Combustion Visualisation Hybrid Rocket Motor. *R&D Journal of the South African Institution of Mechanical Engineering*, 33(1), pp. 97-104.

Thomasnet, 2015. *More about Borosilicate Glass*. [Online]
Available at: <http://www.thomasnet.com/about/borosilicate-glass-34770602.html>
[Accessed 14 January 2016].

ukrocketman, 2008. *Hybrid Rocket Science*. [Online]
Available at: <http://www.ukrocketman.com/rocketry/hybridscience.shtml>
[Accessed 15 March 2015].

Young, S., 2014. *What is density impulse and why do propellants with higher densities have higher density impulses?*. [Online]
Available at: <https://www.quora.com/what-is-density-impulse-and-why-do-propellants-with-higher-densities-have-higher-density-density-impulses>
[Accessed 2 June 2016].

APPENDIX 2A

Table 2A.9.1 illustrates typical hybrid rocket propellant combinations and their optimal O/F ratios.

Table 2A.9.1: Typical hybrid propellant combinations (Chiaverini & Kuo, 2007)

Fuel	Oxidiser	Optimum O/F	Sea level I_{sp} [s]	c^* [m/s]
HTPB	LOX	1.9	280	1820.3
PMM ($C_5H_8O_2$)	LOX	1.5	259	1660.9
HTPB	N_2O	7.1	247	1604.5
HTPB	N_2O_4	3.5	258	1662.9
HTPB	RFNA	4.3	247	1590.7
HTPB	FLOX (OF_2)	3.3	314	2042.5
Li/LiH/ HTPB	FLOX (OF_2)	2.8	326	2118.4
PE	LOX	2.5	279	1791.3
PE	N_2O	8.0	247	1599.6
Paraffin	LOX	2.5	281	1804.4
Paraffin	N_2O	8.0	248	1605.7
Paraffin	N_2O_4	4.0	259	1666.9
HTPB/Al (40%)	LOX	1.1	274	1757.5
HTPB/Al (40%)	N_2O	3.5	252	1636.8
HTPB/Al (40%)	N_2O_4	1.7	261	1679.1
HTPB/Al (60%)	FLOX (OF_2)	2.5	312	2006.2
Cellulose ($C_6H_{10}O_5$)	GOX	1.0	247	1572.5
Carbon	Air	11.3	184	1224.4
Carbon	LOX	1.9	249	1598.7
Carbon	N_2O	6.3	236	1521.6
<i>Cryogenic hybrids</i>				
Pentane (s)	LOX	2.7	279	1789.2
CH_4 (s)	LOX	3.0	291	1870.5
CH_4 (s)/Be (36%)	LOX	1.3	306	1917.8
NH_3 (s)/Be (26%)	LOX	0.47	307	1966.6
<i>Reverse hybrids</i>				
JP-4	AN	17.0	216	1417.6
JP-4	AP	9.1	235	1526.1
JP-4	NP	3.6	259	1669.1

Table 2A.9.2 lists the materials that are compatible with nitrous oxide.

Table 2A.9.2: Nitrous oxide compatibility (Dlamini, et al., 2014)

Material	Compatibility
Metals Aluminium Brass Copper Ferritic Steels Stainless Steels	Satisfactory Satisfactory but corrosive in presence of moisture Satisfactory but corrosive in presence of moisture Satisfactory but corrosive in presence of moisture Satisfactory
Plastics Polytetrafluoroethylene (PTFE) Polychlorotrifluoroethylene (PCTFE) Vinylidene polyfluoride (PVDF) Polyamide (PA) Polypropylene (PP)	Satisfactory Satisfactory Acceptable but possible ignition under certain conditions Acceptable but possible ignition under certain conditions Acceptable but possible ignition under certain conditions
Elastomers Buthyl (isobutene-isoprene) rubber (IIR) Nitrile rubber (NBR) Chloroprene (CR) Chlorofluorocarbons (FKM) Silicon Ethylene-propylene (EPDM)	Not recommended, possible ignition and significant swelling Not recommended, possible ignition and significant swelling Not recommended, possible ignition and significant swelling Not recommended, significant swelling Satisfactory Not recommended, possible ignition and significant swelling
Lubricants Hydrocarbon-based lubricant Fluorocarbon based lubricant	Not recommended, possible ignition Satisfactory

APPENDIX 4A

Fuel grain Dimensions

The equations below were used in the calculations that follow.

Table 4A.9.1: Table of constants for pure paraffin wax

Pure Paraffin	
Variable	Value
O/F ratio	8
Density	900 kg/m ³
Regression rate	1.5 mm/s

Table 4A.9.2: Table of constants for 40% aluminised paraffin wax

40% Aluminised Paraffin	
Variable	Value
O/F ratio	3.5
Density	1250 kg/m ³
Regression rate	2 mm/s

Calculating the oxidiser mass flow rate using various burn times:

Volume of fuel:

$$V_f = l_f \times w_f \times t_f$$

$$V_f = 0.1 \times 0.02 \times 0.015$$

$$V_f = 3 \times 10^{-5}$$

Mass of fuel:

$$m_f = \rho_f \times V_f$$

$$m_f = 800 \times 3 \times 10^{-5}$$

$$m_f = 0.027 \text{ kg}$$

Fuel mass flow rate:

$$\dot{m}_f = \frac{m_f}{b_t}$$

$$\dot{m}_f = \frac{0.027}{10}$$

$$\dot{m}_f = 0.0027 \text{ kg/s}$$

Total mass flow rate:

$$\dot{m}_t = \dot{m}_f \times (1 + O/F)$$

$$\dot{m}_t = 0.0027 \times (1 + 8)$$

$$\dot{m}_t = 0.0243 \text{ kg/s}$$

Oxidiser mass flow rate:

$$\dot{m}_{ox} = \dot{m}_t - \dot{m}_f$$

$$\dot{m}_{ox} = 0.0243 - 0.0027$$

$$\dot{m}_{ox} = 0.0216 \text{ kg/s}$$

Varying the burn time to calculate the oxidiser mass flow rate:

PURE PARAFFIN								
Length (m)	0.1		Density (kg/m ³)	900				
Width (m)	0.02		O/F Ratio	8				
Thickness (m)	0.015		r_dot	0.0015				
Volume (m ³)	0.00003							
Burn Time (s)	10	9	8	7	6	5	4	3
Fuel Mass (kg)	0.027	0.027	0.027	0.027	0.027	0.027	0.027	0.027
Fuel Mass Flow Rate (kg/s)	0.0027	0.003	0.003375	0.003857	0.0045	0.0054	0.00675	0.009
Total Mass Flow Rate (kg/s)	0.0243	0.027	0.030375	0.034714	0.0405	0.0486	0.06075	0.081
Ox Mass Flow Rate (kg/s)	0.0216	0.024	0.027	0.030857	0.036	0.0432	0.054	0.072
m_dot_f [g/s]	2.7							
m_dot_ox [g/s]	21.6							
Burn time [s]	10							
ALUMINISED PARAFFIN								
Length (m)	0.1		Density (kg/m ³)	1250				
Width (m)	0.02		O/F Ratio	3.5				
Thickness (m)	0.015		r_dot	0.002				
Volume (m ³)	0.00003							
Burn Time (s)	10	9	8	7	6	5	4	3
Fuel Mass (kg)	0.0375	0.0375	0.0375	0.0375	0.0375	0.0375	0.0375	0.0375
Fuel Mass Flow Rate (kg/s)	0.00375	0.004167	0.0046875	0.005357	0.00625	0.0075	0.009375	0.0125
Total Mass Flow Rate (kg/s)	0.016875	0.01875	0.02109375	0.024107	0.028125	0.03375	0.042188	0.05625
Ox Mass Flow Rate (kg/s)	0.013125	0.014583	0.01640625	0.01875	0.021875	0.02625	0.032813	0.04375
m_dot_f [g/s]	5							
m_dot_ox [g/s]	17.5							
Burn time [s]	7.5							

Varying the oxidiser mass flow rate to calculate width:

Table 4A.9.3: Table of constants for pure paraffin wax

Pure Paraffin	
Variable	Value
O/F ratio	8
Density	900 kg/m ³
Regression rate	1.5 mm/s
Length	100 mm

Table 4A.9.4: Table of constants for 40% aluminised paraffin wax

40% Aluminised Paraffin	
Variable	Value
O/F ratio	3.5
Density	1250 kg/m ³
Regression rate	2 mm/s
Length	100 mm

An oxidiser mass flow rate was assumed to calculate a width of the fuel grain:

$$\dot{m}_f = \frac{\dot{m}_{ox}}{O/F}$$

$$\dot{m}_f = \frac{0.02}{8}$$

$$\dot{m}_f = 0.0025 \text{ kg/s}$$

Area:

$$A_f = \frac{\dot{m}_f}{\rho_f \times \dot{r}}$$

$$A_f = \frac{0.0025}{900 \times 0.0015}$$

$$A_f = 0.0019 \text{ m}^2$$

Width:

$$w_f = \frac{A_f}{l_f}$$

$$w_f = \frac{0.0019}{0.1}$$

$$w_f = 18.52 \text{ mm}$$

PURE PARAFFIN					ALUMINISED PARAFFIN				
O/F Ratio	8				O/F Ratio	3.5			
Density (kg/m ³)	900				Density (kg/m ³)	1250			
Reg Rate (m/s)	0.0015				Reg Rate (m/s)	0.002			
Length (m)	0.1				Length (m)	0.1			
Ox Mass Flow Rate (kg/s)	0.15	0.2	0.25	0.3	Ox Mass Flow Rate (kg/s)	0.15	0.2	0.25	0.3
Fuel Mass Flow Rate (kg/s)	0.01875	0.025	0.03125	0.0375	Fuel Mass Flow Rate (kg/s)	0.042857143	0.057142857	0.071428571	0.085714
Area (m ²)	0.014	0.019	0.023	0.028	Area (m ²)	0.017	0.023	0.029	0.034
Width (mm)	138.89	185.19	231.48	277.78	Width (mm)	171.43	228.57	285.71	342.86
WIDTH BASED ON INJ OX MASS FLOW RATE					WIDTH BASED ON INJ OX MASS FLOW RATE				
Ox Mass Flow Rate (kg/s)	Fuel Mass Flow Rate (kg/s)	Area (m ²)	Width (mm)		Ox Mass Flow Rate (kg/s)	Fuel Mass Flow Rate (kg/s)	Area (m ²)	Width (mm)	
0.02	0.00250	0.0019	18.5185		0.02	0.00571	0.0030	30.4762	
0.025	0.00313	0.0023	23.1481		0.025	0.00714	0.0038	38.0952	
0.03	0.00375	0.0028	27.7778		0.03	0.00857	0.0046	45.7143	
0.035	0.00438	0.0032	32.4074		0.035	0.01000	0.0053	53.3333	
0.04	0.00500	0.0037	37.0370		0.04	0.01143	0.0061	60.9524	
0.045	0.00563	0.0042	41.6667		0.045	0.01286	0.0069	68.5714	
0.05	0.00625	0.0046	46.2963		0.05	0.01429	0.0076	76.1905	
0.055	0.00688	0.0051	50.9259		0.055	0.01571	0.0084	83.8095	
0.06	0.00750	0.0056	55.5556		0.06	0.01714	0.0091	91.4286	
0.065	0.00813	0.0060	60.1852		0.065	0.01857	0.0099	99.0476	
0.07	0.00875	0.0065	64.8148		0.07	0.02000	0.0107	106.6667	
0.075	0.00938	0.0069	69.4444		0.075	0.02143	0.0114	114.2857	
0.08	0.01000	0.0074	74.0741		0.08	0.02286	0.0122	121.9048	
						0.00000			
0.0216	0.00270	0.0020	20.0000		0.0216	0.00617	0.0033	32.9143	
0.024	0.00300	0.0022	22.2222		0.024	0.00686	0.0037	36.5714	
0.027	0.00338	0.0025	25.0000		0.027	0.00771	0.0041	41.1429	
0.0309	0.00386	0.0029	28.6111		0.0309	0.00883	0.0047	47.0857	
0.036	0.00450	0.0033	33.3333		0.036	0.01029	0.0055	54.8571	
0.0432	0.00540	0.0040	40.0000		0.0432	0.01234	0.0066	65.8286	
0.054	0.00675	0.0050	50.0000		0.054	0.01543	0.0082	82.2857	
0.072	0.00900	0.0067	66.6667		0.072	0.02057	0.0110	109.7143	

PURE PARAFFIN				ALUMINISED PARAFFIN			
O/F Ratio	8			O/F Ratio	3.5		
Density (kg/m ³)	900			Density (kg/m ³)	1250		
Reg Rate (m/s)	0.0015			Reg Rate (m/s)	0.002		
Length (m)	0.1			Length (m)	0.1		
WIDTH BASED ON OX MASS FLOW RATE				WIDTH BASED ON OX MASS FLOW RATE			
Ox Mass Flow Rate (kg/s)	Fuel Mass Flow Rate (kg/s)	Area (m ²)	Width (mm)	Ox Mass Flow Rate (kg/s)	Fuel Mass Flow Rate (kg/s)	Area (m ²)	Width (mm)
0.002	0.00025	0.0002	1.85	0.002	0.00057	0.0002	2
0.008	0.00100	0.0007	7.41	0.008	0.00229	0.0009	9
0.020	0.00250	0.0019	18.52	0.020	0.00571	0.0023	23
0.030	0.00375	0.0028	27.78	0.030	0.00857	0.0034	34
0.050	0.00625	0.0046	46.30	0.050	0.01429	0.0057	57
0.070	0.00875	0.0065	64.81	0.070	0.02000	0.0080	80
0.100	0.01250	0.0093	92.59	0.100	0.02857	0.0114	114
0.130	0.01625	0.0120	120.37	0.130	0.03714	0.0149	149
0.170	0.02125	0.0157	157.41	0.170	0.04857	0.0194	194
0.200	0.02500	0.0185	185.19	0.200	0.05714	0.0229	229
0.250	0.03125	0.0231	231.48	0.250	0.07143	0.0286	286
0.300	0.03750	0.0278	277.78	0.300	0.08571	0.0343	343
0.350	0.04375	0.0324	324.07	0.350	0.10000	0.0400	400
0.400	0.05000	0.0370	370.37	0.400	0.11429	0.0457	457
0.450	0.05625	0.0417	416.67	0.450	0.12857	0.0514	514
0.500	0.06250	0.0463	462.96	0.500	0.14286	0.0571	571
0.600	0.07500	0.0556	555.56	0.600	0.17143	0.0686	686
0.670	0.08375	0.0620	620.37	0.670	0.19143	0.0766	766
0.750	0.09375	0.0694	694.44	0.750	0.21429	0.0857	857
0.800	0.10000	0.0741	740.74	0.800	0.22857	0.0914	914
0.025	0.00313	0.0023	23.15	0.025	0.00714	0.0029	29
0.030	0.00375	0.0028	27.78	0.030	0.00857	0.0034	34
0.035	0.00438	0.0032	32.41	0.035	0.01000	0.0040	40
0.040	0.00500	0.0037	37.04	0.040	0.01143	0.0046	46
0.040	0.00500	0.0037	37.04	0.040	0.01143	0.0046	46
0.045	0.00563	0.0042	41.67	0.045	0.01286	0.0051	51
0.050	0.00625	0.0046	46.30	0.050	0.01429	0.0057	57
0.055	0.00688	0.0051	50.93	0.055	0.01571	0.0063	63
0.060	0.00750	0.0056	55.56	0.060	0.01714	0.0069	69
0.065	0.00813	0.0060	60.19	0.065	0.01857	0.0074	74
0.070	0.00875	0.0065	64.81	0.070	0.02000	0.0080	80
0.075	0.00938	0.0069	69.44	0.075	0.02143	0.0086	86
0.080	0.01000	0.0074	74.07	0.080	0.02286	0.0091	91
0.085	0.01063	0.0079	78.70	0.085	0.02429	0.0097	97
0.090	0.01125	0.0083	83.33	0.090	0.02571	0.0103	103

PURE PARAFFIN				ALUMINISED PARAFFIN			
O/F	8			O/F	3.5		
Fuel density (kg/m ³)	900			Fuel density (kg/m ³)	1250		
Regression Rate (m/s)	0.0015			Regression Rate (m/s)	0.002		
Length (m)	0.1			Length (m)	0.1		
Ox Density (kg/m ³)	743.9			Ox Density (kg/m ³)	743.9		
Pressure Drop (bar)	8.5			Pressure Drop (bar)	8.5		
Cd	0.8			Cd	0.8		
N	1			N	1		
Ox Mass Flow Rate (kg/s)	Fuel Mass Flow Rate (kg/s)	Fuel Surface Area (m ²)	Fuel Width (mm)	Ox Mass Flow Rate (kg/s)	Fuel Mass Flow Rate (kg/s)	Fuel Surface Area (m ²)	Fuel Width (mm)
0.022346932	0.002793367	0.00206916	20.69160413	0.022346932	0.006384838	0.002553935	25.53935138
0.027039788	0.003379974	0.002503684	25.036841	0.027039788	0.007725654	0.003090262	30.90261517
0.032179583	0.004022448	0.002979591	29.79590995	0.032179583	0.009194166	0.003677667	36.77666599
0.037766316	0.004720789	0.003496881	34.96881098	0.037766316	0.010790376	0.00431615	43.16150384
0.043799988	0.005474998	0.004055554	40.55554409	0.043799988	0.012514282	0.005005713	50.05712871
0.050280598	0.006285075	0.004655611	46.55610929	0.050280598	0.014365885	0.005746354	57.46354061
0.057208147	0.007151018	0.005297051	52.97050657	0.057208147	0.016345185	0.006538074	65.38073954
0.064582635	0.008072829	0.005979874	59.79873593	0.064582635	0.018452181	0.007380873	73.8087255
0.072404061	0.009050508	0.00670408	67.04079738	0.072404061	0.020686875	0.00827475	82.74749848
0.080672426	0.010084053	0.007469669	74.69669091	0.080672426	0.023049265	0.009219706	92.19705849
0.08938773	0.011173466	0.008276642	82.76641652	0.08938773	0.025539351	0.010215741	102.1574055
0.044693865	0.005586733	0.004138321	41.38320826	0.044693865	0.012769676	0.00510787	51.07870277
0.054079577	0.006759947	0.005007368	50.07368199	0.054079577	0.015451308	0.006180523	61.80523035
0.064359165	0.008044896	0.005959182	59.59181989	0.064359165	0.018388333	0.007353333	73.53333198
0.075532632	0.009441579	0.006993762	69.93762196	0.075532632	0.021580752	0.008632301	86.32300767
0.087599975	0.010949997	0.008111109	81.11108819	0.087599975	0.025028564	0.010011426	100.1142574
0.100561196	0.01257015	0.009311222	93.11221858	0.100561196	0.02873177	0.011492708	114.9270812
0.114416294	0.014302037	0.010594101	105.9410131	0.114416294	0.03269037	0.013076148	130.7614791
0.12916527	0.016145659	0.011959747	119.5974719	0.12916527	0.036904363	0.014761745	147.617451
0.144808122	0.018101015	0.013408159	134.0815948	0.144808122	0.041373749	0.0165495	165.494997
0.161344852	0.020168107	0.014939338	149.3933818	0.161344852	0.046098529	0.018439412	184.394117
0.17877546	0.022346932	0.016553283	165.532833	0.17877546	0.051078703	0.020431481	204.3148111

Varying the oxidiser mass flow rate to determine a length:

Table 4A.9.5: Table of constants for pure paraffin wax

Pure Paraffin	
Variable	Value
O/F ratio	8
Density	900 kg/m ³
Regression rate	1.5 mm/s
Width	20 mm

Table 4A.9.6: Table of constants for 40% aluminised paraffin wax

40% Aluminised Paraffin	
Variable	Value
O/F ratio	3.5
Density	1250 kg/m ³
Regression rate	2 mm/s
Width	20 mm

An oxidiser mass flow rate was assumed to calculate a length of the fuel grain:

$$\dot{m}_f = \frac{\dot{m}_{ox}}{O/F}$$

$$\dot{m}_f = \frac{0.02}{8}$$

$$\dot{m}_f = 0.0025 \text{ kg/s}$$

Area:

$$A_f = \frac{\dot{m}_f}{\rho_f \times \dot{r}}$$

$$A_f = \frac{0.0025}{900 \times 0.0015}$$

$$A_f = 0.0019 \text{ m}^2$$

Length:

$$l_f = \frac{A_f}{w_f}$$

$$l_f = \frac{0.0019}{0.02}$$

$$l_f = 92.59 \text{ mm}$$

PURE PARAFFIN				ALUMINISED PARAFFIN			
O/F Ratio	8			O/F Ratio	3.5		
Density (kg/m ³)	900			Density (kg/m ³)	1250		
Reg Rate (m/s)	0.0015			Reg Rate (m/s)	0.002		
Width (m)	0.02			Width (m)	0.02		
LENGTH BASED ON INJ OX MASS FLOW RATE				LENGTH BASED ON INJ OX MASS FLOW RATE			
Ox Mass Flow Rate (kg/s)	Fuel Mass Flow Rate (kg/s)	Area (m ²)	Length (mm)	Ox Mass Flow Rate (kg/s)	Fuel Mass Flow Rate (kg/s)	Area (m ²)	Length (mm)
0.02	0.00250	0.0019	92.5926	0.02	0.00571	0.0030	152.3810
0.025	0.00313	0.0023	115.7407	0.025	0.00714	0.0038	190.4762
0.03	0.00375	0.0028	138.8889	0.03	0.00857	0.0046	228.5714
0.035	0.00438	0.0032	162.0370	0.035	0.01000	0.0053	266.6667
0.04	0.00500	0.0037	185.1852	0.04	0.01143	0.0061	304.7619
0.045	0.00563	0.0042	208.3333	0.045	0.01286	0.0069	342.8571
0.05	0.00625	0.0046	231.4815	0.05	0.01429	0.0076	380.9524
0.055	0.00688	0.0051	254.6296	0.055	0.01571	0.0084	419.0476
0.06	0.00750	0.0056	277.7778	0.06	0.01714	0.0091	457.1429
0.065	0.00813	0.0060	300.9259	0.065	0.01857	0.0099	495.2381
0.07	0.00875	0.0065	324.0741	0.07	0.02000	0.0107	533.3333
0.075	0.00938	0.0069	347.2222	0.075	0.02143	0.0114	571.4286
0.08	0.01000	0.0074	370.3704	0.08	0.02286	0.0122	609.5238
0.0216	0.00270	0.0020	100.0000	0.0216	0.00617	0.0033	164.5714
0.024	0.00300	0.0022	111.1111	0.024	0.00686	0.0037	182.8571
0.027	0.00338	0.0025	125.0000	0.027	0.00771	0.0041	205.7143
0.0309	0.00386	0.0029	143.0556	0.0309	0.00883	0.0047	235.4286
0.036	0.00450	0.0033	166.6667	0.036	0.01029	0.0055	274.2857
0.0432	0.00540	0.0040	200.0000	0.0432	0.01234	0.0066	329.1429
0.054	0.00675	0.0050	250.0000	0.054	0.01543	0.0082	411.4286
0.072	0.00900	0.0067	333.3333	0.072	0.02057	0.0110	548.5714

PURE PARAFFIN				ALUMINISED PARAFFIN			
O/F	8			O/F	3.5		
Fuel density (kg/m ³)	900			Fuel density (kg/m ³)	1250		
Regression Rate (m/s)	0.0015			Regression Rate (m/s)	0.002		
Width (m)	0.02			Width (m)	0.02		
Ox Density (kg/m ³)	743.9			Ox Density (kg/m ³)	743.9		
Pressure Drop (bar)	8.5			Pressure Drop (bar)	8.5		
Cd	0.8			Cd	0.8		
N	1			N	1		
Ox Mass Flow Rate (kg/s)	Fuel Mass Flow Rate (kg/s)	Fuel Surface Area (m ²)	Fuel Length (mm)	Ox Mass Flow Rate (kg/s)	Fuel Mass Flow Rate (kg/s)	Fuel Surface Area (m ²)	Fuel Length (mm)
0.022346932	0.002793367	0.00206916	103.4580206	0.022346932	0.006384838	0.002553935	127.6967569
0.027039788	0.003379974	0.002503684	125.184205	0.027039788	0.007725654	0.003090262	154.5130759
0.032179583	0.004022448	0.002979591	148.9795497	0.032179583	0.009194166	0.003677667	183.88333
0.037766316	0.004720789	0.003496881	174.8440549	0.037766316	0.010790376	0.00431615	215.8075192
0.043799988	0.005474998	0.004055554	202.7777205	0.043799988	0.012514282	0.005005713	250.2856436
0.050280598	0.006285075	0.004655611	232.7805465	0.050280598	0.014365885	0.005746354	287.3177031
0.057208147	0.007151018	0.005297051	264.8525329	0.057208147	0.016345185	0.006538074	326.9036977
0.064582635	0.008072829	0.005979874	298.9936797	0.064582635	0.018452181	0.007380873	369.0436275
0.072404061	0.009050508	0.006704068	335.2039869	0.072404061	0.020686875	0.00827475	413.7374924
0.080672426	0.010084053	0.007496669	373.4834545	0.080672426	0.023049265	0.009219706	460.9852925
0.08938773	0.011173466	0.008276642	413.8320826	0.08938773	0.025539351	0.010215741	510.7870277
0.044693865	0.005586733	0.004138321	206.9160413	0.044693865	0.012769676	0.00510787	255.3935138
0.054079577	0.006759947	0.005007368	250.36841	0.054079577	0.015451308	0.006180523	309.0261517
0.064359165	0.008044896	0.005959182	297.9590995	0.064359165	0.018388333	0.007355333	367.7666599
0.075532632	0.009441579	0.006993762	349.6881098	0.075532632	0.021580752	0.008632301	431.6150384
0.087599975	0.010949997	0.008111109	405.5554409	0.087599975	0.025028564	0.010011426	500.5712871
0.100561196	0.01257015	0.009311222	465.5610929	0.100561196	0.02873177	0.011492708	574.6354061
0.114416294	0.014302037	0.010594101	529.7050657	0.114416294	0.03269037	0.013076148	653.8073954
0.12916527	0.016145659	0.011959747	597.9873593	0.12916527	0.036904363	0.014761745	738.087255
0.144808122	0.018101015	0.013408159	670.4079738	0.144808122	0.041373749	0.0165495	827.4749848
0.161344852	0.020168107	0.014939338	746.9669091	0.161344852	0.046098529	0.018439412	921.9705849
0.17877546	0.022346932	0.016553283	827.6641652	0.17877546	0.051078703	0.020431481	1021.574055

Varying the burn time to calculate the lengths of the fuel grain:

Table 4A.9.7: Table of constants for pure paraffin wax

Pure Paraffin	
Variable	Value
O/F ratio	8
Density	900 kg/m ³
Regression rate	1.5 mm/s
Length	100 mm
Width	20 mm
Thickness	15 mm
Volume	30000 mm ²
Burn time	10 s

Table 4A.9.8: Table of constants for 40% aluminised wax

40% Aluminised Paraffin	
Variable	Value
O/F ratio	3.5
Density	1250 kg/m ³
Regression rate	2 mm/s
Length	100 mm
Width	20 mm
Thickness	15 mm
Volume	30000 mm ²
Burn time	10 s

Calculating a length of the fuel grain using various burn times:

Mass of fuel:

$$m_f = \rho_f \times V_f$$

$$m_f = 900 \times 0.00003$$

$$m_f = 0.0375 \text{ kg}$$

Fuel mass flow rate:

$$\dot{m}_f = \frac{m_f}{b_t}$$

$$\dot{m}_f = \frac{0.0375}{10}$$

$$\dot{m}_f = 0.00375 \text{ kg/s}$$

Area:

$$A_f = \frac{\dot{m}_f}{\rho_f \times \dot{r}}$$

$$A_f = \frac{0.00375}{900 \times 0.0015}$$

$$A_f = 0.0015 \text{ m}^2$$

Length:

$$l_f = \frac{A_f}{w_f}$$

$$l_f = \frac{0.0015}{0.02}$$

$$l_f = 0.075 \text{ m}$$

ALUMINISED PARAFFIN LENGTH BASED ON ALUMINISED OX MASS FLOW RATE								
Length (m)	0.1		Density (kg/m ³)	1250				
Width (m)	0.02		O/F Ratio	3.5				
Thickness (m)	0.015		r_dot	0.002				
Volume (m ³)	0.00003							
Burn Time (s)	10	9	8	7	6	5	4	3
Fuel Mass (kg)	0.0375	0.0375	0.0375	0.0375	0.0375	0.0375	0.0375	0.0375
Fuel Mass Flow Rate (kg/s)	0.00375	0.0041667	0.0046875	0.0053571	0.00625	0.0075	0.009375	0.0125
Total Mass Flow Rate (kg/s)	0.016875	0.01875	0.02109375	0.0241071	0.028125	0.03375	0.0421875	0.05625
Ox Mass Flow Rate (kg/s)	0.013125	0.0145833	0.01640625	0.01875	0.021875	0.02625	0.0328125	0.04375
Fuel Mass Flow Rate (kg/s)	0.0038	0.0042	0.0047	0.0054	0.0063	0.0075	0.0094	0.0125
Area (m ²)	0.0015	0.0017	0.0019	0.0021	0.0025	0.0030	0.0038	0.0050
Length (m)	0.0750	0.0833	0.0938	0.1071	0.1250	0.1500	0.1875	0.2500
ALUMINISED PARAFFIN LENGTH BASED ON ORIGINAL OX MASS FLOW RATE								
Length (m)	0.1		Density (kg/m ³)	900				
Width (m)	0.02		O/F Ratio	8				
Thickness (m)	0.015		r_dot	0.0015				
Volume (m ³)	0.00003							
Burn Time (s)	10	9	8	7	6	5	4	3
Fuel Mass (kg)	0.027	0.027	0.027	0.027	0.027	0.027	0.027	0.027
Fuel Mass Flow Rate (kg/s)	0.0027	0.003	0.003375	0.0038571	0.0045	0.0054	0.00675	0.009
Total Mass Flow Rate (kg/s)	0.0243	0.027	0.030375	0.0347143	0.0405	0.0486	0.06075	0.081
Ox Mass Flow Rate (kg/s)	0.0216	0.024	0.027	0.0308571	0.036	0.0432	0.054	0.072
Fuel Mass Flow Rate (kg/s)	0.0054	0.0060	0.0068	0.0077	0.0090	0.0108	0.0135	0.0180
Area (m ²)	0.0029	0.0032	0.0036	0.0041	0.0048	0.0058	0.0072	0.0096
Length (m)	0.1440	0.1600	0.1800	0.2057	0.2400	0.2880	0.3600	0.4800

The calculations mentioned above were used in reverse for the following calculations.

Assuming different lengths to calculate the oxidiser mass flow rate:

PURE PARAFFIN													
O/F Ratio	8	Density (kg/m ³)		Reg Rate (m/s)		Burn Time (s)		0.0015		0.0015		0.0015	
Width (m)	0.02												
Thickness (m)	0.015												
Length (m)	0.0900	0.1000	0.1100	0.1200	0.1300	0.1400	0.1500	0.1600	0.1700	0.1800	0.1900	0.2000	0.2000
Volume (m ³)	0.0000	0.0000	0.0000	0.0000	0.0000	0.0000	0.0000	0.0000	0.0001	0.0001	0.0001	0.0001	0.0001
Fuel Mass (kg)	0.0243	0.0270	0.0297	0.0324	0.0351	0.0378	0.0405	0.0432	0.0459	0.0486	0.0513	0.0540	0.0540
Fuel Mass Flow Rate (kg/s)	0.0049	0.0054	0.0059	0.0065	0.0070	0.0076	0.0081	0.0086	0.0092	0.0097	0.0103	0.0108	0.0108
Ox Mass Flow Rate (kg/s)	0.0389	0.0432	0.0475	0.0518	0.0562	0.0605	0.0648	0.0691	0.0734	0.0778	0.0821	0.0864	0.0864
Length (m)	0.0900	0.1000	0.1100	0.1200	0.1300	0.1400	0.1500	0.1600	0.1700	0.1800	0.1900	0.2000	0.2000
Fuel Mass Flow Rate (kg/s)	0.00243	0.0027	0.00297	0.00324	0.00351	0.00378	0.00405	0.00432	0.00459	0.00486	0.00513	0.0054	0.0054
Ox Mass Flow Rate (kg/s)	0.01944	0.0216	0.02376	0.02592	0.02808	0.03024	0.0324	0.03456	0.03672	0.03888	0.04104	0.0432	0.0432
ALUMINISED PARAFFIN													
O/F Ratio	3.5	Density (kg/m ³)		Reg Rate (m/s)		Burn Time (s)		0.002		0.002		0.002	
Width (m)	0.02												
Thickness (m)	0.015												
Length (m)	0.090000	0.100000	0.110000	0.120000	0.130000	0.140000	0.150000	0.160000	0.170000	0.180000	0.190000	0.200000	0.200000
Volume (m ³)	0.000027	0.000030	0.000033	0.000036	0.000039	0.000042	0.000045	0.000048	0.000051	0.000054	0.000057	0.000060	0.000060
Fuel Mass (kg)	0.033750	0.037500	0.041250	0.045000	0.048750	0.052500	0.056250	0.060000	0.063750	0.067500	0.071250	0.075000	0.075000
Fuel Mass Flow Rate (kg/s)	0.006750	0.007500	0.008250	0.009000	0.009750	0.010500	0.011250	0.012000	0.012750	0.013500	0.014250	0.015000	0.015000
Ox Mass Flow Rate (kg/s)	0.023625	0.026250	0.028875	0.031500	0.034125	0.036750	0.039375	0.042000	0.044625	0.047250	0.049875	0.052500	0.052500
Length (m)	0.0900	0.1000	0.1100	0.1200	0.1300	0.1400	0.1500	0.1600	0.1700	0.1800	0.1900	0.2000	0.2000
Fuel Mass Flow Rate (kg/s)	0.0045	0.005	0.0055	0.006	0.0065	0.007	0.0075	0.008	0.0085	0.009	0.0095	0.01	0.01
Ox Mass Flow Rate (kg/s)	0.01575	0.0175	0.01925	0.021	0.02275	0.0245	0.02625	0.028	0.02975	0.0315	0.03325	0.035	0.035

Varying the widths of the fuel grain to calculate oxidiser mass flow rates:

PURE PARAFFIN														
O/F Ratio	8	Density (kg/m ³)		900	Reg Rate (m/s)		0.0015	Burn Time (s)		5				
Length (m)	0.1													
Thickness (m)	0.015													
Width (m)	0.0100	0.0125	0.0150	0.0200	0.0225	0.0250	0.0275	0.0300	0.0325	0.0350	0.0375	0.0400		
Volume (m ³)	0.0000	0.0000	0.0000	0.0000	0.0000	0.0000	0.0000	0.0000	0.0000	0.0001	0.0001	0.0001		
Fuel Mass (kg)	0.0135	0.0169	0.0203	0.0270	0.0304	0.0338	0.0371	0.0405	0.0439	0.0473	0.0506	0.0540		
Fuel Mass Flow Rate (kg/s)	0.0027	0.0034	0.0041	0.0054	0.0061	0.0068	0.0074	0.0081	0.0088	0.0095	0.0101	0.0108		
Ox Mass Flow Rate (kg/s)	0.0216	0.0270	0.0324	0.0432	0.0486	0.0540	0.0594	0.0648	0.0702	0.0756	0.0810	0.0864		
Width (m)	0.0100	0.0125	0.0150	0.0200	0.0225	0.0250	0.0275	0.0300	0.0325	0.0350	0.0375	0.0400		
Fuel Mass Flow Rate (kg/s)	0.00135	0.0016875	0.002025	0.0027	0.0030375	0.003375	0.0037125	0.00405	0.0043875	0.004725	0.0050625	0.0054		
Ox Mass Flow Rate (kg/s)	0.0108	0.0135	0.0162	0.0216	0.0243	0.027	0.0297	0.0324	0.0351	0.0378	0.0405	0.0432		
ALUMINISED PARAFFIN														
O/F Ratio	3.5	Density (kg/m ³)		1250	Reg Rate (m/s)		0.002	Burn Time (s)		5				
Width (m)	0.02													
Thickness (m)	0.015													
Width (m)	0.0100	0.0125	0.0150	0.0200	0.0225	0.0250	0.0275	0.0300	0.0325	0.0350	0.0375	0.0400		
Volume (m ³)	0.000003	0.000004	0.000005	0.000006	0.000007	0.000008	0.000008	0.000009	0.000010	0.000011	0.000011	0.000012		
Fuel Mass (kg)	0.003750	0.004688	0.005625	0.007500	0.008438	0.009375	0.010313	0.011250	0.012188	0.013125	0.014063	0.015000		
Fuel Mass Flow Rate (kg/s)	0.000750	0.000938	0.001125	0.001500	0.001688	0.001875	0.002063	0.002250	0.002438	0.002625	0.002813	0.003000		
Ox Mass Flow Rate (kg/s)	0.002625	0.003281	0.003938	0.005250	0.005906	0.006563	0.007219	0.007875	0.008531	0.009188	0.009844	0.010500		
Width (m)	0.0100	0.0125	0.0150	0.0200	0.0225	0.0250	0.0275	0.0300	0.0325	0.0350	0.0375	0.0400		
Fuel Mass Flow Rate (kg/s)	0.00005	0.0000625	0.000075	0.0001	0.0001125	0.000125	0.0001375	0.00015	0.0001625	0.000175	0.0001875	0.0002		
Ox Mass Flow Rate (kg/s)	0.00175	0.0021875	0.002625	0.0035	0.0039375	0.004375	0.0048125	0.00525	0.0056875	0.006125	0.0065625	0.007		

Varying lengths to calculate the oxidiser mass flow rates:

PURE PARAFFIN				
O/F Ratio	8		Density (kg/m ²)	900
Width (m)	0.02		Reg Rate (m/s)	0.0015
Thickness (m)	0.015			
Length (m)	Area (m ²)	Fuel Mass Flow Rate (kg/s)	Ox Mass Flow Rate (kg/s)	
0.09	0.0018	0.0024	0.0194	
0.1	0.0020	0.0027	0.0216	
0.11	0.0022	0.0030	0.0238	
0.12	0.0024	0.0032	0.0259	
0.13	0.0026	0.0035	0.0281	
0.14	0.0028	0.0038	0.0302	
0.15	0.0030	0.0041	0.0324	
0.16	0.0032	0.0043	0.0346	
0.17	0.0034	0.0046	0.0367	
0.18	0.0036	0.0049	0.0389	
0.19	0.0038	0.0051	0.0410	
0.2	0.0040	0.0054	0.0432	
ALUMINISED PARAFFIN				
O/F Ratio	3.5		Density (kg/m ²)	1250
Width (m)	0.02		Reg Rate (m/s)	0.002
Thickness (m)	0.015			
Length (m)	Area (m ²)	Fuel Mass Flow Rate (kg/s)	Ox Mass Flow Rate (kg/s)	
0.09	0.0018	0.0045	0.0158	
0.1	0.0020	0.0050	0.0175	
0.11	0.0022	0.0055	0.0193	
0.12	0.0024	0.0060	0.0210	
0.13	0.0026	0.0065	0.0228	
0.14	0.0028	0.0070	0.0245	
0.15	0.0030	0.0075	0.0263	
0.16	0.0032	0.0080	0.0280	
0.17	0.0034	0.0085	0.0298	
0.18	0.0036	0.0090	0.0315	
0.19	0.0038	0.0095	0.0333	
0.2	0.0040	0.0100	0.0350	

Varying widths to calculate the oxidiser mass flow rates:

PURE PARAFFIN				
O/F Ratio	8		Density (kg/m ²)	900
Length (m)	0.1		Reg Rate (m/s)	0.0015
Thickness (m)	0.015			
Width (m)	Area (m ²)	Fuel Mass Flow Rate (kg/s)	Ox Mass Flow Rate (kg/s)	
0.01	0.0010	0.0014	0.0108	
0.0125	0.0013	0.0017	0.0135	
0.015	0.0015	0.0020	0.0162	
0.0175	0.0018	0.0024	0.0189	
0.02	0.0020	0.0027	0.0216	
0.0225	0.0023	0.0030	0.0243	
0.025	0.0025	0.0034	0.0270	
0.0275	0.0028	0.0037	0.0297	
0.03	0.0030	0.0041	0.0324	
0.0325	0.0033	0.0044	0.0351	
0.035	0.0035	0.0047	0.0378	
0.0375	0.0038	0.0051	0.0405	
0.04	0.0040	0.0054	0.0432	
ALUMINISED PARAFFIN				
O/F Ratio	3.5		Density (kg/m ²)	1250
Width (m)	0.02		Reg Rate (m/s)	0.002
Thickness (m)	0.015			
Width (m)	Area (m ²)	Fuel Mass Flow Rate (kg/s)	Ox Mass Flow Rate (kg/s)	
0.01	0.0010	0.0025	0.0088	
0.0125	0.0013	0.0031	0.0109	
0.015	0.0015	0.0038	0.0131	
0.0175	0.0018	0.0044	0.0153	
0.02	0.0020	0.0050	0.0175	
0.0225	0.0023	0.0056	0.0197	
0.025	0.0025	0.0063	0.0219	
0.0275	0.0028	0.0069	0.0241	
0.03	0.0030	0.0075	0.0263	
0.0325	0.0033	0.0081	0.0284	
0.035	0.0035	0.0088	0.0306	
0.0375	0.0038	0.0094	0.0328	
0.04	0.0040	0.0100	0.0350	

APPENDIX 4B

Injector Calculations

Table 4B.9.1: Constants required for injector calculations

Variable	Value
Oxidiser mass flow rate	0.0432 kg/s
Oxidiser density	743.9 kg/m ³
Pressure drop	8.5 bar
Discharge coefficient	0.8

Volumetric flow rate:

$$\dot{V}_{ox} = \frac{\dot{m}_{ox}}{\rho_{ox}}$$

$$\dot{V}_{ox} = \frac{0.0432}{743.9}$$

$$\dot{V}_{ox} = 5.81 \times 10^{-5} \text{ m}^3/\text{s}$$

Area of injector:

$$A_{inj} = \frac{\dot{m}_{ox}}{C_d \times N_{inj} \times \sqrt{2\rho_{ox}\Delta P}}$$

$$A_{inj} = \frac{0.0432}{0.8 \times 1 \times \sqrt{2 \times 743.9 \times 8.5 \times 10^5}}$$

$$A_{inj} = 1.52 \times 10^{-6} \text{ m}^2$$

Diameter of injector orifice:

$$A_{inj} = \frac{\pi d_{inj}^2}{4}$$

Rearranging the formula:

$$d_{inj} = \sqrt{\frac{4 \times A_{inj}}{\pi}}$$

$$d_{inj} = \sqrt{\frac{4 \times 1.52 \times 10^{-6}}{\pi}}$$

$$d_{inj} = 1.39 \text{ mm}$$

Calculating the oxidiser mass flow rate by varying the orifice diameter.

First calculating the injector area:

$$A_{inj} = \frac{\pi d_{inj}^2}{4}$$

$$A_{inj} = \frac{\pi \times 0.001^2}{4}$$

$$A_{inj} = 7.855 \times 10^{-7} \text{ m}^2$$

Calculating the oxidiser mass flow from:

$$\dot{m}_{ox} = C_d \times N_{inj} \times A_{inj} \times \sqrt{2\rho_{ox}\Delta P}$$

$$\dot{m}_{ox} = 0.8 \times 1 \times 7.855 \times 10^{-7} \times \sqrt{2 \times 743.9 \times 8.5 \times 10^5}$$

$$\dot{m}_{ox} = 0.02235 \text{ kg/s}$$

PURE PARAFFIN				
Ox Mass Flow Rate (kg/s)	0.0432			
Ox Density (kg/m ³)	743.9			
Volume Flow Rate (m ³ /s)	5.80723E-05			
15% Pressure Drop of 56.6 bar	8.5			
Hole Diameter (mm)	2			
Discharge Coefficient	0.8			
Area of One Hole (m ²)	0.000003142			
Total Area for Ox Flow Rate (m ²)	1.51849E-06			
Total Area (m ²)	N	N using formula		
1.51849E-06	0.483287808	0.483287808		
VARY NUMBER OF HOLES				
Total Area (m ²)	N	Hole Area (m ²)	Hole Diameter (m)	Hole Diameter (mm)
1.51849E-06	1	1.51849E-06	0.001390378	1.390378089
1.51849E-06	2	7.59245E-07	0.000983146	0.983145775
1.51849E-06	3	5.06163E-07	0.000802735	0.802735164
1.51849E-06	5	3.03698E-07	0.000621796	0.621795984
1.51849E-06	7	2.16927E-07	0.000525514	0.525513522
1.51849E-06	10	1.51849E-07	0.000439676	0.439676157
1.51849E-06	12	1.26541E-07	0.000401368	0.401367582
1.51849E-06	15	1.01233E-07	0.000358994	0.358994079
1.51849E-06	20	7.59245E-08	0.000310898	0.310897992
VARY HOLE DIAMETER				
Hole Diameter (m)	Area of hole (m ²)	N		
0.0005	1.96375E-07	7.732604925		
0.001	7.855E-07	1.933151231		
0.0015	1.76738E-06	0.859178325		
0.002	0.000003142	0.483287808		
0.0025	4.90938E-06	0.309304197		
0.003	7.0695E-06	0.214794581		
0.0035	9.62238E-06	0.157808264		
0.004	0.000012568	0.120821952		
0.0045	1.59064E-05	0.095464258		
0.005	1.96375E-05	0.077326049		

VARY OX FLOW RATE FOR 1 HOLE				
Ox Mass Flow Rate (kg/s)	Total Area (m ²)	Inj Diameter (m)	Inj Diameter (mm)	
0.02	7.03005E-07	0.000946032	0.946032463	
0.025	8.78756E-07	0.001057696	1.057696449	
0.03	1.05451E-06	0.001158648	1.158648408	
0.035	1.23026E-06	0.001251483	1.251483315	
0.04	1.40601E-06	0.001337892	1.33789194	
0.045	1.58176E-06	0.001419049	1.419048695	
0.05	1.75751E-06	0.001495809	1.495808662	
0.055	1.93326E-06	0.001568817	1.56881736	
0.06	2.10901E-06	0.001638576	1.638576292	
0.065	2.28477E-06	0.001705484	1.705484278	
0.07	2.46052E-06	0.001769865	1.769864677	
0.075	2.63627E-06	0.001831984	1.831983988	
0.08	2.81202E-06	0.001892065	1.892064927	
VARY OX FLOW RATE FOR 2 HOLES				
Ox Mass Flow Rate (kg/s)	Total Area (m ²)	Inj Area (m ²)	Inj Diameter (m)	Inj Diameter (mm)
0.02	7.03005E-07	3.51502E-07	0.000668946	0.66894597
0.025	8.78756E-07	4.39378E-07	0.000747904	0.747904331
0.03	1.05451E-06	5.27254E-07	0.000819288	0.819288146
0.035	1.23026E-06	6.15129E-07	0.000884932	0.884932339
0.04	1.40601E-06	7.03005E-07	0.000946032	0.946032463
0.045	1.58176E-06	7.9088E-07	0.001003419	1.003418955
0.05	1.75751E-06	8.78756E-07	0.001057696	1.057696449
0.055	1.93326E-06	9.66632E-07	0.001109321	1.109321394
0.06	2.10901E-06	1.05451E-06	0.001158648	1.158648408
0.065	2.28477E-06	1.14238E-06	0.001205959	1.205959498
0.07	2.46052E-06	1.23026E-06	0.001251483	1.251483315
0.075	2.63627E-06	1.31813E-06	0.001295408	1.295408301
0.08	2.81202E-06	1.40601E-06	0.001337892	1.33789194
VARY OX FLOW RATE FOR 1 HOLE (FUEL DIMENSIONS RATES)				
Ox Mass Flow Rate (kg/s)	Total Area (m ²)	Inj Diameter (m)	Inj Diameter (mm)	
0.0216	7.59245E-07	0.000983146	0.983145775	
0.024	8.43606E-07	0.001036327	1.036326641	
0.027	9.49056E-07	0.00109919	1.099190393	
0.0309	1.08614E-06	0.0011759	1.175899705	
0.036	1.26541E-06	0.001269236	1.269235738	
0.0432	1.51849E-06	0.001390378	1.390378089	
0.054	1.89811E-06	0.00155449	1.554489961	
0.072	2.53082E-06	0.00179497	1.794970395	
VARY OX FLOW RATE FOR 2 HOLES (FUEL DIMENSIONS RATES)				
Ox Mass Flow Rate (kg/s)	Total Area (m ²)	Inj Area (m ²)	Inj Diameter (m)	Inj Diameter (mm)
0.0216	7.59245E-07	3.79623E-07	0.000695189	0.695189045
0.024	8.43606E-07	4.21803E-07	0.000732794	0.732793595
0.027	9.49056E-07	4.74528E-07	0.000777245	0.777244981
0.0309	1.08614E-06	5.43071E-07	0.000831487	0.831486656
0.036	1.26541E-06	6.32704E-07	0.000897485	0.897485197
0.0432	1.51849E-06	7.59245E-07	0.000983146	0.983145775
0.054	1.89811E-06	9.49056E-07	0.00109919	1.099190393
0.072	2.53082E-06	1.26541E-06	0.001269236	1.269235738

ALUMINISED PARAFFIN				
Ox Mass Flow Rate (kg/s)	0.03			
Ox Density (kg/m ³)	743.9			
Volume Flow Rate (m ³ /s)	4.0328E-05			
15% Pressure Drop of 56.6 bar	8.5			
Hole Diameter (mm)	2			
Discharge Coefficient	0.8			
Area of One Hole (m ²)	0.000003142			
Total Area for Ox Flow Rate (m ²)	1.05451E-06			
Total Area (m ²)	N using 1 area	N using formula		
1.05451E-06	0.335616533	0.335616533		
VARY NUMBER OF HOLES				
Total Area (m ²)	N	Hole Area (m ²)	Hole Diameter (m)	Hole Diameter (mm)
1.05451E-06	1	1.05451E-06	0.001158648	1.158648408
1.05451E-06	2	5.27254E-07	0.000819288	0.819288146
1.05451E-06	3	3.51502E-07	0.000668946	0.66894597
1.05451E-06	5	2.10901E-07	0.000518163	0.51816332
1.05451E-06	7	1.50644E-07	0.000437928	0.437927935
1.05451E-06	10	1.05451E-07	0.000366397	0.366396798
1.05451E-06	12	8.78756E-08	0.000334473	0.334472985
1.05451E-06	15	7.03005E-08	0.000299162	0.299161732
1.05451E-06	20	5.27254E-08	0.000259082	0.25908166
VARY HOLE DIAMETER				
Hole Diameter (m)	Area of hole (m ²)	N		
0.0005	1.96375E-07	5.369864531		
0.001	7.855E-07	1.342466133		
0.0015	1.76738E-06	0.596651615		
0.002	0.000003142	0.335616533		
0.0025	4.90938E-06	0.214794581		
0.003	7.0695E-06	0.149162904		
0.0035	9.62238E-06	0.109589072		
0.004	0.000012568	0.083904133		
0.0045	1.59064E-05	0.066294624		
0.005	1.96375E-05	0.053698645		

VARY OX FLOW RATE FOR 1 HOLE				
Ox Mass Flow Rate (kg/s)	Total Area (m ²)	Inj Diameter (m)	Inj Diameter (mm)	
0.02	7.03005E-07	0.000946032	0.946032463	
0.025	8.78756E-07	0.001057696	1.057696449	
0.03	1.05451E-06	0.001158648	1.158648408	
0.035	1.23026E-06	0.001251483	1.251483315	
0.04	1.40601E-06	0.001337892	1.33789194	
0.045	1.58176E-06	0.001419049	1.419048695	
0.05	1.75751E-06	0.001495809	1.495808662	
0.055	1.93326E-06	0.001568817	1.56881736	
0.06	2.10901E-06	0.001638576	1.638576292	
0.065	2.28477E-06	0.001705484	1.705484278	
0.07	2.46052E-06	0.001769865	1.769864677	
0.075	2.63627E-06	0.001831984	1.831983988	
0.08	2.81202E-06	0.001892065	1.892064927	
VARY OX FLOW RATE FOR 2 HOLES				
Ox Mass Flow Rate (kg/s)	Total Area (m ²)	Inj Area (m ²)	Inj Diameter (m)	Inj Diameter (mm)
0.02	7.03005E-07	3.51502E-07	0.000668946	0.66894597
0.025	8.78756E-07	4.39378E-07	0.000747904	0.747904331
0.03	1.05451E-06	5.27254E-07	0.000819288	0.819288146
0.035	1.23026E-06	6.15129E-07	0.000884932	0.884932339
0.04	1.40601E-06	7.03005E-07	0.000946032	0.946032463
0.045	1.58176E-06	7.9088E-07	0.001003419	1.003418955
0.05	1.75751E-06	8.78756E-07	0.001057696	1.057696449
0.055	1.93326E-06	9.66632E-07	0.001109321	1.109321394
0.06	2.10901E-06	1.05451E-06	0.001158648	1.158648408
0.065	2.28477E-06	1.14238E-06	0.001205959	1.205959498
0.07	2.46052E-06	1.23026E-06	0.001251483	1.251483315
0.075	2.63627E-06	1.31813E-06	0.001295408	1.295408301
0.08	2.81202E-06	1.40601E-06	0.001337892	1.33789194
VARY OX FLOW RATE FOR 1 HOLE (FUEL DIMENSIONS RATES)				
Ox Mass Flow Rate (kg/s)	Total Area (m ²)	Inj Diameter (m)	Inj Diameter (mm)	
0.015	5.27254E-07	0.000819288	0.819288146	
0.0167	5.87009E-07	0.000864469	0.864468708	
0.01875	6.59067E-07	0.000915992	0.915991994	
0.02143	7.5327E-07	0.000979269	0.979269272	
0.025	8.78756E-07	0.001057696	1.057696449	
0.03	1.05451E-06	0.001158648	1.158648408	
0.0375	1.31813E-06	0.001295408	1.295408301	
0.05	1.75751E-06	0.001495809	1.495808662	
VARY OX FLOW RATE FOR 2 HOLES (FUEL DIMENSIONS RATES)				
Ox Mass Flow Rate (kg/s)	Total Area (m ²)	Inj Area (m ²)	Inj Diameter (m)	Inj Diameter (mm)
0.015	5.27254E-07	2.63627E-07	0.000579324	0.579324204
0.0167	5.87009E-07	2.93504E-07	0.000611272	0.611271686
0.01875	6.59067E-07	3.29533E-07	0.000647704	0.64770415
0.02143	7.5327E-07	3.76635E-07	0.000692448	0.692447943
0.025	8.78756E-07	4.39378E-07	0.000747904	0.747904331
0.03	1.05451E-06	5.27254E-07	0.000819288	0.819288146
0.0375	1.31813E-06	6.59067E-07	0.000915992	0.915991994
0.05	1.75751E-06	8.78756E-07	0.001057696	1.057696449

Varying the oxidiser mass flow rate to find a suitable injector diameter:

PURE PARAFFIN				ALUMINISED PARAFFIN			
Ox Density (kg/m ³)	743.9			Ox Density (kg/m ³)	743.9		
Pressure Drop (bar)	8.5			Pressure Drop (bar)	8.5		
Cd	0.8			Cd	0.8		
N	1			N	1		
Ox Mass Flow Rate (kg/s)	Total Inj Area (m ²)	Inj Diam (m)	Inj Diam (mm)	Ox Mass Flow Rate (kg/s)	Total Inj Area (m ²)	Inj Diam (m)	Inj Diam (mm)
0.026555909	9.33447E-07	0.001090113	1.090113275	0.021515204	7.56265E-07	0.000981214	0.981214093
0.02942483	1.03429E-06	0.001147488	1.147487658	0.023839561	8.37966E-07	0.001032857	1.032856939
0.032440875	1.1403E-06	0.001204862	1.204862041	0.026283116	9.23858E-07	0.0010845	1.084499786
0.035604044	1.25149E-06	0.001262236	1.262236423	0.028845869	1.01394E-06	0.001136143	1.136142633
0.038914338	1.36785E-06	0.001319611	1.319610806	0.03152782	1.10821E-06	0.001187785	1.18778548
0.042371755	1.48938E-06	0.001376985	1.376985189	0.034328968	1.20667E-06	0.001239428	1.239428327
0.045976297	1.61608E-06	0.00143436	1.434359572	0.037249315	1.30932E-06	0.001291071	1.291071174
0.049727963	1.74795E-06	0.001491734	1.491733955	0.040288859	1.41616E-06	0.001342714	1.342714021
0.053626753	1.88499E-06	0.001549108	1.549108338	0.043447601	1.52719E-06	0.001394357	1.394356868
0.057672667	2.02721E-06	0.001606483	1.606482721	0.04672554	1.64241E-06	0.001446	1.445999715
0.061865705	2.17459E-06	0.001663857	1.663857104	0.050122678	1.76182E-06	0.001497643	1.497642562
0.066205868	2.32715E-06	0.001721231	1.721231487	0.053639013	1.88542E-06	0.001549285	1.549285409
0.070693154	2.48488E-06	0.001778606	1.778605869	0.057274546	2.01321E-06	0.001600928	1.600928256
Ox Density (kg/m ³)	743.9			Ox Density (kg/m ³)	743.9		
Pressure Drop (bar)	8.5			Pressure Drop (bar)	8.5		
Cd	0.8			Cd	0.8		
N	2			N	2		
Ox Mass Flow Rate (kg/s)	Total Inj Area (m ²)	Inj Diam (m)	Inj Diam (mm)	Ox Mass Flow Rate (kg/s)	Total Inj Area (m ²)	Inj Diam (m)	Inj Diam (mm)
0.026555909	4.66723E-07	0.000770826	0.770826489	0.021515204	3.78132E-07	0.000693823	0.693823139
0.02942483	5.17145E-07	0.000811396	0.811396304	0.023839561	4.18983E-07	0.00073034	0.730340146
0.032440875	5.70152E-07	0.000851966	0.851966119	0.026283116	4.61929E-07	0.000766857	0.766857153
0.035604044	6.25745E-07	0.000892536	0.892535935	0.028845869	5.0697E-07	0.000803374	0.803374161
0.038914338	6.83924E-07	0.000933106	0.93310575	0.03152782	5.54105E-07	0.000839891	0.839891168
0.042371755	7.44689E-07	0.000973676	0.973675565	0.034328968	6.03336E-07	0.000876408	0.876408175
0.045976297	8.08039E-07	0.001014245	1.01424538	0.037249315	6.54661E-07	0.000912925	0.912925182
0.049727963	8.73975E-07	0.001054815	1.054815195	0.040288859	7.08081E-07	0.000949442	0.94944219
0.053626753	9.42497E-07	0.001095385	1.095385011	0.043447601	7.63597E-07	0.000985959	0.985959197
0.057672667	1.0136E-06	0.001135955	1.135954826	0.04672554	8.21207E-07	0.001022476	1.022476204
0.061865705	1.0873E-06	0.001176525	1.176524641	0.050122678	8.80912E-07	0.001058993	1.058993212
0.066205868	1.16358E-06	0.001217094	1.217094456	0.053639013	9.42712E-07	0.00109551	1.095510219
0.070693154	1.24244E-06	0.001257664	1.257664271	0.057274546	1.00661E-06	0.001132027	1.132027226

Varying the diameter to identify an oxidiser mass flow rate:

PURE AND ALUMINISED PARAFFIN			
Ox Density (kg/m ³)	743.9		
Pressure Drop (bar)	8.5		
Cd	0.8		
N	1		
Inj Diam (mm)	Inj Diam (m)	Total Inj Area (m ²)	Ox Mass Flow Rate (kg/s)
1	0.001	7.855E-07	0.022346932
1.1	0.0011	9.50455E-07	0.027039788
1.2	0.0012	1.13112E-06	0.032179583
1.3	0.0013	1.3275E-06	0.037766316
1.4	0.0014	1.53958E-06	0.043799988
1.5	0.0015	1.76738E-06	0.050280598
1.6	0.0016	2.01088E-06	0.057208147
1.7	0.0017	2.2701E-06	0.064582635
1.8	0.0018	2.54502E-06	0.072404061
1.9	0.0019	2.83566E-06	0.080672426
2	0.002	0.000003142	0.08938773
Ox Density (kg/m ³)	743.9		
Pressure Drop (bar)	8.5		
Cd	0.8		
N	2		
Inj Diam (mm)	Inj Diam (m)	Total Inj Area (m ²)	Ox Mass Flow Rate (kg/s)
1	0.001	7.855E-07	0.044693865
1.1	0.0011	9.50455E-07	0.054079577
1.2	0.0012	1.13112E-06	0.064359165
1.3	0.0013	1.3275E-06	0.075532632
1.4	0.0014	1.53958E-06	0.087599975
1.5	0.0015	1.76738E-06	0.100561196
1.6	0.0016	2.01088E-06	0.114416294
1.7	0.0017	2.2701E-06	0.12916527
1.8	0.0018	2.54502E-06	0.144808122
1.9	0.0019	2.83566E-06	0.161344852
2	0.002	0.000003142	0.17877546

Assuming oxidiser mass flow rates to determine the lengths and widths of the fuel grain:

Sample calculations for this section can be found in Appendix 4A.

PURE PARAFFIN				ALUMINISED PARAFFIN			
O/F	8			O/F	3.5		
Fuel density (kg/m ³)	900			Fuel density (kg/m ³)	1250		
Regression Rate (mm/s)	0.0015			Regression Rate (mm/s)	0.002		
Length (m)	0.1			Length (m)	0.1		
Ox Density (kg/m ³)	743.9			Ox Density (kg/m ³)	743.9		
Pressure Drop (bar)	8.5			Pressure Drop (bar)	8.5		
Cd	0.8			Cd	0.8		
N	1			N	1		
Ox Mass Flow Rate (kg/s)	Fuel Mass Flow Rate (kg/s)	Fuel Surface Area (m ²)	Fuel Width (mm)	Ox Mass Flow Rate (kg/s)	Fuel Mass Flow Rate (kg/s)	Fuel Surface Area (m ²)	Fuel Width (mm)
0.022346932	0.002793367	0.00206916	20.69160413	0.022346932	0.006384838	0.00253935	25.53935138
0.023079788	0.003379974	0.002053684	25.036841	0.027039788	0.007726564	0.003090262	30.90261517
0.032179583	0.004022448	0.002979591	29.79590955	0.032179583	0.009194166	0.003677667	37.76666599
0.037766316	0.004720789	0.003496881	34.96881098	0.037766316	0.010790376	0.00431615	43.16150384
0.043799988	0.005474998	0.004055554	40.55554409	0.043799988	0.012514282	0.005005713	50.05712871
0.050280598	0.006285075	0.004655611	46.55610929	0.050280598	0.014365885	0.005746354	57.46354061
0.057208147	0.007151018	0.005297051	52.97050657	0.057208147	0.016345185	0.006538074	65.38073954
0.064582635	0.008072829	0.005979874	59.79873593	0.064582635	0.018452181	0.007380873	73.8087255
0.072404061	0.009050508	0.00670408	67.04079938	0.072404061	0.020686875	0.00827475	82.7449848
0.080672426	0.01084053	0.007469669	74.69669601	0.080672426	0.023049265	0.009219706	92.19705849
0.08938773	0.011173466	0.008276642	82.76641652	0.08938773	0.025539351	0.010215741	102.1574055
0.044693865	0.005586733	0.004138321	41.38320826	0.044693865	0.012769676	0.00510787	51.07870277
0.054079577	0.006759947	0.005007368	50.07368199	0.054079577	0.015451308	0.006180523	61.80523035
0.064359165	0.008044896	0.005959182	59.59181989	0.064359165	0.018388333	0.007355333	73.55333198
0.075532632	0.009441579	0.006993762	69.93762196	0.075532632	0.021580752	0.008632301	86.32300767
0.087599975	0.010949997	0.008111109	81.11108819	0.087599975	0.025028564	0.010011426	100.1142574
0.100561196	0.01257015	0.009311222	93.11221858	0.100561196	0.02873177	0.011492708	114.9270812
0.114416294	0.014302037	0.010594101	105.9410131	0.114416294	0.03269037	0.013076148	130.7614791
0.12916527	0.016145659	0.011959747	119.5974719	0.12916527	0.036904363	0.014761745	147.617451
0.144808122	0.018101015	0.013408159	134.0815948	0.144808122	0.041373749	0.0165495	165.494997
0.161344852	0.020168107	0.014939338	149.3933818	0.161344852	0.046098529	0.018439412	184.394117
0.17877546	0.022346932	0.016553283	165.5328333	0.17877546	0.051078703	0.020431481	204.3148111

PURE PARAFFIN				ALUMINISED PARAFFIN			
O/F	8			O/F	3.5		
Fuel density (kg/m³)	900			Fuel density (kg/m³)	1250		
Regression Rate (m/s)	0.0015			Regression Rate (m/s)	0.002		
Width (m)	0.02			Width (m)	0.02		
Ox Density (kg/m³)	743.9			Ox Density (kg/m³)	743.9		
Pressure Drop (bar)	8.5			Pressure Drop (bar)	8.5		
Cd	0.8			Cd	0.8		
N	1			N	1		
Ox Mass Flow Rate (kg/s)	Fuel Mass Flow Rate (kg/s)	Fuel Surface Area (m²2)	Fuel Length (mm)	Ox Mass Flow Rate (kg/s)	Fuel Mass Flow Rate (kg/s)	Fuel Surface Area (m²2)	Fuel Length (mm)
0.022346932	0.002793367	0.00206916	103.4580206	0.022346932	0.006384838	0.002553935	127.6967569
0.027039788	0.003379974	0.002503684	125.184205	0.027039788	0.007725654	0.003090262	154.5130759
0.032179583	0.004022448	0.002979591	148.9795497	0.032179583	0.009194166	0.003677667	183.88333
0.037766316	0.004720789	0.003496881	174.8440549	0.037766316	0.010790376	0.00431615	215.8075192
0.043799988	0.005474998	0.004055554	202.7777205	0.043799988	0.012514282	0.005005713	250.2856436
0.050280598	0.006285075	0.004655611	232.7805465	0.050280598	0.014365885	0.005746354	287.3177031
0.057208147	0.007151018	0.005297051	264.8525329	0.057208147	0.016345185	0.006538074	326.9036977
0.064582635	0.008072829	0.005979874	298.9936797	0.064582635	0.018452181	0.007380873	369.0436275
0.072404061	0.009050508	0.00670408	335.2039869	0.072404061	0.020686875	0.00827475	413.7374924
0.080672426	0.010084053	0.007469669	373.4834545	0.080672426	0.023049265	0.009219706	460.9852925
0.08938773	0.011173466	0.008276642	413.8320826	0.08938773	0.025539351	0.010215741	510.7870277
0.044693865	0.005586733	0.004138321	206.9160413	0.044693865	0.012769676	0.00510787	255.3935138
0.054079577	0.006759947	0.005007368	250.36841	0.054079577	0.015451308	0.006180523	309.0261517
0.064359165	0.008044896	0.005959182	297.9590995	0.064359165	0.018388333	0.007355333	367.7666599
0.075532632	0.009441579	0.0066993762	349.6881098	0.075532632	0.021580752	0.008632301	431.6150384
0.087599975	0.010949997	0.008111109	405.5554409	0.087599975	0.025028564	0.010014126	500.5712871
0.100561196	0.01257015	0.009311222	465.5610929	0.100561196	0.02873177	0.011492708	574.6354061
0.114416294	0.014302037	0.010594101	529.7050657	0.114416294	0.03269037	0.013076148	653.8073954
0.12916527	0.016145659	0.011959747	597.9873593	0.12916527	0.036904363	0.014761745	738.087255
0.144808122	0.018101015	0.013408159	670.4079738	0.144808122	0.041373749	0.0165495	827.4749848
0.161344852	0.020168107	0.014939338	746.9669091	0.161344852	0.046098529	0.018439412	921.9705849
0.178775246	0.022346932	0.016553283	827.6641652	0.178775246	0.051078703	0.020431481	1021.574055

Calculating the number of injector holes:

$$\dot{m}_{ox} = C_d \times N_{inj} \times A_{inj} \times \sqrt{2\rho_{ox}\Delta P}$$

Rearranging the equation:

$$N_{inj} = \frac{\dot{m}_{ox}}{C_d \times A_{inj} \times \sqrt{2\rho_{ox}\Delta P}}$$

$$N_{inj} = \frac{0.02656}{0.8 \times 3.142 \times 10^{-6} \times \sqrt{2 \times 743.9 \times 8.5 \times 10^5}}$$

$$N_{inj} = 0.297$$

PURE PARAFFIN				ALUMINISED PARAFFIN	
Ox Density (kg/m ³)	743.9			Ox Density (kg/m ³)	743.9
Pressure Drop (bar)	8.5			Pressure Drop (bar)	8.5
Cd	0.8			Cd	0.8
D (m)	0.002			D (m)	0.002
Area (m ²)	0.000003142			Area (m ²)	0.000003142
Ox Mass Flow Rate (kg/s)	N			Ox Mass Flow Rate (kg/s)	N
0.026555909	0.297086738			0.021515204	0.240695274
0.02942483	0.329181981			0.023839561	0.266698364
0.032440875	0.362923134			0.026283116	0.294034947
0.035604044	0.398310197			0.028845869	0.322705021
0.038914338	0.43534317			0.03152782	0.352708587
0.042371755	0.474022053			0.034328968	0.384045645
0.045976297	0.514346846			0.037249315	0.416716194
0.049727963	0.556317548			0.040288859	0.450720236
0.053626753	0.599934161			0.043447601	0.486057769
0.057672667	0.645196683			0.04672554	0.522728794
0.061865705	0.692105115			0.050122678	0.560733311
0.066205868	0.740659458			0.053639013	0.60007132
0.070693154	0.79085971			0.057274546	0.64074282

Injector calculations based on different discharge coefficients:

At atmospheric pressure:

CONSTANT VARIABLES		Current injector			
Number of injector holes, N	1				
Oxidiser density, rho(ox) (kg/m ³)	743.9	Coefficient of discharge, Cd	0.8	0.65	0.66
Pressure drop (bar) with supercharging	62.5	Injector diameter (m)	0.0015	0.0015	0.0015
Feed system pressure drop (bar)	2.7	Injector area (m ²)	1.77E-06	1.77E-06	1.77E-06
		Ox mass flow rate (kg/s)	0.136342	0.110778	0.112482
		Coefficient of discharge, Cd	0.8	0.65	0.66
		Injector diameter (m)	0.0013	0.0013	0.0013
		Injector area (m ²)	1.33E-06	1.33E-06	1.33E-06
		Ox mass flow rate (kg/s)	0.102408	0.083207	0.084487

New injector			
Coefficient of discharge, Cd	0.8	0.65	0.66
Ox mass flow rate (kg/s)	0.05	0.05	0.05
Injector area (m ²)	6.48138E-07	7.98E-07	7.86E-07
Injector diameter (m)	0.000908366	0.001008	0.001
Injector diameter (mm)	0.908365792	1.007741	1.000078

For the 5 bar nozzle:

CONSTANT VARIABLES		Current injectors			
Number of injector holes, N	1				
Oxidiser density, rho(ox) (kg/m ³)	743.9	Coefficient of discharge, Cd	0.8	0.65	0.66
Pressure drop (bar) with supercharging	57.3	Injector diameter (m)	0.0015	0.0015	0.0015
Feed system pressure drop (bar)	2.7	Injector area (m ²)	1.77E-06	1.77E-06	1.77E-06
		Ox mass flow rate (kg/s)	0.130547	0.10607	0.107702
		Coefficient of discharge, Cd	0.8	0.65	0.66
		Injector diameter (m)	0.0013	0.0013	0.0013
		Injector area (m ²)	1.33E-06	1.33E-06	1.33E-06
		Ox mass flow rate (kg/s)	0.098056	0.07967	0.080896

New injector			
Coefficient of discharge, Cd	0.8	0.65	0.66
Ox mass flow rate (kg/s)	0.05	0.05	0.05
Injector area (m ²)	6.76909E-07	8.33E-07	8.2E-07
Injector diameter (m)	0.000928308	0.00103	0.001022
Injector diameter (mm)	0.928308057	1.029865	1.022034

For the 10 bar nozzle:

CONSTANT VARIABLES		Current injectors			
Number of injector holes, N	1				
Oxidiser density, rho(ox) (kg/m ³)	743.9	Coefficient of discharge, Cd	0.8	0.65	0.66
Pressure drop (bar) with supercharging	52.3	Injector diameter (m)	0.0015	0.0015	0.0015
Feed system pressure drop (bar)	2.7	Injector area (m ²)	1.77E-06	1.77E-06	1.77E-06
		Ox mass flow rate (kg/s)	0.124722	0.101336	0.102895
		Coefficient of discharge, Cd	0.8	0.65	0.66
		Injector diameter (m)	0.0013	0.0013	0.0013
		Injector area (m ²)	1.33E-06	1.33E-06	1.33E-06
		Ox mass flow rate (kg/s)	0.09368	0.076115	0.077286

New injector				
Coefficient of discharge, Cd	0.8	0.65	0.66	
Ox mass flow rate (kg/s)	0.05	0.05	0.05	
Injector area (m ²)	7.08528E-07	8.72E-07	8.59E-07	
Injector diameter (m)	0.000949741	0.001054	0.001046	
Injector diameter (mm)	0.949741364	1.053643	1.045631	

Final injector calculations:

PURE PARAFFIN										
O/F	8									
Fuel density (kg/m ³)	930									
Regression Rate (m/s)	0.0015									
Ox Density (kg/m ³)	743.9									
Pressure Drop (bar)	8.5									
Cd	0.8									
N	1									
Width (m)	Length (m)	Aspect Ratio	Fuel Surface Area (m ²)	Fuel Mass Flow Rate (kg/s)	Ox Mass Flow Rate (kg/s)	Inj Area (m ²)	Inj Area (m ²)	Inj Diam (m)	Inj Diam (mm)	
0.02	0.1	10	0.002	0.00279	0.02232	7.84553E-07	7.84553E-07	0.000999397	0.99939722	
0.02	0.15	15	0.003	0.004185	0.03348	1.17683E-06	1.17683E-06	0.001224007	1.224006619	
0.025	0.125	10	0.003125	0.004359375	0.034875	1.22586E-06	1.22586E-06	0.001249247	1.249246525	
0.03	0.15	10	0.0045	0.0062775	0.05022	1.76524E-06	1.76524E-06	0.001499096	1.49909583	
0.035	0.175	10	0.006125	0.008544375	0.068355	2.40269E-06	2.40269E-06	0.001748945	1.748945135	
Inj Diam (mm)	Inj Diam (m)	Inj Area (m ²)	Ox Mass Flow Rate (kg/s)	Fuel Mass Flow Rate (kg/s)	Fuel Surface Area (m ²)	Length (m)	Width (m)	Aspect Ratio		
1	0.001	7.855E-07	0.022346932	0.002793367	0.002002413	0.100120665	0.02	10.01206651		
1.2	0.0012	1.13112E-06	0.032179583	0.004022448	0.002883475	0.115339006	0.025	9.2271205		
1.2	0.0012	1.13112E-06	0.032179583	0.004022448	0.002883475	0.144173758	0.02	14.41737578		
1.5	0.0015	1.76738E-06	0.050280598	0.006285075	0.00450543	0.150180998	0.03	10.01206651		
1.7	0.0017	2.2701E-06	0.064582635	0.008072829	0.005786974	0.165342127	0.035	9.448121543		
PURE PARAFFIN										
O/F	7									
Fuel density (kg/m ³)	930									
Regression Rate (m/s)	0.0015									
Ox Density (kg/m ³)	743.9									
Pressure Drop (bar)	8.5									
Cd	0.8									
N	1									
Width (m)	Length (m)	Fuel Surface Area (m ²)	Fuel Mass Flow Rate (kg/s)	Ox Mass Flow Rate (kg/s)	Inj Area (m ²)	Inj Area (m ²)	Inj Diam (m)	Inj Diam (mm)		
0.02	0.1	0.002	0.00279	0.01953	6.86484E-07	6.86484E-07	0.00093485	0.934850497		
0.025	0.125	0.003125	0.004359375	0.030515625	1.07263E-06	1.07263E-06	0.001168563	1.168563122		
0.03	0.15	0.0045	0.0062775	0.0439425	1.54459E-06	1.54459E-06	0.001402276	1.402275746		
0.035	0.175	0.006125	0.008544375	0.059810625	2.10236E-06	2.10236E-06	0.001635988	1.63598837		
Inj Diam (mm)	Inj Diam (m)	Inj Area (m ²)	Ox Mass Flow Rate (kg/s)	Fuel Mass Flow Rate (kg/s)	Fuel Surface Area (m ²)	Length (m)	Width (m)			
1	0.001	7.855E-07	0.022346932	0.002793367	0.002002413	0.100120665	0.02	10.01206651		
1.2	0.0012	1.13112E-06	0.032179583	0.004022448	0.002883475	0.115339006	0.025	9.2271205		
1.2	0.0012	1.13112E-06	0.032179583	0.004022448	0.002883475	0.144173758	0.02	14.41737578		
1.5	0.0015	1.76738E-06	0.050280598	0.006285075	0.00450543	0.150180998	0.03	10.01206651		
1.7	0.0017	2.2701E-06	0.064582635	0.008072829	0.005786974	0.165342127	0.035	9.448121543		

ALUMINISED PARAFFIN											
O/F		3.5									
Fuel density (kg/m ³)		1250									
Regression Rate (m/s)		0.002									
Ox Density (kg/m ³)		743.9									
Pressure Drop (bar)		8.5									
Cd		0.8									
N		1									
Width (m)	Length (m)	Aspect Ratio	Fuel Surface Area (m ²)	Fuel Mass Flow Rate (kg/s)	Ox Mass Flow Rate (kg/s)	Inj Area (m ²)	Inj Diam (mm)	Inj Area (m ²)	Inj Diam (m)	Inj Diam (mm)	
0.02	0.1	10	0.002	0.005	0.0175	0.00084932	0.884932339	6.15129E-07	0.00084932	0.884932339	
0.02	0.15	15	0.003	0.0075	0.02625	0.001083816	1.083816343	9.22694E-07	0.001083816	1.083816343	
0.025	0.125	10	0.003125	0.0078125	0.02734375	0.001106165	1.106165423	9.61139E-07	0.001106165	1.106165423	
0.03	0.15	10	0.0045	0.01125	0.039375	0.001327399	1.327398508	1.38404E-06	0.001327399	1.327398508	
0.035	0.175	10	0.006125	0.0153125	0.05359375	0.001548632	1.548631593	1.88383E-06	0.001548632	1.548631593	
Inj Diam (mm)	Inj Diam (m)	Inj Area (m ²)	Ox Mass Flow Rate (kg/s)	Fuel Mass Flow Rate (kg/s)	Fuel Surface Area (m ²)	Fuel Surface Area (m ²)	Length (m)	Width (m)	Aspect Ratio		
1	0.001	7.855E-07	0.022346932	0.006384838	0.002553935	0.127696757	0.02	12.76967569			
1.2	0.0012	1.13112E-06	0.032179583	0.009194166	0.003677667	0.18388333	0.02	18.388333			
1.2	0.0012	1.13112E-06	0.032179583	0.009194166	0.003677667	0.147106664	0.025	11.76853312			
1.25	0.00125	1.22734E-06	0.034917082	0.009976309	0.003990524	0.159620946	0.03	10.64139641			
1.3	0.0013	1.3275E-06	0.037766316	0.010790376	0.00431615	0.143871679	0.03	9.591445297			
1.35	0.00135	1.43157E-06	0.040727284	0.011636367	0.004654547	0.15515156	0.03	10.34343731			
1.4	0.0014	1.53958E-06	0.043799988	0.012514282	0.005005713	0.166857096	0.03	11.12380638			
1.5	0.0015	1.76738E-06	0.050280598	0.014365885	0.005746354	0.191545135	0.03	12.76967569			
1.7	0.0017	2.2701E-06	0.064582635	0.018452181	0.007380873	0.210882073	0.035	12.05040416			
ALUMINISED PARAFFIN											
O/F		4									
Fuel density (kg/m ³)		1250									
Regression Rate (m/s)		0.002									
Ox Density (kg/m ³)		743.9									
Pressure Drop (bar)		8.5									
Cd		0.8									
N		1									
Width (m)	Length (m)	Fuel Surface Area (m ²)	Fuel Mass Flow Rate (kg/s)	Ox Mass Flow Rate (kg/s)	Inj Area (m ²)	Inj Diam (mm)	Inj Area (m ²)	Inj Diam (m)	Inj Diam (mm)		
0.02	0.1	0.002	0.005	0.02	0.000946032	0.946032463	7.03005E-07	0.000946032	0.946032463		
0.025	0.125	0.003125	0.0078125	0.03125	1.09844E-06	1.18254079	1.09844E-06	0.001182541	1.18254079		
0.03	0.15	0.0045	0.01125	0.045	1.58176E-06	1.419048695	1.58176E-06	0.001419049	1.419048695		
0.035	0.175	0.006125	0.0153125	0.06125	2.15295E-06	1.655556811	2.15295E-06	0.001655557	1.655556811		
Inj Diam (mm)	Inj Diam (m)	Inj Area (m ²)	Ox Mass Flow Rate (kg/s)	Fuel Mass Flow Rate (kg/s)	Fuel Surface Area (m ²)	Fuel Surface Area (m ²)	Length (m)	Width (m)			
1	0.001	7.855E-07	0.022346932	0.005586733	0.002234693	0.111734662	0.02				
1.2	0.0012	1.13112E-06	0.032179583	0.008044896	0.003217958	0.128718331	0.025				
1.5	0.0015	1.76738E-06	0.050280598	0.01257015	0.00502806	0.167601993	0.03				
1.7	0.0017	2.2701E-06	0.064582635	0.016145659	0.006458263	0.184521814	0.035				

For the coefficient of discharge for short tube with conical entrance, these were the calculated oxidiser mass flow rates:

CONSTANT VARIABLES			
Number of injector holes, N	1		
Oxidiser density, rho(ox) (kg/m ³)	743.9		
Pressure drop (bar) with supercharging	62.3		
Feed system pressure drop (bar)	2.7		
ATMOSPHERIC PRESSURE			
Current injectors			
Coefficient of discharge, Cd	0.82	0.788	0.767
Injector diameter (m)	0.001	0.0013	0.0015
Injector area (m ²)	7.855E-07	1.3275E-06	1.76738E-06
Ox mass flow rate (kg/s)	0.062012086	0.100710653	0.130508973

CONSTANT VARIABLES			
Number of injector holes, N	1		
Oxidiser density, rho(ox) (kg/m ³)	743.9		
Pressure drop (bar) with supercharging	57.3		
Feed system pressure drop (bar)	2.7		
5 BAR PRESSURE			
Current injectors			
Coefficient of discharge, Cd	0.82	0.788	0.767
Injector diameter (m)	0.001	0.0013	0.0015
Injector area (m ²)	7.855E-07	1.3275E-06	1.76738E-06
Ox mass flow rate (kg/s)	0.059471601	0.096584781	0.125162336

CONSTANT VARIABLES			
Number of injector holes, N	1		
Oxidiser density, rho(ox) (kg/m ³)	743.9		
Pressure drop (bar) with supercharging	52.3		
Feed system pressure drop (bar)	2.7		
10 BAR PRESSURE			
Current injectors			
Coefficient of discharge, Cd	0.82	0.788	0.767
Injector diameter (m)	0.001	0.0013	0.0015
Injector area (m ²)	7.855E-07	1.3275E-06	1.76738E-06
Ox mass flow rate (kg/s)	0.056817636	0.092274613	0.119576873

APPENDIX 4C

Pressure Loss Calculations

Pressure loss calculations:

Table 4C.9.1: Constants for pressure loss calculations

Variable	Value
Dynamic viscosity, μ	0.000052 Ns/m ²
Oxidiser density	743.9 kg/m ³
Coefficient of discharge	0.8
Oxidiser mass flow rate	0.05 kg/s
Acceleration due to gravity	9.81 m/s ²
Roughness coefficient	0.0000015
k for entrance	0.5
k for exit	1

Area of injector orifice:

$$A_{inj} = \frac{\pi d_{inj}^2}{4}$$

$$A_{inj} = \frac{\pi \times 0.015^2}{4}$$

$$A_{inj} = 1.76738 \times 10^{-6}$$

Velocity of the injector flow:

$$v_{inj} = C_d \times \sqrt{\frac{2\Delta P}{\rho_{ox}}}$$

$$v_{inj} = 0.8 \times \sqrt{\frac{2 \times 8.5 \times 10^5}{743.9}}$$

$$v_{inj} = 38.03 \text{ m/s}$$

Reynold's number:

$$Re = \frac{\rho_{ox} \times v_{inj} \times d_{inj}}{\mu}$$

$$Re = \frac{743.9 \times 38.03 \times 0.0015}{0.000052}$$

$$Re = 816073.38$$

Relative roughness:

$$\frac{e}{D} = \frac{0.0000015}{0.0015} = 0.001$$

The following equations were used to calculate the friction factor and therefore compare them:

Haaland equation:

$$\frac{1}{\sqrt{f}} = 1.8 \times \log\left[\left(\frac{e}{3.7}\right)^{1.11} + \frac{6.9}{Re}\right]$$

$$\frac{1}{\sqrt{f}} = 1.8 \times \log\left[\left(\frac{0.001}{3.7}\right)^{1.11} + \frac{6.9}{816073.38}\right]$$

$$\therefore f = 0.019999778$$

Colebrook equation:

$$\frac{1}{\sqrt{f}} = -2.0 \times \log\left[\left(\frac{e}{3.7}\right) + \frac{2.51}{Re\sqrt{f}}\right]$$

$$\frac{1}{\sqrt{f}} = -2.0 \times \log\left[\left(\frac{0.001}{3.7}\right) + \frac{2.51}{816073.38 \times \sqrt{f}}\right]$$

$$\therefore f = 0.02$$

Once the friction factors have been determined, the head loss can hence pressure loss can be calculated:

$$H_A = \frac{8 \times f \times \dot{m}_{ox}^2 \times 0.02}{\rho_{ox}^2 \times \pi^2 \times L^5 \times g}$$

$$H_A = \frac{8 \times 0.02 \times 0.05^2 \times 0.02}{743.9^2 \times \pi^2 \times 0.012^5 \times 9.81}$$

$$H_A = 11.794 \text{ m}$$

Entrance loss:

$$H_{ent} = \frac{k_{ent} \times v_{inj}^2}{2g}$$

$$H_{ent} = \frac{0.5 \times 38.03^2}{2 \times 9.81}$$

$$H_{ent} = 36.86 \text{ m}$$

Exit loss:

$$H_{exit} = \frac{k_{exit} \times v_{inj}^2}{2g}$$

$$H_{exit} = \frac{1 \times 38.03^2}{2 \times 9.81}$$

$$H_{exit} = 73.71 \text{ m}$$

Total pressure loss:

$$H_t = H_A + H_{ent} + H_{exit}$$

$$H_t = 11.79 + 36.86 + 73.71$$

$$H_t = 122.37 \text{ m}$$

Converting to pressure:

$$P_{l,Pa} = \rho_{ox} \times H_t \times g$$

$$P_{l,Pa} = 743.9 \times 122.37 \times 9.81$$

$$P_{l,Pa} = 892988.08 \text{ Pa}$$

Pressure in bar:

$$P_{l,bar} = P_{l,Pa} \times 10^{-5}$$

$$P_{l,bar} = 892988.08 \times 10^{-5}$$

$$P_{l,bar} = 8.3 \text{ bar}$$

All formulae were obtained from (Fox, et al., 2010).

PURE PARAFFIN							
Dynamic viscosity (Pa)	0.000052						
Density (kg/m ³)	743.9						
Coefficient of Discharge	0.8						
Mass Flow Rate (kg/s)	0.05						
Acceleration due to gravity (m/s ²)	9.81						
Inj Diam (m)	0.0015	Inj Bolt	Length of Inj Diam (m)	Head Loss (m)	Pressure (Pa)	Pressure (bar)	
Inj Area (m ²)	1.76738E-06	M16	0.012	11.79423141	86070.27898	0.86070279	
Inj Vel (m/s)	38.03003614		Entrance Loss	36.85738147	268972.6016	2.689726016	
Reynolds Numb	816073.3813		Exit Loss	73.71476294	537945.2032	5.379452032	
Roughness Coefficient (m)	0.0000015		Total Injector Loss	122.3663758	892988.0838	8.929880838	
Relative Roughness	0.001						
Haaland (1/SQRT(f))	7.071106981						
Friction Factor	0.019999778						
Colebrook f	0.02						
Pressure Drop (bar)	8.4053938						
Inj Bolt Diam (m)	0.006	Inj Bolt	Length of Inj Bolt Diam (m)	Head Loss (m)	Pressure (Pa)	Pressure (bar)	
Inj Bolt Area (m ²)	0.000028278	M20	0.02	0.016465142	120.1569882	0.00120157	
Inj Bolt Vel (m/s)	2.376877259		Entrance Loss	0.143974146	1050.674225	0.010506742	
Reynolds Numb	204018.3453		Exit Loss	0.287948293	2101.34845	0.021013485	
Roughness Coefficient (m)	0.0000015		Total Injector Bolt Loss	0.448387581	3272.179663	0.032721797	
Relative Roughness	0.00025						
Haaland (1/SQRT(f))	7.635085288						
Friction Factor	0.017154269						
Colebrook f	0.017373095						
Pressure Drop (bar)	0.03283357						
Manifold Diam (m)	0.012	Inj Bolt	Length of Manifold Diam (m)	Head Loss (m)	Pressure (Pa)	Pressure (bar)	
Manifold Area (m ²)	0.000113112	M20	0.05	0.00137346	10.02303963	0.00010023	
Manifold Vel (m/s)	0.594219315		Entrance Loss	0.008998384	65.66713906	0.000656671	
Reynolds Numb	102009.1727		Exit Loss	0.017996768	131.3342781	0.001313343	
Roughness Coefficient (m)	0.0000015		Total Manifold Loss	0.028368612	207.0244568	0.002070245	
Relative Roughness	0.000125						
Haaland (1/SQRT(f))	7.388966559						
Friction Factor	0.018316083						
Colebrook f	0.018572352						
Pressure Drop (bar)	0.002052098						
Manifold 1/4" NPT (m)	0.00635	Inj Bolt	Length of 1/4" NPT Diam (m)	Head Loss (m)	Pressure (Pa)	Pressure (bar)	
Manifold 1/4" NPT Area (m ²)	3.16733E-05	M16	0.035	0.02174328	158.6750409	0.00158675	
Manifold 1/4" NPT Vel (m/s)	2.122080261		Entrance Loss	0.114761076	837.4872012	0.008374872	
Reynolds Numb	192773.2397		Exit Loss	0.229522153	1674.974402	0.016749744	
Roughness Coefficient (m)	0.0000015		Total NPT Loss	0.366026509	2671.136645	0.026711366	
Relative Roughness	0.00023622						
Haaland (1/SQRT(f))	7.627758547						
Friction Factor	0.017187239						
Colebrook f	0.017412718						
Pressure Drop (bar)	0.026171475						

ALUMINISED PARAFFIN						
Dynamic viscosity (Pa)	0.000052					
Density (kg/m ³)	743.9					
Coefficient of Discharge	0.8					
Mass Flow Rate (kg/s)	0.038					
Acceleration due to gravity (m/s ²)	9.81					
Inj Diam (m)	0.0015	Inj Bolt	Length of Inj Diam (m)	Head Loss (m)	Pressure (Pa)	Pressure (bar)
Inj Area (m ²)	1.76738E-06	M16	0.012	6.846197421	49961.21423	0.499612142
Inj Vel (m/s)	28.90282747		Entrance Loss	21.28882354	155358.5747	1.553585747
Reynolds Numb	620215.7698		Exit Loss	42.57764708	310717.1494	3.107171494
Roughness Coefficient (m)	0.0000015		Total Injector Loss	70.71266803	516036.9383	5.160369383
Relative Roughness	0.001					
Haaland (1/SQRT(f))	7.053604634					
Friction Factor	0.020099154					
Colebrook f	0.020124031					
Pressure Drop (bar)	4.854955459					
Inj Bolt Diam (m)	0.006	Inj Bolt	Length of Inj Bolt Diam (m)	Head Loss (m)	Pressure (Pa)	Pressure (bar)
Inj Bolt Area (m ²)	0.000028278	M16	0.02	0.009851962	71.89625768	0.000718963
Inj Bolt Vel (m/s)	1.806426717		Entrance Loss	0.083159467	606.8694324	0.006068694
Reynolds Numb	155053.9425		Exit Loss	0.166318934	1213.738865	0.012137389
Roughness Coefficient (m)	0.0000015		Total Injector Bolt Loss	0.259330363	1892.504555	0.018925046
Relative Roughness	0.00025					
Haaland (1/SQRT(f))	7.501512881					
Friction Factor	0.017770608					
Colebrook f	0.018013109					
Pressure Drop (bar)	0.01896467					
Manifold Diam (m)	0.012	Inj Bolt	Length of Manifold Diam (m)	Head Loss (m)	Pressure (Pa)	Pressure (bar)
Manifold Area (m ²)	0.000113112	M20	0.05	0.00137346	10.02303963	0.00010023
Manifold Vel (m/s)	0.594219315		Entrance Loss	0.008998384	65.66713906	0.000656671
Reynolds Numb	102009.1727		Exit Loss	0.017996768	131.3342781	0.001313343
Roughness Coefficient (m)	0.0000015		Total Manifold Loss	0.028368612	207.0244568	0.002070245
Relative Roughness	0.000125					
Haaland (1/SQRT(f))	7.388966559					
Friction Factor	0.018316083					
Colebrook f	0.018572346					
Pressure Drop (bar)	0.001185292					
Manifold 1/4" NPT (m)	0.00635	Inj Bolt	Length of 1/4" NPT Bolt Diam (m)	Head Loss (m)	Pressure (Pa)	Pressure (bar)
Manifold 1/4" NPT Area (m ²)	3.16733E-05	M20	0.035	0.02174328	158.6750409	0.00158675
Manifold 1/4" NPT Vel (m/s)	2.122080261		Entrance Loss	0.114761076	837.4872012	0.008374872
Reynolds Numb	192773.2397		Exit Loss	0.229522153	1674.974402	0.016749744
Roughness Coefficient (m)	0.0000015		Total NPT Loss	0.366026509	2671.136645	0.026711366
Relative Roughness	0.00023622					
Haaland (1/SQRT(f))	7.627758547					
Friction Factor	0.017187239					
Colebrook f	0.017412715					
Pressure Drop (bar)	6.716493175					

APPENDIX 4D

Nozzle Calculations

Table 4D.9.1: Constants for pure paraffin wax

Pure Paraffin	
Variable	Value
O/F ratio	8
Mass flow rate of oxidiser	0.05 kg/s
Total temperature	3000 K
Specific heat ratio, γ	1.25
Gas constant	332

Table 4D.9.2: Constants for 40% aluminised paraffin wax

40% Aluminised Paraffin	
Variable	Value
O/F ratio	3.5
Mass flow rate of oxidiser	0.038
Total temperature	3000
Specific heat ratio, γ	1.25
Gas constant	332

$$\dot{m}_t = \frac{A_t P_t}{\sqrt{T_t}} \times \sqrt{\frac{\gamma}{R}} \times \left(\frac{\gamma + 1}{2}\right)^{-\frac{\gamma+1}{2(\gamma-1)}}$$

In the spreadsheets that follow:

Part 1 –

$$\begin{aligned}
 & \frac{4\dot{m}_t\sqrt{T_t}}{\pi P_t} \\
 &= \frac{4 \times 0.05625 \times \sqrt{3000}}{\pi \times 1} \\
 &= 3.992
 \end{aligned}$$

Part 2 –

$$\begin{aligned} & \left(\frac{\gamma + 1}{2}\right)^{\frac{\gamma+1}{2(\gamma-1)}} \\ &= \left(\frac{1.25 + 1}{2}\right)^{\frac{1.25+1}{2(1.25-1)}} \\ &= 0.973847 \end{aligned}$$

Part 3 –

$$\begin{aligned} & \left(\frac{\gamma}{R}\right)^{-\frac{1}{2}} \\ &= \left(\frac{1.25}{332}\right)^{-\frac{1}{2}} \\ &= 16.29724 \end{aligned}$$

Summing parts 1, 2 and 3:

$$\dot{m}_t = \frac{A_t P_t}{\sqrt{T_t}} \times \sqrt{\frac{\gamma}{R}} \times \left(\frac{\gamma + 1}{2}\right)^{-\frac{\gamma+1}{2(\gamma-1)}}$$

Setting $A_t = \frac{\pi d_{tt}^2}{4}$ and rearranging the equation so that the throat diameter can be the subject of the formula:

$$d_{tt}^2 = \frac{4\dot{m}_t\sqrt{T_t}}{\pi P_t} \times \left(\frac{\gamma + 1}{2}\right)^{\frac{\gamma+1}{2(\gamma-1)}} \times \left(\frac{\gamma}{R}\right)^{-\frac{1}{2}}$$

$$d_{tt}^2 = 3.992 \times 0.973847 \times 16.29724$$

$$d_{tt}^2 = 62.25$$

$$d_{tt} = 7.89 \text{ mm}$$

(Fox, et al., 2010)

PURE PARAFFIN			
O/F Ratio	8		
Mass Flow of Oxidiser (kg/s)	0.05		
Mass Flow of Fuel (kg/s)	0.00625		
Total Mass Flow (kg/s)	0.05625		
Total Temperature (K)	3000		
Specific Heat Ratio (Gamma)	1.25		
Part 2 Base	1.125		
Part 2 Exponent	-0.225		
Part 2	0.973847		
Gas Constant R	332		
Part 3	16.29724		
	Nozzle 1	Nozzle 2	Nozzle 3
Pressure in bar	10	5	1
Pressure (MPa)	1	0.5	0.1
Part 1	3.922	7.845	39.223
Throat Diameter Squared	62.250	124.501	622.503
Throat Diameter (mm)	7.890	11.158	24.950

ALUMINISED PARAFFIN			
O/F Ratio	3.5		
Mass Flow of Oxidiser (kg/s)	0.038		
Mass Flow of Fuel (kg/s)	0.010857		
Total Mass Flow (kg/s)	0.048857		
Total Temperature (K)	3000		
Specific Heat Ratio (Gamma)	1.25		
Part 2 Base	1.125		
Part 2 Exponent	-0.225		
Part 2	0.973847		
Gas Constant R	332		
Part 3	16.29724		
	Nozzle 1	Nozzle 2	Nozzle 3
Pressure in bar	10	5	1
Pressure (MPa)	1	0.5	0.1
Part 1	3.407	6.814	34.068
Throat Diameter Squared	54.069	108.138	540.689
Throat Diameter (mm)	7.353	10.399	23.253

APPENDIX 4E

Heat Transfer Calculations

Table 4E.9.1: Constants for Stainless Steel 304L

Stainless Steel 304L	
Variable	Value
Specific heat capacity	500 J/kgK
Melting point	1723.15 K
Ambient temperature	300 K
Thermal conductivity	21.4 W/mK

Table 4E.9.2: Constants for Brass

Brass C22000	
Variable	Value
Specific heat capacity	376.81 J/kgK
Melting point	1316.48 K
Ambient temperature	300 K
Thermal conductivity	188.52 W/mK

Table 4E.9.3: Constants for Quartz Glass

Quartz Glass	
Variable	Value
Specific heat capacity	670 J/kgK
Melting point	1956 K
Ambient temperature	300 K
Thermal conductivity	2.68 W/mK

Heat transferred:

$$Q = \frac{T_m - T_a}{\frac{t}{\lambda \times A}} \times \frac{1}{1000}$$

$$Q = \frac{1723.15 - 300}{\frac{0.012}{21.4 \times 0.05564}} \times \frac{1}{1000}$$

$$Q = 141 \text{ kW}$$

Maximum heat transferred:

$$Q_{max} = m \times C_p \times \Delta T$$

$$Q_{max} = 1.614 \times 500 \times 1423.15$$

$$Q_{max} = 1148.48 \text{ kW}$$

STAINLESS STEEL 304L					
Specific Heat Capacity (J/kgK)	500		Heat Transfer (kW)		
Melting Point (K)	1723.15		Side Panel	Billet	Top Panels
Ambient Temperature (K)	300		141.2222	175.6221	132.5463
Change in Temperature (K)	1423.15				
Thermal Conductivity (W/mK)	21.4				
Area of Side Panel (m ²)	0.05564416		Max Heat Transfer (kW)		
Mass of Side Panel (kg)	1.614		Side Panel	Billet	Top Panels
Thickness of Side Panel (m ²)	0.012		1148.482	5282.733	2094.877
Area of Billet (m ²)	0.13839681				
Mass of Billet (kg)	7.424				
Thickness of Billet (m ²)	0.024				
Area of Top Panels (m ²) x2	0.10445142				
Mass of Top Panels (kg) x2	2.944				
Thickness of Top Panel (m ²)	0.024				

QUARTZ GLASS					
Specific Heat Capacity (J/kgK)	670		Heat Transfer (kW)		
Melting Point (K)	1956		Side Panel	Billet	Top Panels
Ambient Temperature (K)	300		13.92981	12.02953	10.67219
Change in Temperature (K)	1656				
Thermal Conductivity (W/mK)	2.68				
Area of 10mm Glass (m ²)	0.03138702		Max Heat Transfer (kW)		
Mass of 10mm Glass (kg)	0.288		Side Panel	Billet	Top Panels
Thickness of 10mm Glass (m ²)	0.01		319.5418	382.7844	447.1366
Area of 12mm Glass (m ²)	0.03252632				
Mass of 12mm Glass (kg)	0.345				
Thickness of 12mm Glass (m ²)	0.012				
Area of 14mm Glass (m ²)	0.03366561				
Mass of 14mm Glass (kg)	0.403				
Thickness of 14mm Glass (m ²)	0.014				

APPENDIX 4F

Bolt Calculations

Table 4F.9.1: Table of constants 1

Variable	Value
Chamber Pressure	2 MPa
Number of bolts for bulkheads	12
Number of bolts for side panel	20
Number of bolts for top panel	18
Diameter of bolt, d	5 mm
SAE Class	12.9
Proof Strength, S_p	970 MPa
Bolt stressed area, A_t	14.2 mm ²

Front bulkhead:

Pressurised area: 4426.94 mm²

At a chamber pressure of 20 bar (2 MPa, including a safety factor of 2):

$$F = P \times A$$

$$F = 2 \times 4426.94$$

$$F = 8853.88 \text{ N}$$

Distributed around 12 bolts on the bulkhead:

$$F_b = \frac{8853.88}{12}$$

$$F_b = 737.82 \text{ N}$$

Initial tension/preload:

$$\tau = 5 \text{ N/m}$$

$$d = 0.005 \text{ m}$$

$$F_i = \frac{\tau}{0.2 \times d}$$

$$F_i = \frac{5}{0.2 \times 0.005}$$

$$F_i = 5000 \text{ N}$$

From (Juvinall & Marshek, 2006):

SAE Class 12.9 Bolt

$$A_t = 14.2 \text{ mm}^2$$

$$S_p = 970 \text{ MPa}$$

Total force per bolt:

$$F_t = F_b + F_i$$

$$F_t = 737.82 + 5000$$

$$F_t = 5737.82 \text{ N}$$

Allowable force before shearing of threads:

$$F = A_t \times S_p$$

$$F = 14.2 \times 970$$

$$F = 13774 \text{ N}$$

Safety factor at 20 bar:

$$SF = \frac{F}{F_{bolt}}$$

$$SF = \frac{13774}{5737.82}$$

$$SF = 2.4$$

Chamber pressure required to cause shearing of bolts:

$$F = F_{bolt} + F_i$$

$$13774 = 4426.94\left(\frac{P}{12}\right) + 5000$$

$$P = 23.78 \text{ MPa}$$

$$P = 237.8 \text{ bar}$$

FRONT BULKHEAD CALCULATIONS	
Pressurised Area (mm ²)	4426.94
Chamber Pressure (MPa)	2
Force (N)	8853.88
Number of bolts	12
Force per bolt [N]	737.82333
SAE CLASS 12.9 BOLT	
Diameter of bolt (m)	0.005
Torque (N/m)	5
Thread Engagement Length (mm)	12
Initial Tension (N)	5000
Total Force per bolt (N)	5737.8233
Proof Strength, Sp (MPa)	970
Bolt stressed area, At (mm ²)	14.2
Allowable force during shearing of threads (N)	13774
Safety Factor	2.4005619
Chamber pressure required to cause shearing (MPa)	2
Chamber pressure required to cause shearing (bar)	20
Gasket Area (mm ²)	4496.38
Gasket Seal Stress (MPa)	1.1120057
FRONT BULKHEAD CALCULATIONS	
Pressurised Area (mm ²)	4426.94
Chamber Pressure (MPa)	2
Force (N)	8853.88
Number of bolts	12
Force per bolt [N]	737.82333
SAE CLASS 10.9 BOLT	
Diameter of bolt (m)	0.006
Torque (N/m)	5
Thread Engagement Length (mm)	12
Initial Tension (N)	4166.6667
Total Force per bolt (N)	4904.49
Proof Strength, Sp (MPa)	830
Bolt stressed area, At (mm ²)	14.2
Allowable force during shearing of threads (N)	11786
Safety Factor	2.4031041
Chamber pressure required to cause shearing (MPa)	2
Chamber pressure required to cause shearing (bar)	20
Gasket Area (mm ²)	4496.38
Gasket Seal Stress (MPa)	0.9266714

The following sample calculations represent those used in the spreadsheets:

Table 4F.9.2: Table of constants 2

Variable	Value
Diameter of bolt, d	5 mm
Proof strength, S_p	970 MPa
Bolt stressed area, A_t	14.2 mm ²
Yield %	50
Gasket pressurised area	4496.38 mm ²

Allowable force:

$$F_i = S_p \times A_t$$

$$F_i = 970 \times 14.2$$

$$F_i = 13774 \text{ N}$$

Clamping force:

$$F_c = Y \times F_i$$

$$F_c = \frac{50}{100} \times 13774$$

$$F_c = 6887$$

Torque:

$$\tau = 0.2 \times F_c \times d$$

$$\tau = 0.2 \times 6887 \times 0.005$$

$$\tau = 6.887 \text{ Nm}$$

Sealing stress due to bolt tightening:

$$\sigma_s = \frac{F_c}{A_p}$$

$$\sigma_s = \frac{6887}{4496.38}$$

$$\sigma_s = 1.53 \text{ MPa}$$

Total stress applied on gasket:

$$\sigma_t = \sigma_s + \sigma_{cc}$$

$$\sigma_t = 1.53 + 2$$

$$\sigma_t = 3.53 \text{ MPa}$$

GASKET FOR FRONT BULKHEAD		
SAE CLASS 12.9 BOLT		
Diameter of bolt, d (mm)	0.005	
Proof Strength, Sp (MPa)	970	
Bolt Stressed Area, At (mm ²)	14.2	
Allowable force, Fi (N)	13774	
Yield %	50	
Clamping Force, Fc (N)	6887	
Torque, T (Nm)	6.887	NB: Round to 5 Nm
Gasket Pressurised Area, Ap (mm ²)	4496.38	
Sealing Stress due to bolt tightening (MPa)	1.531677	
Stress applied with 20 bar pressure (MPa)	2	
Total Stress applied on gasket (MPa)	3.531677	DESIGN IS NOT SAFE
Total Stress applied on gasket at T = 5 Nm (MPa)	3.112006	DESIGN IS SAFE
Maximum Sealing Stress of Gasket (MPa)	3.2	
Clamping Force, Fc at T = 5 Nm (N)	5000	
Gasket Pressurised Area, Ap (mm ²)	4496.38	
Stress (MPa)	1.11	
Youngs Modulus of silicone (MPa)	50	
Strain	0.02224	
Initial Gasket Thickness (mm)	1.5	
Change in thickness of gasket at Fc (mm)	0.03336	
Resultant thickness of gasket (mm)	1.46664	
GASKET FOR FRONT BULKHEAD		
SAE CLASS 10.9 BOLT		
Diameter of bolt, d (mm)	0.006	
Proof Strength, Sp (MPa)	830	
Bolt Stressed Area, At (mm ²)	14.2	
Allowable force, Fi (N)	11786	
Yield %	50	
Clamping Force, Fc (N)	5893	
Torque, T (Nm)	7.0716	NB: Round to 5 Nm
Gasket Pressurised Area, Ap (mm ²)	4496.38	
Sealing Stress due to bolt tightening (MPa)	1.31061	
Stress applied with 20 bar pressure (MPa)	2	
Total Stress applied on gasket (MPa)	3.31061	DESIGN IS NOT SAFE
Total Stress applied on gasket at T = 5 Nm (MPa)	3.112006	DESIGN IS SAFE
Maximum Sealing Stress of Gasket (MPa)	3.2	
Clamping Force, Fc at T = 5 Nm (N)	5000	
Gasket Pressurised Area, Ap (mm ²)	4496.38	
Stress (MPa)	1.11	
Youngs Modulus of silicone (MPa)	50	
Strain	0.02224	
Initial Gasket Thickness (mm)	1.5	
Change in thickness of gasket at Fc (mm)	0.03336	
Resultant thickness of gasket (mm)	1.46664	

Nozzle bulkhead (5 bar):

NOZZLE 5 BAR CALCULATIONS	
Pressurised Area (mm ²)	4536.39
Chamber Pressure (MPa)	2
Force (N)	9072.78
Number of bolts	12
Force per bolt [N]	756.065
SAE CLASS 12.9 BOLT	
Diameter of bolt (m)	0.005
Torque (N/m)	5
Thread Engagement Length (mm)	12
Initial Tension (N)	5000
Total Force per bolt (N)	5756.065
Proof Strength, Sp (MPa)	970
Bolt stressed area, At (mm ²)	14.2
Allowable force during shearing of threads (N)	13774
Safety Factor	2.3929542
Chamber pressure required to cause shearing (MPa)	2
Chamber pressure required to cause shearing (bar)	20
Gasket Area (mm ²)	4496.38
Gasket Seal Stress (MPa)	1.1120057
NOZZLE 5 BAR CALCULATIONS	
Pressurised Area (mm ²)	4536.39
Chamber Pressure (MPa)	2
Force (N)	9072.78
Number of bolts	12
Force per bolt [N]	756.065
SAE CLASS 10.9 BOLT	
Diameter of bolt (m)	0.006
Torque (N/m)	5
Thread Engagement Length (mm)	12
Initial Tension (N)	4166.6667
Total Force per bolt (N)	4922.7317
Proof Strength, Sp (MPa)	830
Bolt stressed area, At (mm ²)	14.2
Allowable force during shearing of threads (N)	11786
Safety Factor	2.3941992
Chamber pressure required to cause shearing (MPa)	2
Chamber pressure required to cause shearing (bar)	20
Gasket Area (mm ²)	4496.38
Gasket Seal Stress (MPa)	0.9266714

GASKET FOR NOZZLE 5 BAR		
SAE CLASS 12.9 BOLT		
Diameter of bolt, d (mm)	0.005	
Proof Strength, Sp (MPa)	970	
Bolt Stressed Area, At (mm ²)	14.2	
Allowable force, Fi (N)	13774	
Yield %	50	
Clamping Force, Fc (N)	6887	
Torque, T (Nm)	6.887	NB: Round to 5 Nm
Gasket Pressurised Area, Ap (mm ²)	4496.38	
Sealing Stress due to bolt tightening (MPa)	1.531677	
Stress applied with 20 bar pressure (MPa)	2	
Total Stress applied on gasket (MPa)	3.531677	DESIGN IS NOT SAFE
Total Stress applied on gasket at T = 5 Nm (MPa)	3.112006	DESIGN IS SAFE
Maximum Sealing Stress of Gasket (MPa)	3.2	
Clamping Force, Fc at T = 5 Nm (N)	5000	
Gasket Pressurised Area, Ap (mm ²)	4496.38	
Stress (MPa)	1.11	
Youngs Modulus of silicone (MPa)	50	
Strain	0.02224	
Initial Gasket Thickness (mm)	1.5	
Change in thickness of gasket at Fc (mm)	0.03336	
Resultant thickness of gasket (mm)	1.46664	
GASKET FOR NOZZLE 5 BAR		
SAE CLASS 10.9 BOLT		
Diameter of bolt, d (mm)	0.006	
Proof Strength, Sp (MPa)	830	
Bolt Stressed Area, At (mm ²)	14.2	
Allowable force, Fi (N)	11786	
Yield %	50	
Clamping Force, Fc (N)	5893	
Torque, T (Nm)	7.0716	NB: Round to 5 Nm
Gasket Pressurised Area, Ap (mm ²)	4496.38	
Sealing Stress due to bolt tightening (MPa)	1.31061	
Stress applied with 20 bar pressure (MPa)	2	
Total Stress applied on gasket (MPa)	3.31061	DESIGN IS NOT SAFE
Total Stress applied on gasket at T = 5 Nm (MPa)	3.112006	DESIGN IS SAFE
Maximum Sealing Stress of Gasket (MPa)	3.2	
Clamping Force, Fc at T = 5 Nm (N)	5000	
Gasket Pressurised Area, Ap (mm ²)	4496.38	
Stress (MPa)	1.11	
Youngs Modulus of silicone (MPa)	50	
Strain	0.02224	
Initial Gasket Thickness (mm)	1.5	
Change in thickness of gasket at Fc (mm)	0.03336	
Resultant thickness of gasket (mm)	1.46664	

Nozzle bulkhead (10 bar):

NOZZLE 10 BAR CALCULATIONS	
Pressurised Area (mm ²)	4583.821
Chamber Pressure (MPa)	2
Force (N)	9167.642
Number of bolts	12
Force per bolt [N]	763.97017
SAE CLASS 12.9 BOLT	
Diameter of bolt (m)	0.005
Torque (N/m)	5
Thread Engagement Length (mm)	12
Initial Tension (N)	5000
Total Force per bolt (N)	5763.9702
Proof Strength, Sp (MPa)	970
Bolt stressed area, At (mm ²)	14.2
Allowable force during shearing of threads (N)	13774
Safety Factor	2.3896723
Chamber pressure required to cause shearing (MPa)	2
Chamber pressure required to cause shearing (bar)	20
Gasket Area (mm ²)	4496.38
Gasket Seal Stress (MPa)	1.1120057
NOZZLE 10 BAR CALCULATIONS	
Pressurised Area (mm ²)	4583.821
Chamber Pressure (MPa)	2
Force (N)	9167.642
Number of bolts	12
Force per bolt [N]	763.97017
SAE CLASS 10.9 BOLT	
Diameter of bolt (m)	0.006
Torque (N/m)	5
Thread Engagement Length (mm)	12
Initial Tension (N)	4166.6667
Total Force per bolt (N)	4930.6368
Proof Strength, Sp (MPa)	830
Bolt stressed area, At (mm ²)	14.2
Allowable force during shearing of threads (N)	11786
Safety Factor	2.3903606
Chamber pressure required to cause shearing (MPa)	2
Chamber pressure required to cause shearing (bar)	20
Gasket Area (mm ²)	4496.38
Gasket Seal Stress (MPa)	0.9266714

GASKET FOR NOZZLE 10 BAR		
SAE CLASS 12.9 BOLT		
Diameter of bolt, d (mm)	0.005	
Proof Strength, Sp (MPa)	970	
Bolt Stressed Area, At (mm ²)	14.2	
Allowable force, Fi (N)	13774	
Yield %	50	
Clamping Force, Fc (N)	6887	
Torque, T (Nm)	6.887	NB: Round to 5 Nm
Gasket Pressurised Area, Ap (mm ²)	4496.38	
Sealing Stress due to bolt tightening (MPa)	1.531677	
Stress applied with 20 bar pressure (MPa)	2	
Total Stress applied on gasket (MPa)	3.531677	DESIGN IS NOT SAFE
Total Stress applied on gasket at T = 5 Nm (MPa)	3.112006	DESIGN IS SAFE
Maximum Sealing Stress of Gasket (MPa)	3.2	
Clamping Force, Fc at T = 5 Nm (N)	5000	
Gasket Pressurised Area, Ap (mm ²)	4496.38	
Stress (MPa)	1.11	
Youngs Modulus of silicone (MPa)	50	
Strain	0.02224	
Initial Gasket Thickness (mm)	1.5	
Change in thickness of gasket at Fc (mm)	0.03336	
Resultant thickness of gasket (mm)	1.46664	
GASKET FOR NOZZLE 10 BAR		
SAE CLASS 10.9 BOLT		
Diameter of bolt, d (mm)	0.006	
Proof Strength, Sp (MPa)	830	
Bolt Stressed Area, At (mm ²)	14.2	
Allowable force, Fi (N)	11786	
Yield %	50	
Clamping Force, Fc (N)	5893	
Torque, T (Nm)	7.0716	NB: Round to 5 Nm
Gasket Pressurised Area, Ap (mm ²)	4496.38	
Sealing Stress due to bolt tightening (MPa)	1.31061	
Stress applied with 20 bar pressure (MPa)	2	
Total Stress applied on gasket (MPa)	3.31061	DESIGN IS NOT SAFE
Total Stress applied on gasket at T = 5 Nm (MPa)	3.112006	DESIGN IS SAFE
Maximum Sealing Stress of Gasket (MPa)	3.2	
Clamping Force, Fc at T = 5 Nm (N)	5000	
Gasket Pressurised Area, Ap (mm ²)	4496.38	
Stress (MPa)	1.11	
Youngs Modulus of silicone (MPa)	50	
Strain	0.02224	
Initial Gasket Thickness (mm)	1.5	
Change in thickness of gasket at Fc (mm)	0.03336	
Resultant thickness of gasket (mm)	1.46664	

Side panel:

SIDE WALL CALCULATIONS	
Pressurised Area (mm ²)	11444.292
Chamber Pressure (MPa)	2
Force (N)	22888.584
Number of bolts	20
Force per bolt [N]	1144.4292
SAE CLASS 12.9 BOLT	
Diameter of bolt (m)	0.005
Torque (N/m)	10
Thread Engagement Length (mm)	12
Initial Tension (N)	10000
Total Force per bolt (N)	11144.429
Proof Strength, Sp (MPa)	970
Bolt stressed area, At (mm ²)	14.2
Allowable force during shearing of threads (N)	13774
Safety Factor	1.2359538
Chamber pressure required to cause shearing (MPa)	2
Chamber pressure required to cause shearing (bar)	20
Gasket Area (mm ²)	6956.15
Gasket Seal Stress (MPa)	1.4375768
SIDE WALL CALCULATIONS	
Pressurised Area (mm ²)	11444.292
Chamber Pressure (MPa)	2
Force (N)	22888.584
Number of bolts	12
Force per bolt [N]	1907.382
SAE CLASS 10.9 BOLT	
Diameter of bolt (m)	0.006
Torque (N/m)	10
Thread Engagement Length (mm)	12
Initial Tension (N)	8333.3333
Total Force per bolt (N)	10240.715
Proof Strength, Sp (MPa)	830
Bolt stressed area, At (mm ²)	14.2
Allowable force during shearing of threads (N)	11786
Safety Factor	1.1508962
Chamber pressure required to cause shearing (MPa)	2
Chamber pressure required to cause shearing (bar)	20
Gasket Area (mm ²)	6956.15
Gasket Seal Stress (MPa)	1.1979807

GASKET FOR SIDE WALL		
SAE CLASS 12.9 BOLT		
Diameter of bolt, d (mm)	0.005	
Proof Strength, Sp (MPa)	970	
Bolt Stressed Area, At (mm ²)	14.2	
Allowable force, Fi (N)	13774	
Yield %	50	
Clamping Force, Fc (N)	6887	
Torque, T (Nm)	6.887	NB: Round to 6 Nm
Gasket Pressurised Area, Ap (mm ²)	6956.15	
Sealing Stress due to bolt tightening (MPa)	0.9900592	
Stress applied with 20 bar pressure (MPa)	2	
Total Stress applied on gasket (MPa)	2.9900592	DESIGN IS SAFE
Total Stress applied on gasket at T = 6 Nm (MPa)	2.8625461	DESIGN IS SAFE
Maximum Sealing Stress of Gasket (MPa)	3.2	
Clamping Force, Fc at T = 6 Nm (N)	6000	
Gasket Pressurised Area, Ap (mm ²)	6956.15	
Stress (MPa)	0.86	
Youngs Modulus of silicone (MPa)	50	
Strain	0.0172509	
Initial Gasket Thickness (mm)	1.5	
Change in thickness of gasket at Fc (mm)	0.0258764	
GASKET FOR SIDE WALL		
SAE CLASS 10.9 BOLT		
Diameter of bolt, d (mm)	0.006	
Proof Strength, Sp (MPa)	830	
Bolt Stressed Area, At (mm ²)	14.2	
Allowable force, Fi (N)	11786	
Yield %	50	
Clamping Force, Fc (N)	5893	
Torque, T (Nm)	7.0716	NB: Round to 7 Nm
Gasket Pressurised Area, Ap (mm ²)	6956.15	
Sealing Stress due to bolt tightening (MPa)	0.847164	
Stress applied with 20 bar pressure (MPa)	2	
Total Stress applied on gasket (MPa)	2.847164	DESIGN IS SAFE
Maximum Sealing Stress of Gasket (MPa)	3.2	
Clamping Force, Fc at T = 7 Nm (N)	5833.3333	
Gasket Pressurised Area, Ap (mm ²)	6956.15	
Stress (MPa)	0.84	
Youngs Modulus of silicone (MPa)	50	
Strain	0.0167717	
Initial Gasket Thickness (mm)	1.5	
Change in thickness of gasket at Fc (mm)	0.0251576	
Resultant thickness of gasket (mm)	1.4748424	

Top panel:

TOP WALL CALCULATIONS	
Pressurised Area (mm ²)	12383.562
Chamber Pressure (MPa)	2
Force (N)	24767.124
Number of bolts	18
Force per bolt [N]	1375.9513
SAE CLASS 12.9 BOLT	
Diameter of bolt (m)	0.005
Torque (N/m)	10
Thread Engagement Length (mm)	12
Initial Tension (N)	10000
Total Force per bolt (N)	11375.951
Proof Strength, Sp (MPa)	970
Bolt stressed area, At (mm ²)	14.2
Allowable force during shearing of threads (N)	13774
Safety Factor	1.2107998
Chamber pressure required to cause shearing (MPa)	2
Chamber pressure required to cause shearing (bar)	20
Gasket Area (mm ²)	6956.15
Gasket Seal Stress (MPa)	1.4375768
TOP WALL CALCULATIONS	
Pressurised Area (mm ²)	12383.562
Chamber Pressure (MPa)	2
Force (N)	24767.124
Number of bolts	12
Force per bolt [N]	2063.927
SAE CLASS 10.9 BOLT	
Diameter of bolt (m)	0.006
Torque (N/m)	10
Thread Engagement Length (mm)	12
Initial Tension (N)	8333.3333
Total Force per bolt (N)	10397.26
Proof Strength, Sp (MPa)	830
Bolt stressed area, At (mm ²)	14.2
Allowable force during shearing of threads (N)	11786
Safety Factor	1.1335678
Chamber pressure required to cause shearing (MPa)	2
Chamber pressure required to cause shearing (bar)	20
Gasket Area (mm ²)	6956.15
Gasket Seal Stress (MPa)	1.1979807

GASKET FOR TOP WALL		
SAE CLASS 12.9 BOLT		
Diameter of bolt, d (mm)	0.005	
Proof Strength, Sp (MPa)	970	
Bolt Stressed Area, At (mm ²)	14.2	
Allowable force, Fi (N)	13774	
Yield %	50	
Clamping Force, Fc (N)	6887	
Torque, T (Nm)	6.887	NB: Round to 6 Nm
Gasket Pressurised Area, Ap (mm ²)	6956.15	
Sealing Stress due to bolt tightening (MPa)	0.990059156	
Stress applied with 20 bar pressure (MPa)	2	
Total Stress applied on gasket (MPa)	2.990059156	DESIGN IS SAFE
Total Stress applied on gasket at T = 6 Nm (MPa)	2.862546092	DESIGN IS SAFE
Maximum Sealing Stress of Gasket (MPa)	3.2	
Clamping Force, Fc at T = 6 Nm (N)	6000	
Gasket Pressurised Area, Ap (mm ²)	6956.15	
Stress (MPa)	0.86	
Youngs Modulus of silicone (MPa)	50	
Strain	0.017250922	
Initial Gasket Thickness (mm)	1.5	
Change in thickness of gasket at Fc (mm)	0.025876383	
GASKET FOR TOP WALL		
SAE CLASS 10.9 BOLT		
Diameter of bolt, d (mm)	0.006	
Proof Strength, Sp (MPa)	830	
Bolt Stressed Area, At (mm ²)	14.2	
Allowable force, Fi (N)	11786	
Yield %	50	
Clamping Force, Fc (N)	5893	
Torque, T (Nm)	7.0716	NB: Round to 7 Nm
Gasket Pressurised Area, Ap (mm ²)	6956.15	
Sealing Stress due to bolt tightening (MPa)	0.84716402	
Stress applied with 20 bar pressure (MPa)	2	
Total Stress applied on gasket (MPa)	2.84716402	DESIGN IS SAFE
Maximum Sealing Stress of Gasket (MPa)	3.2	
Clamping Force, Fc at T = 10 Nm (N)	10000	
Gasket Pressurised Area, Ap (mm ²)	6956.15	
Stress (MPa)	1.44	
Youngs Modulus of silicone (MPa)	50	
Strain	0.028751536	
Initial Gasket Thickness (mm)	1.5	
Change in thickness of gasket at Fc (mm)	0.043127305	
Resultant thickness of gasket (mm)	1.456872695	

APPENDIX 4G

Gasket Compression Calculations

The following calculations assisted in identifying the machining depth required for the grooves, which accommodate the glass in the combustion chamber. These calculations utilise the compression set, strain and yield strength of the gaskets. The thickness of the glass is 14 mm and the gasket is 1.5 mm in thickness.

40% Compression thickness:

$$t_c = \left(\frac{C_{set}}{100}\right) \times t_{gt}$$

$$t_c = \left(\frac{40}{100}\right) \times 1.5$$

$$t_c = 0.6 \text{ mm}$$

Compressed gasket thickness:

$$t_t = t_{gt} - t_c$$

$$t_t = 1.5 - 0.6$$

$$t_t = 0.9 \text{ mm}$$

Combined glass and gasket thickness:

$$t_{gs+gt} = t_{gs} + (2 \times t_t)$$

$$t_{gs+gt} = 14 + (2 \times 0.9)$$

$$t_{gs+gt} = 15.8 \text{ mm}$$

Recess in the steel required:

$$S_r = t_{gs+gt} - t_{ge}$$

$$S_r = 15.8 - 15.5$$

$$S_r = 0.3 \text{ mm}$$

In addition, calculations were performed to determine the preload force for the bolt using each compression set.

Strain:

$$\varepsilon = \frac{\Delta l}{l_o}$$

$$\varepsilon = \frac{0.6}{1.5}$$

$$\varepsilon = 0.4$$

Sealing stress required:

Young's Modulus, $E = 50 \text{ GPa}$

$$\sigma = \varepsilon \times E$$

$$\sigma = 0.4 \times 50$$

$$\sigma = 20 \text{ MPa}$$

Clamping force:

Gasket pressurised area = 5989.65 mm^2

$$F_{cl} = \sigma \times A_{gt}$$

$$F_{cl} = 20 \times 5989.65$$

$$F_{cl} = 119792.92 \text{ N}$$

Torque:

Diameter of bolt = 5 mm

$$\tau = 0.2 \times F_{cl} \times d$$

$$\tau = 0.2 \times 119792 \times 0.005$$

$$\tau = 119.79 \text{ Nm}$$

Preload force:

Yield % = 50%

$$F_i = F_{cl} \times \frac{Y}{100}$$

$$F_i = 119792.92 \times \frac{50}{100}$$

$$F_i = 59896.46 \text{ N}$$

This validates that the gasket will not fail under a 40% compression set in loading conditions.

40% Compression Set:

40 % COMPRESSION SET				
Compression (%)	40		Strain	0.4
Gasket thickness (mm)	1.5		Sealing stress required (MPa)	20
Glass thickness (mm)	14		Clamping force, Fc (N)	119792.92
Groove in brass height (mm)	15.5		Torque, T (Nm)	119.79292
Young's Modulus (MPa)	50		Preload force, Fi (N)	59896.46
Gasket Pressurised Area (mm^2)	5989.646			
Bolt diameter (m)	0.005			
Yield (%)	50			
Compression thickness (mm)	0.6			
Compressed gasket thickness (mm)	0.9			
Combined glass and gasket thickness (mm)	15.8			
Recess in steel (mm)	0.3			

35% Compression Set:

35 % COMPRESSION SET				
Compression (%)	35		Strain	0.35
Gasket thickness (mm)	1.5		Sealing stress required (MPa)	17.5
Glass thickness (mm)	14		Clamping force, Fc (N)	104818.81
Groove in brass height (mm)	15.5		Torque, T (Nm)	104.81881
Young's Modulus (MPa)	50		Preload force, Fi (N)	52409.403
Gasket Pressurised Area (mm^2)	5989.646			
Bolt diameter (m)	0.005			
Yield (%)	50			
Compression thickness (mm)	0.525			
Compressed gasket thickness (mm)	0.975			
Combined glass and gasket thickness (mm)	15.95			
Recess in steel (mm)	0.45			

30% Compression Set:

30 % COMPRESSION SET			
Compression (%)	30	Strain	0.3
Gasket thickness (mm)	1.5	Sealing stress required (MPa)	15
Glass thickness (mm)	14	Clamping force, Fc (N)	89844.69
Groove in brass height (mm)	15.5	Torque, T (Nm)	89.84469
Young's Modulus (MPa)	50	Preload force, Fi (N)	44922.345
Gasket Pressurised Area (mm^2)	5989.646		
Bolt diameter (m)	0.005		
Yield (%)	50		
Compression thickness (mm)	0.45		
Compressed gasket thickness (mm)	1.05		
Combined glass and gasket thickness (mm)	16.1		
Recess in steel (mm)	0.6		

25% Compression Set:

25 % COMPRESSION SET			
Compression (%)	25	Strain	0.25
Gasket thickness (mm)	1.5	Sealing stress required (MPa)	12.5
Glass thickness (mm)	14	Clamping force, Fc (N)	74870.575
Groove in brass height (mm)	15.5	Torque, T (Nm)	74.870575
Young's Modulus (MPa)	50	Preload force, Fi (N)	37435.288
Gasket Pressurised Area (mm^2)	5989.646		
Bolt diameter (m)	0.005		
Yield (%)	50		
Compression thickness (mm)	0.375		
Compressed gasket thickness (mm)	1.125		
Combined glass and gasket thickness (mm)	16.25		
Recess in steel (mm)	0.75		

20% Compression Set:

20 % COMPRESSION SET			
Compression (%)	20	Strain	0.2
Gasket thickness (mm)	1.5	Sealing stress required (MPa)	10
Glass thickness (mm)	14	Clamping force, Fc (N)	59896.46
Groove in brass height (mm)	15.5	Torque, T (Nm)	59.89646
Young's Modulus (MPa)	50	Preload force, Fi (N)	29948.23
Gasket Pressurised Area (mm ²)	5989.646		
Bolt diameter (m)	0.005		
Yield (%)	50		
Compression thickness (mm)	0.3		
Compressed gasket thickness (mm)	1.2		
Combined glass and gasket thickness (mm)	16.4		
Recess in steel (mm)	0.9		

15% Compression Set:

15 % COMPRESSION SET			
Compression (%)	15	Strain	0.15
Gasket thickness (mm)	1.5	Sealing stress required (MPa)	7.5
Glass thickness (mm)	14	Clamping force, Fc (N)	44922.345
Groove in brass height (mm)	15.5	Torque, T (Nm)	44.922345
Young's Modulus (MPa)	50	Preload force, Fi (N)	22461.173
Gasket Pressurised Area (mm ²)	5989.646		
Bolt diameter (m)	0.005		
Yield (%)	50		
Compression thickness (mm)	0.225		
Compressed gasket thickness (mm)	1.275		
Combined glass and gasket thickness (mm)	16.55		
Recess in steel (mm)	1.05		

10% Compression Set:

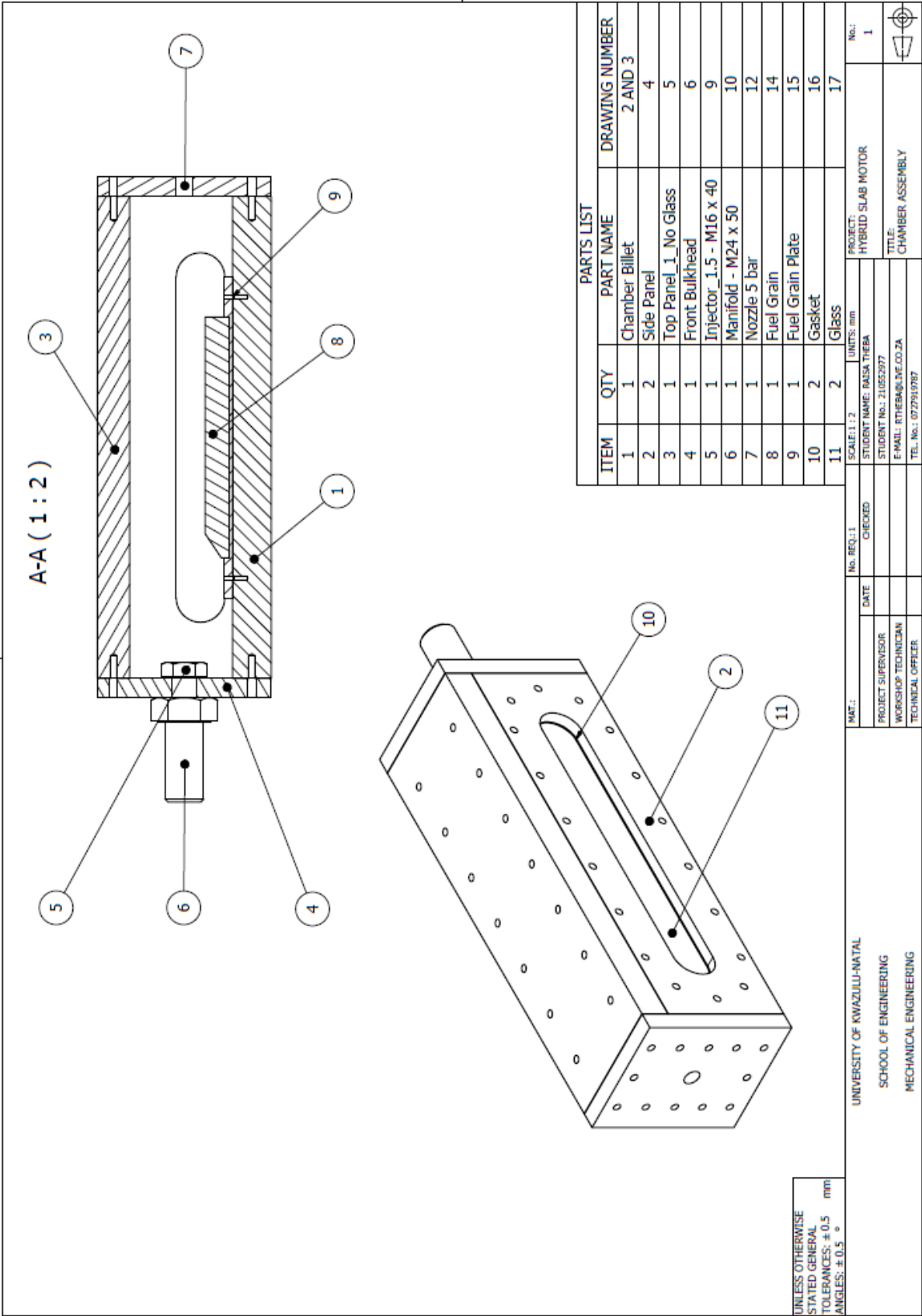
10 % COMPRESSION SET			
Compression (%)	10	Strain	0.1
Gasket thickness (mm)	1.5	Sealing stress required (MPa)	5
Glass thickness (mm)	14	Clamping force, Fc (N)	29948.23
Groove in brass height (mm)	15.5	Torque, T (Nm)	29.94823
Young's Modulus (MPa)	50	Preload force, Fi (N)	14974.115
Gasket Pressurised Area (mm ²)	5989.646		
Bolt diameter (m)	0.005		
Yield (%)	50		
Compression thickness (mm)	0.15		
Compressed gasket thickness (mm)	1.35		
Combined glass and gasket thickness (mm)	16.7		
Recess in steel (mm)	1.2		

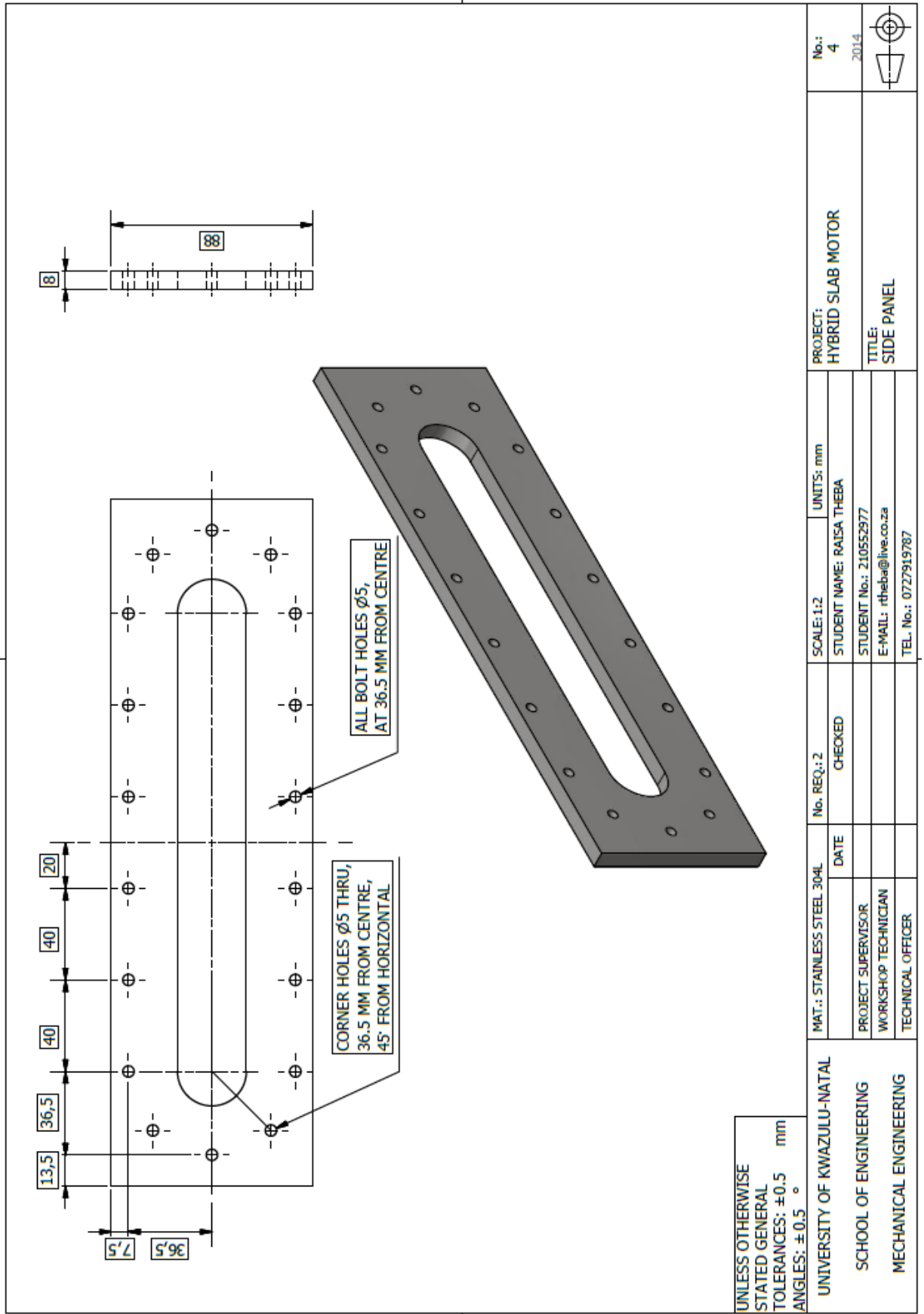
5% Compression Set:

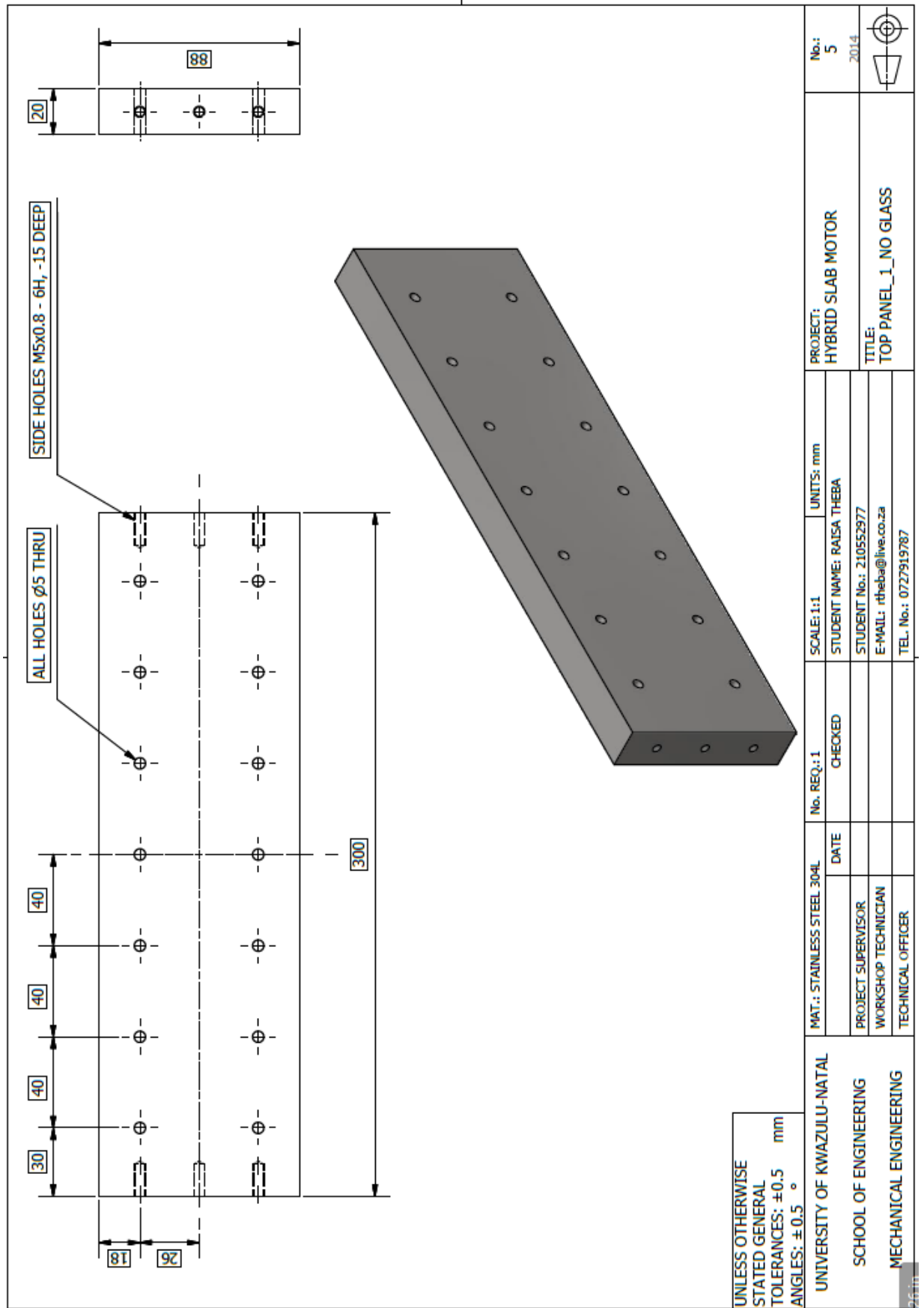
5 % COMPRESSION SET				
Compression (%)	5		Strain	0.05
Gasket thickness (mm)	1.5		Sealing stress required (MPa)	2.5
Glass thickness (mm)	14		Clamping force, Fc (N)	14974.115
Groove in brass height (mm)	15.5		Torque, T (Nm)	14.974115
Young's Modulus (MPa)	50		Preload force, Fi (N)	7487.0575
Gasket Pressurised Area (mm^2)	5989.646			
Bolt diameter (m)	0.005			
Yield (%)	50			
Compression thickness (mm)	0.075			
Compressed gasket thickness (mm)	1.425			
Combined glass and gasket thickness (mm)	16.85			
Recess in steel (mm)	1.35			

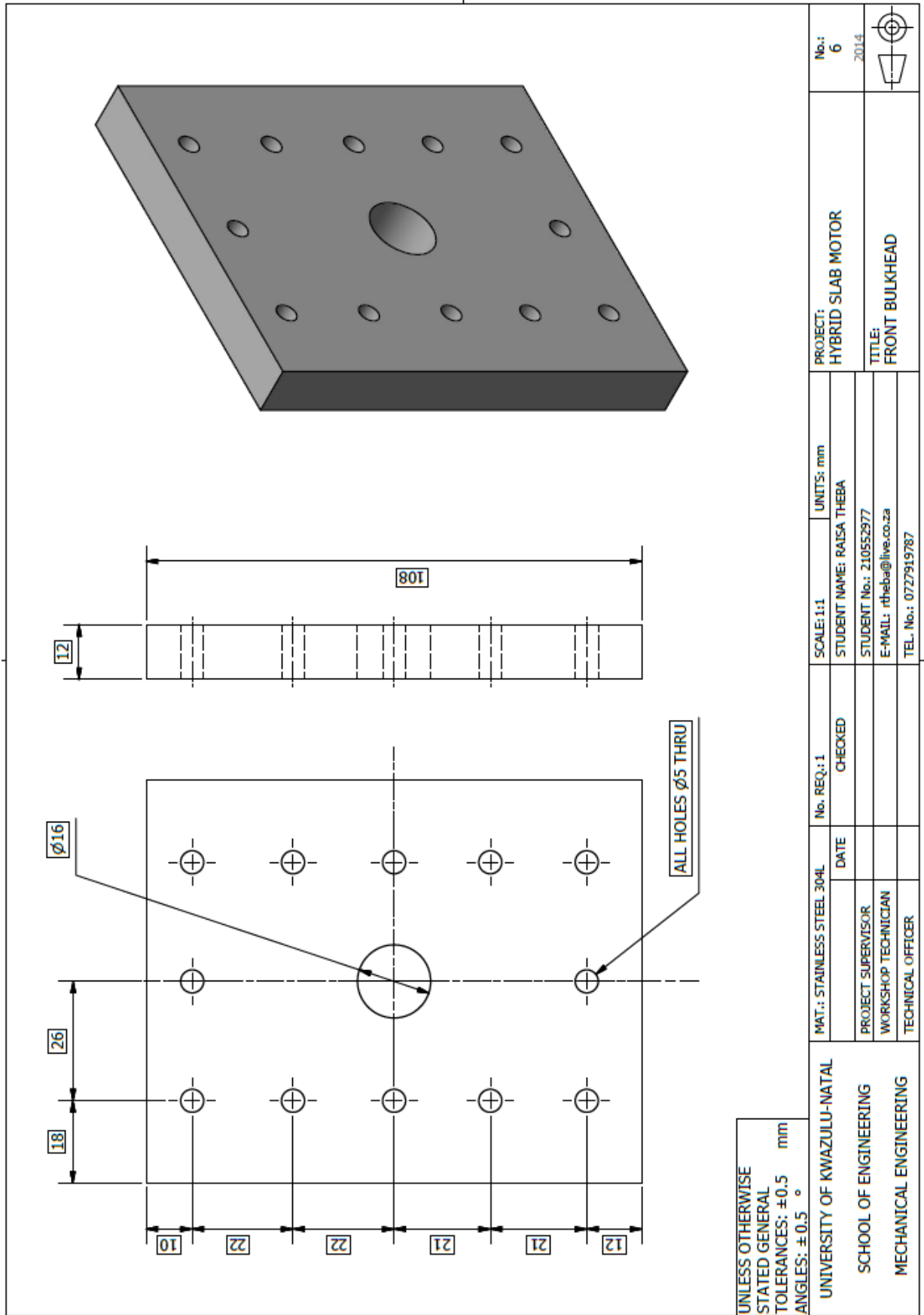
APPENDIX 4H

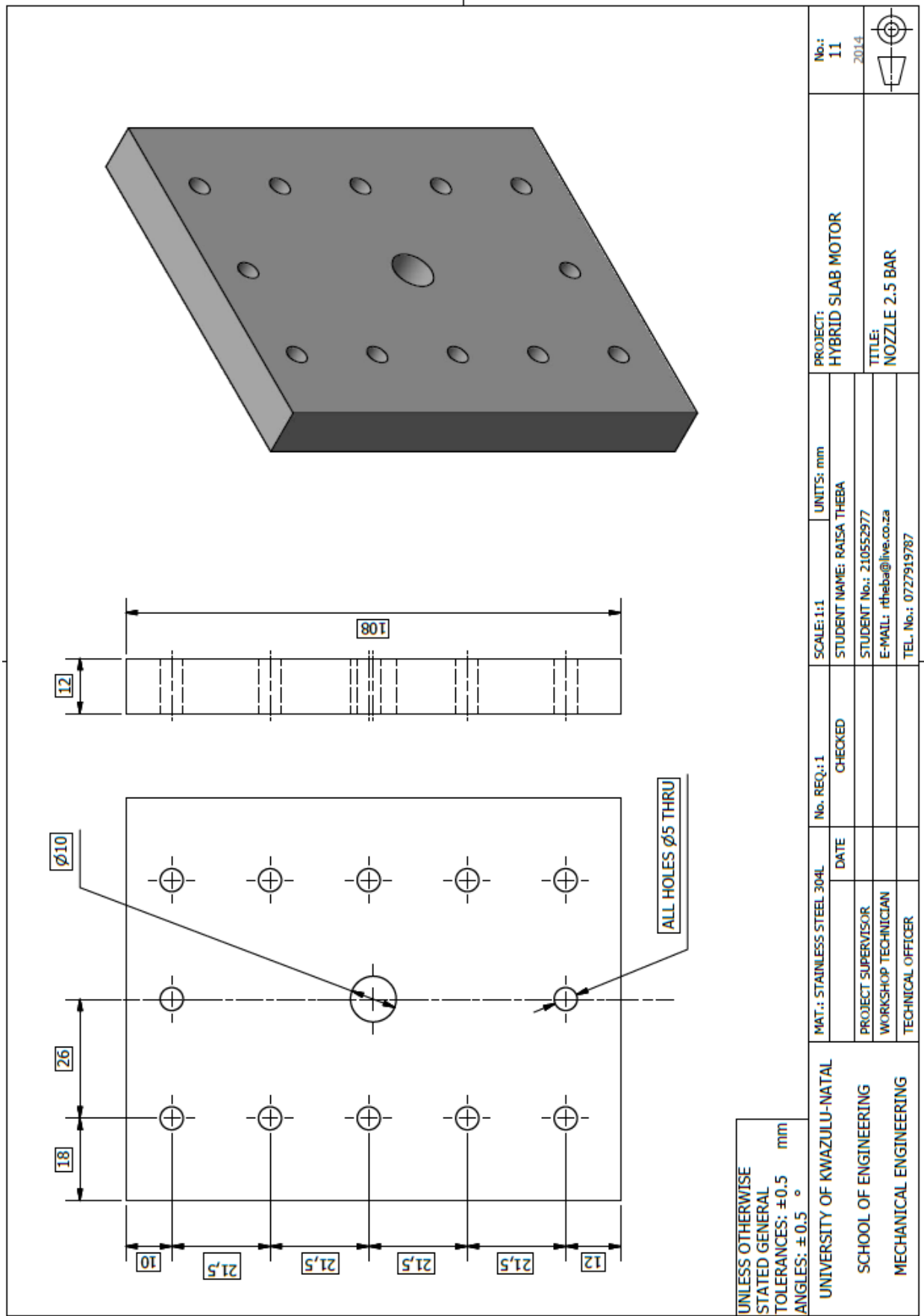
Engineering Drawings

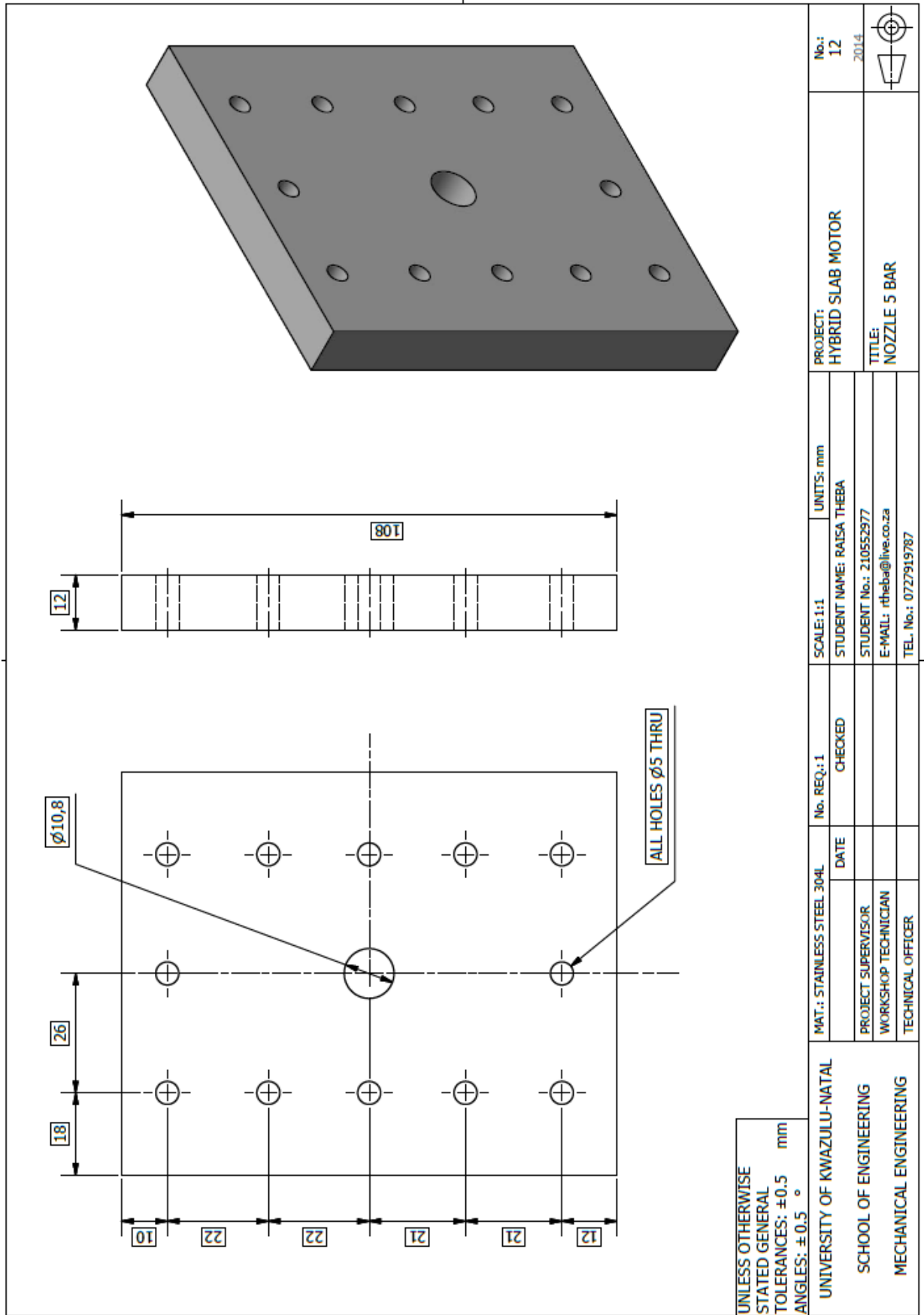


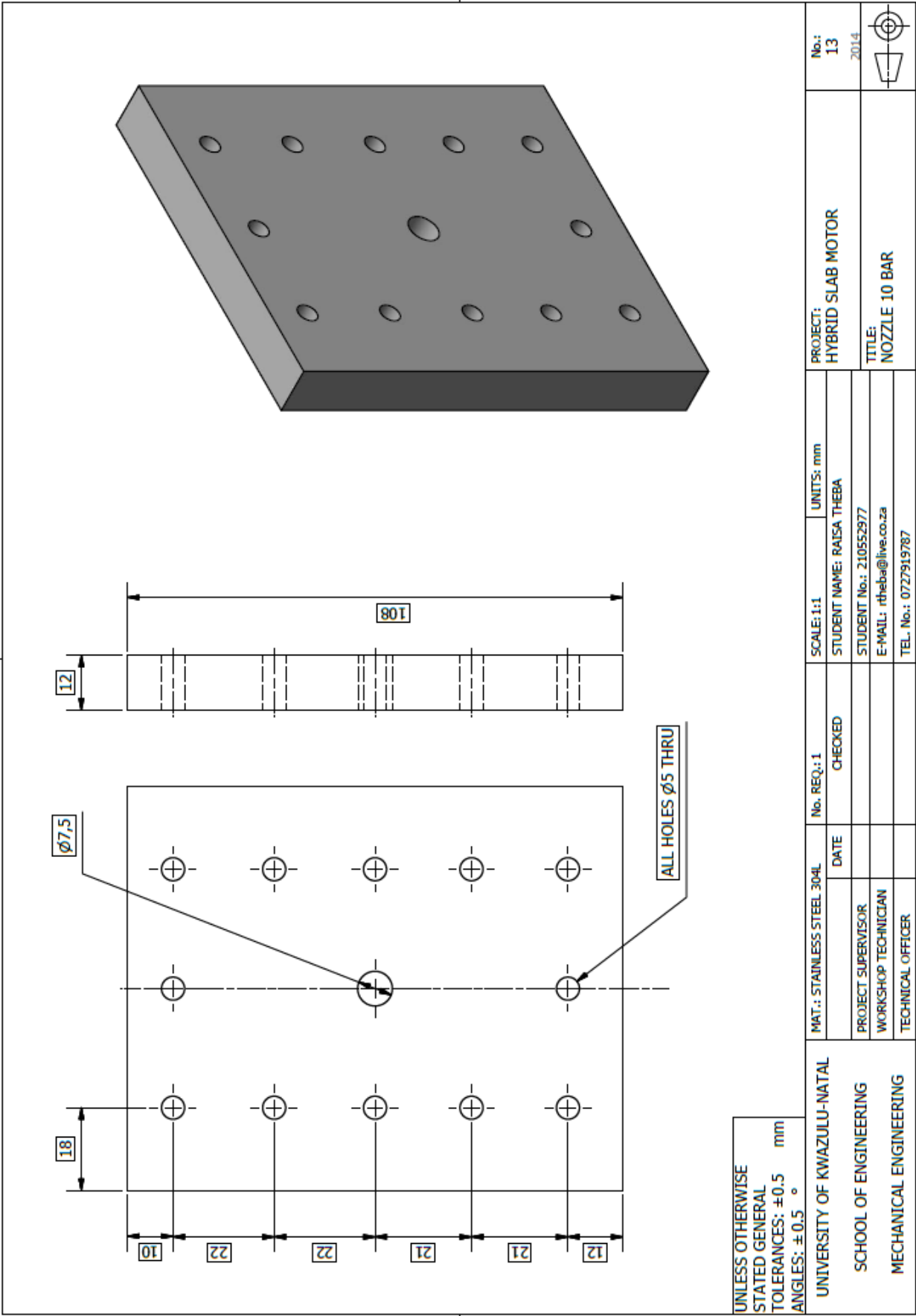


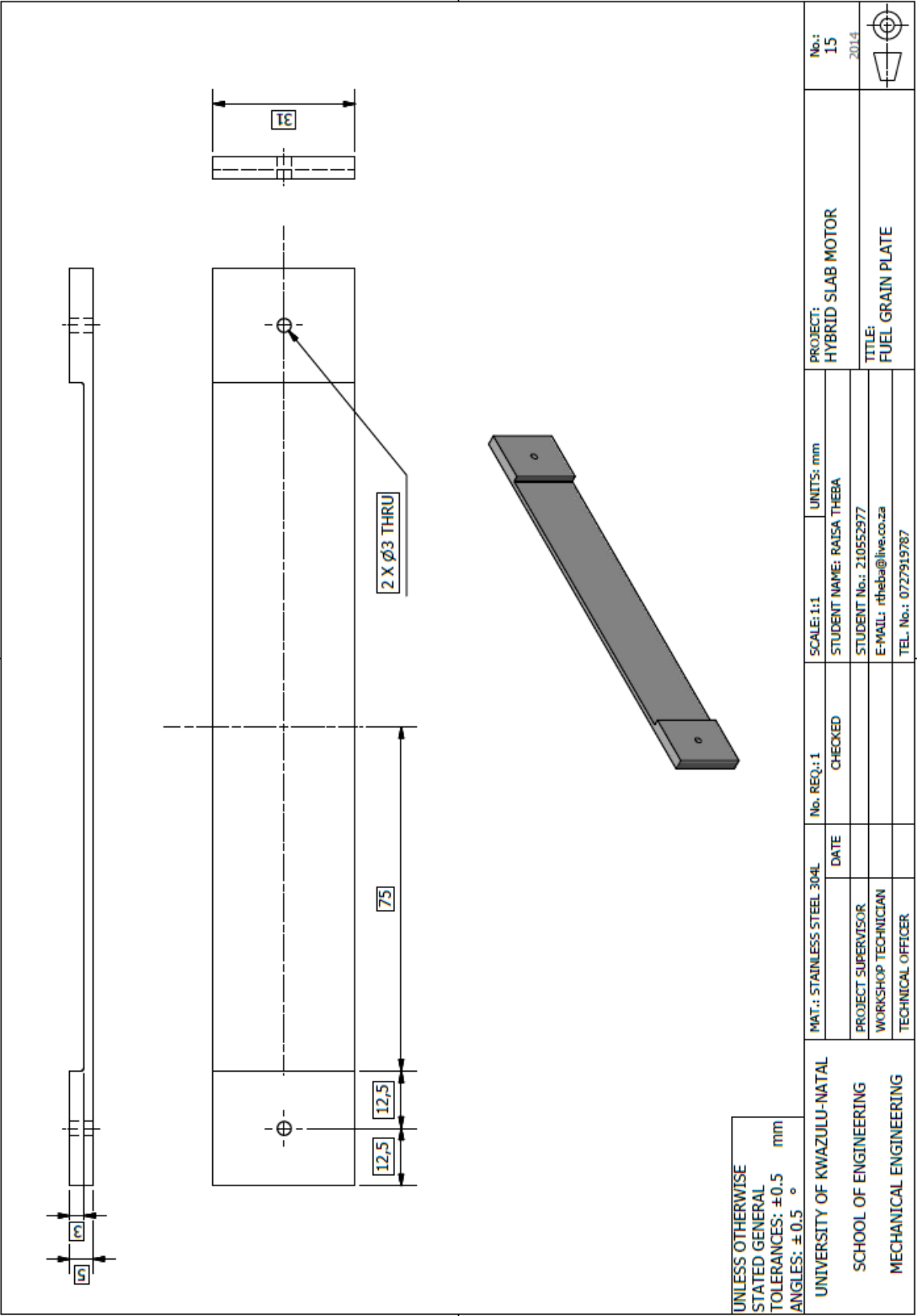


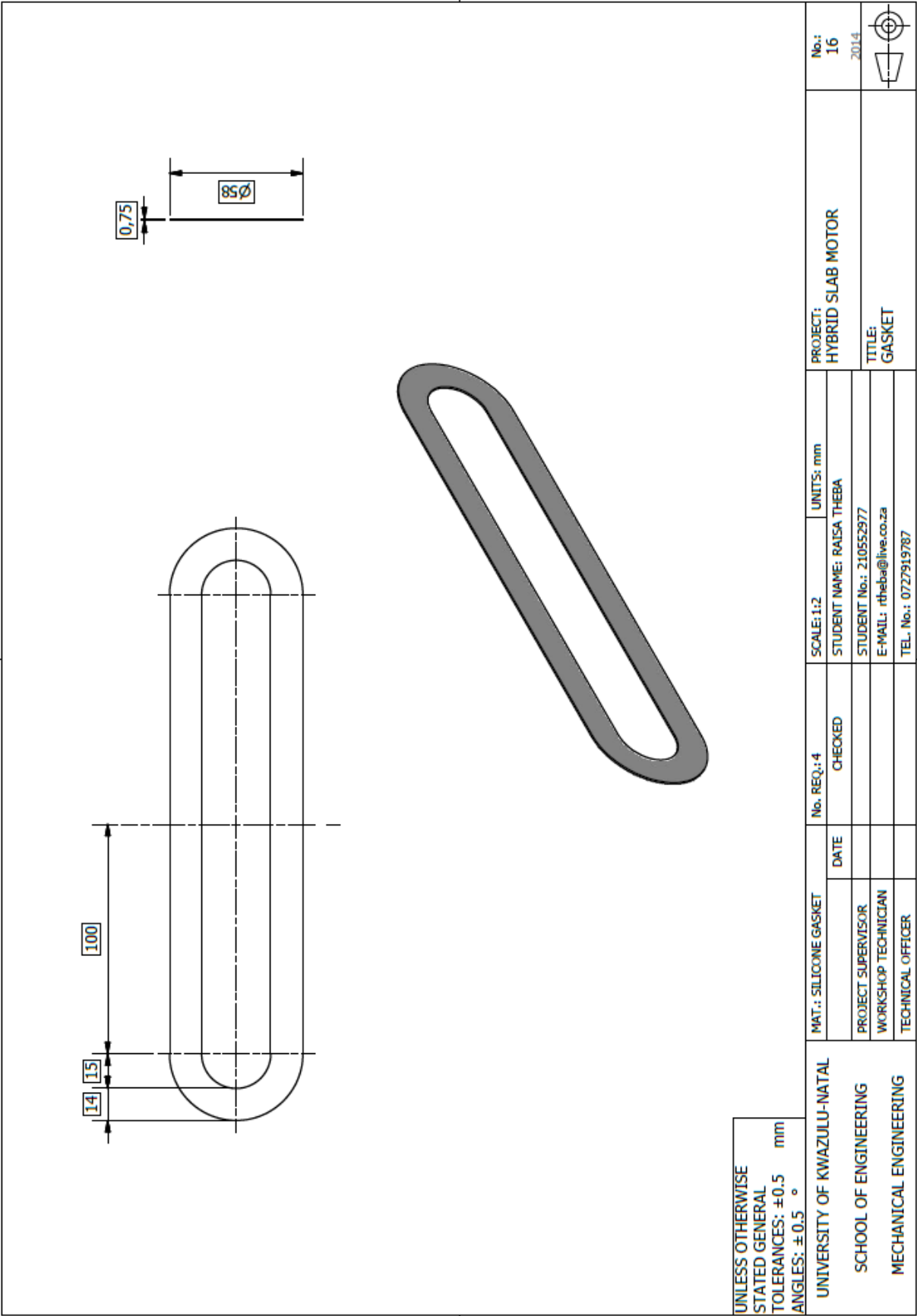


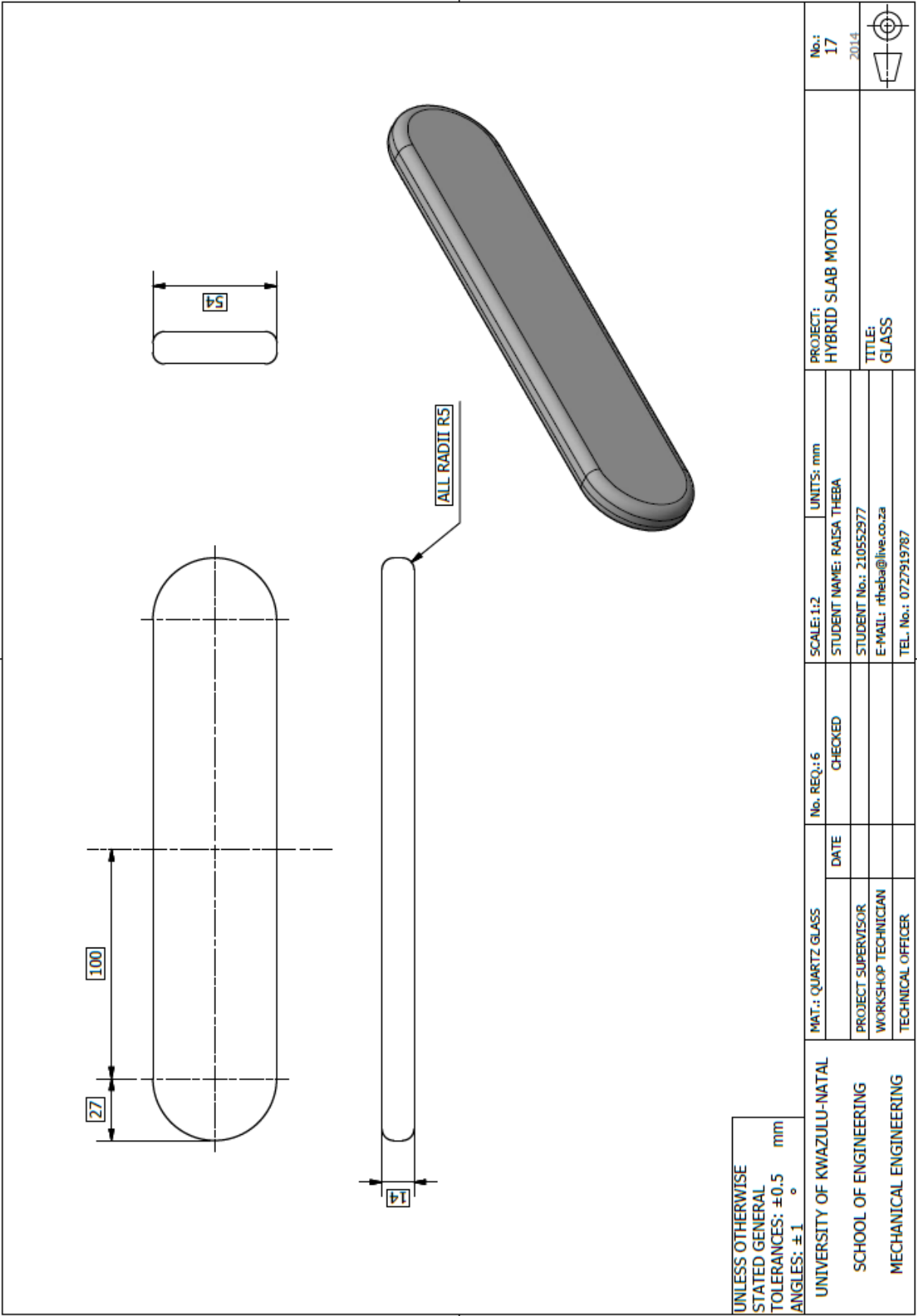












UNLESS OTHERWISE
STATED GENERAL
TOLERANCES: ± 0.5 mm
ANGLES: $\pm 1^\circ$

PARTS LIST				
ITEM	MATERIAL	QTY	PART NAME	DRAWING NUMBER
1	Aluminium 6061	1	Aluminium Fuel Grain Mould_1	1
2	Aluminium 6061	1	Aluminium Fuel Grain Mould_2	2

MAT.: ALUMINIUM		No. REQ.: 1	SCALE: 1:1	UNITS: mm	PROJECT: HYBRID SLAB MOTOR	No.: 18
DATE		CHECKED	STUDENT NAME: RAISA THEBA			2014
PROJECT SUPERVISOR			STUDENT No.: 210552977		TITLE: FUEL GRAIN MOULD	
WORKSHOP TECHNICIAN			E-MAIL: rtheba@live.co.za			
TECHNICAL OFFICER			TEL. No.: 0727919787			

UNIVERSITY OF KWAZULU-NATAL

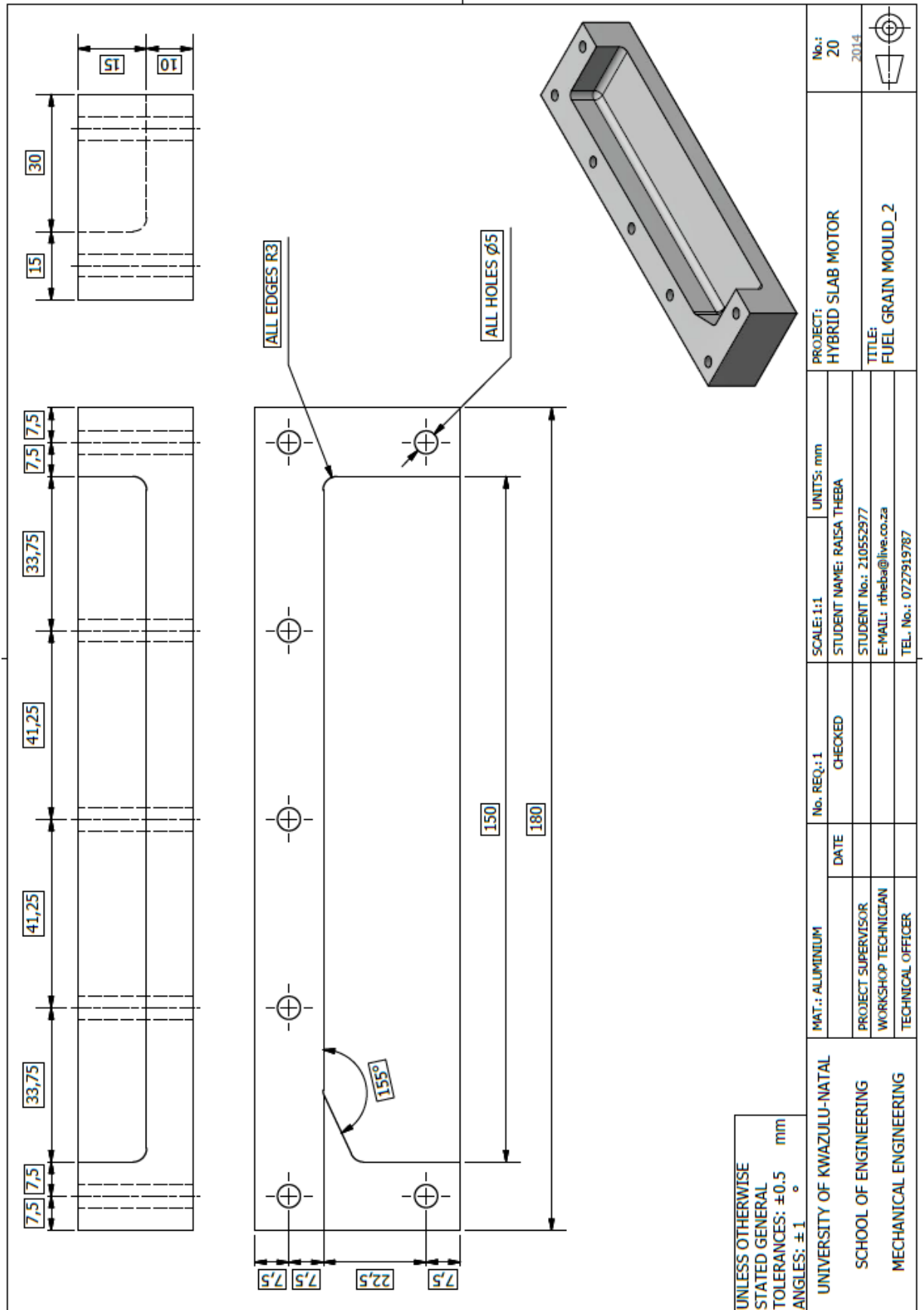
SCHOOL OF ENGINEERING

MECHANICAL ENGINEERING

UNIVERSITY OF KWAZULU-NATAL

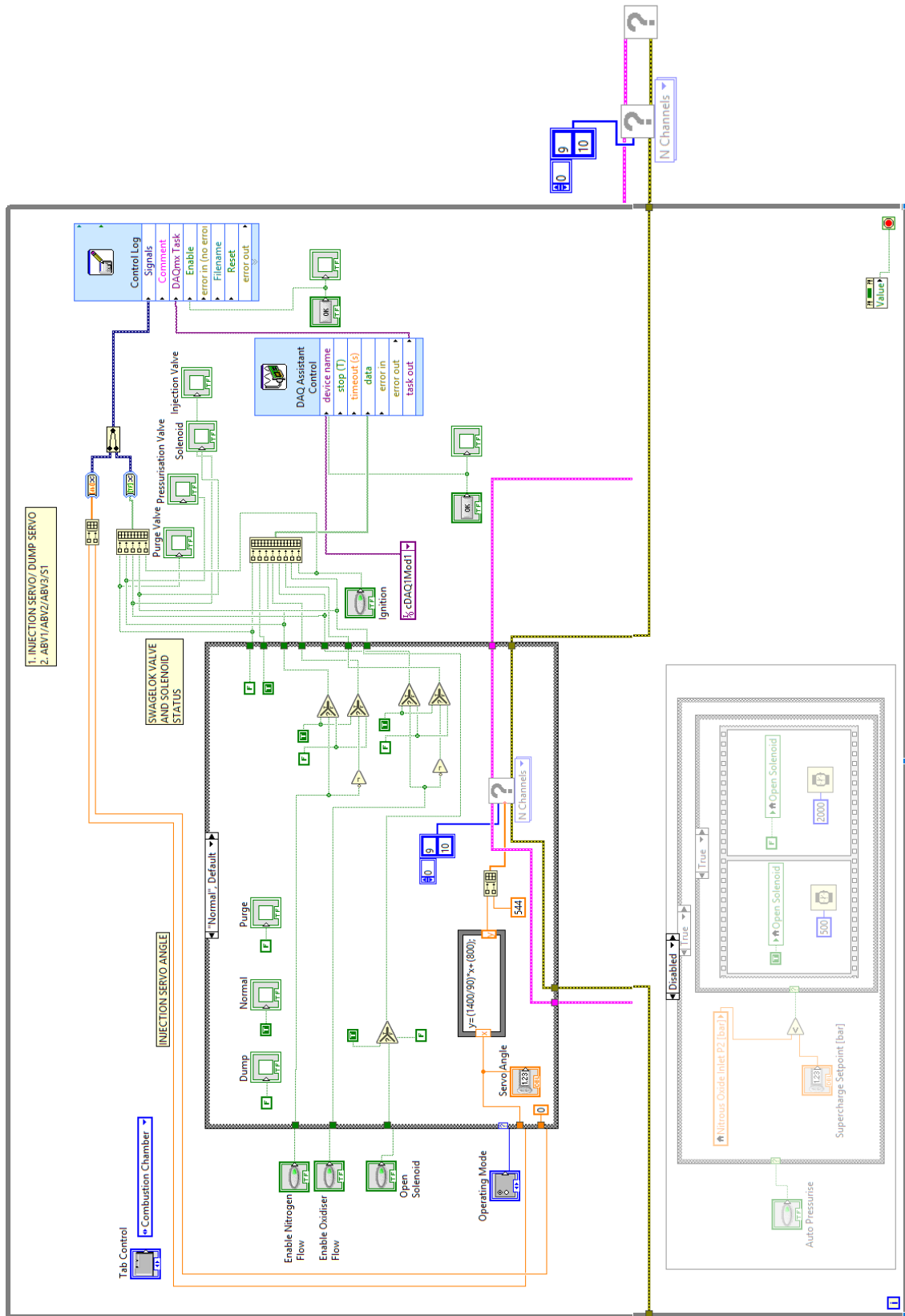
SCHOOL OF ENGINEERING

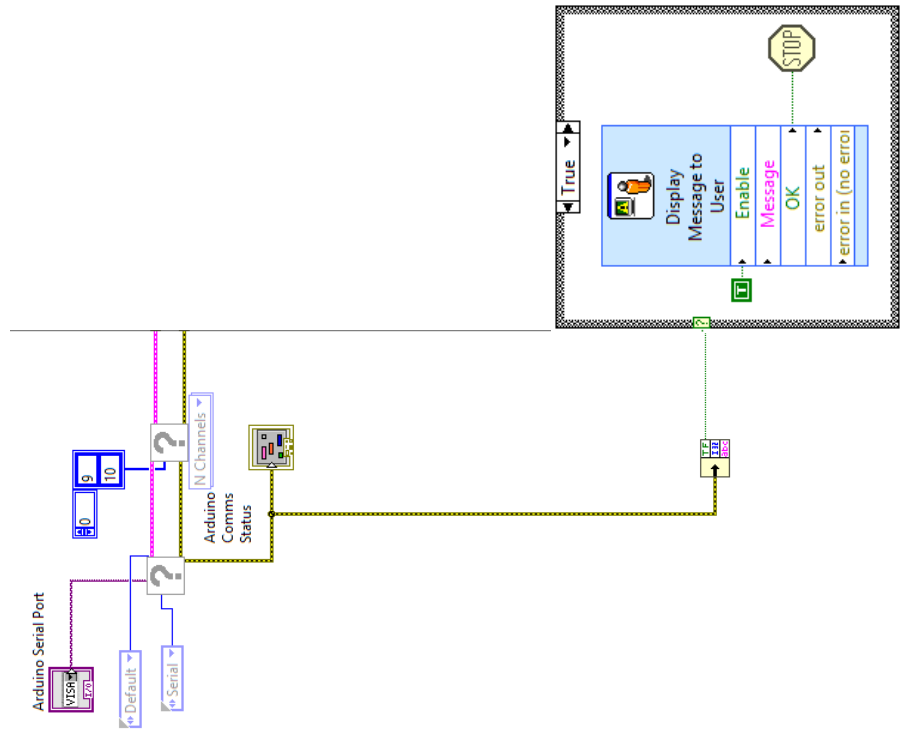
MECHANICAL ENGINEERING



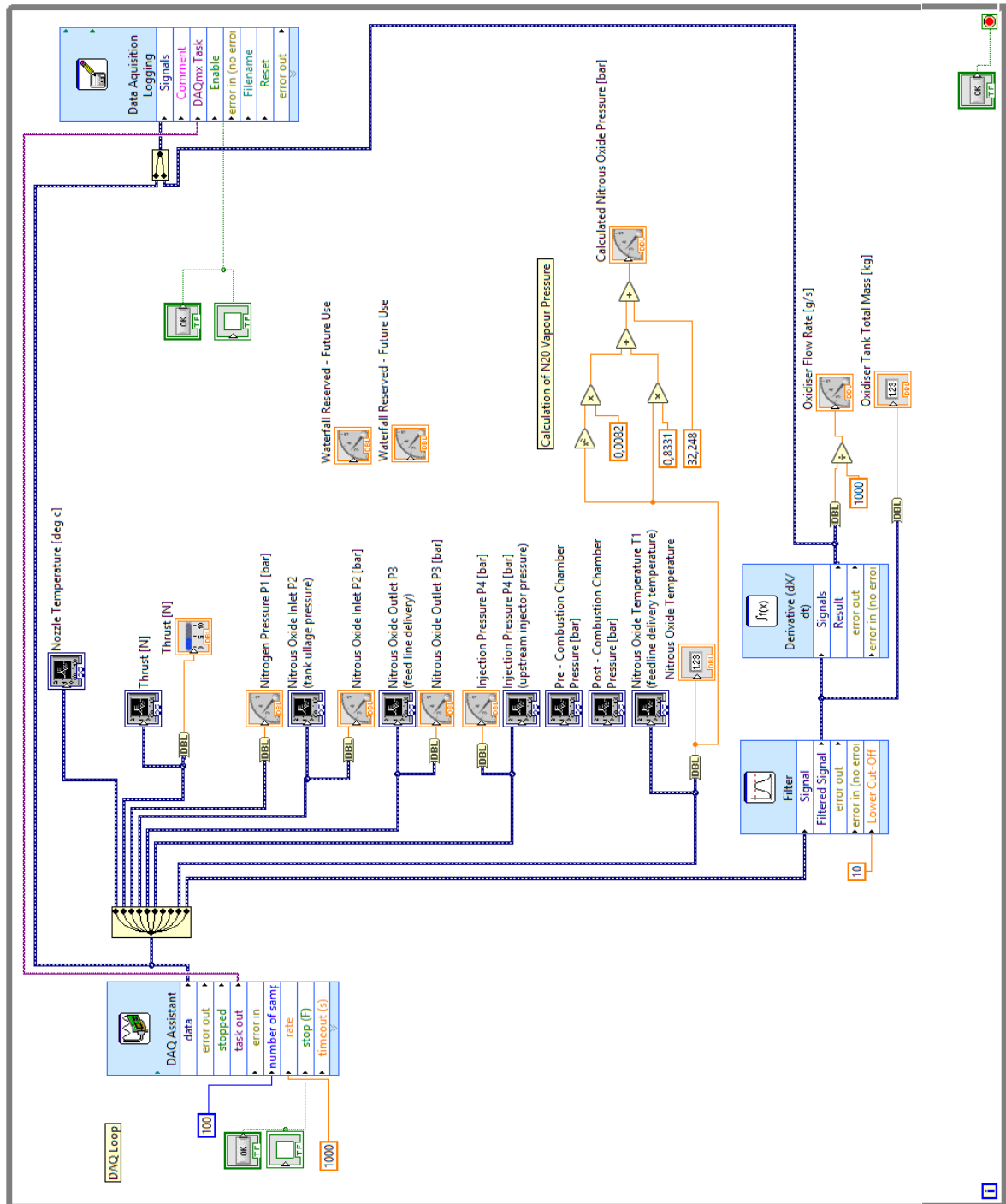
APPENDIX 5A

Control terminal – Control block diagram

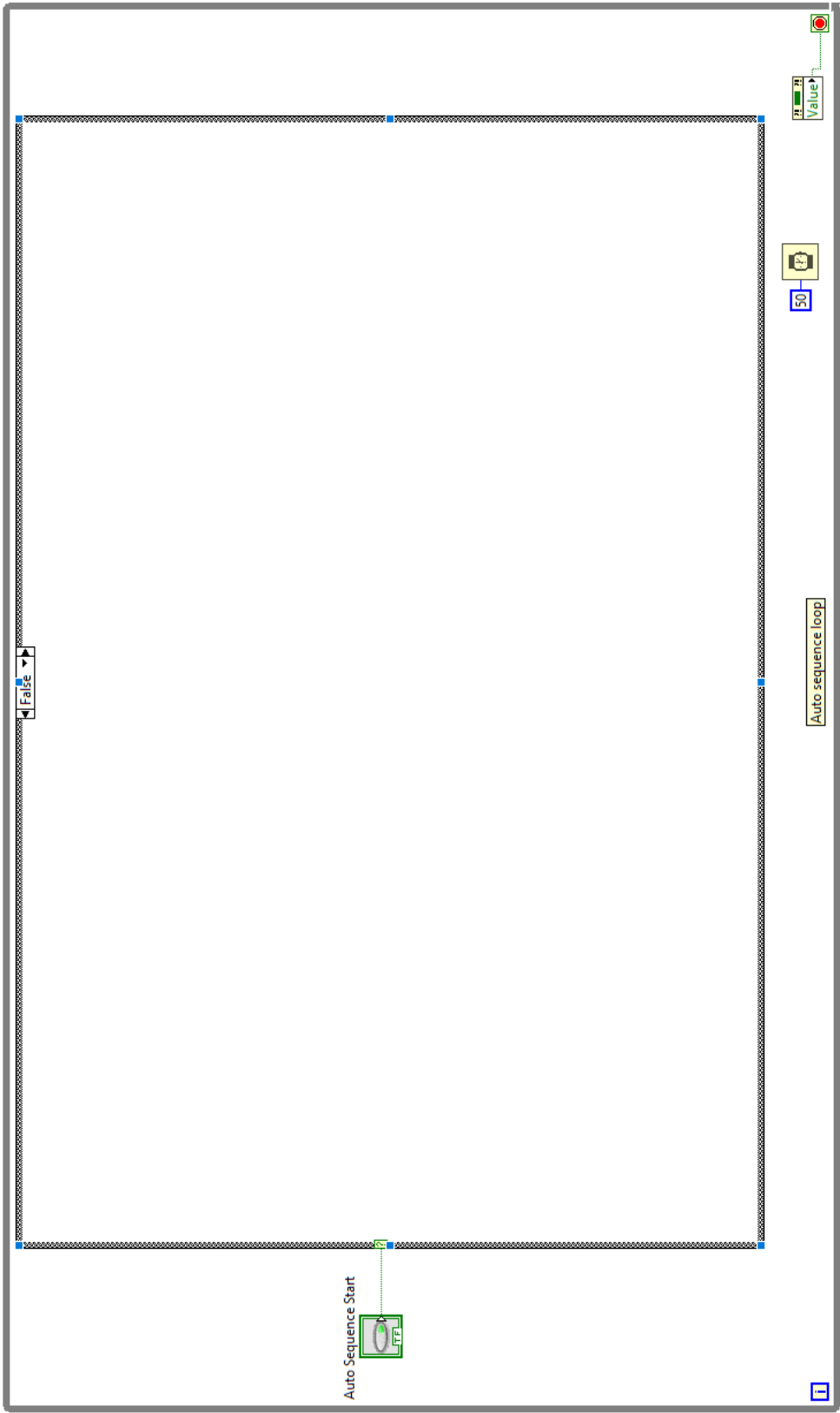




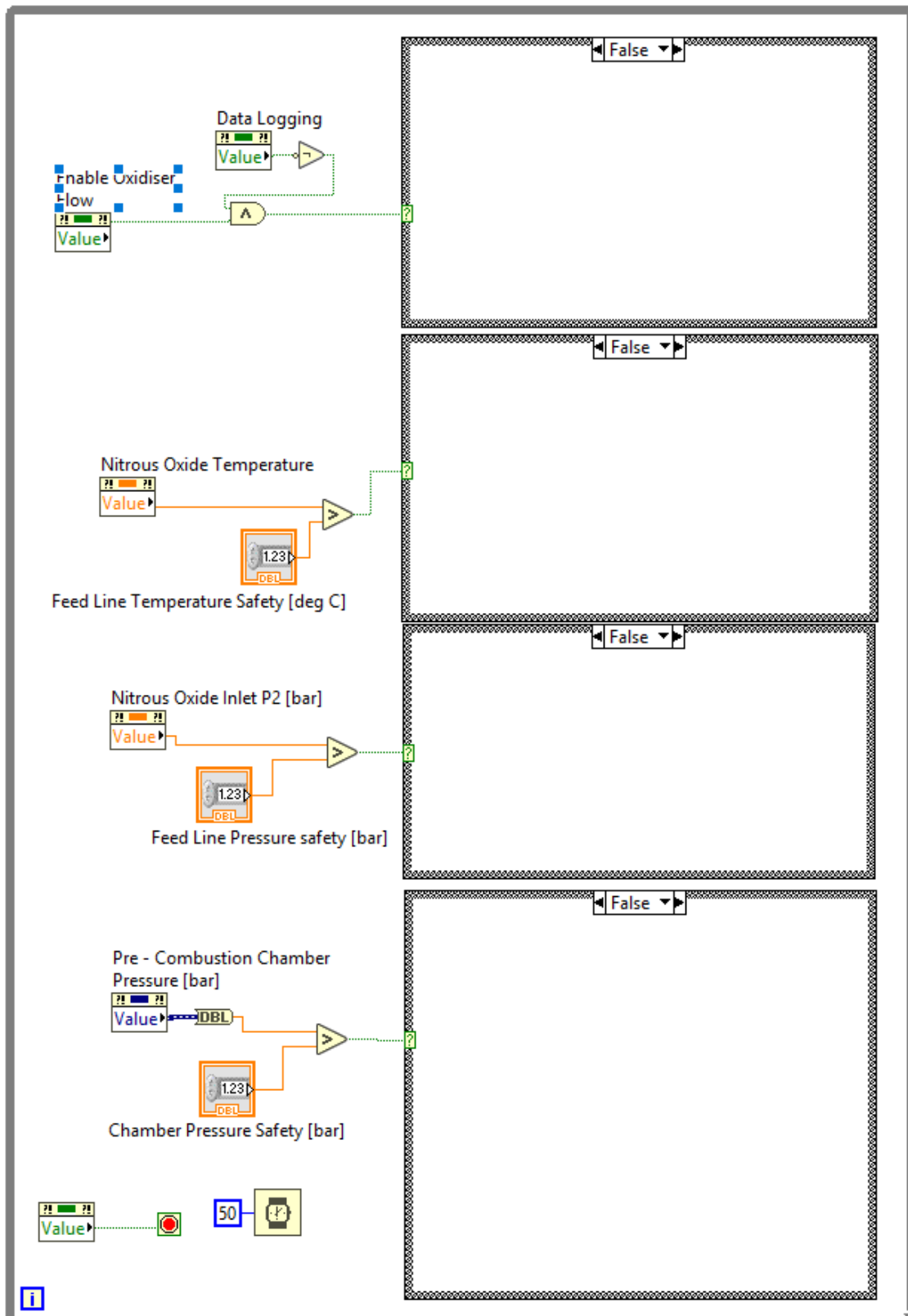
Control terminal – Data acquisition block diagram



Auto - Sequence



Message handling box – Safety



APPENDIX 5B



Propulsion System Test Report

1. Test Information

Date:

Time:

Test #:

Weather:

(Designation explanation: L for lab-scale, S for slab motor, H for hot fire, C for cold flow, 001 for test number one)

Originating Student/Academic: Raisa Theba

Test Manager: Jean Pitot

First Aid Officer: Strini Govender

Safety Marshal 1:

Safety Marshal 2:

Safety Marshal 3:

Safety Marshal 4:

Safety Marshal 5:

EMERGENCY CONTACT INFORMATION

METRO FIRE: 031 361 0000

AMBULANCE: 10177

NETCARE: 082 911

2. Test Details

Oxidiser	Nitrous Oxide (N ₂ O)
Oxidiser Mass [kg]	
Fuel	Paraffin Wax
Fuel Grain Mass [kg]	
Additive	
Additive Mass Fraction	
Pressurant	Nitrogen
Igniter used	

Igniter delay: ____ seconds

Intermediate valve position: ____

Intermediate valve delay: ____

Burn time: ____ seconds

Purge time: ____ seconds

Technical objectives:

3. Advanced Test Preparation Checklist

Item	Tick	Comment:
Test all electronics systems		
Fill N2O run tank		
Seal N2O run tank fittings		
Store N2O run tank in cage 3		
Prepare fuel grain cartridge		
Measure fuel grain mass and volume		
Note down fuel grain dimensions, particularly thickness		
Inspect and clean glass windows		
Inspect glass gaskets and fix into chamber		
Load glass windows into chamber		
Epoxy grain cartridge onto fuel grain fixing plate		
Load grain cartridge into chamber		
Fix chamber onto stand		
Install igniter in chamber		
Test igniter for electrical continuity		
Inspect chamber gaskets		
Close chamber and tighten bulkhead bolts		
Charge battery		
Email test notification to ME Department		
Email test notification to Workshop Manager		
Confirm Workshop Manager has received notification		
Confirm availability of safety marshals		

4. Test Day Preparation Checklist

Item	Tick	Comment
Move test stand to test area		
Power system up		
Test all valves		
Verify auto sequence (dry run)		
Move N2O run tank to test area		
Move N2 tank to test area		
Position fire extinguishers		
Position first aid kit		
Connect N2O run tank		
Connect N2 tank		
Flush main injection line with N2O		
Set N2 regulator pressure		
Confirm all manual ball valves are open		
Confirm N2 dump valve is closed		
Confirm live feed camera is operational		
Confirm battery connection is made		
Confirm igniter electrical continuity		
Position Go-Pro cameras		
Start Go-Pro camera recording		
Confirm test area vacated		
Dispatch safety marshals		

5. Pre-Test Checklist

Item	Tick	Comment
Conduct test briefing		
Confirm rooms 138A and 138B are vacated		
Confirm north entrance is locked		
Confirm lift hold is in place		
Confirm safety marshals are in position		
Confirm fire extinguishers are in place		
Confirm first aid kit is in place		
Confirm that eye and ear protection is being worn		
Confirm system pressures and temperatures		
Confirm range clearance with safety marshal 1		
Confirm range clearance with safety marshal 2		
Confirm range clearance with safety marshal 3		
Confirm range clearance with safety marshal 4		
Confirm range clearance with safety marshal 5		
Verify auto sequence parameters correct		

6. Startup Sequence Checklist

Item	Tick	Comment
Notify marshals of startup sequence commencement		
Enable N2 flow		
Supercharge N2O tank		
Check temperature T1 <40 degrees C		
Enable oxidizer flow		

Confirm no leaks in N2 and N2O lines		
Begin data logging		
Confirm Fluids Lab is clear		
Notify marshals of auto sequence commencement		
Start auto sequence		

7. Post-Test Checklist

Item	Tick	Comment
Check live feed camera for fires or leaks		
Check N2O tank pressure and temperature		
Verify that all other parameters are nominal		
Confirm data & control logging has been turned off		
Confirm data has been saved		
Confirm all automated valves are closed position, except "ENABLE OXIDISER FLOW" valve		
Move to test area		
Close all manual valves		
Break N2O seal and allow venting		
Declare test area safe		
Notify safety marshals of test completion		

8. General Comments

APPENDIX 7A

Dimension changes

Table 7A.9.1: Initial, final, change and average dimensions for the first successful hot fire test

SH003			
Initial Dimensions			
	Width	Thickness	Length
	29	17	148,5
Final Dimensions			
Front	21,87	14,4	139,75
Back	23,75	15,18	
Average	22,81	14,79	
Final Dimension Changes			
Front	7,13	2,6	8,75
Back	5,24	1,82	
Average	6,185	2,21	

Table 7A.9.2: Initial, final, change and average dimensions for the second successful hot fire test

SH004			
Initial Dimensions			
	Width	Thickness	Length
	29,7	20	149,64
Final Dimensions			
Front	23,49	13,76	139,89
Back	23,1	15,91	
Average	23,30	14,84	
Final Dimension Changes			
Front	6,21	6,24	9,75
Back	6,6	4,09	
Average	6,405	5,165	

Table 7A.9.3: Initial, final, change and average dimensions for the third successful hot fire test

SH005			
Initial Dimensions			
	Width	Thickness	Length
	29	19	148
Final Dimensions			
Front	20,57	13,52	138,39
Back	22,11	14,36	
Average	21,34	13,94	
Final Dimension Changes			
Front	8,43	5,48	9,61
Back	6,89	4,64	
Average	7,66	5,06	

Mass changes

Table 7A.9.4: Final mass calculations for the first successful hot fire test

SH003			
	Initial	Final	Difference
Mass (g)	68,9	40,7	28,2

Table 7A.9.5: Final mass calculations for the second successful hot fire test

SH011			
	Initial	Final	Difference
Mass (g)	78,2	39,9	38,3

Table 7A.9.6: Final mass calculations for the third successful hot fire test

SH012			
	Initial	Final	Difference
Mass (g)	71,5	32,9	38,6

Volume changes

Table 7A.9.7: Volumetric differences before and after the first successful hot fire test

SH003			
	Initial	Final	Difference
Volume (cm ³)	69	41	28

Table 7A.9.8: Volumetric differences before and after the second successful hot fire test

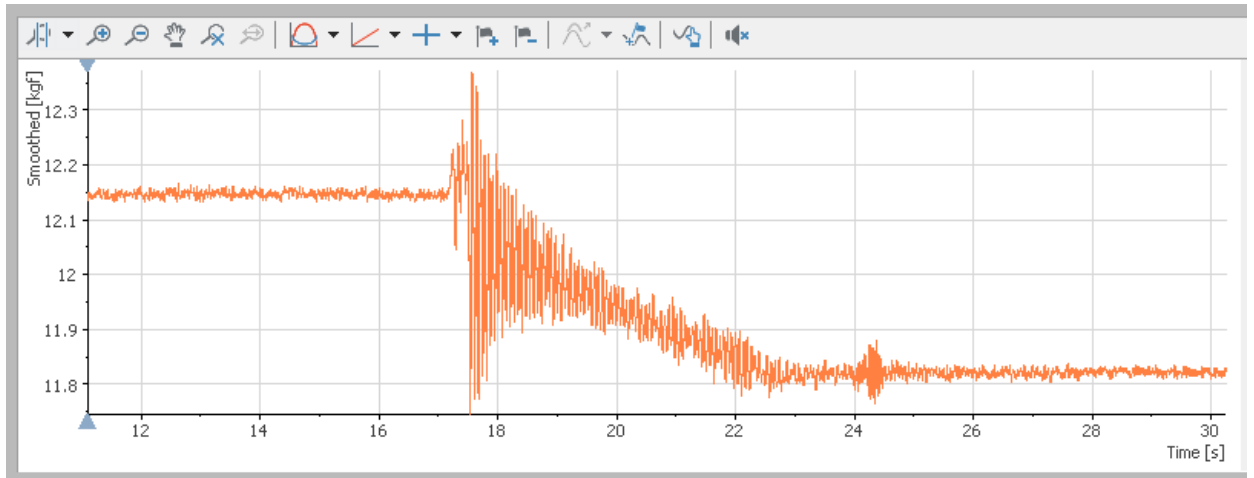
SH011			
	Initial	Final	Difference
Volume (cm ³)	78	40	38

Table 7A.9.9: Volumetric differences before and after the third successful hot fire test

SH012			
	Initial	Final	Difference
Volume (cm ³)	72	32	40

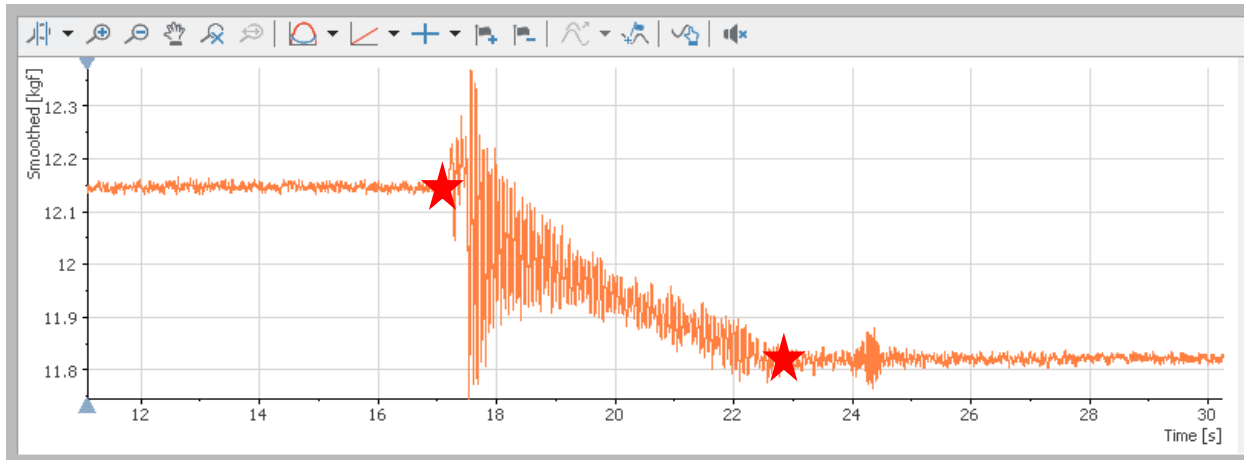
APPENDIX 7B

Test 1 - Tank measurement/oxidiser mass flow rate calculations



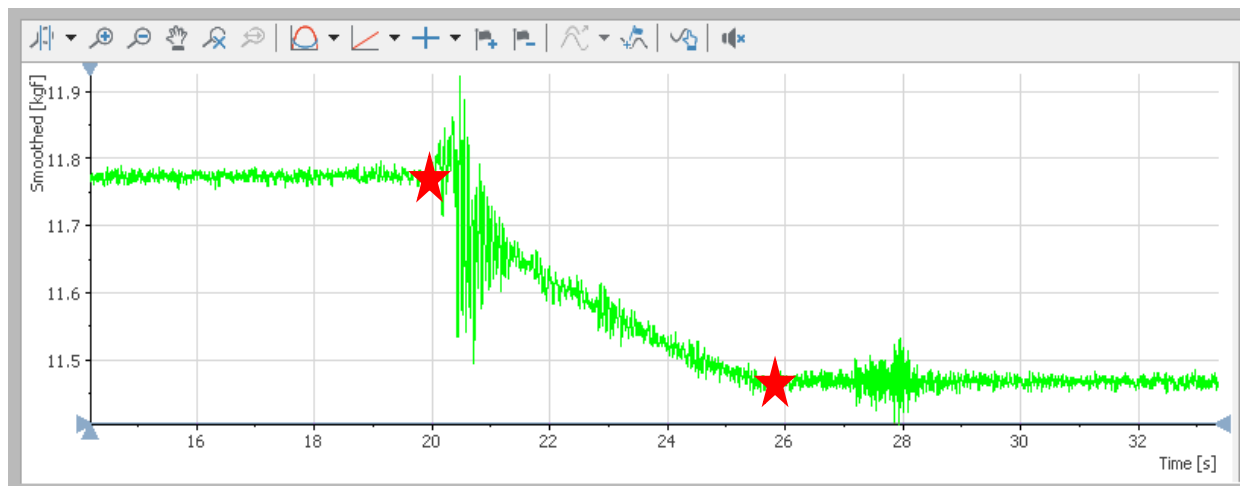
$$\frac{x}{y} = \frac{12.48 - 12.13}{318.83 - 313.24} = 0.0626118 \text{ kg/s}$$

Test 2 - Tank measurement/oxidiser mass flow rate calculations



$$\frac{x}{y} = \frac{11.77 - 11.47}{25.51 - 20.15} = 0.05597015 \text{ kg/s}$$

Test 3 - Tank measurement/oxidiser mass flow rate calculations



$$\frac{x}{y} = \frac{12.14 - 11.82}{22.86 - 17.23} = 0.05683837 \text{ kg/s}$$